

Titre: Bioinspired Tough Materials with Microstructured Sacrificial Bonds
Title: Based on Instability-Assisted 3D Printing

Auteur: Shibo Zou
Author:

Date: 2020

Type: Mémoire ou thèse / Dissertation or Thesis

Référence: Zou, S. (2020). Bioinspired Tough Materials with Microstructured Sacrificial Bonds Based on Instability-Assisted 3D Printing [Ph.D. thesis, Polytechnique Montréal].
Citation: PolyPublie. <https://publications.polymtl.ca/5521/>

 **Document en libre accès dans PolyPublie**
Open Access document in PolyPublie

URL de PolyPublie: <https://publications.polymtl.ca/5521/>
PolyPublie URL:

Directeurs de recherche: Frederick Gosselin, & Daniel Therriault
Advisors:

Programme: Génie mécanique
Program:

POLYTECHNIQUE MONTRÉAL

affiliée à l'Université de Montréal

**BIOINSPIRED TOUGH MATERIALS WITH MICROSTRUCTURED
SACRIFICIAL BONDS BASED ON INSTABILITY-ASSISTED 3D
PRINTING**

SHIBO ZOU

Département de génie mécanique

Thèse présentée en vue de l'obtention du diplôme de *Philosophiæ Doctor*

Génie mécanique

Décembre 2020

POLYTECHNIQUE MONTRÉAL

affiliée à l'Université de Montréal

Cette thèse intitulée:

BIOINSPIRED TOUGH MATERIALS WITH MICROSTRUCTURED SACRIFICIAL BONDS BASED ON INSTABILITY-ASSISTED 3D PRINTING

présentée par **Shibo ZOU**

en vue de l'obtention du diplôme de *Philosophiæ Doctor*

a été dûment acceptée par le jury d'examen constitué de :

M. Eduardo-Antonio-Julian RUIZ, président

M. Frédérick GOSSELIN, membre et directeur de recherche

M. Daniel THERRIAULT, membre et codirecteur de recherche

M. Louis LABERGE LEBEL, membre

M. Jianyu LI, membre externe

DEDICATION

To my grandfather, Baojia Guo (郭保甲).

ACKNOWLEDGEMENTS

I am sincerely grateful for all the guidance and encouragement from my supervisors Prof. Frédéric Gosselin and Prof. Daniel Therriault. They gave me this fantastic opportunity to work in the field of three-dimensional printing of advanced materials, led me into critical and creative thinking, and taught me a lot of research skills through out the over five years of my PhD study. They encouraged me to attend many international conferences and supported me to explore collaboration opportunities with researchers in Germany. They also very generously gave me the opportunities to work on an 8-month industrial project about buckling analysis in a leading aerospace company and to contribute to a COVID-19 box project to help out local hospitals during the pandemic. I feel fortunate and grateful to have them as my PhD supervisors. Their professionalism, kindness and supportiveness will continue inspiring me to be someone like them in my life.

I would like to thank everyone who helped and supported me since the beginning of my PhD study. I appreciate the precious technical advice and assistance from Martin Cardonne, Isabelle Nowlan, Bénédict Besner, Yanik Landry-Ducharme, Jean-Marie Béland, Anic Desforges, Christian-Charles Martel, and Nour Aimene. I am thankful for all the insightful discussions and suggestions from Dr. Fubin Tu, Dr. Masoud Hassani, Dr. Kambiz Chizari, Dr. Rouhollah Farahani, Dr. Sri Markandeya Rajesh Ponnada, Dr. Sampada Bodkhe, Dr. Qinghua Wu, Dr. Ilyass Tabiai, Dr. Chao Xu, Dr. Hongqiu Wei, Dr. Pierre Faucheux, Dr. Bill Baloukas, and Dr. Mohammad Rafiee. I acknowledge the lab and equipment access kindly provided by Prof. Njuki Mureithi, Prof. Nick Virgilio, Prof. Marie-Claude Heuzey, Prof. Eduardo-Antonio-Julian Ruiz, Prof. Thomas Gervais, Prof. Stéphane Étienne, and Prof. Cédric Béguin. I thank Nadine Bernardini for her help on all the purchases.

My colleagues at LM² gave me tremendous help and support during my PhD study. I am thankful for Renaud Passieux and Leigh Guthrie's guidance at the beginning of my project. I thank Yun Yi Lau, Pauline Emschwiller, Hajar Zulaikha Zulkifli, Raul Sainz Villamayor, Sebastian Fierro, Mathieu Beuparlant and Yago Pego Martínez for their help on my project during their internship at LM². I would like to thank Yahya Abderrafai and Rui Tao for their generous help with my experiments. I appreciate Tanja Pelzman and Dr. Amrita Bag's reviewing of my paper. I would like to thank all my LM² colleagues for giving me such a wonderful time at Polytechnique Montréal.

RÉSUMÉ

Une ténacité élevée est requise pour les matériaux structuraux dans de nombreux systèmes d'ingénierie critiques pour la sécurité, tels que le pare-brise d'avion et le confinement des soufflantes de moteurs à réaction. La capacité du matériau à dissiper l'énergie et à résister aux défauts est essentielle pour maintenir l'intégrité structurelle et la sécurité du système en présence de petites fissures ou d'une charge d'impact soudaine. En outre, la multifonctionnalité est souvent requise pour les matériaux de structure, tels que les matériaux légers et la transparence optique, ce qui rend le développement de tels matériaux structuraux un grand défi d'ingénierie.

La soie d'araignée surpasse la plupart des matériaux synthétiques en termes de ténacité spécifique. Le bris des liens hydrogènes sacrificiels et l'extension des chaînes protéiques cachées contribuent à la grande extensibilité et à la dissipation d'énergie élevée de la soie. L'introduction des liens sacrificiels et des longueurs cachées dans les matériaux d'ingénierie traditionnels est prometteuse pour fabriquer des matériaux structuraux à haute ténacité avec des multifonctionnalités. L'impression 3D assistée par instabilité offre un moyen facile de fabriquer des fibres thermoplastiques microstructurées avec des liens sacrificiels et des longueurs cachées. L'instabilité fluide du filament de polymère fondu sur une imprimante 3D de fabrication de filaments fondus (FFF) est exploitée pour induire le phénomène de bouclage, créant des liens faiblement soudés et des structures bouclantes le long de la fibre qui sont analogues aux liens sacrificiels et aux longueurs cachées dans la structure moléculaire de la soie d'araignée, respectivement. Le but de cette thèse est de développer des matériaux résistants bioinspirés avec des liens sacrificiels microstructurés et des longueurs cachées basées sur l'impression 3D assistée par instabilité.

Le développement antérieur de fibres de poly(acide lactique) (PLA) microstructurées par impression 3D assistée par instabilité a souffert de défaillances prématurées, dans lesquelles le squelette de la fibre se fracture avant la rupture de tous les liens sacrificiels. Les défaillances prématurées empêchent les longueurs cachées d'être complètement libérées, ce qui entraîne une ténacité de la fibre microstructurée parfois aussi basse que 25% de celle de la fibre droite de référence. Afin de comprendre les mécanismes derrière les défaillances prématurées, nous avons effectué une analyse complète des défaillances des fibres de PLA microstructurées par des tests mécaniques, des caractérisations par microscopie électronique à balayage (MEB) et des

simulations numériques. Nous avons constaté qu'une contrainte de traction locale élevée induit une initiation de fissure au niveau du squelette de la fibre pendant la déformation couplée flexion-torsion-tension du bouclage de dépliage. La simulation par éléments finis non linéaire montre que l'extension du bouclage de fibre implique une déformation plastique à grande échelle qui contribue à l'essentiel de la dissipation d'énergie.

Par la suite, nous avons mis en œuvre le mécanisme de renforcement des liens sacrificiels et des longueurs cachées à l'échelle microscopique dans un composite transparent absorbant l'énergie. Un processus d'impression facile a été développé pour créer un tissu de fibre de polycarbonate (PC) microstructuré bidirectionnel qui a ensuite été intégré dans une matrice élastomère pendant un processus d'infiltration de résine. La faible adhérence entre la fibre PC et la matrice élastomère permet aux liens sacrificiels de se rompre librement à l'intérieur de la matrice. Sous l'impact, les boucles cachées se déplient après le bris du lien et la fissuration de la matrice, résistant à la pénétration de l'impacteur avec une rupture gracieuse. Le composite présente une absorption d'énergie élevée et une hystérésis de 95.6% (énergie dissipée / énergie totale absorbée \times 100%), qui sont analogues au comportement de dissipation d'énergie des toiles d'araignées lors de la capture des proies. La combinaison de fibres PC transparentes et d'une matrice élastomère transparente avec des indices de réfraction similaires ($n_{\text{fiber}} = 1.58$ et $n_{\text{matrix}} = 1.55$) se traduit par une transmittance optique élevée ($\sim 89\%$) et une faible diffusion de la lumière ($\sim 11\%$).

Nous avons également étudié le mécanisme de défaillance et la tolérance aux dommages du composite absorbant l'énergie avec des fibres PC microstructurées. Des échantillons composites entaillés et non entaillés sollicités en cisaillement pur avec des fibres microstructurées unidirectionnelles ont été testés dans des essais de traction uniaxiale pour comprendre les interactions entre la propagation des fissures, le bris du lien et l'extension du bouclage. Nous avons constaté que la déformation et la rupture du matériau composite sont dominées par la rupture multiple des liens sacrificiels à l'échelle micrométrique et la fracture multiple de la matrice élastomère à l'échelle macroscopique. Le composite présente une très grande zone de dissipation d'énergie à la fois à l'avant et derrière le fond de fissure pendant la propagation de la fissure, ce qui entraîne une courbe de résistance croissante. La combinaison des fibres microstructurées et des fibres droites dans le composite élastomère entraîne une augmentation d'environ 17 fois de la

rigidité et une augmentation d'environ 7 fois de l'énergie totale jusqu'à la rupture par rapport à l'élastomère pur.

La stratégie de conception nouvellement développée utilise des composantes mécaniquement différentes pour obtenir une transparence élevée et une dissipation d'énergie élevée avec un processus de fabrication facile et évolutif. Notre approche ouvre une nouvelle voie pour la conception et la fabrication de composites multifonctionnels avec des capacités de dissipation d'énergie élevées à de grandes déformations pour diverses applications telles que les composants automobiles et aérospatiaux, et la capture des débris spatiaux.

ABSTRACT

High toughness is required for structural materials in many safety-critical engineering systems, such as aircraft windshield and jet engine fan containment. The capability of the material to dissipate energy and resist failure is essential to maintain the structural integrity and system security under the presence of small cracks or a sudden impact load. Also, multifunctionality is often required for structural materials, such as lightweight and optical transparency, making the development of such structural materials a great challenge in engineering.

Spider silk outperforms most synthetic materials in terms of specific toughness. The breaking of sacrificial hydrogen bonds and unfolding of hidden protein chains contribute to the silk's large extensibility and high energy dissipation. Introducing the sacrificial bonds and hidden lengths toughening mechanism into traditional engineering materials is promising to make high-toughness structural materials with multifunctionalities. Instability-assisted 3D printing provides a facile way to fabricate microstructured thermoplastic fibers with sacrificial bonds and hidden lengths. The fluid-mechanical instability of the molten polymer thread on a fused filament fabrication (FFF) 3D printer is harnessed to induce the coiling phenomenon, creating weakly fused bonds and coiling loops along the fiber which are analogous to the sacrificial bonds and hidden lengths in the molecule structure of spider silk, respectively. The purpose of this dissertation is to develop bioinspired tough materials with microstructured sacrificial bonds and hidden lengths based on instability-assisted 3D printing.

Previous development of microstructured poly(lactic acid) (PLA) fibers by instability-assisted 3D printing suffered from premature failures, in which the fiber backbone fractures before the breaking of all sacrificial bonds. The premature failures inhibit the hidden lengths from being fully released, resulting in the microstructured fiber's toughness sometimes as low as 25% of that of the benchmark straight fiber. In order to understand the mechanisms behind the premature failures, we conducted a comprehensive failure analysis of the microstructured PLA fibers through mechanical tests, scanning electron microscopy (SEM) characterization, and numerical simulation. We found that high local tensile stress induces crack initiation at the fiber backbone during the bending-torsion-tension coupled deformation of the unfolding loop. The nonlinear finite element simulation

shows that the straightening of the fiber loop involves with large-scale plastic deformation which contributes to most of the energy dissipation.

Subsequently, we implemented the sacrificial bonds and hidden lengths toughening mechanism at the microscale in a transparent energy-absorbing composite. A facile printing process was developed to create a bidirectional microstructured polycarbonate (PC) fiber fabric which was then embedded in an elastomeric matrix during a resin infiltration process. The weak adhesion between the PC fiber and the elastomeric matrix allows the sacrificial bonds to break freely inside the matrix. Under impact, the hidden loops unfold after the bond breaking and the matrix cracking, resisting the impactor penetration with a graceful failure. The composite shows high energy absorption and a hysteresis of 95.6% (dissipated energy/total absorbed energy \times 100%), which are analogous to the energy dissipating behavior of spider webs during prey capture. The combination of clear PC fibers and transparent elastomeric matrix with similar refractive indexes ($n_{\text{fiber}} = 1.58$ and $n_{\text{matrix}} = 1.55$) results in the composite's high optical transmittance ($\sim 89\%$) and low haze ($\sim 11\%$).

We further investigated the failure mechanism and damage tolerance of the energy-absorbing composite with microstructured PC fibers. Both notched and unnotched composite specimens in the pure shear geometry with unidirectional microstructured fibers were tested in uniaxial tensile tests to understand the interactions between crack propagation, bond breaking and loop unfolding. We found that the deformation and failure of the composite material are dominated by the multiple breaking of sacrificial bonds at the microscale and the multiple fracture of the elastomeric matrix at the macroscale. The composite shows a very large energy dissipation zone both ahead of and behind the crack tip during crack propagation, resulting in a rising resistance curve. Combining the microstructured fibers and straight fibers in the elastomer composite results in a ~ 17 times increase in stiffness and a ~ 7 times increase in total energy to failure compared to the neat elastomer.

The newly developed design strategy uses mechanically dissimilar components to achieve high transparency and high energy dissipation with a facile and scalable fabrication process. Our approach opens a new avenue for the design and manufacturing of multifunctional composites with high energy dissipation capabilities at large deformations for various applications such as automotive and aerospace components, and space debris capture.

TABLE OF CONTENTS

DEDICATION	III
ACKNOWLEDGEMENTS	IV
RÉSUMÉ.....	V
ABSTRACT.....	VIII
TABLE OF CONTENTS	X
LIST OF TABLES	XIV
LIST OF FIGURES.....	XV
LIST OF SYMBOLS AND ABBREVIATIONS.....	XXIX
CHAPTER 1 INTRODUCTION.....	1
1.1 Background	1
1.2 Dissertation structure.....	3
CHAPTER 2 LITERATURE REVIEW.....	4
2.1 Sacrificial bonds and hidden lengths (SBHL) mechanism.....	4
2.1.1 Spider silk and other biological materials	4
2.1.2 Analytical modeling of SBHL.....	9
2.2 Bioinspired engineering design with SBHL.....	12
2.2.1 Single-network method	12
2.2.2 Double-network method.....	18
2.3 Instability-assisted deposition	24
2.3.1 Liquid rope coiling	24
2.3.2 Fluid-mechanical sewing machine	26
2.3.3 Engineering applications	30

CHAPTER 3	RESEARCH OBJECTIVES AND COHERENCE OF ARTICLES.....	36
3.1	Problem identification.....	36
3.2	Research objectives.....	36
3.3	Coherence of articles.....	37
CHAPTER 4	ARTICLE 1: FAILURE MECHANISMS OF COILING FIBERS WITH SACRIFICIAL BONDS MADE BY INSTABILITY-ASSISTED FUSED DEPOSITION MODELING.....	39
4.1	Introduction.....	40
4.2	Results and discussion.....	42
4.3	Conclusion.....	53
4.4	Methods.....	53
4.4.1	Instability-assisted fused deposition modeling.....	53
4.4.2	Uniaxial tensile test.....	54
4.4.3	Three-point bending test.....	54
4.4.4	Finite element analysis.....	54
4.5	Supporting information.....	58
4.5.1	Local strain calculation.....	58
4.5.2	Multilinear plastic FEA.....	60
4.5.3	Tensile curves of straight fibers.....	61
4.5.4	Strain rate estimation.....	61
4.5.5	Differential scanning calorimetry (DSC) test of large and small fibers.....	63
4.5.6	Toughness enhancement.....	64

CHAPTER 5	ARTICLE 2: SPIDERWEB-INSPIRED, TRANSPARENT, IMPACT-ABSORBING COMPOSITE	65
5.1	Introduction	65
5.2	Results and discussion.....	68
5.2.1	Fabric printing and mechanical characterization	68
5.2.2	Composite fabrication and optical characterization	71
5.2.3	Impact test and failure analysis	74
5.3	Conclusion.....	79
5.4	Experimental procedures.....	80
5.4.1	Fabric printing	80
5.4.2	Composite fabrication	82
5.4.3	Optical characterization.....	82
5.4.4	Mechanical characterization.....	83
5.5	Supporting information	91
5.5.1	Refractive index of the materials	91
5.5.2	Properties of the two elastomers	91
5.5.3	Two-layer fiber fabric based on Brun et al.'s model.....	92
5.5.4	Matrix-fiber debonding	94
5.5.5	Static puncture test	94
5.5.6	Contact force-time curves from the impact tests.....	96
5.5.7	Optical images of fractured specimens	97
5.5.8	Cyclic tests of alternating fiber composite specimens	98
5.5.9	Impact behavior of low RI and high RI elastomer composites	99
5.5.10	Optical sensing	99

5.5.11	Geometric model by Brun et al.	102
5.5.12	Volume flow rate calibration on the Prusa printer	103
5.5.13	Resin infiltration.....	105
5.5.14	Design of the falling dart.....	106
5.5.15	Calibration of the force sensor	107
5.5.16	Impact tester calibration	108
CHAPTER 6 ARTICLE 3: TOUGHENING ELASTOMERS VIA MICROSTRUCTURED THERMOPLASTIC FIBERS WITH SACRIFICIAL BONDS AND HIDDEN LENGTHS		110
6.1	Introduction	111
6.2	Experiments.....	114
6.2.1	Microstructured fiber printing	114
6.2.2	PDMS-Microstructured Fiber Composite Fabrication.....	115
6.2.3	Mechanical testing.....	116
6.3	Results and discussion.....	117
6.4	Conclusion.....	125
CHAPTER 7 GENERAL DISCUSSION.....		132
CHAPTER 8 CONCLUSION AND RECOMMENDATIONS.....		136
8.1	Conclusion.....	136
8.2	Recommendations	137
BIBLIOGRAPHY		139

LIST OF TABLES

Table 2.1 Comparison of different bioinspired engineering design methods with SBHL.....	23
Table 4.1 Toughness values of the small fiber with three coiling loops. The benchmark toughness value of the straight fiber is 1.1 kJ/kg.....	64
Table 5.1 Comparison of the physical and mechanical properties of the low RI ⁶⁶⁻⁶⁸ and high RI ⁶⁹ elastomer.....	91
Table 5.2 Calculation of the volume flow rate correction factor C_1 for eight different printing parameter settings. Eight fibers were produced for each setting. Due to the small weight of each fiber, the eight fibers were measured together on a balance, then the weight was divided by eight to get the average value as the measured extruding mass in this table.....	103

LIST OF FIGURES

- Figure 2.1 a) Stress-strain curves of spider dragline silk and capture silk [22]. b) Hysteresis (the ratio of dissipated energy to total absorbed energy) of spider dragline silk and capture silk [22].4
- Figure 2.2 a) Schematic of the fibrous structure in spider dragline silk [30]. b) Hierarchical structure of spider dragline silk consisting of scanning electron microscope (SEM) image of the silk thread, atomic force microscopy (AFM) image of the silk fibrils, and a schematic of the molecular structure in a silk fibril segment [31].5
- Figure 2.3 Structural origin of the nonlinear material behavior of spider dragline silk [32]. a) Stress-strain curve of the spider dragline silk consisting of three regimes: I, homogenous stretching; II, onset of yielding due to the breaking of hydrogen bonds and unfolding of the intramolecular β -sheet in the non-crystalline domain; III, onset of the breaking of β -crystallite. b) Schematic of the unfolding of the intramolecular β -sheet and the breaking of β -crystallite.5
- Figure 2.4 Single-molecule force spectroscopy of recombinant spider dragline silk protein [34]. a) Schematic of the single-molecule force spectroscopy. b) Force-extension curve of one protein molecule.7
- Figure 2.5 a) Force-extension curve of a single titin fragment by AFM [5]. The saw-tooth pattern was fitted by the wormlike chain (WLC) model through 28–29 nm stepwise increases in the contour length of the protein chain, which are close to the total length (30 nm) of individual titin immunoglobulin (Ig)-like domain. b) Force-extension curve of the organic adhesives between nacre tablets by AFM [3]. c) Force-extension curve of the mineralized collagen fibrils in bone by AFM [4]. d) Molecule model with tandem modular structures [3].8
- Figure 2.6 Basic principle of the SBHL mechanism. a) Schematic of the breaking of a sacrificial bond and unfolding of a hidden length. b) The comparison of energy absorption by breaking a sacrificial bond and unfolding a hidden length based on WLC model. [38].10
- Figure 2.7 Different molecule configurations and their simulated pulling curves based on WLC model [38]. (a) Two parallel molecules: one with sacrificial bonds breaks in the order of bond strength, the other acts as an exponential spring. The pulling curve shows increasing rupture

forces. (b) Six molecules in parallel with same end bond strength. The length increment of adjacent molecules is constant. The pulling curve shows decreasing rupture forces. 11

Figure 2.8 Stacked-cup carbon nanofiber. a) Schematic of the continuous cone-helix structure [13].

b) Transmission electron microscopy (TEM) image of the continuous helical graphene sheet unravelled from the hollow fiber [41]. The average periodical length of the helical graphene sheet matches exactly the average perimeter of the fiber cross section (214 nm). 13

Figure 2.9 Schematic of the interaction between the stacked-cup CNFs and a propagating crack

with SEM images of embedded nanofibers splaying between adjacent graphene layers and exposed nanofibers unraveling continuously after the matrix cracking [13]. 14

Figure 2.10 Microstructured PLA fiber with sacrificial bonds and hidden lengths. a) Stress-strain

curves of a straight fiber and a microstructured fiber [15]. b) SEM images of the corresponding tested straight fiber and microstructured fiber [15]. c) Optical images of the premature failures of microstructured PLA fibers printed by instability-assisted fused filament fabrication (IFFF) [16]. 15

Figure 2.11 Carbon nanotube microfibers with a slip knot. a) Schematic of the sliding of the hidden

length in a knotted fiber [49]. b) SEM image of a microscale slip knot of a carbon nanotube microfiber (dia. = 31 μm) [50]. The carbon nanotube microfiber was made by a dry-spinning process of drawable carbon nanotube arrays. The slip knot was introduced with a tweezer. c) Stress-strain curves of the carbon nanotube microfiber with slip knots at different tightening levels [50]. 17

Figure 2.12 3D-printed hydrogel modular structure [17]. a) Schematic of the modular design of

sacrificial bonds and backbone chain. b) Load-displacement curve of the 3D-printed hydrogel modular structure with five sacrificial bonds and corresponding snapshots of the tensile test. 18

Figure 2.13 Double-network (DN) composite based on the polyamide fabric mesh and VHB tapes

[51]. a) Schematic of the DN composite. b) Stress-strain curves of the VNB tape, fabric mesh and DN composite with test snapshots of the DN composite. c) Fabric mesh fragmentation inside the VHB tape. 19

- Figure 2.14 Double-network composite fiber with a low-melting-point metal core and a polymer shell [52]. a) Schematic of the composite fiber. b) Multiple breaks of the metal core inside the polymer shell. c) Tensile curves of the metal core fiber, hollow polymer fiber, and composite fiber.20
- Figure 2.15 Double-network composite with a low-melting-point metal mesh and a hydrogel matrix [53]. a) Optical images of the metal mesh and hydrogel composite. b) Tensile curves of the metal mesh, hydrogel matrix, and composite.....21
- Figure 2.16 Double-network composite with a 3D-printed acrylate-based plastic mesh and a silicone elastomer matrix [54]. a) Schematic of the double-network composite. b) Tensile curves of the plastic mesh, elastomer matrix and composite.22
- Figure 2.17 Coiling phenomenon in various materials. (a) Honey [58]. (b) Silicone oil (PDMS) [59]. (c) Glucose syrup [60]. (d) Molten glass [62]. (e) Elastic rod [61].....24
- Figure 2.18 Dimensionless coiling frequency $\Omega = (\nu/g^2)^{1/3}$ versus dimensionless deposition height $H = H(g/\nu^2)^{1/3}$ [65]. Four regimes are shown: (1) Viscous regime, $0.03 < H < 0.08$, dimensionless deposition height (2) Gravitational regime, $0.2 \leq H \leq 0.6$. (3) Inertio-gravitational regime, $0.7 < H < 1.4$. (4) Inertial regime, $H > 1.8$. The red curve is from numerical prediction. The dotted segments of the curve represent unstable solutions from numerical calculations.25
- Figure 2.19 a) Schematic of the “fluid-mechanical sewing machine”. b) Three different patterns: straight, meandering, and translated coiling. [67].....27
- Figure 2.20 Experimental setup for the “fluid-mechanical sewing machine” and Fourier analysis of different patterns [69]. (a) A 45° camera is used to capture simultaneously x and y views of the thread. The y view shows the motion of the thread, which is parallel to the belt motion, while the x view captured in the mirror shows the motion of the thread which is transverse to the belt motion. The horizontal line is used to determine the motion of the thread which is proportional to the motion of the contact point. (b) From left to right: Fourier spectra for the meandering, alternating and coiling pattern. Top plots are the reconstructed patterns on the belt based on the motion of the thread. Inset plots are the reconstructed traces of contact point.28

- Figure 2.21 (a) Comparison between numerical simulations based on DVR algorithm and experimental data [70]. The numerical simulations successfully reproduced nine out of ten different patterns observed from previous experiments [73]. (A: Translated coiling; B: Meandering; C: Alternating; D: Disorder) (b) Schematic of the deposition trace with respect to the nozzle projection [72]. Black line is the pattern on the belt and red line is the corresponding trace of contact point. (c) Geometrical predictions for different patterns (green lines) compared with numerical simulation results (brown lines) [72].29
- Figure 2.22 Helical fibers based on liquid rope coiling [78]. a) Schematic of the fabrication process. b) Optical and SEM images of the helical fibers. c) Tensile curves of the helical fibers fabricated under different spinning height.31
- Figure 2.23 Looped fibers based on instability-assisted 3D printing. a) Schematic of instability-assisted solvent-cast direct write 3D printing [16]. b) Different fiber patterns printed by instability-assisted fused filament fabrication (orange fibers) and instability-assisted solvent-cast direct write (translucent fibers) [16]. c) Ashby plot of the specific toughness to the apparent stiffness of different fiber patterns [16]. d) Strain sensing performance of a coiling fiber with three loops [47]. e) Schematic of the self-healing strain sensor. The black segments represent the electronic pathways [46]. f) Cyclic test of the self-healing strain sensor subjected to tensile loading and unloading at a maximum strain of 10% [46].32
- Figure 2.24 Instability-assisted 3D printing of multilayered structures. a) Bidirectional hydrogel fabric with anisotropic tensile behavior [79]. b) Cellular structures [80]. c) Optical image and computerized X-ray tomography scanning image of 3D-printed glass with coiling patterns [63].33
- Figure 2.25 a) Schematic of electro-coiling [84]. b) Rapid switch between coiling pattern and meandering pattern through voltage control [84]. c) Optical and SEM images of 4-layer core/shell scaffold with coiling loops, and tensile curves of three 4-layer scaffolds (all with coiling loops): polycaprolactone (PCL) scaffold, PCL scaffold dipped in cellulose solution, core/shell scaffold with PCL as the core and cellulose as the shell. [77] d) Melt electrowriting of overhang, branching and scaffold structures based on layer shifting [85].34

Figure 4.1 a) Schematic of the IFDM. The ratio of the filament extruding speed V_E to the belt moving speed V_B dictates the fiber pattern on the belt. The ratio of the deposition height H to the fiber diameter d dictates the size of the loop. Sacrificial bonds are formed via fusion at the intersections in the coiling pattern after the polymer is solidified by cooling. b) The produced coiling fiber has a constant hidden length l_h which can be released by the breaking of sacrificial bonds (α , β) in uniaxial tensile test. c) Schematic comparison of the tensile test sequences and force-displacement curves between expected failure (blue solid line) and premature failure (red dashed line). In expected failure, sacrificial bonds α and β break one by one, resulting in a saw-tooth tensile curve. The ultimate axial tensioning after all hidden lengths are released breaks the fiber backbone, leading to high energy absorption indicated by the blue area under the tensile curve. In premature failure, the fiber backbone is broken during the unfolding process of loop β , before bond α breaks. The truncated tensile curve displays reduced fiber strength and energy absorption.41

Figure 4.2 Failure modes observed from uniaxial tensile tests of coiling fibers: axial (\times), bending (\blacktriangle), torsional (\bullet), bond (\blacksquare) and dynamic (\blacklozenge) failure. Each failure mode is characterized by: (i) sequential camera captures of the unfolding process after the breaking of sacrificial bond. Time zero is defined at the breaking of sacrificial bond; (ii) microscopy images of the fracture pieces; (iii) SEM images of the fracture surfaces. All specimens shown here are from the large fiber with a diameter of 1.20 mm, except the camera captures of dynamic failure, which are from the small fiber with a diameter of 0.37 mm for the sake of convenience in shooting with high speed camera. Scale bars are 5 mm in (i), and 0.5 mm in (ii), (iii).....43

Figure 4.3 The breaking of sacrificial bonds in two coiling loops under uniaxial tension from linear elastic FEA (blue dotted line), multilinear plastic FEA (red dashed line) and tensile test (grey solid line). The breaking sequence of sacrificial bonds in the FEAs is set the same as that in the tensile test: first bond β , then bond α . The force threshold for each sacrificial bond in the FEAs is also set the same as that in the tensile test: 23.4 N for bond β and 21.6 N for bond α . The unfolding shapes are obtained at five given apparent strain values. The color gradient represents the magnitude of von Mises stress in the FEA contour plots. The FEAs and test results here are all for the large fiber with a diameter of 1.20 mm.44

Figure 4.4 a) Distribution of the five failure modes in coiling fibers illustrated by failure points overlaid on a representative force-displacement curve of a single coiling loop. Failure points are defined as the final break of fiber backbone from the following failure modes: axial (*), bending (▲), torsional (●), bond (■) and dynamic (◆) failure. For bending failure, crack initiation (△) and the following force curves (blue dashed lines) are also marked. Local b) curvature, c) shear strain, d) axial strain calculated from the multilinear plastic FEA are used to explain the fracture location of each failure mode along the fiber during the unfolding process. Arc length L_a is calculated based on the loop α in the simulation, starting from the fixed end. The bond-breaking defects locates at $L_a = 3.12$ and 20.31 mm. All failure points here are for the large fiber with a diameter of 1.20 mm.....46

Figure 4.5 Illustration of the crack initiation in torsional and bond failure due to high local tensile stress: a) SEM images of torsional failure specimen showing large material distortion in the middle of the loop. Fractures of b) torsional failure and c) bond failure specimen are characterized by sequential camera captures and SEM images. The relative location of crack initiation region with reference to the bond-breaking defect in both failure modes can be seen in the SEM images. d) Contour plot of one coiling loop at $p = 80\%$ from the plastic FEA. The color gradient represents the magnitude of the first principal stress. Cross-sectional contour plots of the fiber are shown at $L_a = 15.63, 18.05, 19.27, 20.47$ and 23.63 mm along the loop. The inner side of the beam element at $L_a = 20.47$ mm corresponds to the bond-breaking defect. The fracture location along the fiber (at $L_a = 12$ mm to 24 mm) are shown by ● for torsional failure and ■ for bond failure. Both torsional and bond failures can be attributed to a large region of tensile stress. Scale bars are 5 mm in camera captures and 0.5 mm in SEM images.48

Figure 4.6 Comparison of the failure behavior in a) two geometrically similar coiling fibers with different diameters: 1.20 mm (in black) and 0.37 mm (in red). b) The number of actually broken bonds n_b in both large and small fibers varying with different initial number of bonds n_t in the uniaxial tensile tests. The error bar stands for the standard deviation based on a sample size of 10 for each data point. The proportion of axial (grey), bending (blue), torsional (yellow), bond (red) and dynamic (green) failures in c) large and d) small fibers varying with different n_t . e) SEM images of the fracture surfaces in axial (i), bending (ii) and dynamic (iii)

failures of the small fibers. Scale bars are 0.2 mm. f) Comparison of the unfolding geometries and apparent stress-strain curves of the large (black lines) and small (red lines) fibers with two coiling loops. The oscillations on the red curves are due to the vibration of the 5 N load cell induced by the bond breakage. Scale bars are 5 mm. g) Comparison of the engineering stress-strain curves, test sequences and post-test microscopy images of the large (black lines) and small (red lines) straight fibers in the three-point bending test. At the bottom of the fiber where the bending stress is maximum in tension, the large fiber specimens either show sharp crack or large plastic deformation (corresponding to the black solid and dashed lines respectively on the stress-strain diagram), while all the small fiber specimens show large plastic deformation. All stress-strain curves from ten specimens for each fiber are shown in the plot. Besides the three representative curves, other curves are shown in gray or pink for the large and small fibers respectively to show the measurement deviations. Scale bars are 5 mm in camera captures, and 1 mm in microscopy images.50

Figure 4.7 Local strain results calculated from beam and solid elements at the unfolding percentage of 80%: a) deformed meshes of beam and solid elements; b) curvature, c) shear strain, and d) axial strain calculated from beam (blue markers) and solid (red markers) elements. The shear strains in solid elements are averaged over 40 values (black markers) around the circumference at each L_a59

Figure 4.8 Piece-wise linear stress-strain curve for multilinear isotropic hardening in the plastic FEA. The first stress-strain point defines the yield stress (12 MPa). Subsequent points define the multilinear isotropic hardening behavior of the material. The last point corresponds to the fracture of the fiber in tensile test, while in the plastic FEA, the fiber behaves perfectly plastically after the material reaches the tensile strength (70.5 MPa). The data points are collected from one of the uniaxial tensile tests of straight PLA fiber with the diameter of 1.20 mm (gauge length = 250 mm, strain rate = 0.01 mm/mm/s). The tensile strength with a standard deviation for 7 specimens is 71.3 ± 0.95 MPa.60

Figure 4.9 Stress-strain curves of straight fibers under uniaxial tension. Gauge length is 100 mm and crosshead rate is 500 mm/min for both fibers.61

- Figure 4.10 Estimation of the local strain rate at the top surface in the middle of the unfolding loop:
 a) von Mises strain (blue solid line, left Y axis) and von Mises strain rate (red dashed line, right Y axis) at the top surface in the middle of the unfolding loop, during the normal unfolding process of the loop without dynamic failure. The bottom and top X axis represent the unfolding percentage and elapsed time, respectively. They correspond to each other and serve as different references for the unfolding process. b) High speed imaging of the loop retraction after the breaking of sacrificial bond in dynamic failure. The speed of the loop retraction at $t_d = 33 \mu\text{s}$, $66 \mu\text{s}$ and $99 \mu\text{s}$ is calculated by measuring the moving distance of the tracking point in ii – iv relative to its initial position at $t_d = 0 \mu\text{s}$ in i. Scale bar is 5 mm. c) Linear fit of the loop retraction speed over elapsed time. d) von Mises strain (blue solid line, left Y axis) and von Mises strain rate (orange dashed line, right Y axis) at the top surface in the middle of the unfolding loop, during the rapid unfolding process of the loop in dynamic failure. Simulation results, such as the von Mises strain and strain rate, are extracted from 101 load substeps and plotted as continuous lines here for the sake of visual demonstration.62
- Figure 4.11 DSC results of FDM-extruded PLA fibers. The fibers were extruded at $230 \text{ }^\circ\text{C}$ on the conveyor belt in ambient air with two nozzles with different diameters (1 mm and 0.3 mm). The belt speed is equal to the extruding speed. The large and small fibers are 1.2 mm and 0.37 mm in diameter, respectively.63
- Figure 4.12 Apparent stress-strain curves of small fiber with three coiling loops. All ten test specimens are plotted to show the deviation. The stress-strain curve of the straight small fiber is also plotted as a benchmark to show the toughness enhancement in coiling fibers.64
- Figure 5.1 Design of the spider web-inspired transparent impact-absorbing composite.66
- Figure 5.2 Fabrication and mechanical behavior of the two-layer fabric of microstructured fibers.69
- Figure 5.3 Fabrication and optical characterization of the microstructured-fiber composite.72
- Figure 5.4 Impact tests of different transparent films based on the low RI elastomer.75
- Figure 5.5 Ellipsometry analysis of the polycarbonate, high RI elastomer and low RI elastomer. The refractive index was obtained by the Cauchy model from 350 to 2500 nm.91

Figure 5.6 An ideal thought experiment of two-layer fiber fabric based on Brun et al.'s model. The single fiber pattern is generated at a speed ratio $v_e/v_m =$: **a**, 1.6; **b**, 1.9; **c**, 2.1; **d**, 2.4. Then the fiber was manually aligned to a 2D array (red dashed lines) with a unit size equalling to the distance between adjacent loops along the fiber. The steady coiling radius $R_c = 1.8$ mm was used for all calculations. The three ordinary differential equations in the model were solved via the ode23 function in MATLAB, with initial conditions $[r, \psi, \phi] = [1, 0, 3\pi/4]$93

Figure 5.7 Matrix-fiber debonding due to thermal expansion in the alternating fiber composite film with the high RI elastomer. The composite was cured at 140°C for 2 hours. The photo was taken after the cooling down of the composite. The scale bar is 2 mm.94

Figure 5.8 Static puncture test of different transparent films based on the low RI elastomer. **a**, Optical images of the pure elastomer film (black circle), straight fiber composite film (blue square), alternating fiber composite film (green diamond) and hybrid fiber composite film (red star). **b**, Front view and **c**, Bottom view of the static puncture test of a hybrid fiber composite specimen. **d**, Representative force-displacement curves for the pure elastomer film (black curve), straight fiber composite film (blue curve), alternating fiber composite film (green curve) and hybrid fiber composite film (red curve). **e**, Energy to puncture calculated by the integration of the force-displacement curve. Three repeats were conducted for each specimen, and the standard deviation was plotted as the error bar. All tests were conducted with a puncture head covered with a P60 grade sandpaper.95

Figure 5.9 Contact force-time curves of different transparent films from the falling dart impact test. **a**, Elastomer film; **b**, Straight fiber composite film; **c**, Alternating fiber composite film; **d**, Hybrid fiber composite film; **e**, Polycarbonate (PC) film. The images of the films after the test are shown in the insets. The test was repeated three times in **a-d**. The dart penetrated all test films in **a** and **b**, but was successfully caught by all test films in **c** and **d**, due to the high energy dissipation of the architected composites. All test films have a length of 100 mm and width of 100 mm. The test films in **a-d** are all based on the low RI elastomer and have a thickness of 1.5 mm. The PC film (McMaster-Carr, 85585K102) in **e** has a thickness of 0.127 mm. The weight of the test PC film is 1.524 g, which is even more than the weight of the fabric of alternating fibers (1.333 g) in **c**. The fact that the dart penetrated both the elastomer film and PC film, but was caught by the alternating fiber composite film, proves the dominating

contribution from the composite architecture to the high energy dissipation over the material components.....96

Figure 5.10 Optical images of fractured transparent films after impact test. **a**, Elastomer film; **b**, Straight fiber composite film; **c**, Alternating fiber composite film; **d**, Hybrid fiber composite film. The inset in **c** shows a close view of the fiber cut-outs. All scale bars are 5 mm.97

Figure 5.11 Cyclic impact test of the alternating fiber composite film based on the low RI elastomer. Two specimens were tested at different impact energy levels: **a**, 5 J and **b**, 1.4 J, respectively. **c**, Snapshots of the specimen at the end of each cycle of the impact test at 1.4J. For the impact test at 5J, the snapshots of the 1st cycle can be seen in Figure 4I. The same drop height (0.9 m) was used in both tests, leading to an impact velocity of 4.2 m/s. To achieve the corresponding impact energy level, the drop weight was 0.568 kg in **a**, and 0.158 kg in **b**. The drop weight fell on the same location on the specimen during the cyclic test. The drop weight fully penetrated the specimen in the 2nd cycle in **a**, and the 5th cycle in **b**. The scale bar is 20 mm.....98

Figure 5.12 Comparison of the impact absorption performance between the alternating fiber composite films made from the low RI elastomer and high RI elastomer. **a**. Contact-displacement curves; **b**. Optical image of the fractured low RI elastomer composite film; **c**. Optical image of the fractured high RI elastomer composite film. Both specimens were tested with an impact energy of 5 J and impact velocity of 4.2 m/s. All scale bars are 5 mm.....99

Figure 5.13 Optical waveguides made from the transparent composites based on the low RI elastomer. **a**, Demonstration of the strain sensing with the meandering fiber composite waveguide. **b**, Cyclic tensile test of the meandering fiber composite waveguide. **c**, Design of the electric circuit to measure the resistance of the photoresistor during the tensile cyclic test. **d**. Measured output voltage under the cyclic tensile test. Under stretching, more light was transmitted through the waveguide to the photoresistor, resulting in the decrease of the resistance and the increase of the circuit output voltage. **e**, Optical images (top view and side view) of the alternating fiber composite waveguide. **f**, The light transmission loss of the alternating fiber composite waveguide under uniaxial tensile test (gauge length: 45 mm;

crosshead speed: 5 mm/min). The force-displacement curve is similar as Figure 1C and has been explained in the paper. 101

Figure 5.14 Schematic of the deposition trace with respect to the projection of the nozzle. The speed v_m is the horizontal moving speed of the extruder relative to the printing bed. The vector r represents the position of the fiber-platform contact point regarding to the nozzle's projection point. The angle ψ is measured between the vector r and the x axis (direction of the relative moving speed v_m). The angle ϕ is measured between the vector r and the tangent vector t of the polymer thread at the contact point. These three geometric parameters are functions of the Lagrangian coordinate s which is a time-like variable and represents the arc length along the deposition trace. The coordinates of the deposited trace can be reconstructed by the solution of the geometric model: $x(s) = r(s) \cdot \cos [\psi(s)] + v_m(s_{last} - s)/v_e$, $y(s) = r(s) \cdot \sin [\psi(s)]$ (s_{last} is the last point from the solution). This schematic was modified from Brun et al.'s work⁴⁸. 102

Figure 5.15 Calibration of the volume flow rate of polycarbonate filament on the Prusa 3D printer. The dashed line in **a** represents that the actual volume flow rate equals to the theoretical one. 104

Figure 5.16 Resin infiltration setup. **a**, A micropump infiltrates the resin from the syringe into the bottom of the plastic mold via a Teflon tube. **b**, Close-up view of the infiltration process with the low RI elastomer (RI = 1.41 @589nm). **c**, Close-up view of the infiltration process with the high RI elastomer (RI = 1.55 @589nm). The alternating fiber fabric almost disappears inside the high RI elastomer resin, due to the small RI difference between the fiber (RI = 1.58 @589nm) and the high RI elastomer. 105

Figure 5.17 Design of the falling dart integrated with a force sensor. **a**, When the dart is overhanging, there is a gap between the force sensor and the aluminium rod inside the dart, ensuring no force is measured. **b**, When the dart is pressed, the aluminium rod will hit on the force sensor. The cross-sectional area of the aluminium rod is the same as the sensing area of the force sensor. 106

Figure 5.18 Calibration of the force sensor under static loading. We calibrated the sensor on an electromechanical machine (MTS Insight). The inset shows the setup. We used an acrylic

puck with the cross-sectional area matching the sensing area of the force sensor. A compressive displacement was manually applied on the top clamp, until a certain force is reached. Then the conductance was measured under this force value with a digital multimeter (PCI-4070, National Instruments) and a LabVIEW program. The linear fitting was shown in the plot..... 107

Figure 5.19 Displacement measurement and calibration in the falling dart impact test. **a**, Five consecutive high-speed camera snapshots from the impact test of the alternating fiber composite specimen. A black and white calibration paper was attached on the falling dart. **b**, The intensities of the pixels along the yellow arrow in **a** extracted by a MATLAB code. **c**, Sgolayfilt fitting of the curves in **b** with a polynomial order of 9 and frame size of 41. The MATLAB code automatically measures the shift of each curve in the unit of pixels. **d**, Displacement of the dart which is converted from the shift in pixels in **c** by the MATLAB code. The time 0 ms corresponds to the initial contact and is selected manually from the high-speed camera snapshots. **e**, Velocity of the dart which is calculated based on the 6th order polynomial fitting function in **d**. The time 28.4 ms corresponds to zero velocity. The calculation of momentum change between the initial contact and the zero-velocity time is shown in the plot. **f**, Contact force-time curve measured from the force sensor. The impulse between the initial contact and the zero-velocity time is calculated, based on the direction of gravity. The as-conducted calibration for the impact test of the alternating fiber composite specimen has a discrepancy $\delta = 8.35\%$ 109

Figure 6.1 Overview of toughening elastomers via microstructured thermoplastic fibers with sacrificial bonds and hidden lengths. (a) Schematic illustration of the IFFF process. The extruding speed v_e is 2.06 times faster than the extruder moving speed v_m , producing the alternating pattern. (b) Force-effective strain curve of the as-fabricated microstructured fibers with six alternating loops. The breaking of sacrificial bonds and the unfolding of hidden lengths from one of the six loops are illustrated as an example. The fiber contours with fake color are traced from camera snapshots during the tensile test of the microstructured fiber. (c) Schematic illustration of multiple breaking of sacrificial bonds and multiple cracking of the matrix in an elastomer composite with a precrack under tension. 113

Figure 6.2 Fracture of the unnotched PDMS-alternating fiber composite specimen under uniaxial tension. (a) Camera snapshots of the fracture of the specimen at different effective strains: i. $\varepsilon = 0$; ii. $\varepsilon = 0.24$; iii. $\varepsilon = 0.41$; iv. $\varepsilon = 1.32$; v. $\varepsilon = 3.04$. Scale bar is 10 mm in the camera snapshot and 3 mm in the inset. (b) Force-effective strain curve of the PDMS-alternating fiber composite. 119

Figure 6.3 Comparison of the fracture behavior of the notched plain PDMS specimen and the notched PDMS-alternating fiber composite specimen under tensile loading. (a) Camera snapshots of the notched plain PDMS specimen at different effective strains: i. $\varepsilon = 0.19$; ii. $\varepsilon = 0.23$; iii. $\varepsilon = 0.25$. (b) Camera snapshots of the notched PDMS-alternating fiber composite specimen at different effective strains: iv. $\varepsilon = 0.17$; v. $\varepsilon = 0.38$; vi. $\varepsilon = 1.38$. All scale bars are 10 mm. (c) Force-effective strain curves of the notched plain PDMS (in black) and PDMS-alternating fiber composite (in red) specimens. (d) Crack growth resistance curves of the notched plain PDMS (in black) and PDMS-alternating fiber composite (in red) specimens. The error bar represents the standard deviation of the effective energy release rate with the strain energy density measured from three unnotched specimens with identical dimensions as the notched specimen. In the notched plain PDMS specimen, when the crack extension exceeds 50 mm, the crack propagation accelerates rapidly, making it difficult to measure the crack extension from the camera snapshots. Since the effective energy release rate stays almost at the same level, we extrapolated the dashed line after the crack extension exceeds 50 mm. The inset shows the critical effective energy release rate of the plain PDMS ($196 \pm 74 \text{ J/m}^2$) and PDMS-alternating fiber composite ($340 \pm 49 \text{ J/m}^2$) at the onset of crack growth. 119

Figure 6.4 Tensile test of the plain PDMS specimen and PDMS-unidirectional fiber composite specimens with and without a precrack. (a) Optical images of test specimens: plain PDMS (\circ), PDMS-straight fiber composite (\square), PDMS-alternating fiber composite (\diamond), PDMS hybrid fiber composite (\star). (b) Force-effective strain curves of unnotched specimens. (c) Force-effective strain curves of notched specimens. (d) Comparison of total energy to failure of test specimens. Solid blocks represent unnotched specimens, while hollow blocks represent notched specimens. All scale bars are 5 mm. 121

Figure 6.5 Static puncture test of the plain PDMS specimen and PDMS-bidirectional fiber composite specimens. (a) Optical images of test specimens: plain PDMS (●), PDMS-straight fiber composite (■), PDMS-alternating fiber composite (◆), PDMS-hybrid fiber composite (★). Scale bars are 2 mm. (b) Camera snapshots of the static puncture test of PDMS-hybrid fiber composite with a rough indenter head in front and bottom views. Scale bars are 10 mm. Force-displacement curves of test specimens with (c) a smooth indenter head, and (d) a rough indenter head attached with a P60 grade sandpaper. (e) Total energy to failure of test specimens. Solid blocks represent tests with the smooth indenter head, while hollow blocks represent tests with the rough indenter head. 123

LIST OF SYMBOLS AND ABBREVIATIONS

3D	Three-dimensional
AFM	Atomic force microscopy
APDL	ANSYS Parametric Design Language
CNF	Carbon nanofiber
CVD	Chemical vapor deposition
DN	Double network
DSC	Differential scanning calorimetry
DVR	Discrete viscous rods
ESM	Elastic sewing machine
FDM	Fused deposition modeling
FEA	Finite element analysis
FFF	Fused filament fabrication
FMSM	Fluid-mechanical sewing machine
IFDM	Instability-assisted fused deposition modeling
IFFF	Instability-assisted fused filament fabrication
Ig	Immunoglobulin
MPC	Multipoint constraint
ODEs	Ordinary differential equations
PAAm	Polyacrylamide
PC	Polycarbonate
PCL	Polycaprolactone
PDMS	Polydimethylsiloxane
PEEK	Polyether ether ketone

PLA	Poly(lactic acid)
PUMA	Poly(2-ureidoethyl methacrylate)-co-(methacrylic acid)
QR	Quick response
RI	Refractive index
SBHL	Sacrificial bonds and hidden lengths
SEBS	Poly(styrene-ethylene butylene-styrene)
SEM	Scanning electron microscopy
TEM	Transmission electron microscopy
VHB	Very-high-bond
WLC	Wormlike chain
b	Persistence length of a molecule
d	Fiber diameter
D_{filament}	Diameter of the 3D printing filament
d_{nozzle}	Nozzle diameter
ΔE	Energy absorption increase
E_s	Total energy absorption of the engineering structure with SBHL
E_n	Total energy absorption of the engineering structure without SBHL
F	Pulling force
F_v	viscous force
F_G	Gravitational force
F_I	Centrifugal inertial force
G	Energy release rate
g	Gravitational acceleration
H	Deposition height

h	Distance between the nozzle and the printing platform
\hat{H}	Dimensionless deposition height
J	Impulse
k_B	Boltzmann's constant
K_{Ic}	Critical stress intensity factor
l	Distance between adjacent deposition paths for the bidirectional fiber fabric
L_a	Arc length along the coiling fiber
L_A	Available contour length of a molecule
L_C	Total contour length of a molecule including all hidden lengths
L_D	Moving distance of the printing head
L_E	Extruding length of the 3D printing filament in the g-code
l_h	Hidden length of the coiling loop
l_i	Length of the i^{th} hidden loop
l_n	Length of the n^{th} hidden loop
n	Number of sacrificial bonds
n_b	Number of actually broken bonds during tensile test
n_t	Initial number of sacrificial bonds in tested fibers
n^*	Relative refractive index at the interface between two materials
n_{air}	Refractive index of air
n_{fiber}	Refractive index of the fiber
n_{matrix}	Refractive index of the matrix
p	Unfolding percentage
Δp	Momentum change
Q	Volume flow rate

\vec{r}	Distance vector from the nozzle's projection point to contact point
R	Reflectance
R_C	Steady coiling radius
s	Lagrangian coordinate of the contact point
T	Temperature
T_{diffuse}	Diffuse transmittance
T_{specular}	Specular transmittance
T_{total}	Total transmittance
U_C	Stead coiling velocity
V_B	Belt velocity
V_E	Extruding velocity
V_F	Feedrate of the printing head moving motor in the g-code
v_e	Extruding velocity
v_m	Relative moving velocity of the extruder to the printing platform
W	Strain energy density
x	Extension of a molecule
X_C	Degree of crystallinity
δ	Impact test discrepancy between the impulse and momentum change
ε^*	Apparent strain
η	Zero-shear viscosity
θ	Angle between the direction of belt velocity and the trace's tangent at contact point
κ	Curvature
λ	Stretch ratio
ν	Kinematic viscosity

ρ	Density
$\Delta\sigma$	Strength increase
σ_s	Strength of the engineering structure with SBHL
σ_n	Strength of the engineering structure without SBHL
ψ	Angle between \vec{r} and the direction of belt velocity
Ω	Coiling frequency

CHAPTER 1 INTRODUCTION

1.1 Background

Tough materials that absorb large amounts of energy and resist fracture are required in many safety-critical engineering systems. For example, the material of the jet engine fan blade containment system on an aircraft must be tough enough to absorb high levels of kinetic energy for blade-out containment and fuselage protection; the windshield material must also be tough enough to resist fracture with the presence of small cracks induced by a bird strike. In these applications, multifunctionalities are also required, such as the lightweight of the fan blade containment material and the optical transparency of the windshield material. Developing multifunctional materials with exceptional strength and toughness is difficult in engineering, since the properties of strength and toughness are mutually exclusive in many engineering materials [1]. Nature overcomes the conflict between strength and toughness by building hierarchical architectures in biological materials. Spider silk is one of the strongest and toughest biological materials known, featuring a hierarchical fibrillar structure of crystalline and semi-amorphous proteins [2]. Upon stretching, the breaking of sacrificial hydrogen bonds in the semi-amorphous domains unravels the hidden lengths of protein chains, contributing to the large extensibility and high toughness of spider silk. Sacrificial bonds and hidden lengths toughening mechanisms are also found in nacre [3] bone [4], and muscle [5]. There have been several studies reporting the successful implementation of the sacrificial bonds and hidden lengths toughening mechanism at the molecular scale in hydrogels [6]–[8] and elastomers [9]–[12]. Whereas introducing sacrificial bonds and hidden lengths into the microstructure of a material is promising to transfer the toughening strategy to a wider range of engineering materials, achieving high toughness and multifunctionalities.

The breaking of sacrificial bonds in the molecules of biological materials has been reproduced in engineering materials through the single-network or double-network method at multiple length scales ranging from nanoscale to macroscale. In the single-network method, sacrificial bonds are introduced to a single fiber in the form of π - π interactions [13], slip knots [14], or physically fused bonds [15]–[17]. The breaking of sacrificial bonds unravels the hidden lengths along the single fiber, dissipating large amounts of energy and maintaining the structural integrity of the fiber backbone for large deformations. The single-network method produces a perfect analogy to the

breaking of hydrogen bonds and the unfolding of protein chains in the molecular structure of spider silk. In the double-network method, the material contains a stiff and brittle reinforcement as the sacrificial “first network” to break and dissipate energy, and a soft and stretchable matrix as the “second network” to maintain the structural integrity under large deformations. The “first network” can be low-melting-point metal and plastic fiber/fabric. The “second network” is often made from elastic polymers that recover the original shape after unloading. The multiple fracture of the “first network” triggered by shear stresses or interlocking mechanisms is analogous to the breaking of sacrificial bonds in the molecular structure of spider silk. Compared to the double-network method, the single-network method results in higher energy dissipation (the area between loading and unloading curves), since the unraveling of hidden lengths in the single-network method often involves with friction or plastic deformation, increasing the energy dissipation.

The advent of three-dimensional (3D) printing technologies, such as solvent-cast [15] or UV-assisted [18] direct write and fused filament fabrication (FFF) [19], brought great opportunities to tailor the mechanical properties of advanced engineering materials by building various complex architectures [20]. Instability-assisted 3D printing is a facile and robust single-network method for producing microstructured fibers with sacrificial bonds and hidden lengths. Any material that can be melted or dissolved in a solvent is suitable for the method. The fluid-mechanical instability of a polymer thread is harnessed to trigger the periodic coiling of the fiber on itself, producing coiling or alternating loop patterns. After cooling or solvent evaporation, the self-intersections along the fiber form physically fused bonds which are weaker than the fiber backbone and act as sacrificial bonds under mechanical loads. Upon stretching, the breaking of sacrificial bonds and the unfolding of fiber loops dissipates large amounts of energy, resulting in a 240–340% toughness enhancement in poly(lactic acid) (PLA) fibers. However, some specimens show worse toughness as low as 25% of that of the benchmark straight fiber due to premature failures. In this dissertation, we seek to understand the mechanics behind these premature failures and build microstructured sacrificial bonds and hidden lengths into multifunctional energy-absorbing materials by instability-assisted 3D printing.

1.2 Dissertation structure

This dissertation includes seven chapters. Chapter 1 introduces the background of the study and the structure of the dissertation. Chapter 2 provides a literature review on the sacrificial bonds and hidden lengths toughening mechanism in biological materials, bioinspired design via the single-network and double-network methods, and the instability-assisted deposition. Chapter 3 presents the research objectives and the coherence of the articles. The main results of this dissertation are given in the form of three articles published or submitted to peer-reviewed scientific journals in Chapters 4 to 6. Chapter 4 presents the failure mechanisms of microstructured fibers with sacrificial bonds and coiling loops based on fractography and finite element analyses. Chapter 5 demonstrates the concept of transparent energy-absorbing composites based on microstructured fibers with sacrificial bonds and alternating loops for impact-protection applications. Chapter 6 illustrates the fracture resistance and damage tolerance of the energy-absorbing composites based on microstructured fibers with sacrificial bonds and alternating loops. Chapter 7 provides a general discussion of the research. Chapter 8 summarizes the conclusion of the research and gives recommendations for future work.

CHAPTER 2 LITERATURE REVIEW

2.1 Sacrificial bonds and hidden lengths (SBHL) mechanism

Section 2.1 reviews the SBHL mechanism found in spider silk and other biological materials, and the analytical models of the SBHL mechanism.

2.1.1 Spider silk and other biological materials

Spider web is one of nature's exquisite designs that optimize function based on weak building blocks such as proteins and hydrogen bonds. After millions of years' evolution since the early Triassic period, today's orb webs (Fig. 2.1a) consist of stiff radial threads (spider dragline silk) and compliant spiral threads (spider capture silk) [21].

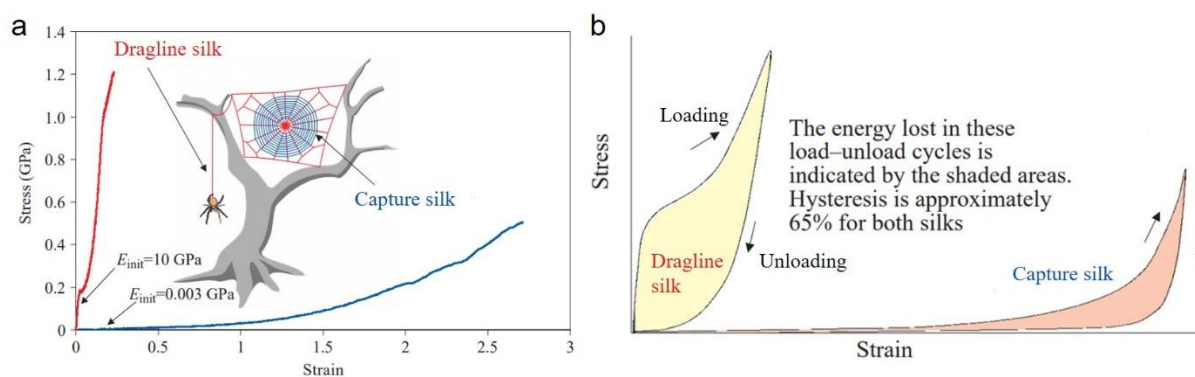


Figure 2.1 a) Stress-strain curves of spider dragline silk and capture silk [22]. b) Hysteresis (the ratio of dissipated energy to total absorbed energy) of spider dragline silk and capture silk [22].

The mechanical properties of the silk threads outperform most engineering materials. Spider dragline silk has a tensile strength of ~ 1.2 GPa [23], which is ~ 2 times that of stainless steel [24] and ~ 0.5 times that of Kevlar fiber [25]. Spider capture silk has an elongation at break of 300–1100% [26], which is comparable to that of silicone rubbers [27], while the tensile strength of spider capture silk [22] is two orders of magnitude higher than silicone rubbers [27]. Both spider dragline silk and capture silk show high toughness (the area under the stress-strain curve) of 150–160 MJ/m³ [22], which is more than 4 times that of Kevlar 49 fiber [25]. The loading-unloading curves of the silk threads (Fig. 2.1b) show that 65% of the total absorbed energy is dissipated away. The high toughness of the silk threads makes spider web capable of absorbing the

enormous kinetic energy from the flying prey. While the high hysteresis (dissipated energy/total absorbed energy) of the silk threads minimizes the oscillation of spider web during prey capture, avoiding the catapulting of insects. Despite the structural benefits like energy efficiency and prey retention brought by the combination of stiff and compliant threads [21], the high hysteresis and nonlinear material behaviour of the spider dragline silk are essential for the spider web's high energy-dissipation [28] and damage tolerance [29].

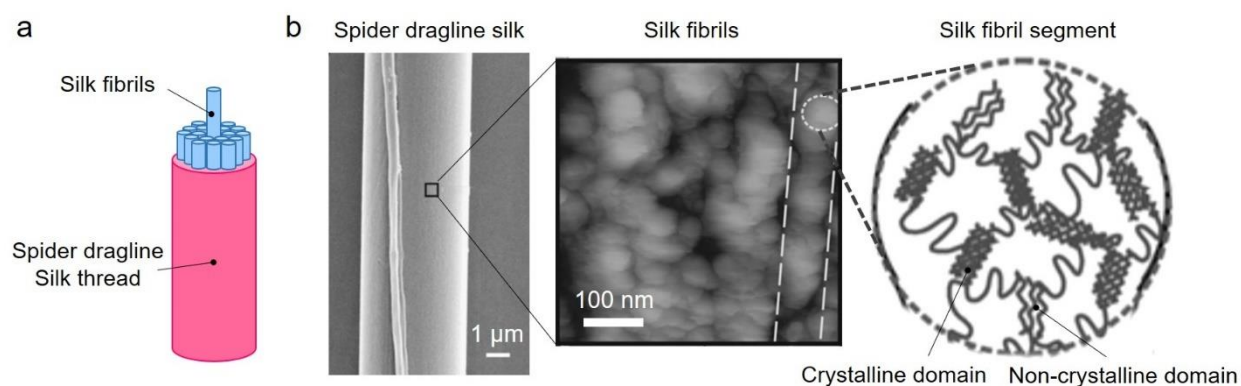


Figure 2.2 a) Schematic of the fibrous structure in spider dragline silk [30]. b) Hierarchical structure of spider dragline silk consisting of scanning electron microscope (SEM) image of the silk thread, atomic force microscopy (AFM) image of the silk fibrils, and a schematic of the molecular structure in a silk fibril segment [31].

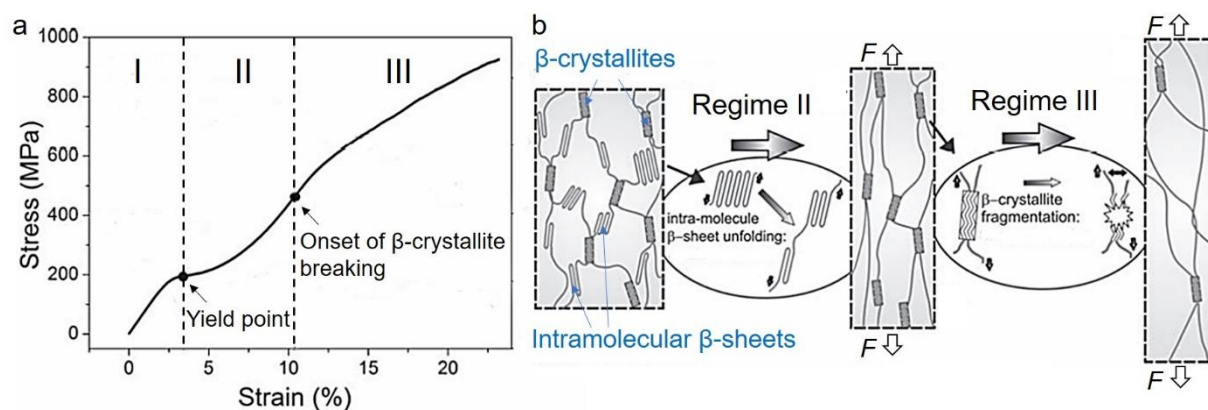


Figure 2.3 Structural origin of the nonlinear material behavior of spider dragline silk [32]. a) Stress-strain curve of the spider dragline silk consisting of three regimes: I, homogenous stretching; II, onset of yielding due to the breaking of hydrogen bonds and unfolding of the intramolecular β -

sheet in the non-crystalline domain; III, onset of the breaking of β -crystallite. b) Schematic of the unfolding of the intramolecular β -sheet and the breaking of β -crystallite.

The structural origin of the exceptional mechanical properties of spider dragline silk has been studied for more than three decades. The spider dragline silk possesses a hierarchical fibrillar structure [30] (Fig. 2.2a). The microscale silk thread is constructed by many nanoscale silk fibrils which contain crystalline and non-crystalline domains. The crystalline domain includes highly organized antiparallel β -crystallites assembled by hydrogen bonds [33]. The non-crystalline domain consists of less orderly intramolecular β -sheets, 3_1 helices and β -turns [30], [31]. The stress-strain curve of spider dragline silk from a tensile test and schematic molecular model [2], [32] are shown in Fig. 2.3. Regime I corresponds to the homogeneous stretching of silk fibrils. In regime II, the hydrogen bonds in the non-crystalline domain start to break after the yield point, releasing the hidden protein chains of the intramolecular β -sheets in the non-crystalline domain [32]. The onset of the breaking of the weak hydrogen bonds causes the tangent stiffness to drop significantly. As the protein chains unfold and align along the loading direction, the protein backbones and the crystalline domain start to carry the load, resulting in the strain hardening behavior of spider dragline silk. In regime III, the β -crystallites begin to break under further stretching, leading to the decrease of tangent stiffness. The breaking of sacrificial hydrogen bonds and unfolding of hidden protein chains in the non-crystalline domain not only contribute to the silk thread's high extensibility, but also help dissipate the energy away, leading to the high toughness and high hysteresis of spider dragline silk.

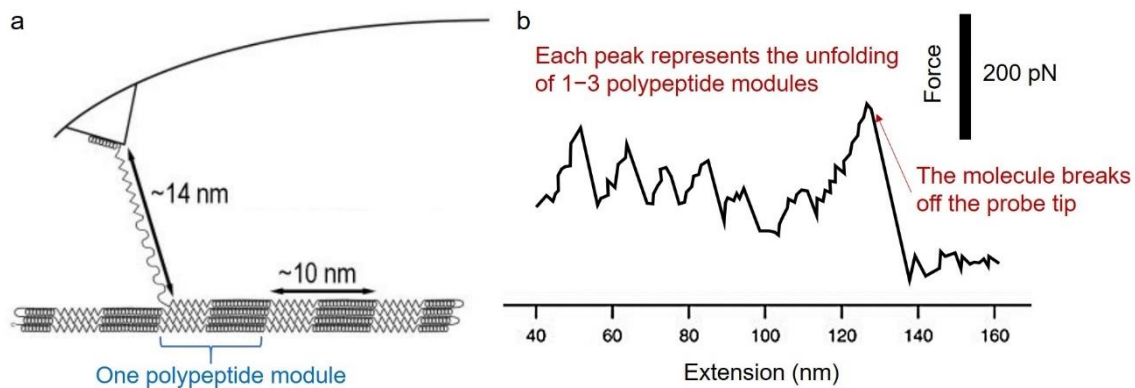


Figure 2.4 Single-molecule force spectroscopy of recombinant spider dragline silk protein [34]. a) Schematic of the single-molecule force spectroscopy. b) Force-extension curve of one protein molecule.

Figure 2.4 shows the single-molecule force spectroscopy of recombinant spider dragline silk protein [34] which also proved the sacrificial bonds and hidden lengths mechanism in the silk protein molecules. Upon stretching, the silk protein molecule rarely unfolds at once, instead, the breaking of intramolecular hydrogen bonds releases one to three polypeptide modules each time along the silk protein molecule, resulting in the saw-tooth pattern of the force-extension curve. The breaking of hydrogen bonds, the increase of entropy, and the production of internal heat during the molecule unfolding process together effectively dissipate the mechanical energy away [35].

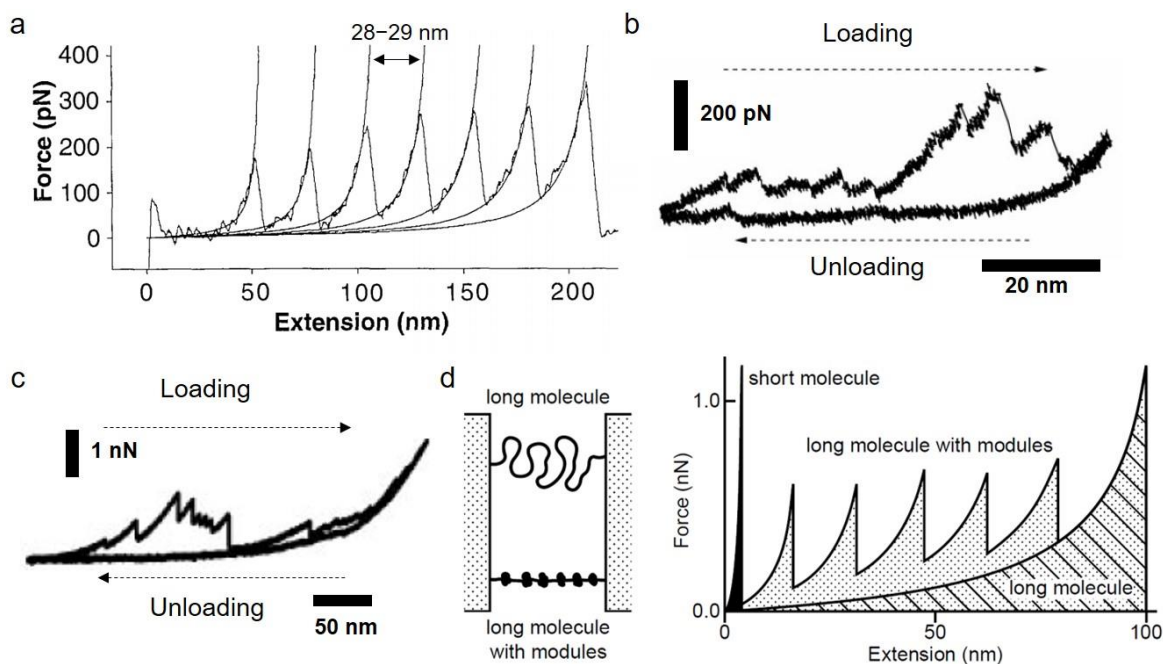


Figure 2.5 a) Force-extension curve of a single titin fragment by AFM [5]. The saw-tooth pattern was fitted by the wormlike chain (WLC) model through 28–29 nm stepwise increases in the contour length of the protein chain, which are close to the total length (30 nm) of individual titin immunoglobulin (Ig)-like domain. b) Force-extension curve of the organic adhesives between nacre tablets by AFM [3]. c) Force-extension curve of the mineralized collagen fibrils in bone by AFM [4]. d) Molecule model with tandem modular structures [3].

Similar saw-tooth patterns were also observed from the force-extension curves of muscle protein titin [5] (Fig. 2.5a), organic adhesives in nacre [3] (Fig. 2.5b), collagen fibrils in bone [4] (Fig. 2.5c). Titin is a giant sarcomeric protein composed of tandem immunoglobulin (Ig)-like domains. Compared to the force-extension curves of nacre and bone, the saw-tooth pattern looks more regular on the force-extension curve of titin, because the AFM tip pulls on only a few amino acids in the Ig domain [36], leading to the sequential unfolding of Ig domains. The force-extension curve of titin can be accurately fitted by the wormlike chain model which will be described in more details in Section 2.1.2. Fig. 2.5a shows that the prediction of the contour length of the unfolding chain from the fitting results is very close to the total length of individual Ig domain, proving the independent unfolding of each Ig domain. However, the AFM tip may pull on several molecules with sacrificial inter-chain bonds [3], leading to the more complex saw-tooth patterns in nacre and

bone, which will be further discussed in Section 2.1.2. As illustrated by Smith *et al.* [3] in Fig. 2.5d, compared to long molecule without modules or short molecule, long molecule with modules requires more energy to stretch and break, since the breaking of sacrificial bonds and unfolding of hidden lengths in the modules dissipate large amounts of energy before the failure of molecular backbone. This modular structure with sacrificial bonds and hidden lengths is an ideal strategy for shock-absorber [37].

2.1.2 Analytical modeling of SBHL

Although different biological materials show similar saw-tooth patterns of the pulling curves, some look regular like the spider silk protein in Fig. 2.4b and the titin in Fig. 2.5a, while others look more complex like the nacre adhesives in Fig. 2.5b and collagen fibrils in Fig. 2.5c. The variation in the saw-tooth patterns comes from the difference in the sacrificial bond configurations in protein molecules. Fantner *et al.* [38] used the wormlike chain (WLC) model to investigate the influence of different configurations of sacrificial bonds on the pulling curves, since the WLC model successfully interpreted the pulling curves of biomolecules through entropic elasticity [5], [34], [37], [39]. The WLC model predicts the pulling force of a molecule chain by

$$F(x) = \frac{k_B T}{b} \left[\frac{1}{4} \times \frac{1}{\left(1 - \frac{x}{L_A}\right)^2} - \frac{1}{4} + \frac{x}{L_A} \right], \quad L_A = L_C - \sum_{i=1}^n l_i, \quad (2-1)$$

where, F is the pulling force, x is the extension of molecule, k_B is Boltzmann's constant, T is the temperature, b is the persistence length which serves as a characteristic length scale, L_A is available contour length of the molecule, which does not include hidden lengths, L_C is the total contour length of the molecule which includes all hidden lengths, n is the number of sacrificial bonds, l_i is the length of individual hidden loop.

The simulation of the breaking of sacrificial bonds is achieved via a fracture threshold criterion [38]. At the beginning of the pulling, all hidden lengths are not included in molecule's available contour length. The pulling force is equivalent to pulling a molecule with an available contour length of $L_A = L_C - \sum_{i=1}^n l_i$. Once the pulling force reaches the strength of one sacrificial bond, this bond is removed imaginarily, and the corresponding hidden length l_n is released. Further pulling is equivalent to pulling of a molecule with an available contour length of $L_A = L_C - \sum_{i=1}^{n-1} l_i$.

In this way, pulling curves can be obtained by varying different internal variables like the strength and number of sacrificial bonds, bond configurations, *etc.*

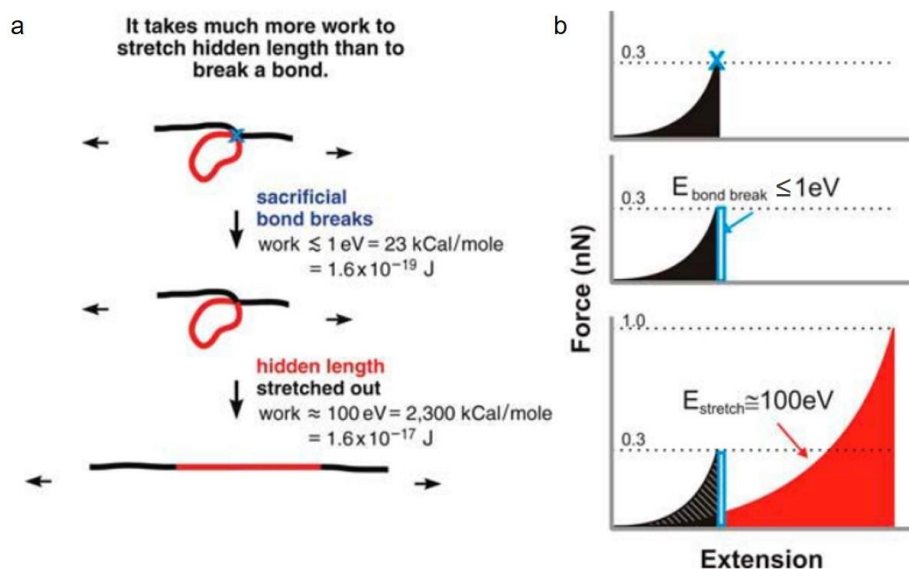


Figure 2.6 Basic principle of the SBHL mechanism. a) Schematic of the breaking of a sacrificial bond and unfolding of a hidden length. b) The comparison of energy absorption by breaking a sacrificial bond and unfolding a hidden length based on WLC model. [38].

With the WLC model, Fantner *et al.* [38] found that the unfolding of hidden lengths absorbs much more energy than the breaking of sacrificial bonds. Fig. 2.6 shows the pulling of a molecule with one sacrificial bond. The sacrificial bond blocks one hidden length of the molecule from external loading. Before the breaking of the sacrificial bond, only the molecule chain along the load path endures the pulling force via entropy elasticity. After the bond strength is reached, the sacrificial bond is broken by only a small amount of energy ($\leq 1 \text{ eV}$). After the breaking of the sacrificial bond, the hidden length of the molecule is released, resulting in a sudden drop of the force-extension curve. Further stretching requires much more energy ($\approx 100 \text{ eV}$) against the entropy of the whole molecule chain.

Fantner *et al.* [38] also found that some complex patterns of the force-extension curve can be explained by specific combinations of molecule chains with or without sacrificial bonds (Fig. 2.7). The parallel pulling of one molecule with sacrificial bonds and one exponential string molecule leads to a stepwise increase of force peaks on the force-extension curve. While the pulling of

several molecules with different contour lengths results in a stepwise decrease of force peaks on the force-extension curve. The findings are not only helpful to interpret the complex force-extension curves from the AFM pulling of biomolecules, but also provides structural insights for engineering designs to achieve the saw-tooth force-extension behaviour with high energy absorption.

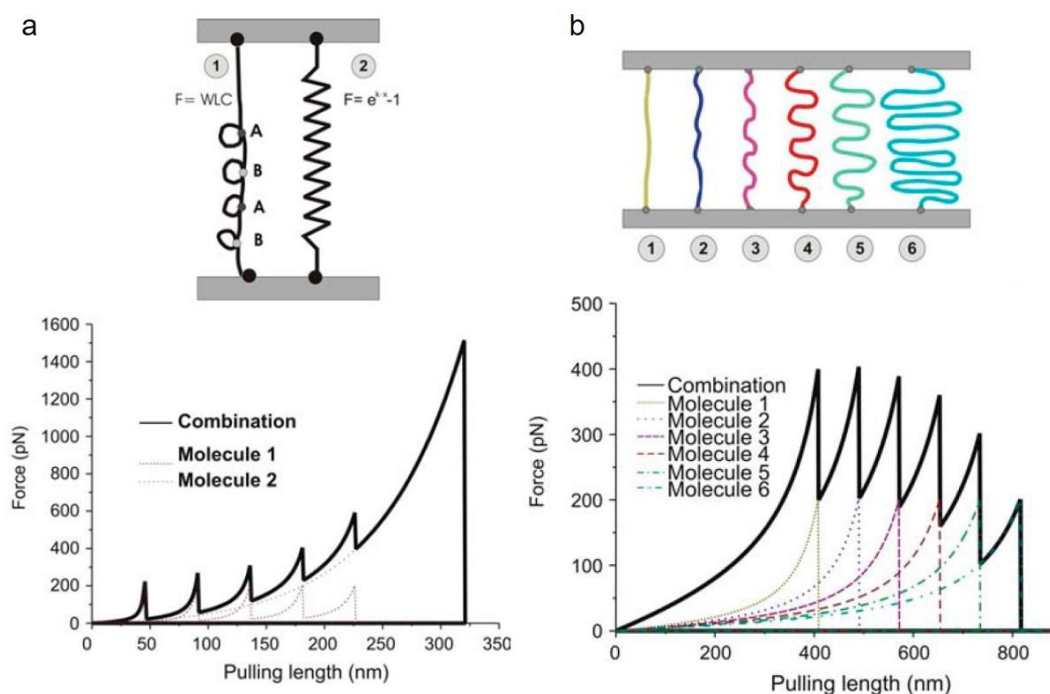


Figure 2.7 Different molecule configurations and their simulated pulling curves based on WLC model [38]. (a) Two parallel molecules: one with sacrificial bonds breaks in the order of bond strength, the other acts as an exponential spring. The pulling curve shows increasing rupture forces. (b) Six molecules in parallel with same end bond strength. The length increment of adjacent molecules is constant. The pulling curve shows decreasing rupture forces.

Elbanna *et al.* [40] further investigated the influence of the number of sacrificial bonds on the toughness enhancement of the SBHL mechanism. Since the toughness is related to the area under the force-extension curve, the variation of force-extension curves when the number of sacrificial bonds n approaches infinite was investigated through the derivative of a continuum version of Equation (2-1) over n :

$$\frac{\partial F}{\partial n} = -\frac{k_B T}{b} \frac{x}{L_A^2} \left[\frac{1}{2} \times \frac{1}{\left(1 - \frac{x}{L_A}\right)^3} + 1 \right] \frac{dL_A}{dn}. \quad (2-2)$$

With the assumption of equally distributed hidden length, *i.e.*, $l_i = L_C / (2n+1)$, the contour length L_A would be $[(n+1) / (2n+1)] \cdot L_C$. Then, when $n \rightarrow \infty$, $L_A \rightarrow L_C/2$ and $dL_A / dn = -(2n+1)^{-2} \rightarrow 0$. Therefore, $\partial F / \partial n \rightarrow 0$, meaning that when the number of bonds n is sufficiently large, the force F would not be sensitive to n anymore. As the number of bonds n increases, the toughness would first increase but eventually reach a plateau. By performing numerical simulations with different number of sacrificial bonds, an optimum number of sacrificial bonds can be found. Further increase of the number of sacrificial bonds would contribute little to the increase of toughness. For the strength of sacrificial bonds, it was found that the molecule's toughness and ductility can be reduced if the sacrificial bond's strength is higher than the molecule backbone, or if the end bonds which connect molecule chains to the attached surface are weaker than the molecule backbone. Both cases result in the premature failure of the molecule backbone and the incomplete unfolding of hidden lengths.

The structure-property relationship of the SBHL mechanism studied above provides important guidelines for the implementation of the SBHL mechanism in engineering materials, which is reviewed in the next section.

2.2 Bioinspired engineering design with SBHL

The Section 2.2 reviews the implementations of the SBHL mechanism in engineering materials at multiple length scales ranging from nanoscale to macroscale. The methods from the literature were divided into two categories depending on whether the sacrificial bonds and hidden lengths belong to a single network or two separate networks.

2.2.1 Single-network method

In the single-network method, sacrificial bonds are introduced to a single fiber in the form of π - π interactions [13], slip knots[14], or physically fused bonds [15], [16]. The breaking of sacrificial bonds unravels the hidden lengths along the single fiber. During the sequential breaking of sacrificial bonds and unfolding of hidden lengths, the structural integrity of the fiber is maintained,

and large amounts of energy are dissipated before the failure of the fiber backbone. The structured fibers in the single-network method are analogous to the biological molecules with tandem modules in Fig. 2.5d.

The stacked-cup carbon nanofibers (CNF) have a continuous cone-helix structure [41] (Fig. 2.8a). This type of carbon nanofiber is produced by catalytic chemical vapor deposition (CVD). The helically coiled graphene layers are bonded with weak π - π interactions [13]. When one end of the fiber is stretched, the weak interlayer bonds are sequentially broken, unraveling the helical graphene sheet off the hollow fiber (Fig. 2.8b). Compared to the single-walled carbon nanotube, the stacked-cup CNF shows higher extensibility and higher energy dissipation [13], [42].

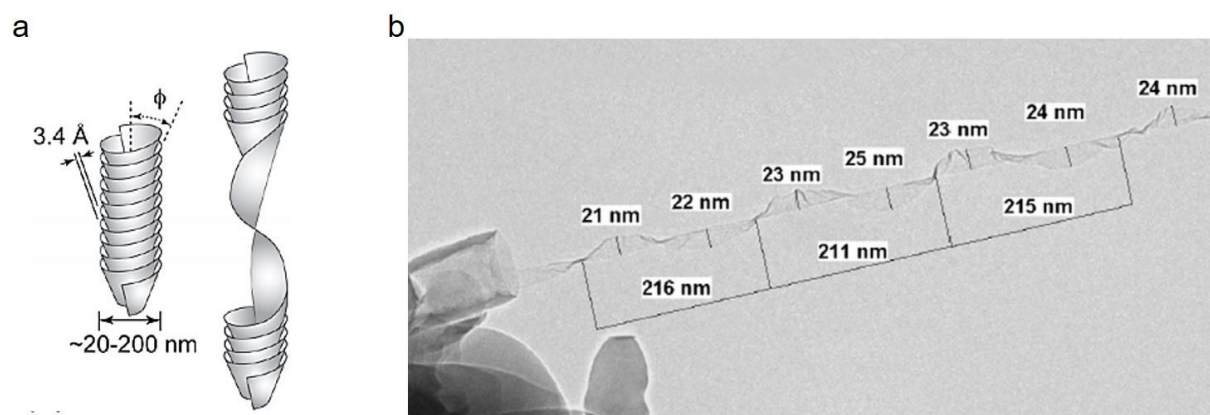


Figure 2.8 Stacked-cup carbon nanofiber. a) Schematic of the continuous cone-helix structure [13]. b) Transmission electron microscopy (TEM) image of the continuous helical graphene sheet unravelled from the hollow fiber [41]. The average periodical length of the helical graphene sheet matches exactly the average perimeter of the fiber cross section (214 nm).

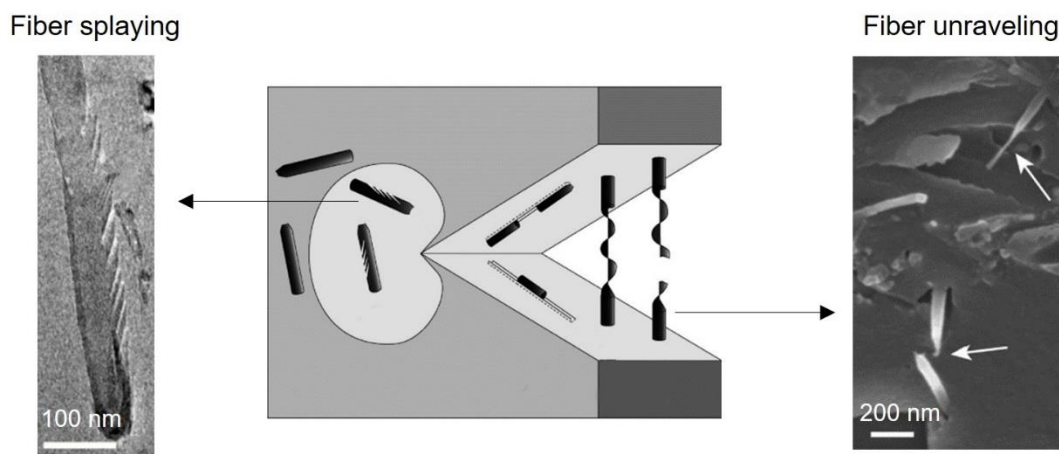


Figure 2.9 Schematic of the interaction between the stacked-cup CNFs and a propagating crack with SEM images of embedded nanofibers splaying between adjacent graphene layers and exposed nanofibers unraveling continuously after the matrix cracking [13].

Palmeri *et al.* [13] dispersed the stacked-cup CNFs in epoxy resins, reproducing the SBHL mechanism in high-performance nanocomposite. Besides the toughening mechanisms commonly seen in short-fiber-reinforced composites, such as crack deflection, fiber-matrix debonding, fiber pullout and rupture, two new mechanisms, *i.e.* fiber splaying between adjacent graphene layers and fiber unraveling of the continuous graphene sheet, were found in the stacked-cup-CNF-reinforced composites (Fig. 2.9). The high stress in front of the crack tip induces the breaking of the weak π - π interactions between the graphene layers, resulting in the fiber splaying. Behind the crack tip, the stacked-cup CNFs which are perpendicular to the crack plane unravel continuously under the tensile stress, contributing to extra energy dissipation before the final rupture. Palmeri *et al.* [13] achieved a 45–80% increase in fracture toughness (critical stress intensity factor K_{Ic}) in the epoxy composites with 0.68 wt% non-functionalized stacked-cup CNFs. While similar epoxy composites reinforced by 0.5 wt% non-functionalized and functionalized double-walled carbon nanotubes show ~31% and ~43% increases of the fracture toughness K_{Ic} , respectively [43]. Therefore, it is convincing that the fiber splaying and fiber unraveling mechanisms in the stacked-cup CNFs effectively increase the energy dissipation and thus the fracture toughness.

In Palmeri *et al.*'s work [13], the stacked-cup CNFs not only enhance the nanocomposite's mechanical properties, but also significantly increase the electrical and thermal conductivity, resulting in truly multifunctional composites. However, there are two limitations of the stacked-

cup-CNF-reinforced composites. First, the energy dissipation brought by the fiber splaying and unraveling can be offset by CNF agglomeration under high fiber contents [44], limiting the fracture toughness enhancement. Second, the exposed nanofibers after the matrix cracking in Fig. 2.9 show a transition between thin unraveled graphene sheet and thick intact fibers, indicating the incomplete unraveling of nanofibers and meaning that the full energy dissipation potential of the nanofibers remains to be exploited.

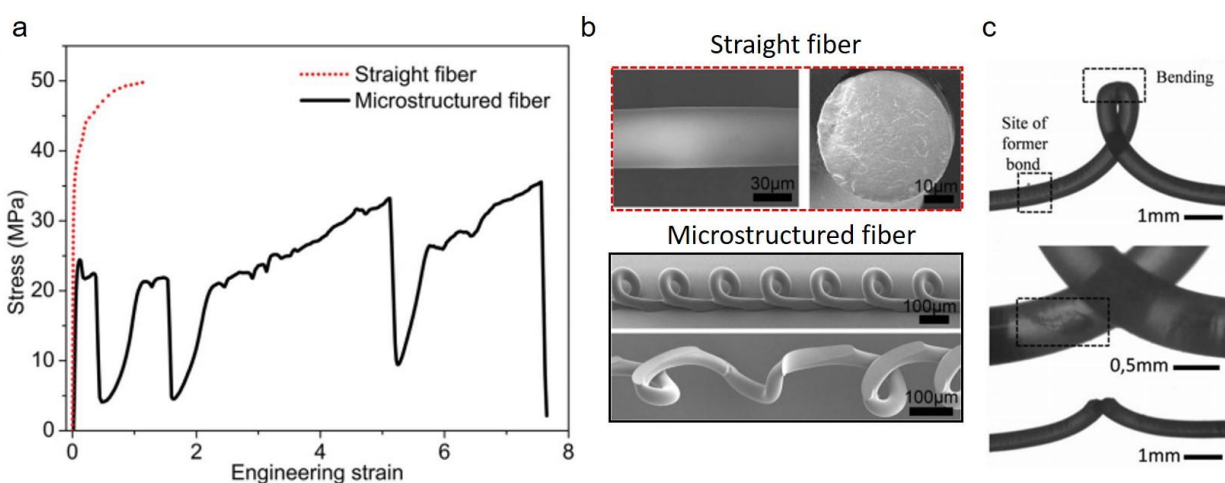


Figure 2.10 Microstructured PLA fiber with sacrificial bonds and hidden lengths. a) Stress-strain curves of a straight fiber and a microstructured fiber [15]. b) SEM images of the corresponding tested straight fiber and microstructured fiber [15]. c) Optical images of the premature failures of microstructured PLA fibers printed by instability-assisted fused filament fabrication (IFFF) [16].

Guo *et al.* [15] introduced microstructured sacrificial bonds into a PLA fiber with a diameter of 30 μm via an instability-assisted deposition process which will be reviewed in Section 2.3. The periodic coiling of the polymer thread during the fabrication process creates physically fused bonds along the fiber. These fused bonds are weaker than the fiber backbone and act as sacrificial bonds under a mechanical load. The comparison between the stress-strain curves of straight PLA fiber and microstructured PLA fiber is shown in Fig. 2.10a. SEM images of the fibers before and after fracture are shown in Fig. 2.10b. Under stretching, the straight PLA fiber breaks at an engineering strain of ~ 1.16 , while the microstructured PLA fiber breaks at an engineering strain of ~ 7.66 . The straight PLA fiber fails after the fracture of the fiber backbone, while the sacrificial bonds are broken in the microstructured PLA fiber, unraveling the “hidden” fiber loops. The breaking of

sacrificial bonds and unfolding of hidden lengths in the microstructured PLA fiber significantly increase the extensibility and toughness, compared to the straight fiber. Surprisingly, the looped structure physically and functionally resembles the micro-looped silk spun by the recluse spider in nature [45].

Novel fiber systems with self-healing [46] and strain sensing capabilities [47] were also developed based on the microstructured fibers, demonstrating a great potential of the microstructured fiber strategy in multifunctional material developments. However, premature failures were observed in the microstructured PLA fibers (Fig. 2.10c). In these premature failures, the fiber backbone fails before the breaking of sacrificial bonds, and the hidden lengths cannot be fully released, severely hindering the energy dissipation capability of the fiber. Passieux *et al.* [16] found that the toughness of the microstructured PLA fibers can be as high as 340% and as low as 25% of the toughness of the straight fiber benchmark. Passieux *et al.* [16] attributed these premature failures to the surface defect left by bond breaking and the cusp formed during the loop unfolding process (Fig. 2.10c), but the mechanics behind these premature failures remained unknown.

Pugno [14] came up with the idea of introducing slip knots into fibers as frictional elements to increase the energy dissipation and enhance the toughness (Fig. 2.11a and b). Under stretching, the slip knot acts as a “sacrificial bond”. The hidden length along the fiber loop is released by sliding through the knot, resulting in a plateau on the stress-strain curve and large amounts of friction energy dissipation (Fig. 2.11c). Pugno [14] concluded four design criteria to achieve the maximum enhancement of the fiber’s specific toughness: (1) maximizing the ratio of hidden length to the total length of the fiber; (2) minimizing the degradation of fiber strength during sliding; (3) maximizing the stress plateau during sliding; (4) minimizing the mass of the slider. These design criteria maximize the area under the stress-strain curve and lead to a maximal specific toughness. However, the second and the third criteria are often conflicted to each other, since a tighter knot increases the stress plateau but also more possibly degrades the fiber strength during sliding. The fiber strength degradation results in premature failures of the fiber backbone especially in certain knot configurations [48] or when the fiber surface is rough [49]. The compromise with a looser knot offsets the energy-dissipation benefits of the frictional slider. Bosia *et al.* [50] found that the premature failure happens to Kevlar aramid fibers, but not Zylon polybenzoxazole fibers, indicating the underlying material factor in the frictional slider performance.

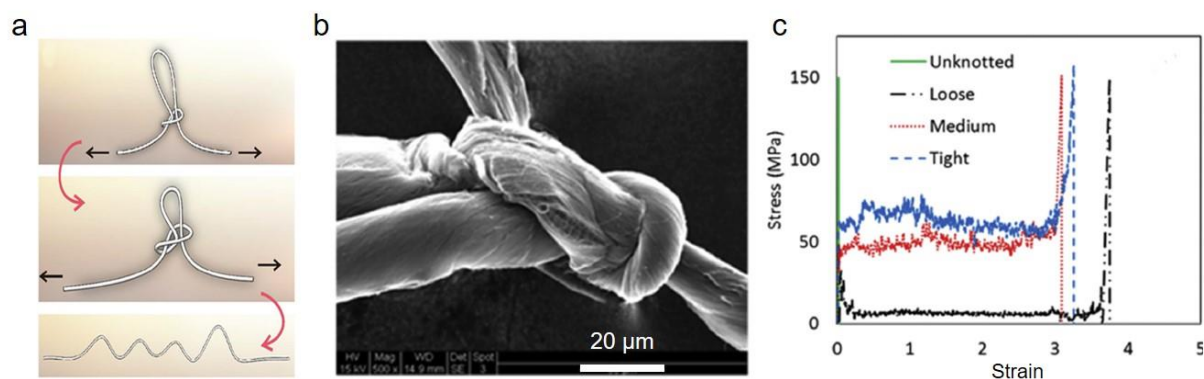


Figure 2.11 Carbon nanotube microfibers with a slip knot. a) Schematic of the sliding of the hidden length in a knotted fiber [49]. b) SEM image of a microscale slip knot of a carbon nanotube microfiber (dia. = 31 μm) [50]. The carbon nanotube microfiber was made by a dry-spinning process of drawable carbon nanotube arrays. The slip knot was introduced with a tweezer. c) Stress-strain curves of the carbon nanotube microfiber with slip knots at different tightening levels [50].

The slip-knot method achieved a $\sim 200\%$ toughness increase in silk fibers [49] and $\sim 2900\%$ in carbon nanotube microfibers [50] without significantly reducing the fiber strength, demonstrating a great potential in achieving the combination of strength and toughness. However, the slip-knot method involves intricate tweezer manipulations of microscale fibers [48] and has not been scaled up to bulk materials.

Zhu *et al.* [17] further increased the number of sacrificial bonds in each loop module with the help of dual-nozzle 3D printing (Fig. 2.12). A thick fiber (dia. = 0.4 mm) was printed by a nozzle with a diameter of 0.7 mm and a nozzle moving speed of 5 mm/s, while a thin fiber (dia. = 0.2 mm) was printed by a nozzle with a diameter of 0.3 mm and a nozzle moving speed of 10 mm/s. The thick fiber was printed with square-wave shape modules, acting as the backbone, and the thin fiber was printed between the thick fibers in each module, acting as the sacrificial bond. Under stretching, the breaking of sacrificial bonds releases the hidden lengths along the fiber backbone, increasing the extensibility and energy dissipation.

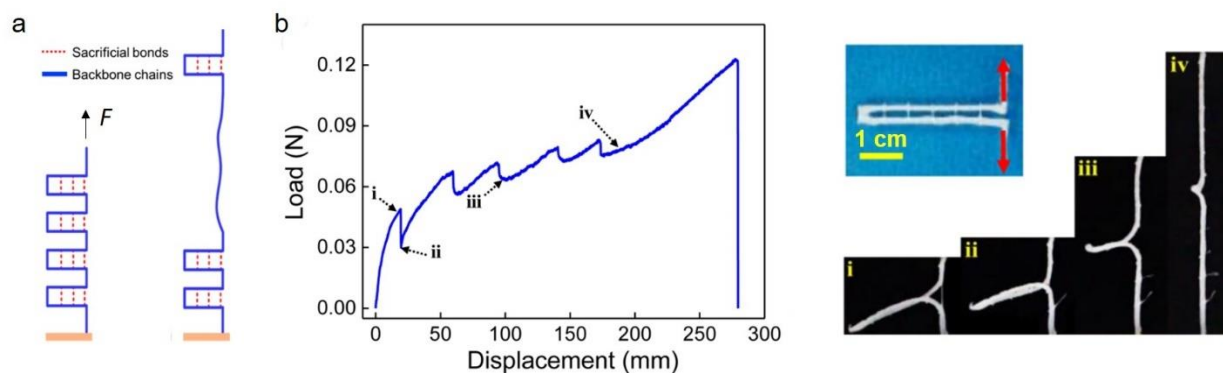


Figure 2.12 3D-printed hydrogel modular structure [17]. a) Schematic of the modular design of sacrificial bonds and backbone chain. b) Load-displacement curve of the 3D-printed hydrogel modular structure with five sacrificial bonds and corresponding snapshots of the tensile test.

2.2.2 Double-network method

In the double-network method, the material is composed by a stiff and brittle reinforcement (fiber or fabric mesh) and a soft and stretchable matrix. Under stretching, the shear stresses or the interlocking between the reinforcement and matrix induce multiple fracture events of the reinforcement, like the breaking of “sacrificial bonds”. After the fracture of the reinforcement, the soft matrix acts as the “hidden length” and can be significantly stretched before failure. Since the reinforcement is often stiffer than the matrix, the stiffness of the composite is much higher than the neat matrix material. Also, large amounts of energy are dissipated by the breaking of “sacrificial bonds” along the reinforcement, resulting in higher toughness than the neat matrix material.

Feng *et al.* [51] embedded a polyamide fabric mesh in between Very-High-Bond (VHB) acrylic tapes without using additional adhesives (Fig. 2.13). The tensile curve of the resulting composite shows three regimes: (1) linear-elastic and homogeneous deformation of the fabric mesh and matrix; (2) stress plateau due to multiple fracture events of the fabric mesh inside the matrix; (3) strain hardening due to the interlayer sliding and the stretching of the matrix. In the second regime, the fabric mesh fractures under the shear stress between the mesh and the matrix. The multiple fracture events of the fabric mesh continue until all mesh fragments reach a critical length, at which the shear stress is not high enough to further fracture the fabric. Then the third regime begins, and the strain hardening is supported by the interlayer sliding and the deformation of the matrix. Feng

et al. [51] also developed a one-dimensional analytical model based on the rule of mixtures and the shear-leg model, successfully predicting the peak stress in the first regime and the plateau stress in the second regime with different fabric volume ratios. The resulting composite achieves a $\sim 400\%$ increase in stiffness and a $\sim 107\%$ increase in total energy to failure compared to the acrylic tape.

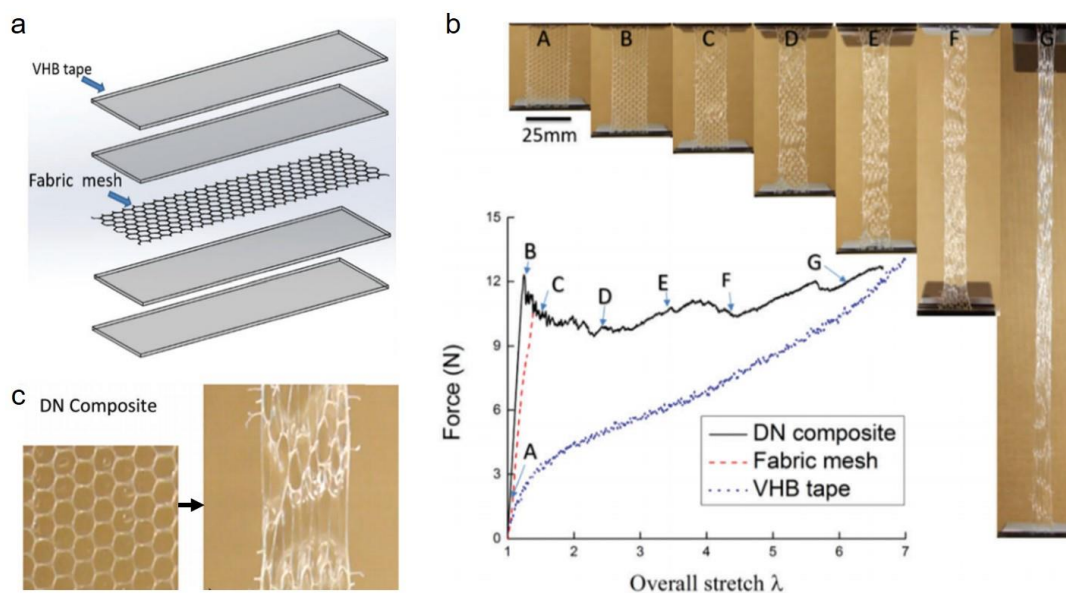


Figure 2.13 Double-network (DN) composite based on the polyamide fabric mesh and VHB tapes [51]. a) Schematic of the DN composite. b) Stress-strain curves of the VNB tape, fabric mesh and DN composite with test snapshots of the DN composite. c) Fabric mesh fragmentation inside the VHB tape.

Cooper *et al.* [52] developed a double-network composite fiber with a low-melting-point metal gallium as the reinforcement and an elastic polymer poly(styrene-ethylene butylene-styrene) (SEBS) as the matrix (Fig. 2.14a). The metal has a melting temperature around 30°C and can be injected into the hollow SEBS fiber without causing any distortions. After the metal core transforms into the solid phase, the stiffness of the composite is drastically increased. Once the metal core breaks, a polymer bridge is formed and continues to carry the load. Since the force required to break the metal core is less than that to break the polymer bridge, the shear stress between the core and the shell induces the repetitive and sequential breaking of the metal core (Fig. 2.14b), like the breaking of “sacrificial bonds”. The breaking of the metal core and straining of the

polymer bridge results in a stress plateau on the tensile curve of the composite fiber (Fig. 2.14c), effectively increasing the energy dissipation.

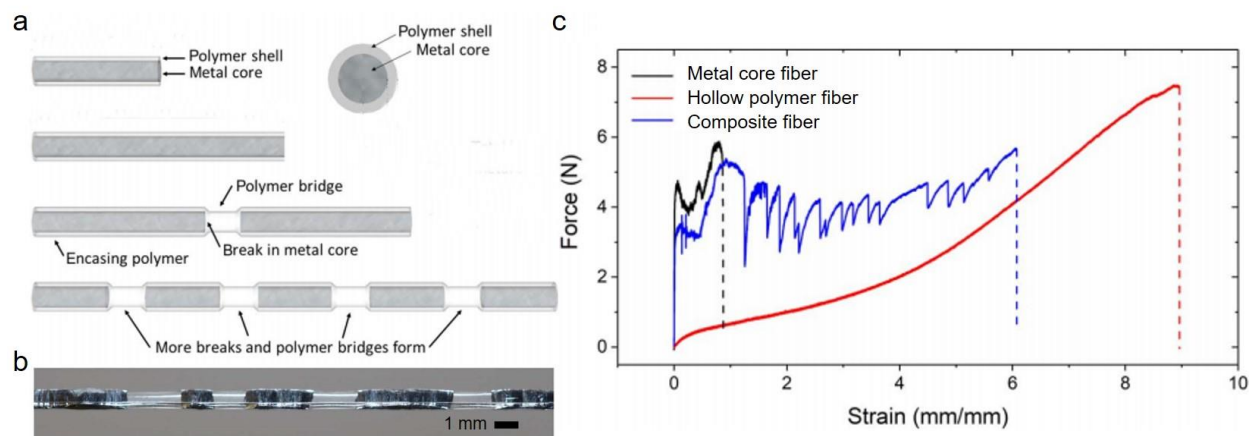


Figure 2.14 Double-network composite fiber with a low-melting-point metal core and a polymer shell [52]. a) Schematic of the composite fiber. b) Multiple breaks of the metal core inside the polymer shell. c) Tensile curves of the metal core fiber, hollow polymer fiber, and composite fiber.

Takahashi *et al.* [53] molded an alloy with a low melting temperature around 60°C into a honeycomb-shaped mesh and created a stiff and tough hydrogel composite (Fig. 2.15a). Similar to the one-dimensional design in Cooper *et al.*'s work [52], the metal reinforcement significantly increases the stiffness of the composite, and the multiple breaks of the metal reinforcement and the straining of the matrix effectively increase the energy dissipation (Fig. 2.15b). One slight difference is that, the multiple breaks of the metal core in Cooper *et al.*'s work [52] are induced by the shear stress between the polymer shell and the metal core, while the multiple breaks of the metal mesh in Takahashi *et al.*'s work [53] are caused by the interlocking between the metal mesh and the hydrogel matrix.

Although the low melting temperature of the metal reinforcement in above studies restricts the engineering applications of the composite, an amazing self-healing property was achieved by immersing the composite under hot water (80°C) and demonstrated by Takahashi *et al.* [53], opening up new possibilities for multifunctional composites.

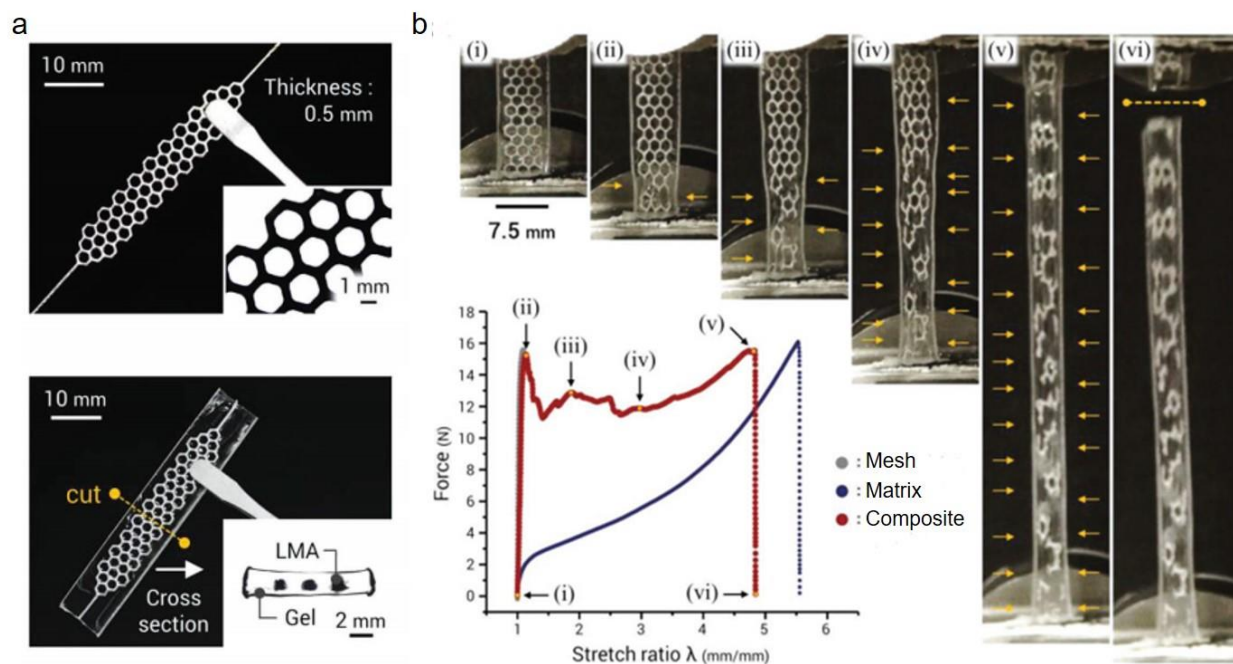


Figure 2.15 Double-network composite with a low-melting-point metal mesh and a hydrogel matrix [53]. a) Optical images of the metal mesh and hydrogel composite. b) Tensile curves of the metal mesh, hydrogel matrix, and composite.

King et al. [54] developed a double-network composite using a 3D-printed plastic mesh as the “sacrificial network” and an elastomer matrix (Fig. 2.16). The multiple breaks of the plastic mesh are induced by an interlocking mechanism similar to that in Takahashi *et al.*'s work [53]. Since the mesh is fabricated by 3D printing, the “sacrificial bonds” can be designed and fabricated with different cross section areas, leading to different bond strengths. Therefore, the stress plateau on the composite's tensile curve and the breaking sequence of the “sacrificial bonds” can be controlled by designing the bond strength within each sacrificial section (Fig. 2.16a) along the mesh. The resulting double-network elastomer composite achieves a ~60 time increase in stiffness and a ~0.5 time increase in total energy to failure, compared to the neat elastomer.

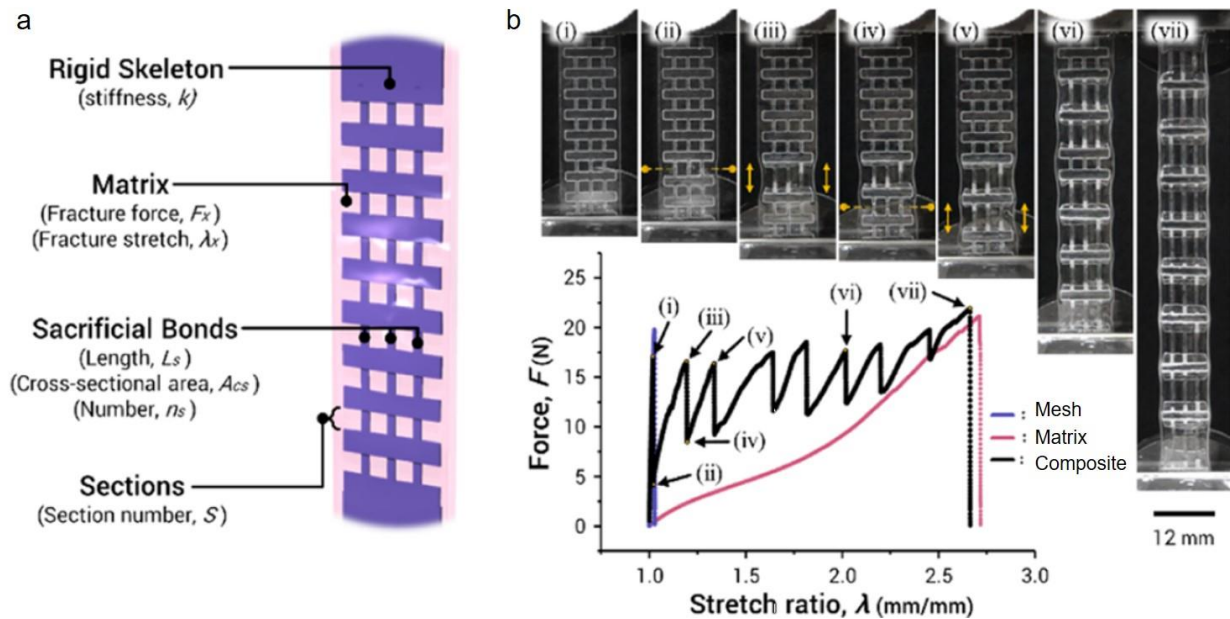


Figure 2.16 Double-network composite with a 3D-printed acrylate-based plastic mesh and a silicone elastomer matrix [54]. a) Schematic of the double-network composite. b) Tensile curves of the plastic mesh, elastomer matrix and composite.

The comparison of different bioinspired engineering design methods with SBHL is given in Table 2.1. Due to the drastic difference between the stiffness of the reinforcement and the matrix, the double-network method often leads to a significant increase in stiffness compared to the neat matrix material, while the enhancement in total energy absorption is not as high as the stiffness enhancement. The main reason is that the strength of the reinforcement has to be lower than the strength of the matrix, otherwise the matrix would break after the first break of the reinforcement and the sequential breaking of “sacrificial bonds” would be impossible. Also, without extra energy dissipating mechanisms in the matrix itself like reference [53], the hysteresis (the ratio of dissipated energy to total absorbed energy) of the composite ($\sim 50\text{--}60\%$ [51], [54]) has an upper bound which is brought by the elastic recovery of the matrix. Although the elastic recovery of the matrix can be useful in fatigue-related applications [55], [56], it restricts the energy dissipation capability of the composite.

Table 2.1 Comparison of different bioinspired engineering design methods with SBHL.

Method	Sacrificial bond	Hidden length	SBHL Fabrication method	Material	Scale	Strength increase $\Delta\sigma^1$	Energy absorption increase ΔE^1	Ref
Single-network	π - π interactions	Helically coiled graphene sheet	Catalytic chemical vapor deposition	Stacked-cup carbon nanofibers	20-200 nm (fiber dia.)	N/A	N/A	[41]
	Physically fused bond after solvent evaporation	Coiling loops	Solvent-cast direct write	PLA	30 μ m (fiber dia.)	-29.00%	231%	[15]
	Thermally fused bond after cooling	Coiling or alternating loops	Fused filament fabrication	PLA	0.5 mm (fiber dia.)	-40%	up to 240%	[16]
	Overhand micro slip-knot	Knotted loop	Tweezer manipulation	Caron nanotube microfibrils	30-41 μ m (fiber dia.)	0%	up to 2900%	[50]
	Single and double turned slip knots	Knotted loop	Tweezer manipulation	Raw silk and degummed silk	12-21 μ m (fiber dia.)	~-32% to 8%	up to 200%	[49]
	Thin fiber	Thick fiber	Dual-extruder 3D printing	Polyion complex hydrogel	0.2-0.4 mm (fiber dia.)	N/A	N/A	[17]
Double-network	Fabric mesh	Viscoelastic matrix	Lamination	- Polyamide fabric mesh - VHB acrylic tapes	0.2 mm (Mesh thickness)	~-53% to 23%	up to 107%	[51]
	Low-melting-point metal fiber core	Elastomeric shell	Liquid metal injection	- Gallium fiber core - SEBS polymer shell	1.2 mm (fiber dia.)	-56%	70% (at 450% strain)	[52]
	Low-melting-point alloy mesh	Hydrogel matrix	Liquid metal casting	- LMT alloy (32.5% Bi, 51% In, 16.5% Sn) - PUMA and PAAm hydrogel ²	0.5 mm (Mesh thickness)	-3%	51%	[53]
	Plastic mesh	Elastomeric matrix	UV-assisted material jetting 3D printing	- Acrylate-based plastic mesh - silicone elastomer	0.3 mm (Mesh thickness)	4%	21% to 51%	[54]

¹Strength increase $\Delta\sigma = (\sigma_s - \sigma_n)/\sigma_n$, energy absorption increase $\Delta E = (E_s - E_n)/E_n$, where the subscript s represents the structured fiber in single-network methods and the composite material in double-network methods, the subscript n represents the straight fiber in single-network methods and the neat matrix material in double-network methods.

²PUMA: poly(2-ureidoethyl methacrylate)-co-(methacrylic acid); PAAm: polyacrylamide.

2.3 Instability-assisted deposition

The Section 2.3 focuses on the theoretical and experimental studies of a thin viscous thread falling onto a stationary surface (liquid rope coiling) or a moving surface (fluid-mechanical sewing machine), and their applications in materials manufacturing.

2.3.1 Liquid rope coiling

When a thin viscous thread is deposited from a certain height onto a horizontal surface, the thread coils instead of crushes onto the surface. This phenomenon is called liquid rope coiling, which was first studied in 1958 by Barnes and Woodcock [57]. The coiling motion is induced by the buckling instability of the thread under axial compression. As shown in Fig. 2.17, The coiling phenomenon has been seen in many materials from purely viscous ones like honey [58], silicone oil [59], glucose syrup [60], to purely elastic ones like an elastic rod [61], or viscoelastic ones like shear-thinning polymer ink [15] and molten glass [62], [63].

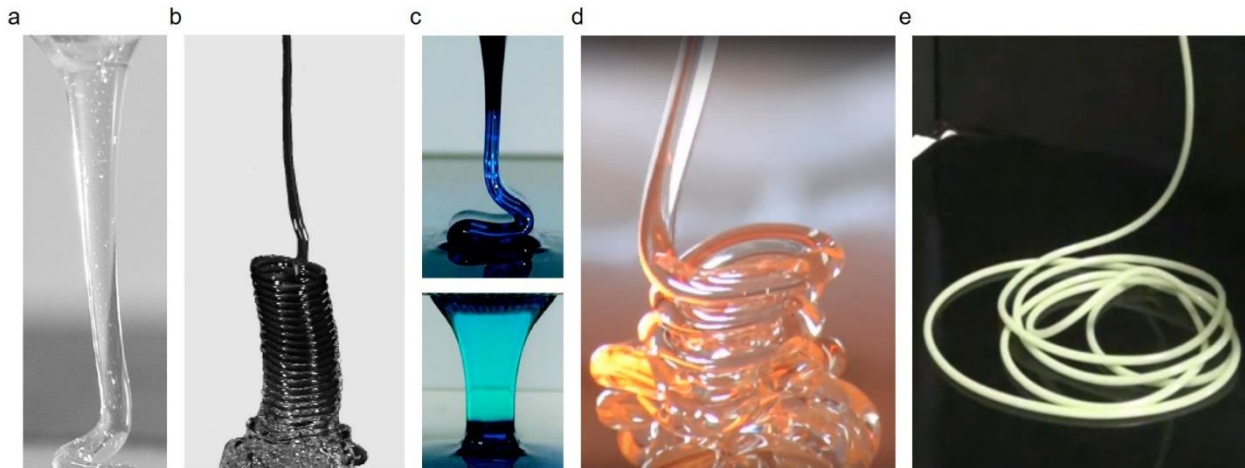


Figure 2.17 Coiling phenomenon in various materials. (a) Honey [58]. (b) Silicone oil (PDMS) [59]. (c) Glucose syrup [60]. (d) Molten glass [62]. (e) Elastic rod [61].

Numerical modeling of the coiling phenomenon in a viscous thread highlights three types of force that cause the bending and twisting deformation of the thread [64]. Per unit length of the thread, the magnitudes of the viscous (F_V), gravitational (F_G), and centrifugal inertial (F_I) forces [64] are

$$F_V \sim \rho \nu r^4 U R^{-4}, \quad F_G \sim \rho g r^2, \quad F_I \sim \rho r^2 U^2 R^{-1}, \quad (2-3)$$

where r is the rope radius at the coiling region, R is the coiling radius, U is the axial velocity, ν is the kinematic viscosity of the fluid. Three regimes of steady coiling were found depending how these three forces are balanced, as shown in Figure 2.18. The coiling frequencies [64] at the three regimes are

$$\Omega_V = \frac{Q}{Hr^2}, \quad \Omega_G = \left(\frac{gQ^3}{\nu r^8}\right)^{\frac{1}{4}}, \quad \Omega_I = \left(\frac{Q^4}{\nu r^{10}}\right)^{\frac{1}{3}}, \quad (2-4)$$

where, $Q = U\pi r^2$ is the volume flow rate at the coiling region of the rope, H is the deposition height. Experimental measurements and numerical predictions of coiling frequencies under different deposition height are shown in Figure 2.18.

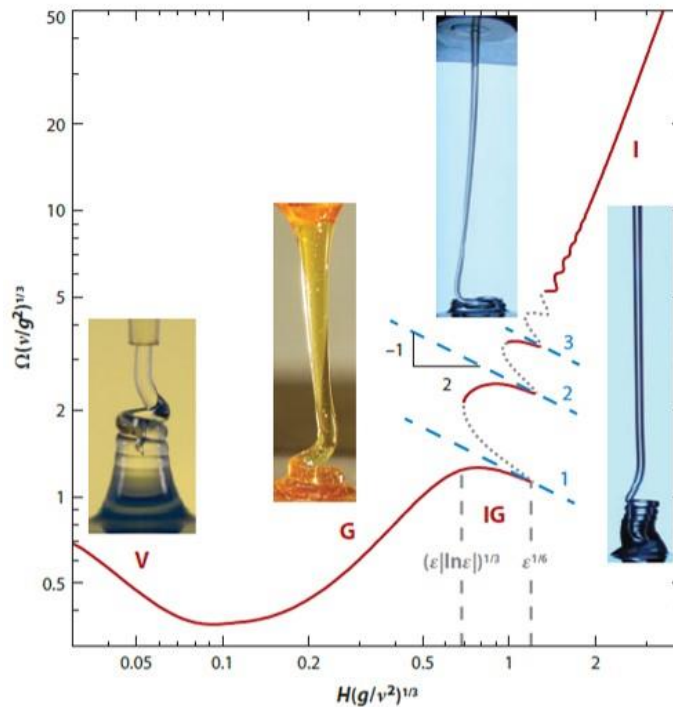


Figure 2.18 Dimensionless coiling frequency $\hat{\Omega} = (\nu/g^2)^{1/3}$ versus dimensionless deposition height $\hat{H} = H(g/\nu^2)^{1/3}$ [65]. Four regimes are shown: (1) Viscous regime, $0.03 < \hat{H} < 0.08$, dimensionless deposition height (2) Gravitational regime, $0.2 \leq \hat{H} \leq 0.6$. (3) Inertio-gravitational regime, $0.7 < \hat{H} < 1.4$. (4) Inertial regime, $\hat{H} > 1.8$. The red curve is from numerical prediction. The dotted segments of the curve represent unstable solutions from numerical calculations.

In the viscous regime, gravity and inertia are negligible ($F_V \gg F_G, F_I$), the coiling frequency is independent of viscosity, and the velocity of the rope is fully determined by the deposition volume flow rate Q . In the gravitational regime, inertia is still negligible ($F_V \approx F_G \gg F_I$), the viscous and gravitational forces are balanced. In the inertial regime, gravity is negligible ($F_V \approx F_I \gg F_G$), the viscous force is balanced by the inertial force. Between the gravitational and inertial regime, the coiling frequency is determined by the force balancing along the long stretching part of the rope. In this case, all three forces should be involved to resist stretching. In this so-called inertio-gravitational regime, the coiling frequency [66] is

$$\Omega_{IG} = C \left(\frac{g}{H} \right)^{\frac{1}{2}}, \quad (2-5)$$

where, C is a constant determined numerically. The coiling frequency is proportional to $(g/H)^{1/2}$, as shown by blue dashed lines in Figure 2.18.

2.3.2 Fluid-mechanical sewing machine

As a variant of steady liquid rope coiling, a viscous thread falling onto a moving belt, so-called “fluid-mechanical sewing machine (FMSM)”, was initially studied by Chiu-Webster and Lister [67]. They developed a simple experimental setup to investigate the diverse patterns in this phenomenon. In their experiments, a fluid thread (syrup) with a kinematic viscosity ν was deposited at a volumetric rate Q from a nozzle with diameter d at a deposition height H , onto a horizontally moving belt with velocity U_0 , as shown in Figure 2.19. When the belt velocity U_0 is very large, a steady dragged catenary is created after the fluid was extruded from the nozzle, and a stretched straight pattern is formed on the belt. As the belt velocity decreases to a critical value U_C , a backward heel is created just before the thread hit on the belt, and a meandering pattern is formed on the belt. As the belt velocity continues to decrease, several intermediate patterns appear until a translated coiling pattern is finally produced, which can be expected according to the steady liquid rope coiling mentioned in Section 2.3.1. Chiu-Webster and Lister [67] developed a pure stretching model without considering bending stresses of the viscous thread which successfully predicted the critical belt velocity U_C under different deposition heights.

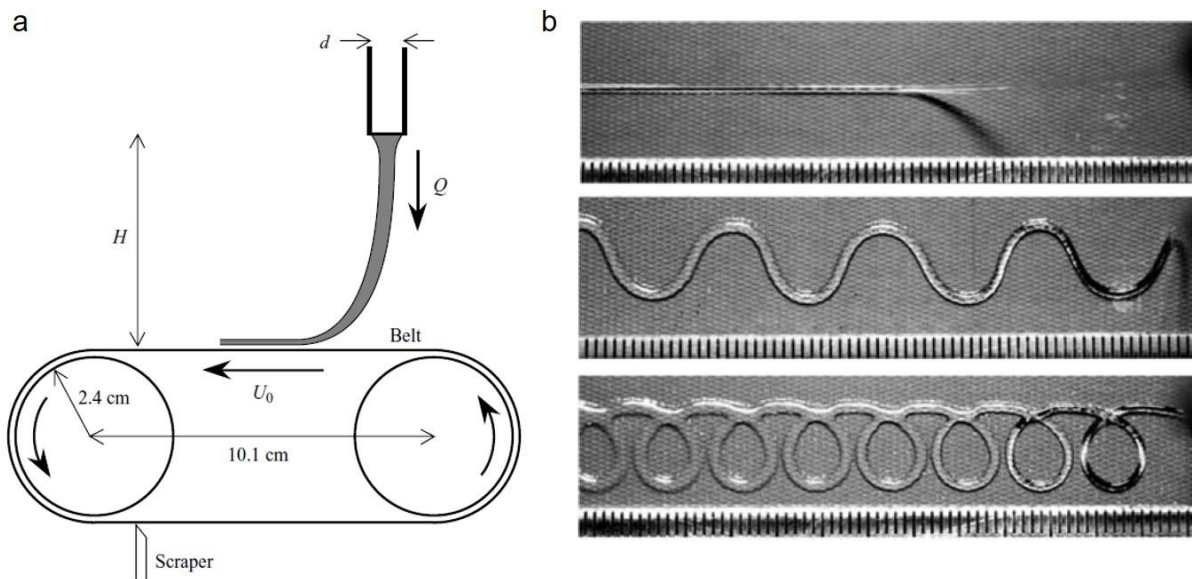


Figure 2.19 a) Schematic of the “fluid-mechanical sewing machine”. b) Three different patterns: straight, meandering, and translated coiling. [67]

Ribe *et al.* [68] used a viscous rod model which takes the bending and torsional stresses of the viscous thread into account, and found that the critical belt velocity is nearly identical to the vertical speed of the viscous thread just before the thread hits on the belt and the corresponding critical frequency is nearly identical to the coiling frequency in steady liquid rope coiling. Welch *et al.* [69] further carried out extensive experiments on the evolution of various patterns between unstable meandering and periodic coiling. In their experimental setup, a side camera and a 45° mirror was used to capture the transverse and longitudinal motions of the thread at the same time, and an indirect way was used to reconstruct the motion of contact point through digital image analysis, by extracting cross points of the thread centerline and a horizontal line set just above the belt in the image, as shown in Figure 2.20a. By Fourier spectra analysis of transverse and longitudinal motions of the thread, Welch *et al.* [69] categorized different patterns according to their frequencies, amplitudes and phase relationships, as shown in Figure 2.20b.

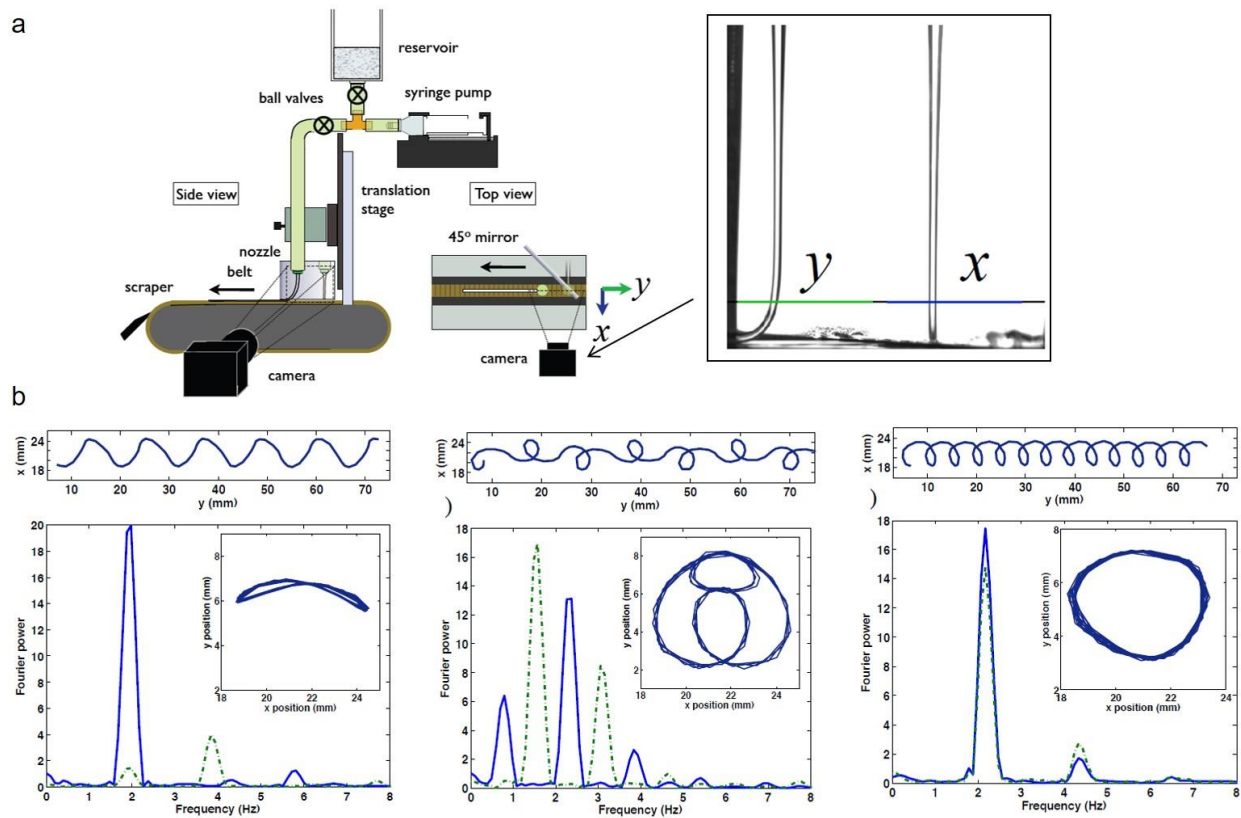


Figure 2.20 Experimental setup for the “fluid-mechanical sewing machine” and Fourier analysis of different patterns [69]. (a) A 45° camera is used to capture simultaneously x and y views of the thread. The y view shows the motion of the thread, which is parallel to the belt motion, while the x view captured in the mirror shows the motion of the thread which is transverse to the belt motion. The horizontal line is used to determine the motion of the thread which is proportional to the motion of the contact point. (b) From left to right: Fourier spectra for the meandering, alternating and coiling pattern. Top plots are the reconstructed patterns on the belt based on the motion of the thread. Inset plots are the reconstructed traces of contact point.

Brun *et al.* [70] developed a nonlinear numerical simulation of FMSM using a Discrete Viscous Rods (DVR) computational algorithm [71] which accurately predicted various FMSM patterns (Figure 2.21a). The phase diagram as a function of belt velocity and deposition height from simulation results agrees well with the experimental one. With DVR simulation results, Brun *et al.* [72] developed a quasistatic geometrical model for FMSM. The geometrical model includes three ordinary differential equations (ODEs):

$$r' = \cos(\theta - \psi) + \frac{V_B}{U_c} \cos \psi, \quad (2-6)$$

$$r\psi' = \sin(\theta - \psi) - \frac{V_B}{U_c} \sin \psi, \quad (2-7)$$

$$\theta' = \kappa(r, \theta - \psi) = \frac{1}{R_c} \sqrt{\frac{r}{R_c}} \left(1 + \frac{0.715^2 \cos(\theta - \psi)}{1 - 0.715 \cos(\theta - \psi)} \cdot \frac{r}{R_c} \right) \sin(\theta - \psi), \quad (2-8)$$

where, V_B is the belt velocity, U_c is the steady coiling velocity, R_c is the steady coiling radius, r is the distance between the contact point and the nozzle's reflection position on the plate, ψ is the angle between \vec{r} and the direction of belt velocity, θ is the angle between the direction of belt velocity and the trace's tangent at contact point, κ is the curvature at the contact point along the deposition trace $q(s, t)$, as shown in Figure 2.21b. Equations (2-6) and (2-7) are kinematic equations which are derived from the quasi-static geometrical model for the deposition trace and the non-slip boundary condition at contact point. Equation (2-8) is a curvature function fit from three variables from DVR simulations: the distance r , the curvature κ , the angle Φ ($\theta - \psi$) between the trace's tangent at contact point and \vec{r} .

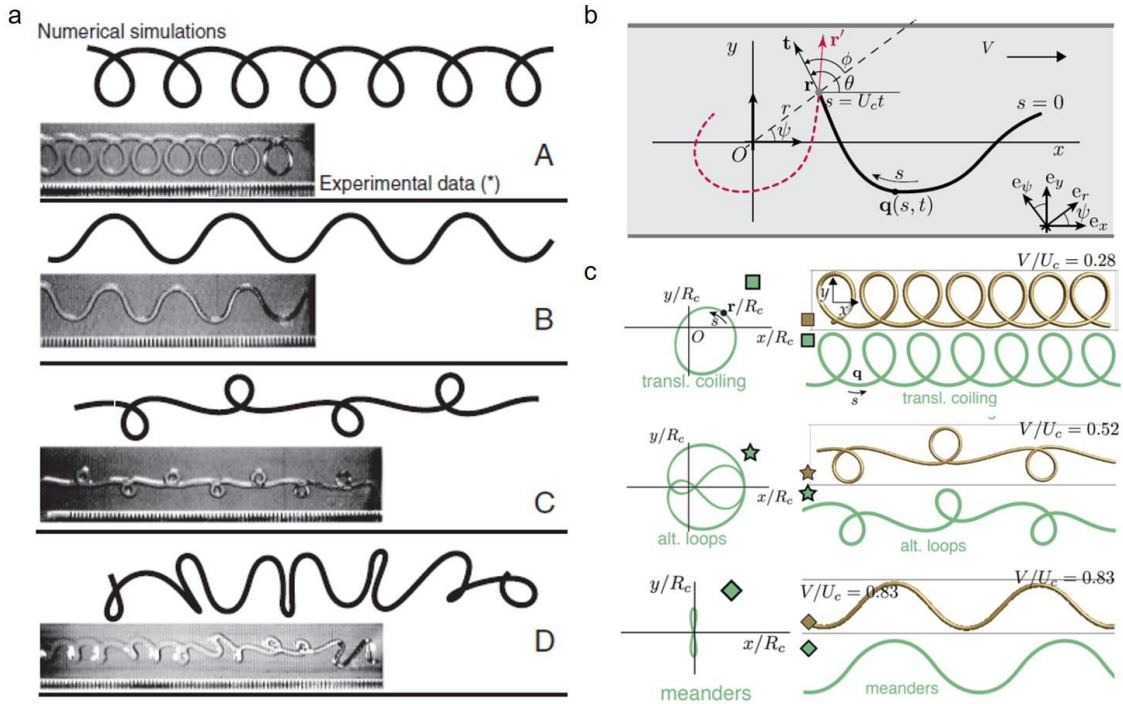


Figure 2.21 (a) Comparison between numerical simulations based on DVR algorithm and experimental data [70]. The numerical simulations successfully reproduced nine out of ten different

patterns observed from previous experiments [73]. (A: Translated coiling; B: Meandering; C: Alternating; D: Disorder) (b) Schematic of the deposition trace with respect to the nozzle projection [72]. Black line is the pattern on the belt and red line is the corresponding trace of contact point. (c) Geometrical predictions for different patterns (green lines) compared with numerical simulation results (brown lines) [72].

The solution to Equations (2-6) to (2-8) are three functions: $r = r(s)$, $\psi = \psi(s)$, $\theta = \theta(s)$. x and y coordinates of the thread motion can be calculated by

$$x_i = r(s_i) \cdot \cos(\psi(s_i)) + \frac{V_B}{U_c}(s_n - s_i), \quad (2-9)$$

$$y_i = r(s_i) \cdot \sin(\psi(s_i)), \quad (2-10)$$

where, i is the index in the numerical solution to Equations (2-6) to (2-8), with the value from 1 to n , s_n is to the last value of s in the numerical solution corresponding to the contact point at the final step of calculation. The geometric prediction from this model agrees well with DVR simulation results as shown in Figure 2.21c and the geometrical model is much simpler with only three ordinary differential equations.

Due to the geometrical similarity between the elastic sewing machine (ESM) and the FMSM, similar methodologies have been adapted for experimental investigation [74], numerical simulation [61] and geometrical modeling [75] of ESM.

2.3.3 Engineering applications

Liquid rope coiling has been adapted in several manufacturing technologies such as 3D printing and electrohydrodynamic process to produce functional structures for toughness enhancement [15], [16], strain sensing [46], [47], food printing [76] and tissue regeneration [77] applications. Various complex structures such as helical [78] or looped [16] fibers, anisotropic fabrics [79], cellular foams [80], and biomedical scaffolds [77] were achieved with the help of the coiling instability.

Jia *et al.* [78] deposited the viscous thread into a coagulating bath (Fig. 2.22a) instead of a solid surface used in previous experimental investigations reviewed in Sections 2.3.1 and 2.3.2. After falling into the coagulating bath, the coiled thread is rapidly coagulated by the bath solution. The deposition of the viscous thread into a horizontally moving coagulating bath results in continuous

helical fibers as shown in Fig. 2.22b. The resulting helical fiber shows a large extensibility of $\sim 160\%$. The increase in spinning height reduces the diameter of the helical structure, leading to a higher stress plateau on the tensile curve (Fig. 2.22c). Hollow helical fiber membranes were also fabricated by this technique [81].

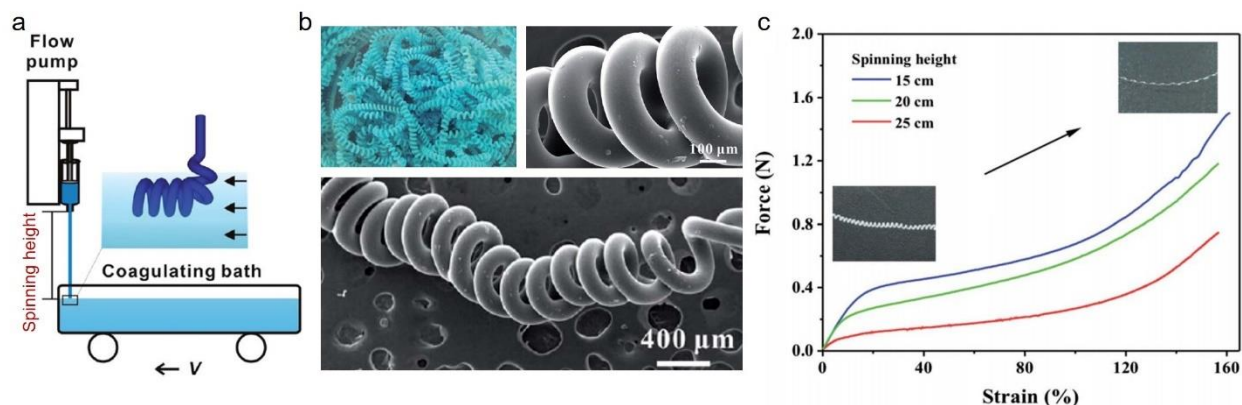


Figure 2.22 Helical fibers based on liquid rope coiling [78]. a) Schematic of the fabrication process. b) Optical and SEM images of the helical fibers. c) Tensile curves of the helical fibers fabricated under different spinning height.

Extrusion-based 3D printing technologies often involve with a shear-thinning thread or a molten thread. The fluidic instabilities on these 3D printers have been harnessed to produce various functional structures. Guo *et al.* [15] developed a solvent-cast direct write technology to print free-form structures with a thin polymer thread which solidifies after solvent evaporation. They transformed the solvent-cast direct write 3D printer into a fluid-mechanical sewing machine by elevating the nozzle above the printing surface (Fig. 2.23a). Weakly fused bonds were formed at the intersections of the coiling fibers after solvent evaporation. These weak bonds act as sacrificial bonds under a tensile load and increase the fiber's toughness, as shown in Fig. 2.10. Passieux *et al.* [16] reproduced the various FMSM patterns by harnessing the fluidic instability of the molten polymer thread on an FFF 3D printer. They compared the patterns produced by the FFF 3D printer and the patterns produced by Guo *et al.*'s method [15], demonstrating the pattern similarity despite the more than one order of magnitude difference in fiber diameters (Fig. 2.23b). They also demonstrated that fibers with various stiffness and toughness can be produced by simply manipulating the speed ratio of extruding speed to platform moving speed on a 3D printer (Fig. 2.23c). Wei *et al.* [47] replaced the PLA ink in Guo *et al.*'s method [15] with a conductive

nanocomposite ink, creating a coiling fiber with a strain sensing capability. The coiling fiber's overall electrical resistance showed a step-increase behavior under a tensile load, which was believed to be related with the breaking of sacrificial bonds and unfolding of hidden lengths (Fig. 2.23d). Wu *et al.* [46] further improved the repeatability of the coiling-fiber strain sensor by depositing a conductive self-healing nanocomposite thread onto a stretchable elastomer substrate (Fig. 2.23e). Due to the strong adhesion between the coiling fiber and the elastomer substrate, all sacrificial bonds along the coiling fiber can break at once when the substrate is stretched, resulting in the increase of the fiber resistance. As the elastomer substrate is unloaded, the coiling fiber recovers its original shape and the fiber resistance is also recovered due to the self-healing of sacrificial bonds. The resulting sensor demonstrated a good repeatability through 1000 cycles (Fig. 2.23f).

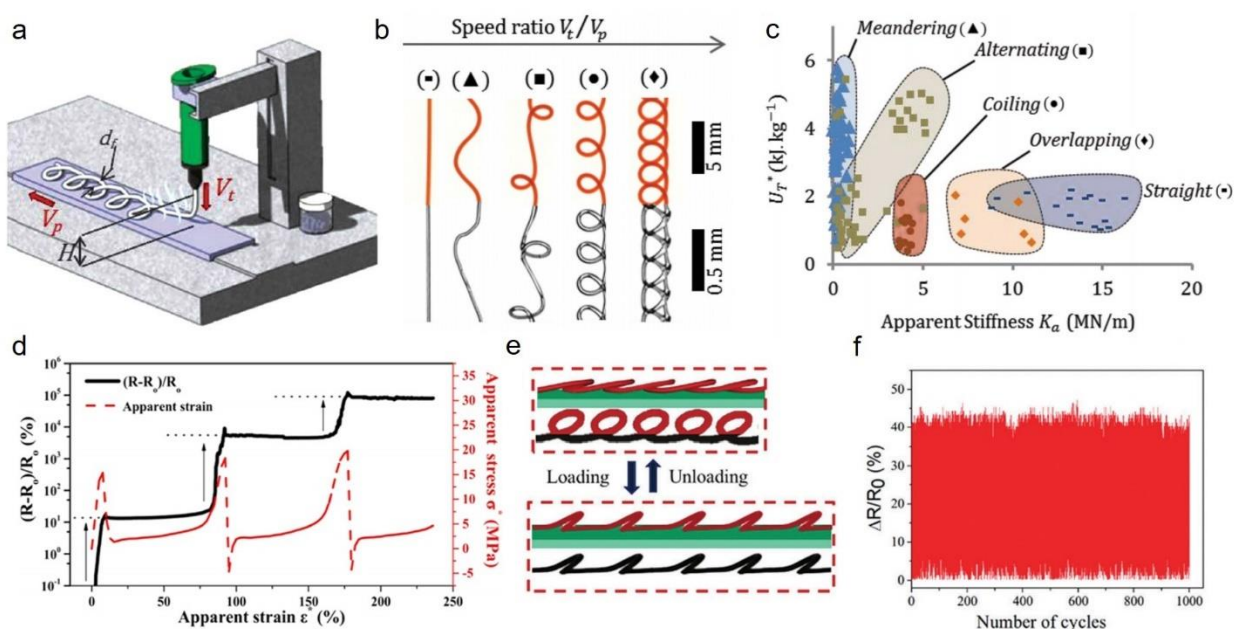


Figure 2.23 Looped fibers based on instability-assisted 3D printing. a) Schematic of instability-assisted solvent-cast direct write 3D printing [16]. b) Different fiber patterns printed by instability-assisted fused filament fabrication (orange fibers) and instability-assisted solvent-cast direct write (translucent fibers) [16]. c) Ashby plot of the specific toughness to the apparent stiffness of different fiber patterns [16]. d) Strain sensing performance of a coiling fiber with three loops [47]. e) Schematic of the self-healing strain sensor. The black segments represent the electronic

pathways [46]. f) Cyclic test of the self-healing strain sensor subjected to tensile loading and unloading at a maximum strain of 10% [46].

The layer-by-layer fashion of 3D printing offers more structural possibilities than a one-dimensional fluid-mechanical sewing machine. Yuk *et al.* [79] printed a bidirectional hydrogel fabric with straight fibers along x direction and meandering fibers along y direction. The fabric shows anisotropic properties under tensile loads (Fig. 2.24a). Lipton *et al.* [80] printed cellular foams with various mechanical properties and demonstrated the printing of cellular structure with complex geometries by instability-assisted 3D printing (Fig. 2.24b). Brun *et al.* [63] printed an architected glass with coiling patterns by harnessing the fluidic instability of a molten glass thread (Fig. 2.24c). In these examples, the feature size of the printed structures exceeds the native resolution of the 3D printer, benefiting from the harnessing of the fluidic instability of the printing thread.

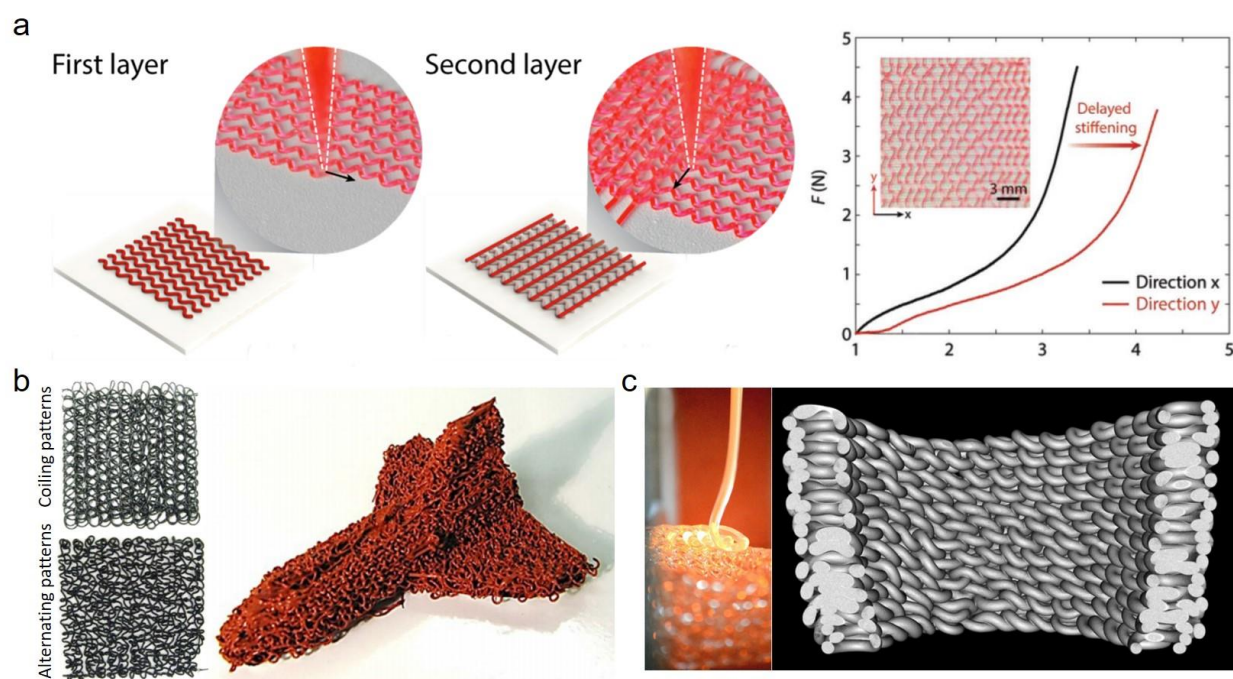


Figure 2.24 Instability-assisted 3D printing of multilayered structures. a) Bidirectional hydrogel fabric with anisotropic tensile behavior [79]. b) Cellular structures [80]. c) Optical image and computerized X-ray tomography scanning image of 3D-printed glass with coiling patterns [63].

The electric stress in a charged viscous thread accelerates and stretches the thread, breaking the frequency-height relationship shown in Fig. 2.18 in a noncharged viscous thread and achieving high coiling frequencies even at a small deposition height [82]. The deposition of the charged thread onto a horizontally moving platform results in similar coiling patterns to the fluid-mechanical sewing machine [83]. Li *et al.* [84] developed an electrocoiling-guided printing system and achieved the rapid switching between different FMSM patterns within one single wavelength by controlling the voltage applied between the nozzle and the collecting platform (Fig. 2.25a and b). Choe *et al.* [77] developed an electro-jetting process and printed scaffolds with controllable microscale and macroscale pores for tissue regeneration applications. Their scaffolds were built with coiling loops and exhibited saw-tooth patterns on the tensile curves (Fig. 2.25c), which were probably attributed to the breaking of adhesions between coiling fibers and the unfolding of coiling loops. The instability-assisted electrohydrodynamic process allows the fabrication of nano- or microscale fibers at a high deposition speed (~ 100 mm/s), showing a great potential in building complex fiber networks with tunable structures and properties.

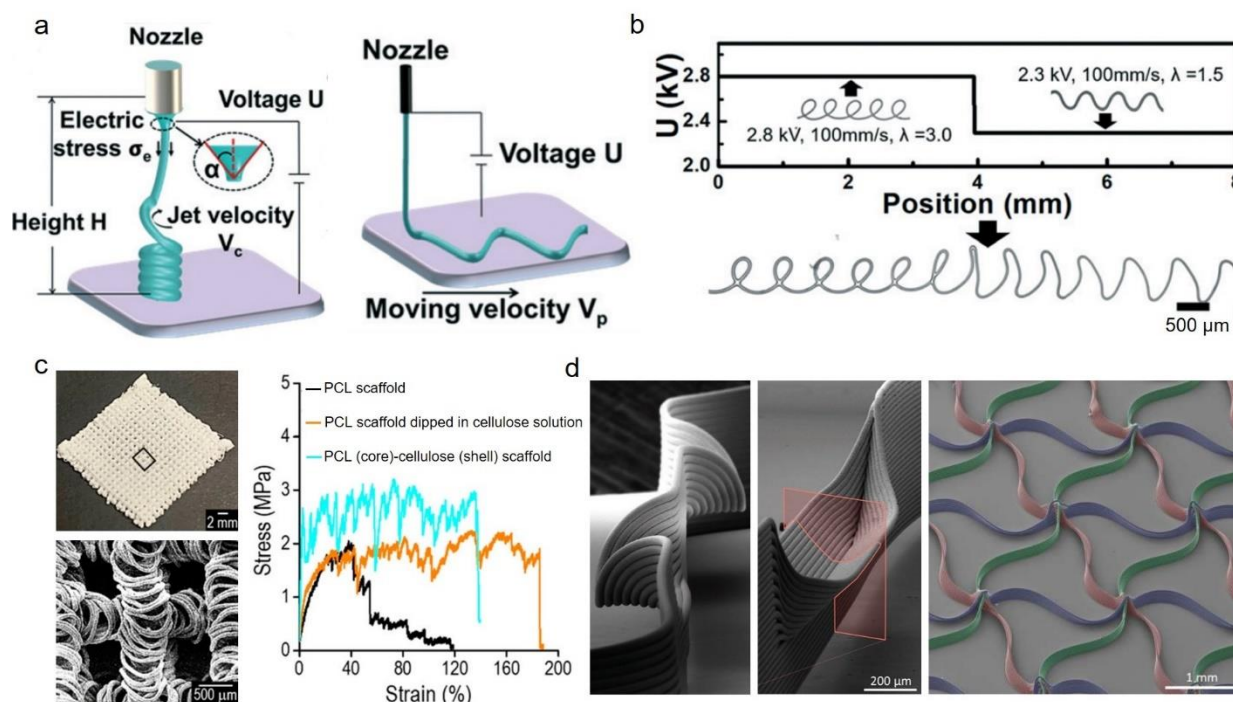


Figure 2.25 a) Schematic of electro-coiling [84]. b) Rapid switch between coiling pattern and meandering pattern through voltage control [84]. c) Optical and SEM images of 4-layer core/shell

scaffold with coiling loops, and tensile curves of three 4-layer scaffolds (all with coiling loops): polycaprolactone (PCL) scaffold, PCL scaffold dipped in cellulose solution, core/shell scaffold with PCL as the core and cellulose as the shell. [77] d) Melt electrowriting of overhang, branching and scaffold structures based on layer shifting [85].

Fig. 2.20 and 2.21 indicate that the nature of the pattern formation in FMSM lies in the instability-induced mismatch between the nozzle projection and the contact point. Hence, various complex structures can be achieved by a simple nozzle movement. Whereas most of the above-mentioned instability-assisted deposition processes focused on a speed ratio (of extruding speed to platform moving speed) above one in order to produce meandering or looped structures. Yuk *et al.* [79] and Liashenko *et al.* [85] investigated the case when the speed ratio is smaller than one. Yuk *et al.* [79] found that the thread is stretched and thinned before becoming discontinuous, leading to a possibility of achieving a smaller printing resolution than the diameter of the nozzle. Liashenko *et al.* [85] found that the mismatch between the nozzle projection and the contact point leads to a layer-shifting behavior during multilayer printing. They took the advantage of this layer-shifting behavior and built overhang, branching and scaffold structures (Fig. 2.25d) with relatively simple printing paths, unlocking new possibilities for the fabrication of complex fiber networks.

CHAPTER 3 RESEARCH OBJECTIVES AND COHERENCE OF ARTICLES

3.1 Problem identification

Instability-assisted fused filament fabrication (IFFF) shows a great potential in introducing microstructured sacrificial bonds and hidden lengths into a wide range of engineering materials to achieve high toughness and multifunctionalities. However, the following issues concerning this approach need to be solved:

- Premature failures of the fiber backbone often happen to IFFF-printed PLA fibers with sacrificial bonds and hidden lengths, significantly hindering the toughness enhancement.
- Previous studies focused on toughening one-dimensional fibers by IFFF, while most engineering applications demand two-dimensional or three-dimensional tough material systems with multifunctionalities like lightweight and transparency to handle various mechanical loads such as static puncture and impact loads.
- It has been found that the sequential breaking of sacrificial bonds and unfolding of hidden lengths increase the energy absorption of the IFFF-printed microstructured fibers under tensile loads. However, the microstructured fibers' behavior in a composite material system remains unknown.

3.2 Research objectives

The main objective of this research is to develop high-energy absorbing composites with microstructured sacrificial bonds and hidden lengths based on IFFF. The specific objectives are presented as the following:

- I. **Deepen the understanding of premature failures of IFFF-printed PLA fibers with microstructured sacrificial bonds and hidden lengths:** characterize the failure mechanisms of microstructured PLA fibers; analyze the local strain and stress along the fiber during the bond breaking and loop unfolding process; find the root causes of premature failures based on the local strain and stress analysis; investigate the influence of material

and structural properties on the failure behavior of microstructured PLA fibers; demonstrate an effective strategy to avoid the premature failures.

- II. **Develop a transparent impact-absorbing composite based on IFFF-printed fibers with microstructured sacrificial bonds and hidden lengths:** print a fiber fabric with functional microstructured sacrificial bonds and hidden lengths; improve the optical transparency and reduce the haze of the composite; demonstrate the energy-absorption enhancement of the composite under static puncture and impact loads.
- III. **Investigate the toughening mechanisms of IFFF-printed fibers with microstructured sacrificial bonds and hidden lengths in a composite material system:** characterize the failure mechanisms of the composite with microstructured fibers; investigate the microstructured fibers' influence on the fracture toughness and crack growth resistance of the composite; compare the energy absorbing behavior of the composite with microstructured fibers to the composite with non-structured fibers.

3.3 Coherence of articles

The main results of this research are presented in the form of accepted or submitted peer-reviewed journal articles in Chapter 4, 5, and 6, which complete the above-mentioned research objectives I, II, and III, respectively.

Chapter 4 presents the article, “*Failure mechanisms of coiling fibers with sacrificial bonds made by instability-assisted fused deposition modeling*”, published in Soft Matter as an inner front cover publication (DOI: 10.1039/C8SM01589A). In this work, five failure modes were defined for IFFF-printed coiling PLA fibers by mechanical tests, optical and SEM characterization. A nonlinear finite element analysis was performed to simulate the breaking of sacrificial bonds and unfolding of hidden lengths along the fiber under a tensile load. Local strain and stress data were calculated from the simulation results to help define the root causes of different failure modes of the fiber. The structural and material effects on the mechanical behavior of the coiling fiber were studied experimentally and numerically. Both experimental and numerical results show that large-scale plastic deformation of the material is indispensable for the breaking of more sacrificial bonds and the full release of hidden lengths.

Chapter 5 presents the article, “*Spiderweb-Inspired, Transparent, Impact-Absorbing Composite*”, published in Cell Reports Physical Science as a front cover publication (DOI: 10.1016/j.xcrp.2020.100240). In this work, polycarbonate filament was chosen to fabricate microstructured fibers with sacrificial bonds in order to avoid premature failures of the fiber backbone, due to polycarbonate’s excellent strain hardening behavior. A bidirectional fiber fabric was printed by IFFF. A facile fabrication process was developed for the transparent elastomeric composite. The influence of the refractive index difference between the fiber and matrix on the optical properties of the composite was investigated experimentally. Low-velocity impact tests were performed on a falling-dart impact tester to investigate the energy absorption performance of the resulting transparent composites.

Chapter 6 presents the article, “Toughening elastomers via microstructured thermoplastic fibers with sacrificial bonds and hidden lengths”, submitted to Extreme Mechanics Letters. In this work, the failure mechanisms of the elastomeric composite with microstructured polycarbonate fibers were characterized by tensile and static puncture tests. Fracture tests of the composite in the pure-shear configuration were performed to investigate the enhancement of fracture toughness and crack growth resistance of the composite. The interactions between crack propagation, bond breaking and loop unfolding were studied to deepen the understanding of the toughening mechanisms. The energy absorption and damage tolerance of composites with different fiber reinforcements were compared in tensile and static puncture tests.

CHAPTER 4 ARTICLE 1: FAILURE MECHANISMS OF COILING FIBERS WITH SACRIFICIAL BONDS MADE BY INSTABILITY- ASSISTED FUSED DEPOSITION MODELING

Shibo Zou¹, Daniel Therriault¹, Frédérick P. Gosselin^{1*}

¹Laboratory for Multiscale Mechanics (LM²), Department of Mechanical Engineering, École Polytechnique de Montréal, Montréal, Canada

Published in Soft Matter on November 2nd, 2018

Abstract

Instability-assisted 3D printing is a method for producing microstructured fibers with sacrificial bonds and hidden lengths which mimic nature's toughening mechanisms found in spider silk. This hierarchical structure increases the effective toughness of poly(lactic acid) (PLA) fibers by 240% – 340% in some specimens. Nevertheless, many specimens show worse toughness as low as 25% of that of the benchmark straight fiber due to the incomplete release of hidden lengths caused by premature failures. Here, we report mechanical tests and simulations of microstructured fibers with coiling loops that identify the material plastic deformation as being crucial to fully release the hidden lengths. Without sufficient material yielding, high local tensile stress results from the bending-torsion-tension coupled deformation of the coiling loop and induces crack initiation at the fiber backbone during the loop unfolding process. On the other hand, the influence of bond-breaking defect is found to be negligible here. Moreover, for a number of broken bonds beyond a critical value, the accumulated elastic energy along the released loops induces a high strain rate (~ 1500 mm/mm/s) in quasi-static tensile test, which fractures the fiber backbone within 0.1 ms after the breaking of a new bond. We also show a size effect in fused deposition modeling (FDM) extruded PLA fibers, which results in higher effective toughness (~ 5 times the performance of the straight fiber benchmark) in small coiling fibers (dia. = 0.37 mm), due to the better ductility in bending and torsion than large fibers (dia. = 1.20 mm). The failure mechanisms of single microstructured fiber presented here lay the groundwork for further optimizations of fiber arrays in the next generation of high energy-absorption composites for impact protection and safety-critical applications.

4.1 Introduction

Spider silk outperforms most synthetic materials in terms of specific toughness.¹ This toughness has been attributed to the unique protein structure in spider silk: stiff nanocrystals embedded in a less orderly semi-amorphous matrix which is rich in hydrogen bonding.² Upon stretching, these weak hydrogen bonds act as sacrificial bonds³ whose early breakage releases the entangled protein chains in the semi-amorphous domain. The breaking of hydrogen bonds and the unravelling of hidden protein chains contribute to the high extensibility and toughness of spider silk. Similar toughening mechanisms are also found in bone⁴, nacre⁵ and mussel byssus threads.⁶

Recently, the concept of sacrificial bonds and hidden length for toughness enhancement has inspired several experimental⁷⁻¹⁰ and numerical¹¹ studies of structured fibers at the microscale. This hierarchical structure consisting of sacrificial bonds and hidden length is successfully implemented by introducing slip knots⁷⁻⁹ or weak self-adhesions^{10,11} into natural or synthetic fibers. However, premature failures which cause incomplete release of fiber hidden length are also found in these studies, resulting in an occasional overall toughness decrease. Pugno *et al.*⁸ found that a too tight overhand loop knot in silk fiber can lead to early fiber failure at the knot entrance, leaving the hidden length unreleased. They further optimized the knot configuration and achieved the full release of the fiber hidden length, resulting in 300% – 400% toughness enhancement in silk fibers⁸ and up to 3000% in carbon nanotube microfibers⁹ with one single noose knot. Passieux *et al.*¹⁰ introduced weakly fused bonds as sacrificial bonds into poly(lactic acid) (PLA) fibers with coiling or alternating loops by instability-assisted 3D printing. They found that the fiber backbone sometimes fails early before all hidden lengths are released. These premature failures result in the large scatter in the toughness values of microstructured fibers. The toughness of the microstructured fiber is sometimes as low as 25% of that of the straight fiber. They attributed these premature failures to the cusp formed during the loop unfolding process and the surface defect left by bond breaking. Koebley *et al.*¹¹ found similar hierarchical structure with coiling loops in *loxosceles* silk. They supposed that the cusp and bond-breaking defect can be avoided by the slender ribbon structure and silk-to-silk adhesion in *loxosceles* silk, instead of the cylindrical fiber structure and physically fused bond in Passieux *et al.*'s work. However, premature failures are still found in *loxosceles* silk to inhibit the hidden length from being fully released, resulting in the structured fibers' overall toughness being only 27% – 64% of the straight fibers. Koebley *et al.*¹¹

attributes these premature failures to material imperfections and incorrect test conditions. Nevertheless, the mechanics behind these premature failures in microstructured fibers with sacrificial bonds is still unclear.

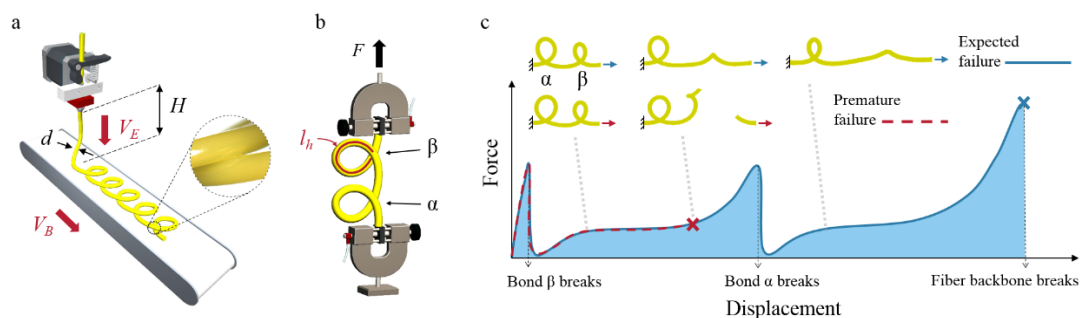


Figure 4.1 a) Schematic of the IFDM. The ratio of the filament extruding speed V_E to the belt moving speed V_B dictates the fiber pattern on the belt. The ratio of the deposition height H to the fiber diameter d dictates the size of the loop. Sacrificial bonds are formed via fusion at the intersections in the coiling pattern after the polymer is solidified by cooling. b) The produced coiling fiber has a constant hidden length l_h which can be released by the breaking of sacrificial bonds (α , β) in uniaxial tensile test. c) Schematic comparison of the tensile test sequences and force-displacement curves between expected failure (blue solid line) and premature failure (red dashed line). In expected failure, sacrificial bonds α and β break one by one, resulting in a saw-tooth tensile curve. The ultimate axial tensioning after all hidden lengths are released breaks the fiber backbone, leading to high energy absorption indicated by the blue area under the tensile curve. In premature failure, the fiber backbone is broken during the unfolding process of loop β , before bond α breaks. The truncated tensile curve displays reduced fiber strength and energy absorption.

In this article, we use the instability-assisted fused deposition modeling (IFDM) technique developed by Passieux *et al.*¹⁰ to fabricate microstructured fibers with sacrificial bonds. As shown in Fig. 4.1a, the molten PLA filament is deposited in ambient condition onto a moving belt. The filament swings and coils on itself due to a similar instability as found in the “elastic¹² / fluid mechanical¹³ / molten glass¹⁴ sewing machine”. After the polymer is solidified in ambient air, weakly fused bonds are formed at the intersections along the fiber (Fig. 4.1a). As described by Passieux *et al.*¹⁰, these bonds, *i.e.*, bonds α and β in Fig. 4.1b, act as sacrificial bonds in uniaxial tensile test. They are supposed to break one by one, leading to a saw-tooth tensile curve as shown

in Fig. 4.1c. The area under the tensile curve represents the energy absorption contributed by the breaking of bonds and the unfolding of corresponding loops. The premature failure, in which the fiber backbone fractures before bond α breaks, reduces fiber strength and toughness. Passieux *et al.*¹⁰ found that the failure modes are different with respect to fracture time and location due to the interrelation between the varying slenderness with fiber patterns and the number and strength of sacrificial bonds. Among their specimens, those with a coiling pattern exhibit varieties of failure modes and the lowest toughness value. Therefore, we purposely select these underperforming coiling pattern fibers to understand their failure. We do so by fixing the ratio of the filament extruding speed V_E to the belt moving speed V_B (Fig. 4.1a). The relative strength of the bonds to the fiber backbone is kept constant in two coiling fibers at different scales (large fiber: $d = 1.20$ mm; small fiber: $d = 0.37$ mm) by fixing the ratio of the deposition height H to the fiber diameter d (Fig. 4.1a). We systematically categorized the failure modes of coiling fibers by testing specimens with varying number of sacrificial bonds. Complementing this experimental study, we performed nonlinear finite element analysis (FEA) in order to find the root cause for each failure mode.

4.2 Results and discussion

According to the differences in fracture time and location among coiling fiber specimens in uniaxial tensile test, we categorize five failure modes: axial, bending, torsional, bond and dynamic failure. In axial failure, the coiling loop is unfolded and fully straightened until the fiber breaks in the middle of the loop (Fig. 4.2a [i]). Apparent necking is observed at both fracture ends (Fig. 4.2a [ii]). The fracture surface shows extended polymer tongues which indicates a large amount of plastic deformation (Fig. 4.2a [iii]). In bending failure, the fiber also breaks in the middle of the loop (Fig. 4.2b [i]). Compared to axial failure, the crack in bending failure initiates much earlier from the cusp at the top of the loop. Typical butterfly pattern can be seen on the fracture surface with stress whitening at the two sides (Fig. 4.2b [ii]). Similar extended polymer tongues as in the axial failure are also found at the bottom half of the fracture surface (Fig. 4.2b [iii]).

In torsional and bond failure, the fiber does not break in the middle of the loop but near it (Fig. 4.2c [i] and d [i]). In torsional failure, the fracture shows a spiral pattern (Fig. 4.2c [ii]) which indicates that the fiber breaks due to the maximum tensile stress under torsion. Smooth crack initiation region

with crazing and rough crack propagation region with hackles can be seen on the fracture surface (Fig. 4.2c [iii]), which indicate the brittle nature of the fracture.¹⁵ In bond failure, a similar spiral fracture pattern is observed (Fig. 4.2d [ii]). The fracture plane is found right across the surface defect left by the bond breaking, which would suggest that the defect might have played a bigger role in this fracture. However, the scanning electron microscopy (SEM) image shows that the crack initiates not from the defect, but from a pigment aggregate inside the fiber (Fig. 4.2d [iii]). This indicates that in this case, the fracture is more likely caused by a combination of the flaw and the maximum tensile stress, but not the bond-breaking defect.

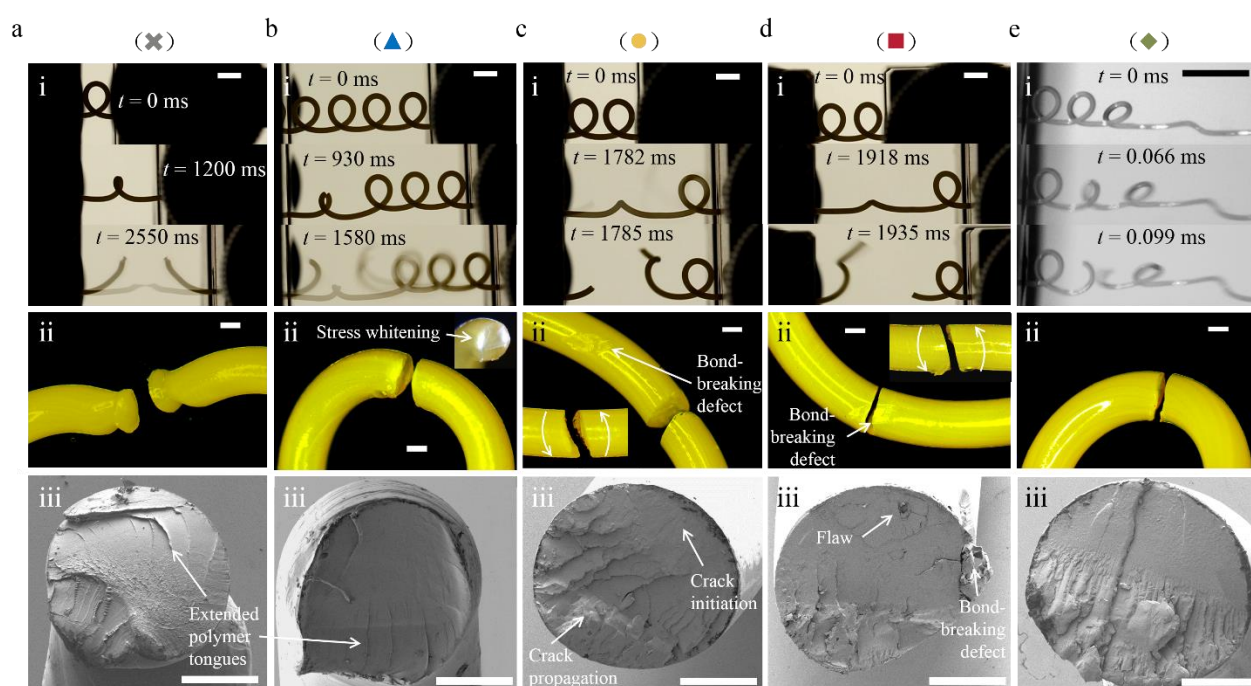


Figure 4.2 Failure modes observed from uniaxial tensile tests of coiling fibers: axial (\times), bending (\blacktriangle), torsional (\bullet), bond (\blacksquare) and dynamic (\blacklozenge) failure. Each failure mode is characterized by: (i) sequential camera captures of the unfolding process after the breaking of sacrificial bond. Time zero is defined at the breaking of sacrificial bond; (ii) microscopy images of the fracture pieces; (iii) SEM images of the fracture surfaces. All specimens shown here are from the large fiber with a diameter of 1.20 mm, except the camera captures of dynamic failure, which are from the small fiber with a diameter of 0.37 mm for the sake of convenience in shooting with high speed camera. Scale bars are 5 mm in (i), and 0.5 mm in (ii), (iii).

The dynamic failure is different from all the above failure modes in terms of the fracture timescale after the breaking of sacrificial bond. In the above failure cases, the fracture of the fiber backbone happens at least 930 ms after the breaking of a sacrificial bond during the unfolding process. While in dynamic failure, the fiber backbone breaks within only 0.099 ms after the breaking of a sacrificial bond (Fig. 4.2e [i]). The fiber breaks at a similar location as in bending failure, but has a more brittle appearance. No material distortion is observed near the fracture surface and the two fracture pieces fit with each other perfectly (Fig. 4.2e [ii]). On the fracture surface, the smooth crack initiation region suddenly translates to the rough crack propagation region (Fig. 4.2e [iii]), which indicates a sharp increase of stress and crack propagation speed.¹⁶

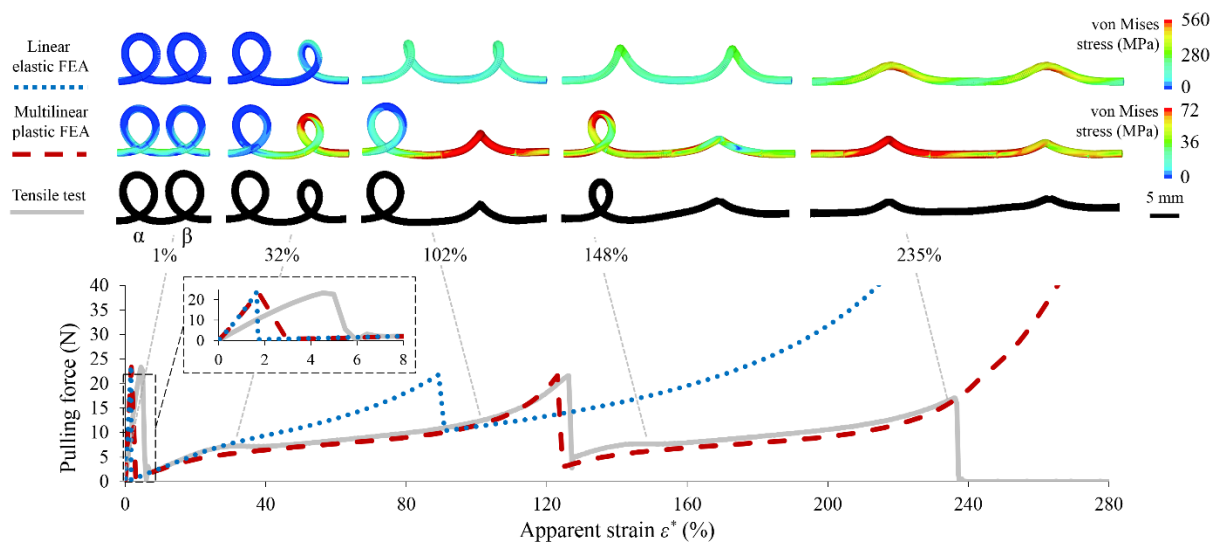


Figure 4.3 The breaking of sacrificial bonds in two coiling loops under uniaxial tension from linear elastic FEA (blue dotted line), multilinear plastic FEA (red dashed line) and tensile test (grey solid line). The breaking sequence of sacrificial bonds in the FEAs is set the same as that in the tensile test: first bond β , then bond α . The force threshold for each sacrificial bond in the FEAs is also set the same as that in the tensile test: 23.4 N for bond β and 21.6 N for bond α . The unfolding shapes are obtained at five given apparent strain values. The color gradient represents the magnitude of von Mises stress in the FEA contour plots. The FEAs and test results here are all for the large fiber with a diameter of 1.20 mm.

In order to understand the failure mechanisms of the coiling fiber, we performed quasi-static FEA of two coiling loops under uniaxial tension. First, to explore the effect of material characteristics

on structure behavior, we compared the bond breaking process of the coiling fiber with two different material models: linear elasticity and multilinear plasticity (Fig. 4.3). In order to compensate the difference in gauge length between tensile test and simulation, we define an apparent strain as $\varepsilon^* = \Delta l / l_0 \times 100\%$, where Δl is the axial displacement and l_0 is the initial length of the coiling fiber between the grips. Before the first bond (bond β in Fig. 4.3) breaks, the coiling fiber is stiff as the hidden lengths is bypassed by the load path. Both the elastic and plastic FEA overestimate the stiffness of the overall structure (Fig. 4.3 inset). This is probably due to the fiber slippage in the grips during the tensile test, or the imperfect modeling of sacrificial bond via rigid surface constraint in the simulation. After bond β breaks, the pulling force drops due to the release of hidden length (loop β). Then the force increases as loop β is unfolded and straightened. The elastic FEA overestimates the pulling force and thus predicts the breaking of the next bond (bond α) significantly earlier than the plastic FEA. After bond α breaks, the two loops in the elastic FEA share the same amount of deformation (Fig. 4.3, contour plot at $\varepsilon^* = 102\%$ in the elastic FEA) due to the recovery of elastic strain along loop β . Under further stretching, the two loops behave similarly to a coiled elastic spring^{17, 18} due to the absence of plastic deformation in the elastic FEA. However, in the tensile test, loop α and β display unequal amount of deformation after the breaking of bond α (Fig. 4.3, at $\varepsilon^* = 148\%$). This indicates a large amount of plastic deformation along loop β , which cannot be recovered after the breaking of sacrificial bond α . The plastic FEA's prediction of the deformation of the two loops after the breaking of bond α is much closer to the experimental result. The two loops behave very differently from the coiled elastic spring^{17, 18} due to the plastic strain accumulated along the loops each time after the bond breaks. Even though some loops, like the loop β in Fig. 4.3, experience cyclic loading, fatigue¹⁹ is not considered here, because the fiber breaks within the last unfolded loop in 157 out of 160 failure cases observed in this work.

The plastic FEA is in quantitative and qualitative agreement with the tensile test in respect of the bond breaking, the reaction force and unfolding geometry of the coiling loop (Fig. 4.3). We hence calculate local curvature, as well as shear and axial strains (calculation details are illustrated in Fig. 4.7) along the fiber to further analyze the variation of fracture time and location in test specimens. In order to simplify the analysis, we define an unfolding percentage of the hidden length in each coiling loop as $p = 100 \times s / l_h$, where s is the axial displacement after the breaking of corresponding sacrificial bond and l_h is the hidden length. The hidden length of each coiling loop is considered

constant in all test specimens. In Fig. 4.4a, the fibers' fracture force and unfolding percentage at break for all failure modes are superimposed on a schematic representation of the force-displacement curve of one coiling loop from axial failure specimen. In Fig. 4.4b - d, the fracture location along the coiling loop and unfolding percentage at break are plotted for each failure mode against local curvature, shear and axial strains along the second releasing loop α in Fig. 4.3. This superimposition of statistical test data of failure modes on simulation results enables us to analyze the influence of different deformation components on each failure mode. Since the large fiber provides more comprehensive experimental data on each failure mode than the small fiber, only simulation and test results of the large fiber are presented in Fig. 4.4. Due to the geometric similarity, the small fiber is expected to have the same local strain as the large fiber at equivalent location along the fiber in the static simulation.

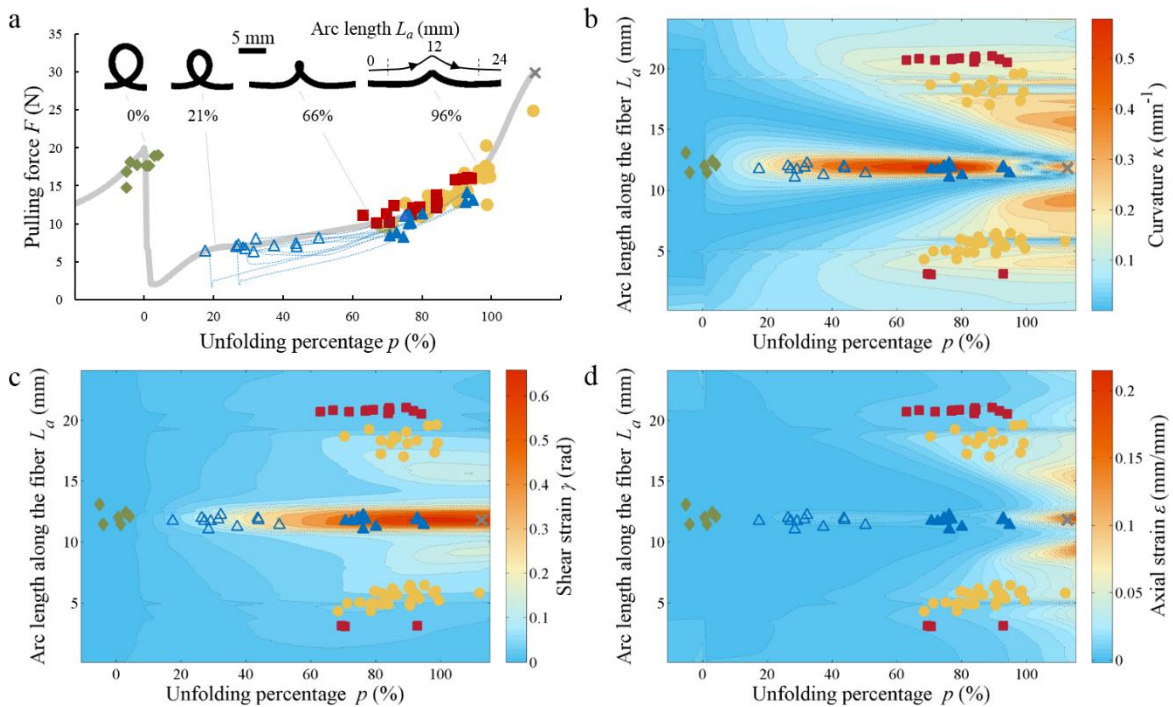


Figure 4.4 a) Distribution of the five failure modes in coiling fibers illustrated by failure points overlaid on a representative force-displacement curve of a single coiling loop. Failure points are defined as the final break of fiber backbone from the following failure modes: axial (*), bending (\blacktriangle), torsional (\bullet), bond (\blacksquare) and dynamic (\blacklozenge) failure. For bending failure, crack initiation (\triangle) and the

following force curves (blue dashed lines) are also marked. Local b) curvature, c) shear strain, d) axial strain calculated from the multilinear plastic FEA are used to explain the fracture location of each failure mode along the fiber during the unfolding process. Arc length L_a is calculated based on the loop α in the simulation, starting from the fixed end. The bond-breaking defects locates at $L_a = 3.12$ and 20.31 mm. All failure points here are for the large fiber with a diameter of 1.20 mm.

After the breaking of a sacrificial bond, the pulling force rises rapidly mainly due to the increase of curvature in the middle of the loop. As the unfolding process proceeds, although the curvature continues to increase (Fig. 4.4b), the pulling force reaches a short plateau after p exceeds 20% (Fig. 4.4a). From the FEA contour plots with equivalent unfolding percentage (at $\varepsilon^* = 148\%$) in Fig. 4.3, it can be seen that the middle of the loop has reached the tensile strength of the material (70.5 MPa, Fig. 4.8). Material yielding in the middle of the loop slows down the rate of increase of the pulling force. At this stage, the bending-dominated deformation of the coiling loop leads to high tensile stresses. This induces crack initiation at the top of the middle loop (Fig. 4.2b, at $t = 930$ ms), giving rise to a sudden drop on the pulling force curve (Fig. 4.4a, Δ and blue dashed lines). As the crack propagates, the remaining material in the middle of the loop continues to carry the load. Further stretching straightens the two broken loop pieces, causing the force to increase even after the crack initiation. In the end, the final fracture of the fiber in bending failure (Fig. 4.4a, \blacktriangle) happens at $p = 70\% - 95\%$ with a relatively lower fracture force compared to the representative pulling force curve.

After p exceeds 50%, shear strain increases rapidly in the middle of the loop (Fig. 4.4c). However, the fiber in torsional failure (Fig. 4.4c, \bullet) never breaks in the middle of the loop. Large material distortion is observed in the middle of the loop in SEM images of the torsional failure specimen (Fig. 4.5a). This indicates a large amount of plastic deformation which may prevent the crack initiation as in bending failure. The fiber in torsional failure can break at either side of the loop around 5 to 8 mm away from the middle (Fig. 4.4c, \bullet , $L_a = 4$ to 7 mm and 17 to 20 mm). The fiber in bond failure breaks at similar unfolding percentages (Fig. 4.4c, \blacksquare , $p = 60\% - 100\%$), with the fracture location restricted around the bond-breaking defect.

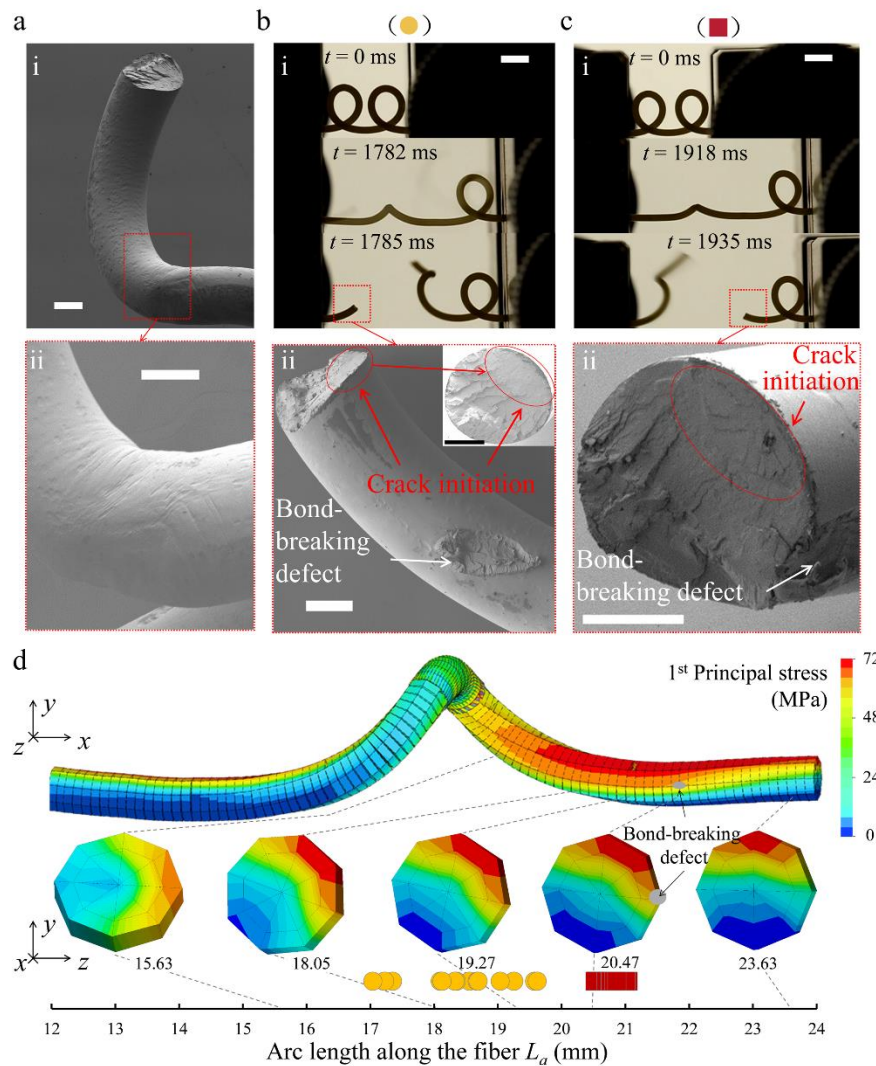


Figure 4.5 Illustration of the crack initiation in torsional and bond failure due to high local tensile stress: a) SEM images of torsional failure specimen showing large material distortion in the middle of the loop. Fractures of b) torsional failure and c) bond failure specimen are characterized by sequential camera captures and SEM images. The relative location of crack initiation region with reference to the bond-breaking defect in both failure modes can be seen in the SEM images. d) Contour plot of one coiling loop at $p = 80\%$ from the plastic FEA. The color gradient represents the magnitude of the first principal stress. Cross-sectional contour plots of the fiber are shown at $L_a = 15.63, 18.05, 19.27, 20.47$ and 23.63 mm along the loop. The inner side of the beam element at $L_a = 20.47$ mm corresponds to the bond-breaking defect. The fracture location along the fiber (at $L_a = 12$ mm to 24 mm) are shown by ● for torsional failure and ■ for bond failure. Both torsional

and bond failures can be attributed to a large region of tensile stress. Scale bars are 5 mm in camera captures and 0.5 mm in SEM images.

In order to understand the fracture in torsional and bond failure (Fig. 4.5b, c), the distribution of the first principal stress across the fiber section is given at selected locations along the fiber at $p = 80\%$ in Fig. 4.5d. As L_a increases from 15.63 mm to 23.63 mm, the first principal stress reaches the maximum 70.5 MPa near the top surface of the fiber. It can be seen that this maximum stress region across the fiber section is relatively larger at $L_a = 17$ to 21 mm than other places along the fiber. This corresponds well with the distribution of the fracture locations along the fiber in torsional failure (Fig. 4.5d, ●) and bond failure (Fig. 4.5d, ■). Also, the location of the maximum stress region within the fiber cross section (Fig. 4.5d, at $L_a = 18.05, 19.27$ and 20.47 mm) perfectly matches with the crack initiation region in SEM images of the torsional failure (Fig. 4.5b [ii]) and bond failure specimen (Fig. 4.5c [ii]). This indicates that the fiber fails due to the maximum tensile stress in torsional and bond failure. This also reinforces our previous speculation about the insignificance of bond-breaking defect in bond failure based on fractographic analysis. Therefore, if the fiber avoids the bending crack by sufficient material yielding in the middle of the loop, further stretching results in two growing maximum tensile stress regions along the fiber at $L_a = 3$ to 7 mm and 17 to 21 mm. These tensile stress regions are generated by the combination of bending, torsion and axial tension. The crack in torsional and bond failure initiates from the largest maximum stress region, then propagates through a spiral pattern due to the torsional strain along the fiber. This explains the spiral fracture morphology in torsional and bond failure. Since the size of the maximum stress region is similar from $L_a = 3$ to 7 mm and 17 to 21 mm along the fiber, the crack always initiates at the weakest point. This is sometimes contributed by a flaw, such as a color pigment shown in Fig. 4.5c [ii]. This maximum stress region leads to the large variation of fracture location in torsional and bond failure. The hidden length is fully released when p reaches 100%. The pulling force increases rapidly due to the tensioning of the fiber backbone. The final axial failure (Fig. 4.4d, *) happens in the middle of the loop, where the maximum axial strain locates.

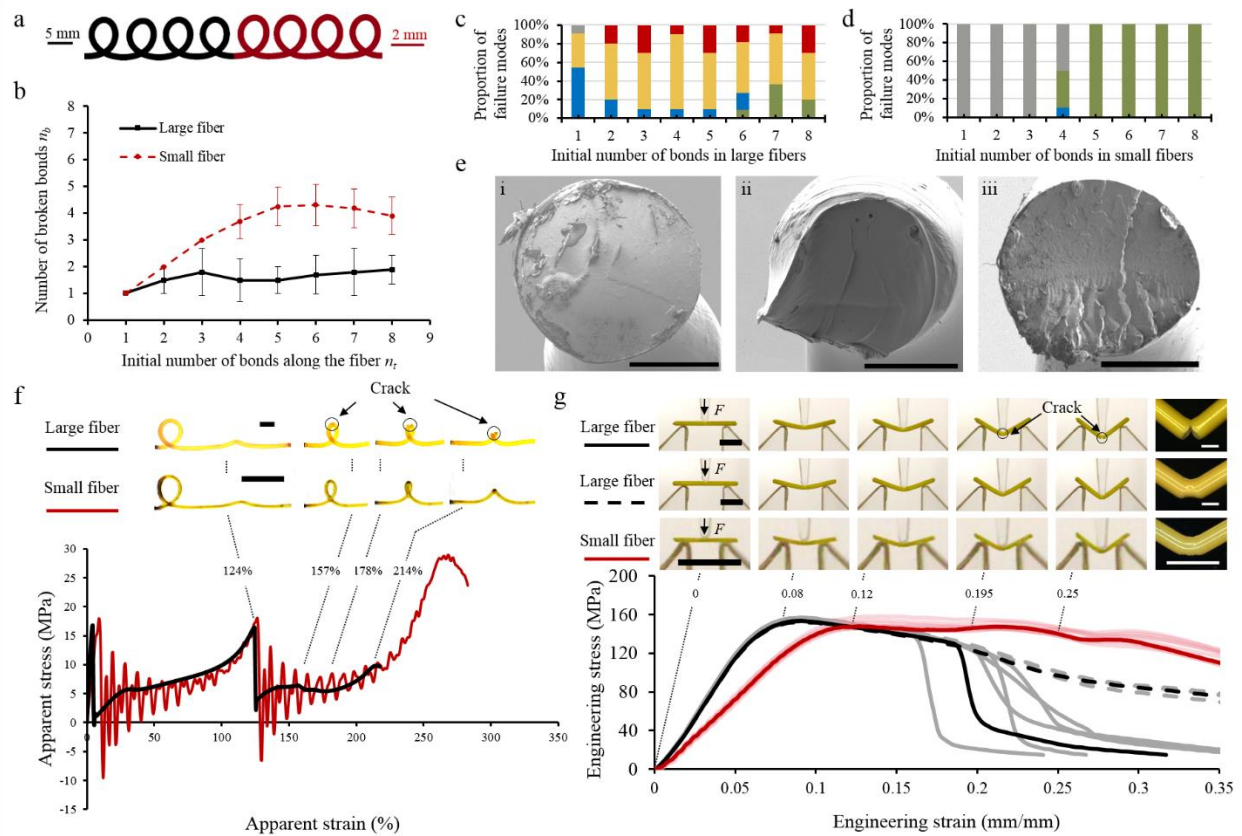


Figure 4.6 Comparison of the failure behavior in a) two geometrically similar coiling fibers with different diameters: 1.20 mm (in black) and 0.37 mm (in red). b) The number of actually broken bonds n_b in both large and small fibers varying with different initial number of bonds n_t in the uniaxial tensile tests. The error bar stands for the standard deviation based on a sample size of 10 for each data point. The proportion of axial (grey), bending (blue), torsional (yellow), bond (red) and dynamic (green) failures in c) large and d) small fibers varying with different n_t . e) SEM images of the fracture surfaces in axial (i), bending (ii) and dynamic (iii) failures of the small fibers. Scale bars are 0.2 mm. f) Comparison of the unfolding geometries and apparent stress-strain curves of the large (black lines) and small (red lines) fibers with two coiling loops. The oscillations on the red curves are due to the vibration of the 5 N load cell induced by the bond breakage. Scale bars are 5 mm. g) Comparison of the engineering stress-strain curves, test sequences and post-test microscopy images of the large (black lines) and small (red lines) straight fibers in the three-point bending test. At the bottom of the fiber where the bending stress is maximum in tension, the large fiber specimens either show sharp crack or large plastic deformation (corresponding to the black

solid and dashed lines respectively on the stress-strain diagram), while all the small fiber specimens show large plastic deformation. All stress-strain curves from ten specimens for each fiber are shown in the plot. Besides the three representative curves, other curves are shown in gray or pink for the large and small fibers respectively to show the measurement deviations. Scale bars are 5 mm in camera captures, and 1 mm in microscopy images.

The probabilities of different failure modes are also found to be related to the size of the fiber (Fig. 4.6a, b) and the number of sacrificial bonds n_t in test fibers (Fig. 4.6b - d). In large fibers, axial failure happens only when there is one bond in the test fiber (Fig. 4.6c). As n_t increases, the proportion of bending failure decreases, probably due to the less strict lateral constraints associated with the existence of more loops. The average number of actually broken bonds n_b stays around two (Fig. 4.6b, black solid line). However, different results are observed in a geometrically similar coiling fiber with a smaller diameter (0.37 mm, Fig. 4.6a in red). All test bonds can be broken when $n_t \leq 3$ (Fig. 4.6b, red dashed line). The fracture surface of axial failure (Fig. 4.6e [i]) shows very similar necking characteristics to those of the large fiber (Fig. 4.2a [iii]). Bending, torsional and bond failures are almost absent in the small fiber, except for one bending failure case at $n_t = 4$ (Fig. 4.6d), which is probably caused by the pigment aggregate in the crack initiation region on the fracture surface (Fig. 4.6e [ii]). In order to investigate the difference of the failure behavior between the large and small fibers, bending failure at $n_t = 2$ in the large fiber is chosen to compare with the small fiber in Fig. 4.6f. The two fibers show very similar apparent stress-strain curves and bond strengths, which is attributed to the same V_E / V_B and H / d ratios kept in their fabrication. Due to the geometric similarity, we have $\kappa_L / \kappa_S = d_S / d_L$, where κ is the fiber curvature; d is the fiber diameter; the indices L and S stand for the large and small fiber, respectively. Therefore, the maximum bending stress at the top of the loop $\sigma = E\kappa d / 2$ is the same for the large and small fibers, assuming a constant Young's modulus E in both fibers. However, the crack initiates in the large fiber, but not in the small fiber (Fig. 4.6f). This indicates a size effect concerning the fiber's ductility, despite the fact that in uniaxial tensile tests, large and small straight fibers exhibit identical behavior (Fig. 4.9).

In order to further understand this size effect, we performed three-point bending tests on the large and small straight fibers under the strain rate (0.33 mm/mm/s, Fig. 4.10a) which corresponds to what the middle of the loop experiences during the unfolding process. Whereas the large and small

straight fibers behave identically in tensile test (Fig. 4.9), they differ in ductility in three-point bending test (Fig. 4.6g). Six out of ten large fiber specimens show bending cracks at the bottom of the fiber around the engineering strain of 0.2, while all ten small fiber specimens survive until the engineering strain of 0.35 without any visible cracks. The small difference in crystallinity (large fiber: 2.5%; small fiber: 1.1%. Fig. 4.11) might account for this size effect. Compared with the large fiber, the relatively faster cooling rate in the small fiber after extrusion leads to two times lower crystallinity and thus more amorphous structure with higher ductility. Another possible explanation for this size effect is the strain gradient plasticity theory.²⁰ In tension, the fiber has a uniform strain distribution within the cross sectional area, while in bending and torsion, the strain is maximum at the surface but zero along the neutral axis, resulting in a strain gradient. The strain gradient enhances material hardening, which has been also observed in polymers such as epoxy and polycarbonate.²¹ Hence, the greater strain gradient makes the small fiber more ductile than the large fiber in the three-point bending test. We are led to believe that the higher ductility prevents bending, torsional and bond failures in the small fiber, resulting in more broken bonds than that in the large fiber.

After $n_t \geq 5$, the small fibers always fail in dynamic failure with n_b around 4 (Fig. 4.6b, d). This indicates that dynamic failure is somehow related to the number of already broken bonds in the test fiber. Recollecting from Fig. 4.2e [i], in dynamic failure, the newly releasing loop is suddenly retracted due to the springback of previously unfolded loops after the breaking of a sacrificial bond. According to the simulation, this springback is also related to the material's characteristic, as the loop retraction after the breaking of a sacrificial bond in the elastic FEA is much larger than that in the plastic FEA. Therefore, we think that dynamic failure is triggered once the accumulated elastic energy along previously unfolded loops reaches a critical value. The inducing retraction causes a local strain rate as high as 1492 mm/mm/s (Fig. 4.10d) on the top surface in the middle of the newly releasing loop, which fractures the fiber backbone immediately. That is the reason why both the fracture surfaces of the small (Fig. 4.6e [iii]) and large (Fig. 4.2e [iii]) fibers in dynamic failure show a sharp transition from the smooth crack initiation region to the rough crack propagation region.

4.3 Conclusion

Simulation and experiment both indicate that material yielding is indispensable to fully release the hidden length of the coiling fiber. If material yielding is insufficient along the fiber throughout the loop unfolding process, the fiber backbone will fracture at or besides the middle of the loop due to high local tensile stress, resulting in bending, torsional or bond failures. After the breaking of a certain number of bonds, the accumulated elastic energy along the already unfolded loops will induce a high strain rate recoil that fractures the fiber backbone immediately in the middle of the loop. The influence of bond-breaking defect is found to be negligible in the coiling fibers tested here. A size effect concerning the ductility in bending and torsion is also found in FDM-extruded PLA filament, which has profound implications for FDM 3D printing. The maximum number of sacrificial bonds which can be all broken in tensile test is three in the small PLA coiling fibers tested here (Fig. 4.12), resulting in an effective toughness 468% – 533% times the performance of the straight fiber benchmark (Table 4.1). In order to further improve the toughness, material selection is as essential as the structure optimization, just as the damage tolerance property of spider web comes from the integration of structure and the nonlinear material behavior of spider silk²². FDM with continuous-fiber reinforced polymer^{23, 24} provides new opportunities to develop a good material candidate for microstructured fibers, utilizing ductile polymer matrix and strong continuous-fiber reinforcement. With the understanding of the failure mechanisms of a microstructured fiber in tension, we will be able to further optimize fiber arrays in composites or cellular structures²⁵ for high energy absorption and damage tolerance properties.

4.4 Methods

4.4.1 Instability-assisted fused deposition modeling

A PLA filament (MakerBot PLA Yellow) was extruded through the printing head of a MakerBot 3D printer onto a conveyor belt. The filament was fused at 230 °C in the heater block, then extruded out of the nozzle. Two nozzles with different diameters (0.3 mm and 1 mm) were used in this paper. An open source 3D printing software ReplicatorG was used to control the speed of the stepper motor. In order to achieve stable deposition, the stepper motor was set at 2 rpm (revolutions per minute) and 8 rpm for the small and large nozzle, respectively. This led to the volume flow rate

of 2.53 mm³/s and 10.5 mm³/s, respectively. Due to die swell, the extruded polymer threads had diameters of 0.37 mm and 1.20 mm, respectively. Geometrically similar coiling fibers were fabricated at $V_E / V_B = 3.71$ and $H / d = 11$. The straight fibers were fabricated at $V_E / V_B = 1$ and $H / d = 11$.

4.4.2 Uniaxial tensile test

Uniaxial tensile test of the coiling fiber was performed on an electromechanical machine (MTS Insight 50 kN) in ambient environment. The fiber was clamped with a constant force of 100N at both ends by a pair of pneumatic grips (TestResources G94) with an air pressure of 100 psi. The crosshead speed was 500 mm/min. Forces were measured with 5 N and 100 N load cell for the small and large fiber respectively. Coiling fibers with 1 to 8 loops were tested, with 10 repetitions each for both small and large fibers.

4.4.3 Three-point bending test

Custom-made acrylic fixtures were used for the three-point bending test of straight fiber on the MTS Insight machine. The diameters of the loading noses and supports are 0.8 mm and 2 mm for the small and large fiber respectively. The spans are 3 mm and 10 mm, respectively. The small and large straight fibers were cut into 5 mm and 16 mm long pieces. Reaction forces of the loading nose were measured with 5 N and 100 N load cell, respectively. The crosshead speed is 84.8 mm/min for the small fiber and 275 mm/min for the large fiber.

4.4.4 Finite element analysis

The geometrical data of the coiling fiber was generated in MATLAB via digital image analysis and then imported into ANSYS to create the mesh. Nonlinear FEA was adopted to simulate the bond breaking and loop unfolding process of the coiling fiber under tension, with both elastic and plastic material model. In the elastic FEA, the fiber is assumed isotropic with Young's modulus $E = 3$ GPa, and Poisson's ratio $\nu = 0.36$. In the plastic FEA, multilinear isotropic hardening plasticity and von Mises yield criterion were used to create the constitutive law, which was calibrated based on the uniaxial tensile test of straight PLA fiber (Fig. 4.8). The elastic FEA modeled the fiber with 3D beam element (BEAM189), while the plastic FEA utilized a beam-solid assembly (Fig. 4.7a). Solid

elements (SOLID186) were used in the middle of the coiling loop in order to avoid the convergence difficulty caused by beam elements under large inelastic deformation due to torsional loading.²⁶ The fiber segment modeled by solid elements shared the same diameter as the one modeled by beam elements. They were connected by rigid surface constraint.²⁷ In both elastic and plastic FEA, the sacrificial bond was modeled by a 3D beam-to-beam contact²⁷ with the multipoint constraint (MPC) approach which constrained three translational degrees of freedom of crossing beam elements. The simulation was conducted in a displacement-controlled manner. A force threshold criterion³ was used to break sacrificial bonds. The displacement was incrementally applied at the pulling end using a do-loop in ANSYS Parametric Design Language (APDL). The reaction force at the pulling end was examined in each step. Once the reaction force reached the threshold, the MPC contact elements were deactivated by the program, simulating the breaking of the sacrificial bond. After the death of the MPC contact elements, the incremental displacement continued to be applied on the model and the simulation restarted based on the solution from the previous run. The breaking sequence and force thresholds of sacrificial bonds were set exactly as in the test.

Acknowledgements

We are thankful for the technical help from research associate Isabelle Nowlan and technician Bénédict Besner. We acknowledge the support of the Fonds de Recherche du Québec: Nature et Technologies (FRQNT), [funding reference number 63014], the Natural Sciences and Engineering Research Council of Canada (NSERC), [funding reference number 175791953], and the Canadian Foundation for Innovation.

References

1. F. Vollrath and D. P. Knight, *Nature*, 2001, 410, 541.
2. A. Nova, S. Keten, N. M. Pugno, A. Redaelli and M. J. Buehler, *Nano Letters*, 2010, 10, 2626-2634.
3. G. E. Fantner, E. Oroudjev, G. Schitter, L. S. Golde, P. Thurner, M. M. Finch, P. Turner, T. Gutschmann, D. E. Morse, H. Hansma and P. K. Hansma, *Biophysical Journal*, 2006, 90, 1411-1418.

4. G. E. Fantner, T. Hassenkam, J. H. Kindt, J. C. Weaver, H. Birkedal, L. Pechenik, J. A. Cutroni, G. A. G. Cidade, G. D. Stucky, D. E. Morse and P. K. Hansma, *Nature Materials*, 2005, 4, 612.
5. B. L. Smith, T. E. Schaffer, M. Viani, J. B. Thompson, N. A. Frederick, J. Kindt, A. Belcher, G. D. Stucky, D. E. Morse and P. K. Hansma, *Nature*, 1999, 399, 761-763.
6. M. J. Harrington, H. S. Gupta, P. Fratzl and J. H. Waite, *Journal of Structural Biology*, 2009, 167, 47-54.
7. N. M. Pugno, *PLOS ONE*, 2014, 9, e93079.
8. M. F. Pantano, A. Berardo and N. M. Pugno, *Scientific Reports*, 2016, 6, 18222.
9. F. Bosia, E. Lepore, N. T. Alvarez, P. Miller, V. Shanov and N. M. Pugno, *Carbon*, 2016, 102, 116-125.
10. R. Passieux, L. Guthrie, S. H. Rad, M. Lévesque, D. Therriault and F. P. Gosselin, *Advanced Materials*, 2015, 27, 3676-3680.
11. S. R. Koebley, F. Vollrath and H. C. Schniepp, *Materials Horizons*, 2017, 4, 377-382.
12. M. K. Jawed, F. Da, J. Joo, E. Grinspun and P. M. Reis, *Proceedings of the National Academy of Sciences*, 2014, 111, 14663-14668.
13. S. Chiu-Webster and J. R. Lister, *Journal of Fluid Mechanics*, 2006, 569, 89-111.
14. P. T. Brun, C. Inamura, D. Lizardo, G. Franchin, M. Stern, P. Houk and N. Oxman, *Philosophical Transactions of the Royal Society A: Mathematical, Physical and Engineering Sciences*, 2017, 375.
15. M. D. Hayes, D. B. Edwards and A. R. Shah, in *Fractography in Failure Analysis of Polymers*, William Andrew Publishing, Oxford, 2015, DOI: <https://doi.org/10.1016/B978-0-323-24272-1.00004-0>, pp. 48-92.
16. D. Hull, in *Fractography: observing, measuring and interpreting fracture surface topography*, Cambridge University Press, United Kingdom, 1999, pp. 121-150.
17. X. Chen, S. Zhang, D. A. Dikin, W. Ding, R. S. Ruoff, L. Pan and Y. Nakayama, *Nano Letters*, 2003, 3, 1299-1304.

18. S. Nohut and G. A. Schneider, *Journal of the European Ceramic Society*, 2009, 29, 1013-1019.
19. G. Eggeler, E. Hornbogen, A. Yawny, A. Heckmann and M. Wagner, *Materials Science and Engineering: A*, 2004, 378, 24-33.
20. N. A. Fleck, G. M. Muller, M. F. Ashby and J. W. Hutchinson, *Acta Metallurgica et Materialia*, 1994, 42, 475-487.
21. A. C. M. Chong and D. C. C. Lam, *Journal of Materials Research*, 2011, 14, 4103-4110.
22. S. W. Cranford, A. Tarakanova, N. M. Pugno and M. J. Buehler, *Nature*, 2012, 482, 72.
23. R. Matsuzaki, M. Ueda, M. Namiki, T.-K. Jeong, H. Asahara, K. Horiguchi, T. Nakamura, A. Todoroki and Y. Hirano, *Scientific Reports*, 2016, 6, 23058.
24. M. Domm, J. Schlimbach and P. Mitschang, presented in part at the 21st International Conference on Composite Materials, Xi'an, China, 2017.
25. J. I. Lipton and H. Lipson, *Scientific Reports*, 2016, 6, 29996.
26. ANSYS Mechanical APDL Element Reference (Release 15.0), ANSYS Inc., Canonsburg, PA, 2013.
27. ANSYS Mechanical APDL Contact Technology Guide (Release 15.0), ANSYS Inc., Canonsburg, PA, 2013.
28. ANSYS Mechanical APDL Element Reference (Release 15.0), ANSYS Inc., Canonsburg, PA, 2013.
29. J. Korsawe, Circlefit3d - fit circle to three points in 3d space, MATLAB Central File Exchange. Retrieved March 10, 2017.
30. M. Ivey, G. W. Melenka, J. P. Carey and C. Ayranci, *Advanced Manufacturing: Polymer & Composites Science*, 2017, 3, 81-91.

4.5 Supporting information

4.5.1 Local strain calculation

The plastic FEA utilized a beam-solid element assembly (Fig. 4.7a). Solid elements were used in the middle of the coiling loop in order to avoid the convergence difficulty caused by beam elements under large inelastic deformation due to torsional loading.²⁸ Since the solid element does not provide direct cross-sectional outputs for curvature, torsional strain and axial strain along the fiber like the beam element does, we extract nodes displacements from each load substep in the simulation and calculate local strains along the fiber during the unfolding process. Results at the unfolding percentage of 80% are shown here as an example. For the curvature, the trace of center nodes (Fig. 4.7a) in solid elements is rebuilt in MATLAB. A circle is fitted to every three adjacent points along the trace.²⁹ The apparent curvature κ_a is calculated as the inverse of the radius of the circle. The bending curvature κ (Fig. 4.7b, red markers) which correlates with the bending stress is calculated as $\kappa = \kappa_a - \kappa_i$, where κ_i is the corresponding initial curvature of the fiber center line. The as-calculated κ is equivalent to $\sqrt{\kappa_Y^2 + \kappa_Z^2}$ (Fig. 4.7b, blue markers), where κ_Y and κ_Z are element outputs for the bending curvature about the Y and Z centroid axis of the beam element. The shear strain γ is calculated based on the corner angle of the surface mesh (Fig. 4.7a): $\gamma = \theta_d - \theta_i$, where θ_d is the angle on the deformed mesh, and θ_i is the angle on the initial mesh. The shear strain at each L_a is averaged by 40 values around the circumference (Fig. 4.7c). The as-calculated γ is equivalent to $r\gamma_{TE}$ (Fig. 4.7c, blue markers), where, r is the fiber radius, γ_{TE} is the element output of torsional strain from the beam element. The axial strain is calculated as $\varepsilon = (l_d - l_i)/l_i$, where l_d is the length between two adjacent center nodes after deformation, l_i is the initial length. The as-calculated ε is equivalent to the beam element output of axial strain. Discontinuities exist in all three local strain results at the transition from beam element to solid element. This is caused by the rigid surface constraint which is necessary to assemble beam and solid element.

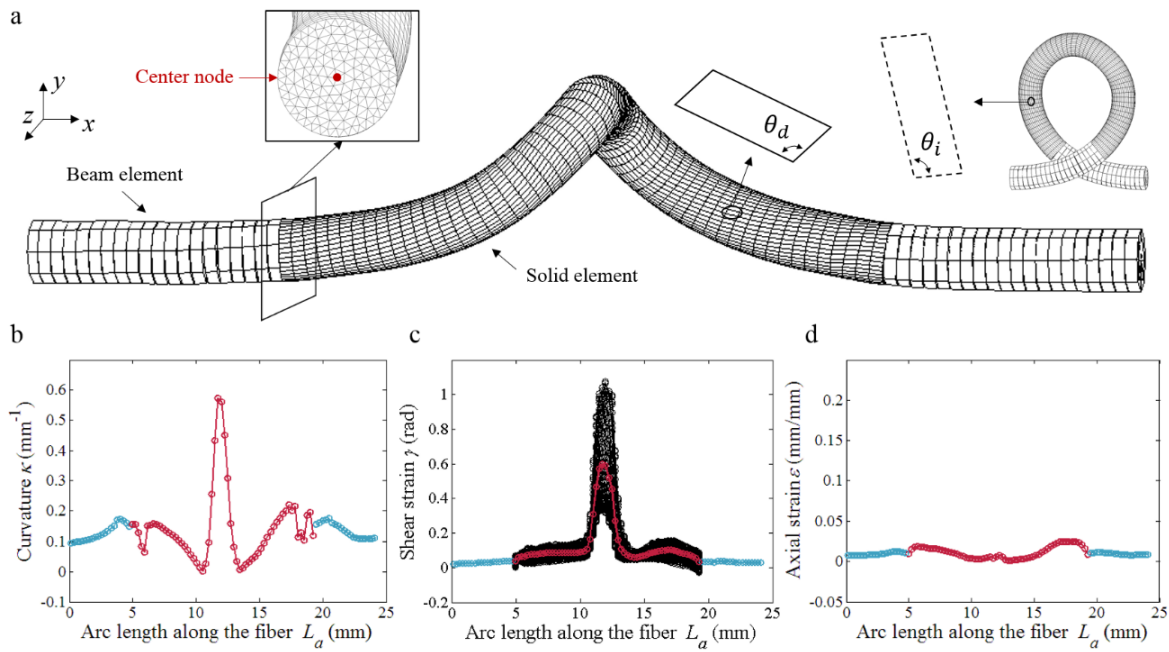


Figure 4.7 Local strain results calculated from beam and solid elements at the unfolding percentage of 80%: a) deformed meshes of beam and solid elements; b) curvature, c) shear strain, and d) axial strain calculated from beam (blue markers) and solid (red markers) elements. The shear strains in solid elements are averaged over 40 values (black markers) around the circumference at each L_a .

4.5.2 Multilinear plastic FEA

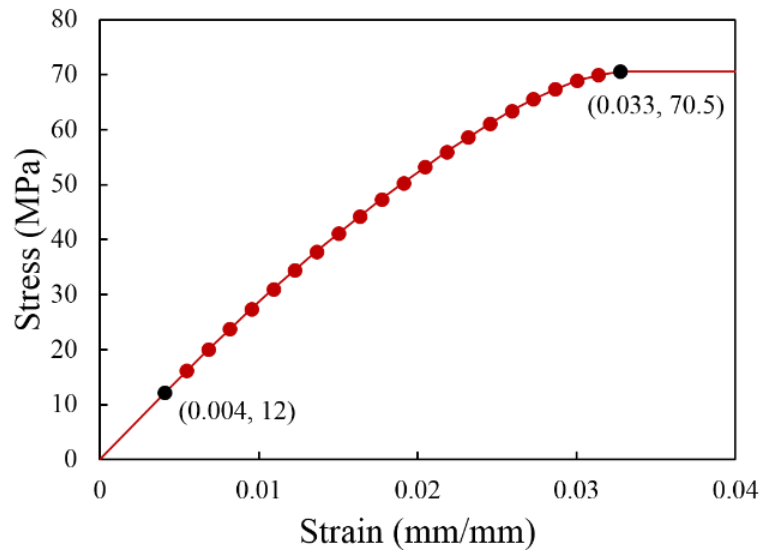


Figure 4.8 Piece-wise linear stress-strain curve for multilinear isotropic hardening in the plastic FEA. The first stress-strain point defines the yield stress (12 MPa). Subsequent points define the multilinear isotropic hardening behavior of the material. The last point corresponds to the fracture of the fiber in tensile test, while in the plastic FEA, the fiber behaves perfectly plastically after the material reaches the tensile strength (70.5 MPa). The data points are collected from one of the uniaxial tensile tests of straight PLA fiber with the diameter of 1.20 mm (gauge length = 250 mm, strain rate = 0.01 mm/mm/s). The tensile strength with a standard deviation for 7 specimens is 71.3 ± 0.95 MPa.

4.5.3 Tensile curves of straight fibers

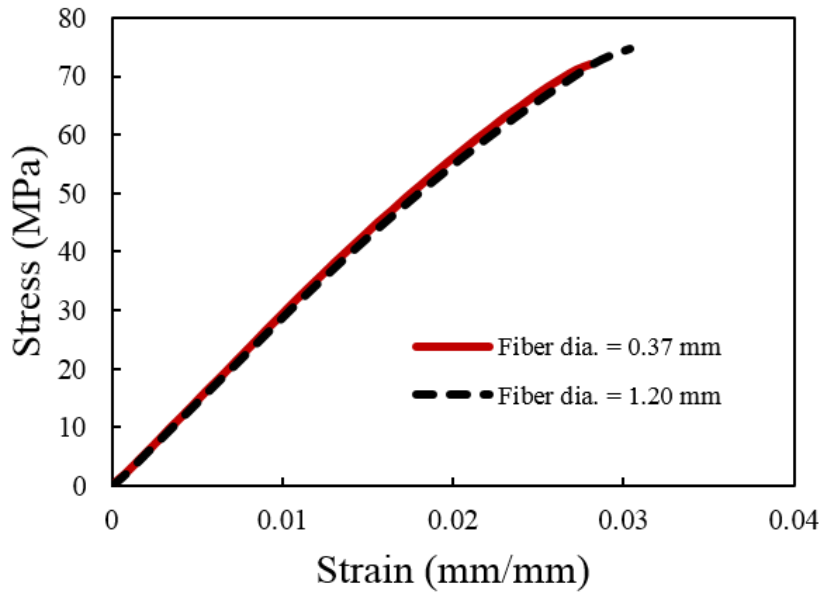


Figure 4.9 Stress-strain curves of straight fibers under uniaxial tension. Gauge length is 100 mm and crosshead rate is 500 mm/min for both fibers.

4.5.4 Strain rate estimation

Von Mises strain ε_{VM} (Fig. 4.10a, blue solid line) at the top surface in the middle of the unfolding loop is extracted from the plastic FEA. In order to have the von Mises strain rate $\dot{\varepsilon}_{VM}$ (Fig. 4.10a, red dashed line), we first calculate the equivalent elapsed time t after the breaking of sacrificial bond in the simulation, based on the pulling end displacement in the simulation and actual crosshead speed (8.33 mm/s with an initial acceleration of 52 mm/s²) in the uniaxial tensile test. Then the local strain rate $\dot{\varepsilon}_{VM}$ is obtained by differentiating ε_{VM} over the elapsed time t . The strain rate reaches the peak of 0.33 mm/mm/s at $p = 35\%$, around which the bending crack initiates at the top middle of the loop (Fig. 4.4a). This peak strain rate is used for both the large and small fibers in the three-point bending test. We approximate the strain rate in dynamic failure by the same method. In order to calculate the instantaneous speed after the breaking of sacrificial bond in dynamic failure, we track the adjacent bond in the traction direction from the high speed camera captures (Fig. 4.10b) and calculate the average pulling speed of the unfolding loop between each frame. The acceleration (1.327×10^5 m/s²) was obtained by a linear fit (Fig. 4.10c), based on which,

we calculate the equivalent elapsed time t_d after the breaking of sacrificial bond in the simulation. The von Mises strain rate (Fig. 4.10d, orange dashed line) in dynamic failure is obtained by differentiating the von Mises strain (Fig. 4.10d, blue solid line) over the elapsed time t_d . The fiber backbone breaks in the middle of the loop within $99 \mu\text{s}$ after the breaking of sacrificial bond (Fig. 4.10b). The strain rate at the top middle of the loop is 274 mm/mm/s (Fig. 4.10d) at $t_d = 99 \mu\text{s}$. With the acceleration unchanged, the strain rate at the top middle of the loop would reach the peak of 1492 mm/mm/s at $t_d = 235 \mu\text{s}$ if the fiber backbone did not break.

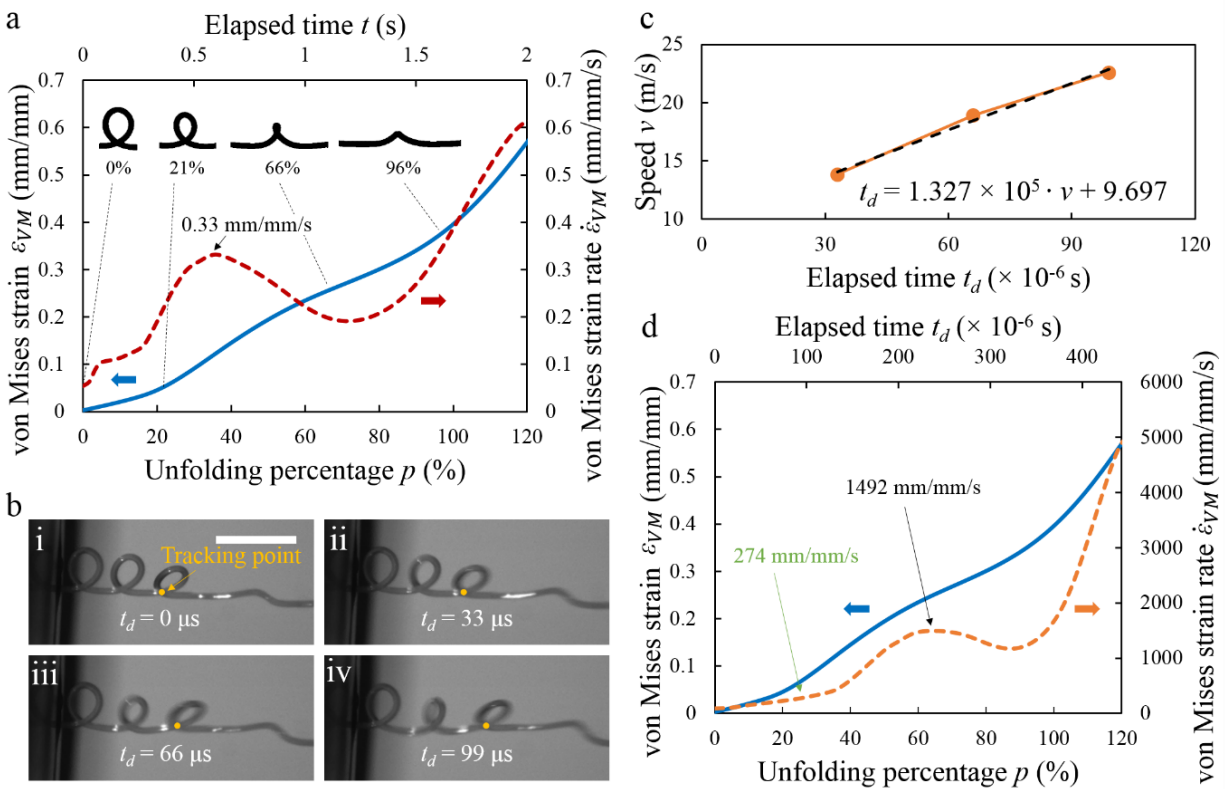


Figure 4.10 Estimation of the local strain rate at the top surface in the middle of the unfolding loop: a) von Mises strain (blue solid line, left Y axis) and von Mises strain rate (red dashed line, right Y axis) at the top surface in the middle of the unfolding loop, during the normal unfolding process of the loop without dynamic failure. The bottom and top X axis represent the unfolding percentage and elapsed time, respectively. They correspond to each other and serve as different references for the unfolding process. b) High speed imaging of the loop retraction after the breaking of sacrificial bond in dynamic failure. The speed of the loop retraction at $t_d = 33 \mu\text{s}$, $66 \mu\text{s}$ and $99 \mu\text{s}$ is calculated by measuring the moving distance of the tracking point in ii – iv relative to its initial position at t_d

= 0 μ s in i. Scale bar is 5 mm. c) Linear fit of the loop retraction speed over elapsed time. d) von Mises strain (blue solid line, left Y axis) and von Mises strain rate (orange dashed line, right Y axis) at the top surface in the middle of the unfolding loop, during the rapid unfolding process of the loop in dynamic failure. Simulation results, such as the von Mises strain and strain rate, are extracted from 101 load substeps and plotted as continuous lines here for the sake of visual demonstration.

4.5.5 Differential scanning calorimetry (DSC) test of large and small fibers

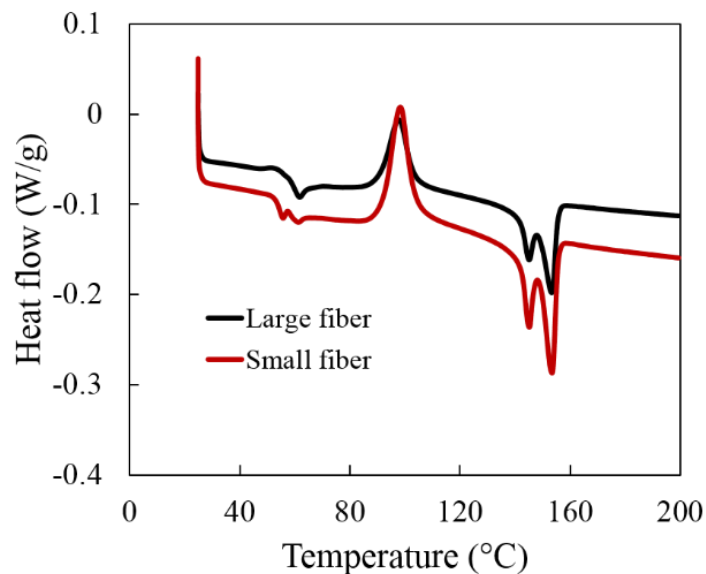


Figure 4.11 DSC results of FDM-extruded PLA fibers. The fibers were extruded at 230 °C on the conveyor belt in ambient air with two nozzles with different diameters (1 mm and 0.3 mm). The belt speed is equal to the extruding speed. The large and small fibers are 1.2 mm and 0.37 mm in diameter, respectively.

Thermal analysis of PLA fibers was performed in a DSC instrument (DSC Q2000) with the heating program found in the literature.³⁰ The temperature was first held at 25 °C for 3 min, and then increased to 200 °C with a rate of 2 °C/ min. The samples were cut from the same batch of straight fibers for the three-point bending test. The sample weight was 5.8 mg for the large fiber and 5.2 mg for the small fiber. The degree of crystallinity X_C of the specimen was calculated by the following equation:

$$X_C = \frac{\Delta H_m - \Delta H_c}{\Delta H_{100}} \times 100, \quad (4-1)$$

where, ΔH_m is the enthalpy of fusion, ΔH_c is the enthalpy of cold crystallization, ΔH_{100} is fusion enthalpy of 100% crystalline PLA, which is 93 J/g.³

The calculated crystallinity is approximately 2.5% for the large fiber and 1.1% for the small fiber, which are around the crystallinity of as-received PLA filament (2.4%) reported in the literature.³

4.5.6 Toughness enhancement

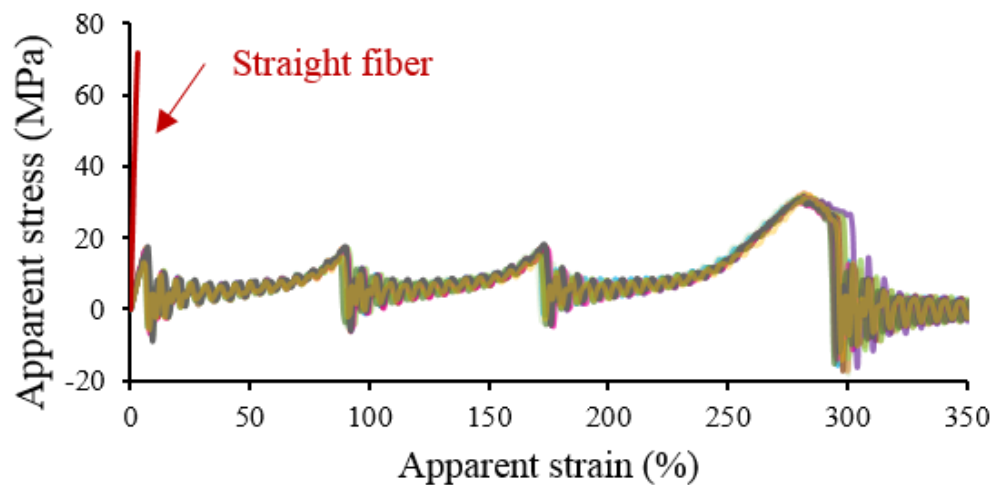


Figure 4.12 Apparent stress-strain curves of small fiber with three coiling loops. All ten test specimens are plotted to show the deviation. The stress-strain curve of the straight small fiber is also plotted as a benchmark to show the toughness enhancement in coiling fibers.

Table 4.1 Toughness values of the small fiber with three coiling loops. The benchmark toughness value of the straight fiber is 1.1 kJ/kg.

	Toughness (kJ/kg)		
	Average	Maximum	Minimum
3 coiling loops (small fiber)	5.51	5.86	5.15
%Benchmark	500%	533%	468%

CHAPTER 5 ARTICLE 2: SPIDERWEB-INSPIRED, TRANSPARENT, IMPACT-ABSORBING COMPOSITE

Shibo Zou¹, Daniel Therriault¹, Frédérick P. Gosselin^{1*}

¹Laboratory for Multiscale Mechanics (LM²), Department of Mechanical Engineering, École Polytechnique de Montréal, Montréal, Canada

Published in Cell Reports Physical Science on October 28th, 2020

Abstract

Transparent materials with high impact absorption are required in many safety-critical engineering systems. Existing transparent tough composites show increased impact resistance, but often fail catastrophically due to poor impact absorption. We propose a transparent impact-absorbing composite that reproduces the toughening mechanism involving sacrificial bonds and hidden lengths in spider silk. Our material consists of an elastomer matrix and an instability-assisted 3D-printed bidirectional fabric of microstructured fibers with sacrificial bonds and alternating loops. Under impact, the hidden loops unfold after the bond breaking and matrix cracking, resisting the impactor penetration with a graceful failure. The large-scale plastic deformation of the unfolding loops significantly increases the energy dissipation and leads to a hysteresis of 95.6% (dissipated energy/total absorbed energy \times 100%), minimizing the released elastic energy and reducing the rebounding damage. Our approach opens a new avenue for the design and manufacturing of transparent high-energy absorbing composites for impact protection applications.

5.1 Introduction

Spider webs evolved with their weavers to dissipate the tremendous kinetic energy involved during prey capture¹⁻³. Unlike other tough biological materials such as tendon⁴, in which only 10% of its absorbed energy is dissipated away and 90% is stored as elastic energy in the material⁵, up to 70% of the energy absorbed by the spider web is dissipated out of the system³. The spider web dissipates the energy mainly through molecular bond breaking, entropy increase and internal heat production^{3,6,7} in the radial threads⁸. Hence, the elastic energy released upon unloading is minimized to avoid the catapulting of insects by the oscillating web after impact. The energy dissipation in the radial threads is attributed to the silk fibril nanostructure which consists of beta-

sheet nanocrystals and semi-amorphous domains^{7,9,10} (Fig. 5.1A). Upon stretching, the breaking of hydrogen bonds and uncoiling of protein chains in the semi-amorphous domains contribute to the large extensibility and high energy dissipation. This is known as the sacrificial bonds and hidden lengths (SBHL) mechanism¹¹. Variations of this energy dissipating mechanism have been successfully applied at the molecular scale in hydrogels^{12–14} and elastomers^{15–17}, resulting in high hysteresis up to 85%^{14,18}. We seek to scale up this molecular level mechanism at the microscopic scale to make new impact-absorbing architected composites, which can dissipate a large amount of energy and catch the projectile like the spider web does (Fig. 5.1B and a general concept overview available in Video S1).

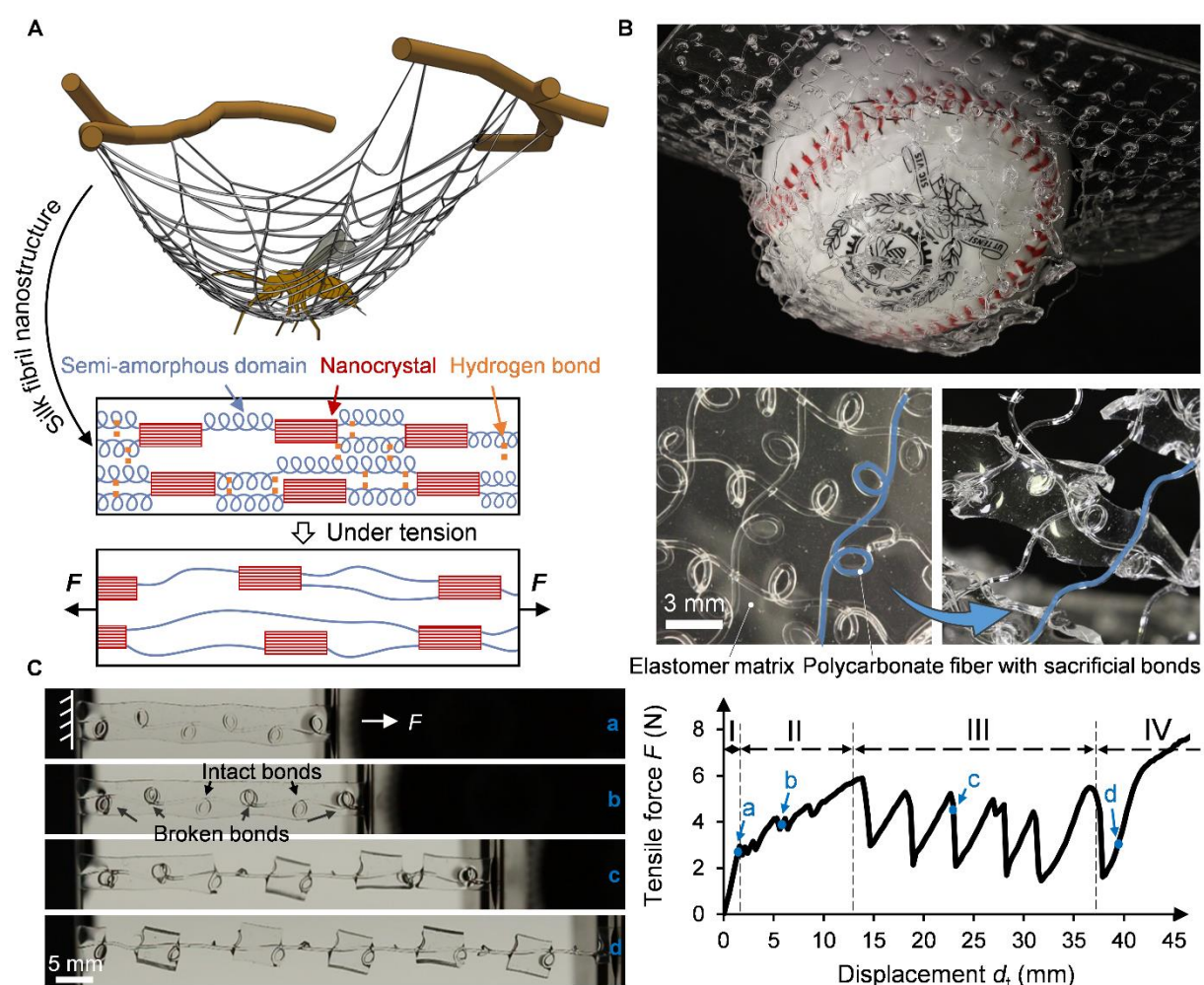


Figure 5.1 Design of the spider web-inspired transparent impact-absorbing composite.

(A) Schematic of a spider web catching a flying prey. The high energy dissipation of the spider web results from the beta-sheet nanocrystals and semi-amorphous domains in the silk fibril nanostructure^{7,9,10}. The latter contains highly extensible protein chains with intra- and interchain hydrogen bonds. Under tension, the breaking of hydrogen bonds within the semi-amorphous domains unravels the hidden portion of the protein chains, increasing the extensibility and toughness of the spider silk.

(B) The spider web-inspired transparent impact-absorbing composite catching a free-falling baseball after five repeated impacts. The baseball was attached to a 0.5 kg weight and dropped from a 0.66 m height on a falling dart impact tester. Images of the composite before and after the impact show the breaking of sacrificial bonds and unfolding of hidden lengths, reproducing the energy dissipating mechanism in spider silk.

(C) Mechanical behavior of a single microstructured fiber reinforced composite during tensile test. Camera snapshots of the tensile test at four representative instants a, b, c and d are from the four regimes on the tensile curve, respectively: I, homogeneous stretching of the fiber and matrix; II, breaking of sacrificial bonds inside the matrix and fiber-matrix detaching around the loops; III, onset of cracking and segmentation of the matrix around the loops; IV, final stretching of the fiber backbone.

There are several studies^{19–27} which scaled up the SBHL mechanism at the microscopic or macroscopic scales. Sacrificial bonds were constructed via physical fusion of polymer thread^{19,21,23–25}, sliding knot²⁰, embedding liquid metal²⁶ or 3D-printed hierarchical network^{22,27}. All these studies observed a similar sequential fracture of sacrificial bonds, during which extra energy is dissipated via friction²⁰ or plasticity²³. Some works^{19–21,23–25} even physically and functionally resemble the micro-looped silk spun by the recluse spider in nature²⁸. However, all these studies focused on designing a uniaxially toughened system, due to the difficulty of integrating the design in a bulk panel without compromising the SBHL performance, limiting the material's potential in impact protection applications. Here, we propose a transparent and impact-absorbing architected composite with a bidirectional SBHL system made by instability-assisted fused filament fabrication (IFFF) based on our previous experimental²¹ and simulation²³ studies. Under impact, the kinetic energy of the projectile, as demonstrated by a baseball in Fig. 5.1B, is largely dissipated by the breaking of sacrificial bonds and unfolding of the hidden loops after

matrix cracking. Finally, the composite can catch the projectile gracefully. The mechanical and optical properties of the fiber and matrix are critical to harness the maximum dissipated energy and achieve an excellent transparency: (i) the fiber should have a good plasticity to avoid premature failures caused by stress concentrations along the unfolding loop²³; (ii) the matrix should favor the sequential unfolding of the hidden loops, which contributes to most of the energy dissipation via plasticity²³; (iii) both the fiber and matrix should have a good transparency, and more preferably, a similar refractive index (RI)²⁹ to reduce the geometric scattering³⁰ at the matrix-fiber interface. Polycarbonate (PC) shows a good strain hardening behavior with a true strain at break up to 0.8³¹ and has a ~90% transmittance in the visible light spectrum³². Also, it has a low viscosity below 200 Pa·s when extruded by an FFF 3D printer at 290 °C³³, making it possible for the viscous coiling regime^{34,35} in IFFF (see details in the Fabric Printing section in Experimental Procedures). Hence PC is a perfect candidate that fits all the mechanical, optical and fabrication requirements. Based on the PC fiber with an RI $n_{\text{fiber}} = 1.58$ @589 nm (Fig. 5.5), two transparent elastomers with different RI values ($n_{\text{matrix}} = 1.41$ or 1.55 @589 nm, Fig. 5.5) were selected to construct the composites in order to investigate the RI's effect on the optical properties of the composites. The stiff fiber and soft matrix system has been largely practiced in tough hydrogel³⁶⁻³⁸ or viscoelastic polymer^{27,39,40} composites. The design principles of these tough composites are to dissipate substantial energy via the fiber and maintain high elasticity via the soft matrix⁴¹. The resistance to crack propagation is considerably increased compared to the neat matrix, but the hysteresis is limited by the high elasticity of the soft matrix. We deliberately chose the elastomer matrix with a weak adhesion to PC and low strength to allow the sacrificial bonds to freely break inside the matrix (regime II in Fig. 5.1C), and enable the sequential fracture of the matrix and complete unfolding of the hidden loops (regime III in Fig. 5.1C). Therefore, almost all the mechanical energy is dissipated out of the system through the breaking of sacrificial bonds, friction between the fiber and matrix, matrix cracking and plastic deformation of the fiber.

5.2 Results and discussion

5.2.1 Fabric printing and mechanical characterization

Fig. 5.2A shows the IFFF fabrication of a two-layer bidirectional fabric of microstructured fibers with SBHL. In the IFFF process, the PC filament is partially molten, then extruded at a speed v_e

onto the printing platform from a height h . In the meantime, the extruder is moving at a speed v_m relative to the printing platform. When the speed ratio v_e/v_m exceeds 1, the longitudinal compressive stress in the polymer thread triggers the buckling instability, producing a series of nonlinear patterns^{42,43}. Thermally-fused sacrificial bonds can be formed by fiber self-intersections in some patterns, such as alternating, coiling and overlapping patterns²¹. This phenomenon, firstly called as a fluid-mechanical sewing machine (FMSM)⁴⁴, has been found not only in viscous threads^{44,45}, but also in elastic rods⁴⁶. We adapted the quasistatic geometrical model developed by Brun et al.⁴⁷ as a fabrication guide to create the bidirectional fabric of microstructured fibers (Note S1; Fig. 5.6). This model has been validated for both viscous threads^{47,48} and elastic rods⁴⁹, indicating the dominating role of geometry and kinematics over material properties in the FMSM.

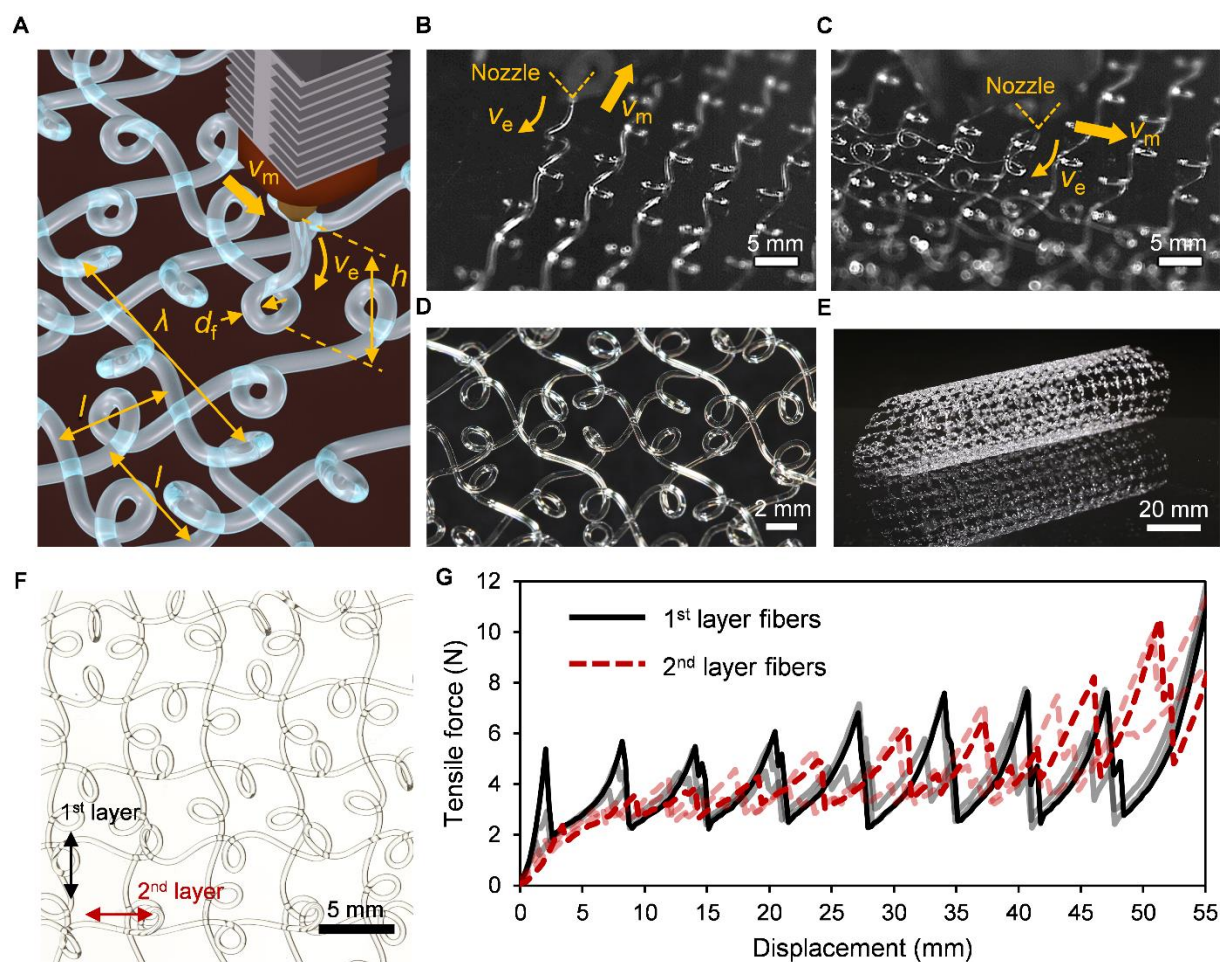


Figure 5.2 Fabrication and mechanical behavior of the two-layer fabric of microstructured fibers.

(A) Schematic of the IFFF process. The alternating pattern is determined by the ratio of the filament extruding speed v_e to the extruder moving speed v_m . The transverse and longitudinal size of the pattern are determined by the ratio of deposition height h to fiber diameter d_f . The distance between adjacent deposition paths in both layers is l , which is set to be half of the wavelength of the pattern in order to reduce loop overlapping between the two layers.

(B and C) High-speed camera snapshots of the deposition process of the (B) 1st and (C) 2nd layer of the fabric of alternating fibers.

(D and E) As-fabricated two-layer fabric (D) at rest and (E) under bending, demonstrating the flexibility and interlayer bonding of the two-layer fabric.

(F) Optical image of the two-layer fabric: the fibers of the 1st layer are vertical, and the fibers of the 2nd layer are horizontal.

(G) Tensile curves of the 1st and 2nd layer fibers. Three tensile curves are shown in the plot for each layer. Besides the two representative curves, other curves are shown in gray and pink for the 1st and 2nd layer fibers, respectively. Each curve represents the tensile test of three fibers in parallel.

In order to catch the impact projectile at any random location on the composite, the highest possible surface coverage (the fraction of the printing platform area covered by the fiber) of the two-layer fabric of microstructured fibers is desired. Although coiling and overlapping patterns bring the highest surface coverage⁵⁰, the structure of the 2nd layer coiling loops can be highly distorted due to the disturbed deposition on top of the 1st layer loops^{51,52}. The distortion will dramatically hinder the energy dissipation of the SBHL system, since the distorted fiber tends to fail prematurely²³. Compared to the coiling and overlapping patterns, alternating pattern shows a higher potential in avoiding the 2nd layer loop distortion and achieving a fully functional SBHL system in the bidirectional fabric of microstructured fibers (Fig. 5.6). A surface coverage of ~33% can be achieved by selecting an alternating pattern with a small wavelength. The distance l between each adjacent printing path in both layers is set to be half of the wavelength λ of the alternating pattern. The loops in the 1st layer can be partially aligned under a stable polymer extruding speed (Fig. 5.2B). Then the paths of the 2nd layer are designed in the 3D printer g-code to be in-between the alternating loops of the 1st layer. This way, the 2nd layer fiber mostly coils on or in-between the fiber segments (Fig. 5.2C), not directly on the loops of the 1st layer. The as-fabricated two-layer

fabric of microstructured fibers (Fig. 5.2D) retains sacrificial bonds and alternating loops in both layers. Also, the fabric is flexible and has an interlayer adhesion that is strong enough to keep the fabric integrity under bending (Fig. 5.2E).

In order to compare the mechanical properties of the fibers from each layer, we manually separated the two layers of a sample of as-fabricated fabric (Fig. 5.2F). For the fibers from each layer, we tested three fibers in parallel in each test and repeated for three times to have a comprehensive comparison of the fibers' tensile properties. The tensile curves of the fibers in both layers are identical (Fig. 5.2G), except the average sacrificial bond strength in the 2nd layer fiber is 79% of that in the 1st layer, which is probably due to the disturbance by the 1st layer fiber during the deposition of the 2nd layer fiber.

5.2.2 Composite fabrication and optical characterization

Fig. 5.3A shows the infiltration of the as-fabricated fabric with an elastomer resin inside a plastic mold to obtain a transparent composite after curing. Previous studies on transparent composites with a thickness of a few millimeters either used sparse micro-defect arrays (the ratio of defect line spacing to defect width = 25 ~ 100)⁵³, or matrix-filler RI matching^{29,54} to achieve the overall transparency of the composite. In our study, the as-fabricated fabric of alternating fibers has a ratio of fiber spacing to fiber diameter of ~15. A lower ratio than this value would cause the distortion of the 2nd layer fiber and hinder the energy dissipation of the fabric. A higher ratio than this value results in a lower fiber volume fraction which increases the transparency but decreases the energy dissipation capability of the composite. With the selected ratio of ~15, the fabric with functional SBHL in both layers displays a decent transparency with a little blur in front of distant objects (Fig. 5.3B). However, the circular cross section of the fiber causes image distortion, which makes a Quick Response (QR) code behind the fabric unrecognizable by a QR code scanner (Fig. 5.3B). The image distortion is caused by the refraction at the air-fiber interface due to the large relative RI $n^* = n_{\text{fiber}}/n_{\text{air}} \approx 1.58$. After the fabric is infiltrated with the low RI elastomer, the n^* at the matrix-fiber interface is reduced to $n_{\text{fiber}}/n_{\text{matrix}} = 1.58/1.41 = 1.12$. It is ~30% lower than the air-fiber interface, making the QR code scannable (Fig. 5.3C). A further decrease of the n^* by the high RI elastomer ($n^* = n_{\text{fiber}}/n_{\text{matrix}} = 1.58/1.55 = 1.02$) makes the fiber less visible inside the matrix (Fig. 5.3D).

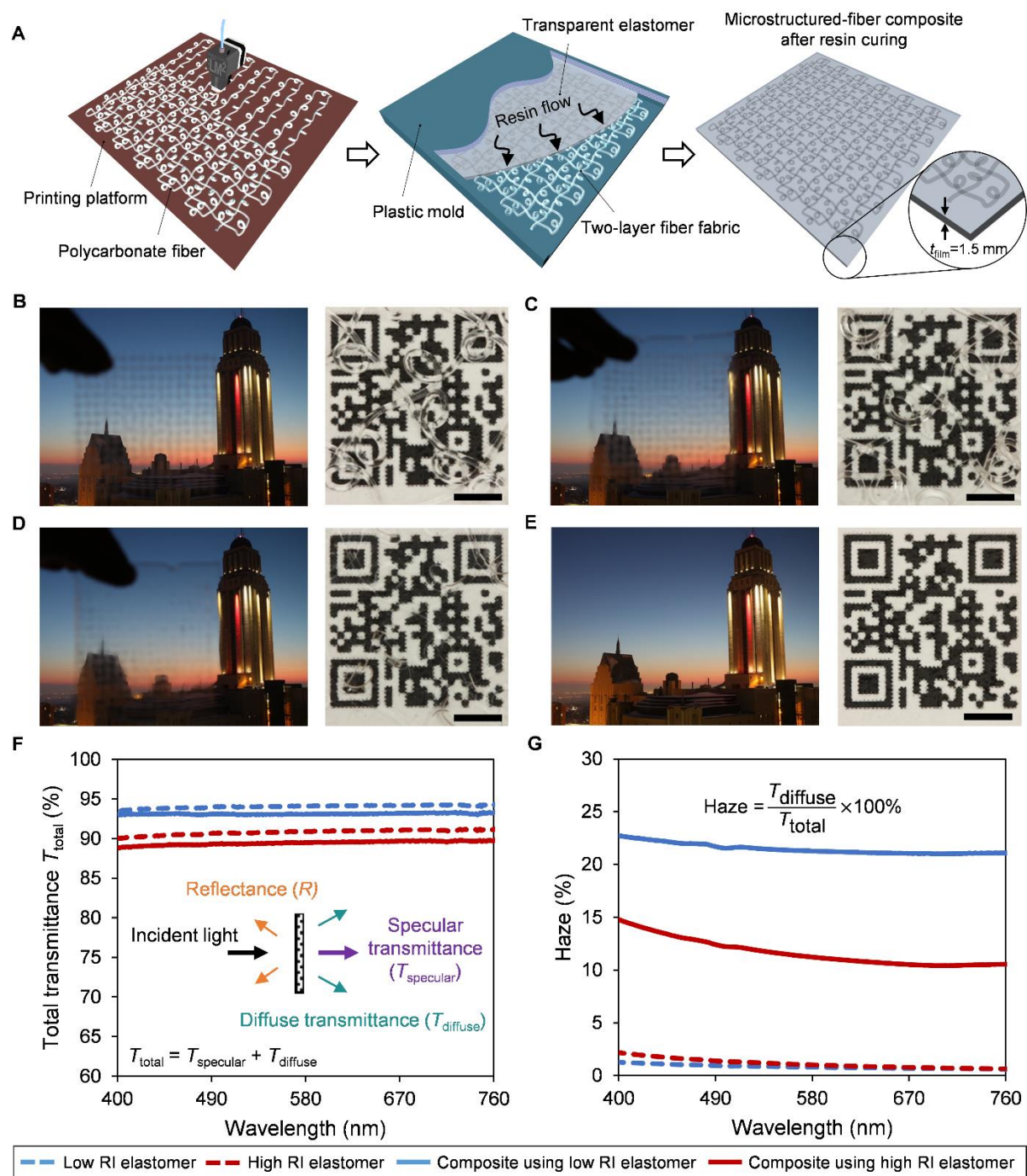


Figure 5.3 Fabrication and optical characterization of the microstructured-fiber composite.

(A) Schematic of the composite fabrication process. A two-layer fabric consisting of microstructured PC fibers is made by IFFF, and then infiltrated by a transparent elastomer inside a

mold with an inner size of $100 \times 100 \times 1.5$ mm (length \times width \times thickness). Two transparent elastomers with different RI values (1.41 and 1.55 @ 589nm) were used to make the composite.

(B–E) Comparison of the transparency and image distortion of (B) Two-layer fabric of alternating fibers, (C) Composite film using the low RI elastomer, (D) Composite film using the high RI elastomer in front of a distant building and lying on top of a QR code. (E) Reference photos of the distant building and QR code. Both composite films have a thickness $t_{\text{film}} = 1.5$ mm. All scale bars are 3 mm.

(F and G) (F) Total transmittance and (G) Haze of the low RI elastomer film, high RI elastomer film, and composites films based on them. All test films have a thickness $t_{\text{film}} = 1.5$ mm.

We further characterized the optical transmittance of both elastomers and their composites. The total transmittance T_{total} of the low RI and high RI elastomer films (Fig. 5.3F, dashed curves) are 94.05 % and 90.79 % (averaged over the visible light spectrum), respectively. The high RI elastomer has a lower T_{total} , which is because a higher n^* ($= n_{\text{elastomer}} / n_{\text{air}}$) at the air-elastomer interface leads to a higher reflectance R , according to Fresnel's formula at normal incidence⁵⁵:

$$R = \left(\frac{n^* - 1}{n^* + 1} \right)^2. \quad (5-1)$$

The high RI elastomer film has a 4.65% reflectance ($n^* \approx 1.55$, @589 nm) per air-elastomer interface, while the low RI elastomer has a 2.89% reflectance ($n^* \approx 1.41$, @589 nm) per interface. The integration of the two-layer fabric of alternating fibers inside the elastomer matrix further decreases the T_{total} due to the increase in reflectance at the additional matrix-fiber interfaces (Fig. 5.3F, solid curves). The average T_{total} of the low RI and high RI elastomer composite films in the visible light spectrum are 93.12% and 89.45%, respectively.

The transmitted light through the sample film includes a specular component, which is perpendicular to the sample surface like the incident light, and a diffuse component, which deviates from the normal direction (Fig. 5.3F inset). The latter is often related to the light scattering in a heterogeneous material³⁰. In our case, it is mainly caused by the light refraction at the matrix-fiber interface, which is also the main reason for the image distortion. In order to quantify the matrix RI's influence on the light diffusing, we define haze⁵⁶ as the ratio of diffuse transmittance to total transmittance. The haze in both elastomer films are very low in the visible light spectrum (Fig.

5.3G, dashed curves), indicating the insignificance of light scattering in both elastomer films. The average haze of the low RI and high RI elastomer composite films in the visible light spectrum are 21.48% and 11.66%, respectively. This proves that the matrix-fiber RI matching can effectively reduce the light diffusing of the composite.

It should be noted that the difference in the coefficient of thermal expansion between PC ($6.8 \times 10^{-5}/^{\circ}\text{C}^{32}$) and the elastomer matrix (low RI elastomer: $2.6 \times 10^{-4}/^{\circ}\text{C} \sim 3.1 \times 10^{-4}/^{\circ}\text{C}$; high RI elastomer: $2.1 \times 10^{-4}/^{\circ}\text{C}$; Table 5.1) would cause the debonding at some interfaces between the fiber and the matrix after curing at elevated temperature (Fig. 5.7). The matrix-fiber debonding would reduce the optical transmittance and increase the haze of the composite material due to additional interfaces. Since the length scale of the matrix-fiber debonding is more than one order of magnitude smaller than that of the fiber and composite film, the influence of the matrix-fiber debonding on the optical properties of the composite is believed to be negligible compared to that of the matrix-fiber RI difference.

5.2.3 Impact test and failure analysis

Since the two elastomers have similar mechanical properties (Table 5.1), we chose the low RI elastomer for economic reasons to demonstrate the impact absorption of the composite on a falling dart impact tester (Fig. 5.4A, B). We tested four materials: elastomer film (Fig. 5.4C), straight fiber composite film (Fig. 5.4D), alternating fiber composite film (Fig. 5.4E), and hybrid fiber composite film (Fig. 5.4F) which contains both the straight fiber fabric and the alternating fiber fabric.

In order to simulate a more realistic projectile with an irregular surface, a P60 grade sandpaper was attached to the hemispherical head of the falling dart, which led to microscopic defects in the impacted sample. Based on the static puncture test results (Note S2; Fig. 5.8), we chose the impact energy of 5 J at an impact velocity of 4.2 m/s for all test specimens (100 mm \times 100 mm \times 1.5 mm). We tested three specimens for each type of film and obtained the contact force-time curves in Fig. 5.9A-D. Then we calibrated the displacement of the falling dart with the help of the high-speed camera (see details in the Mechanical Characterization section in Experimental Procedures) and obtained the representative contact force-displacement curve for each type of film in Fig. 5.4B.

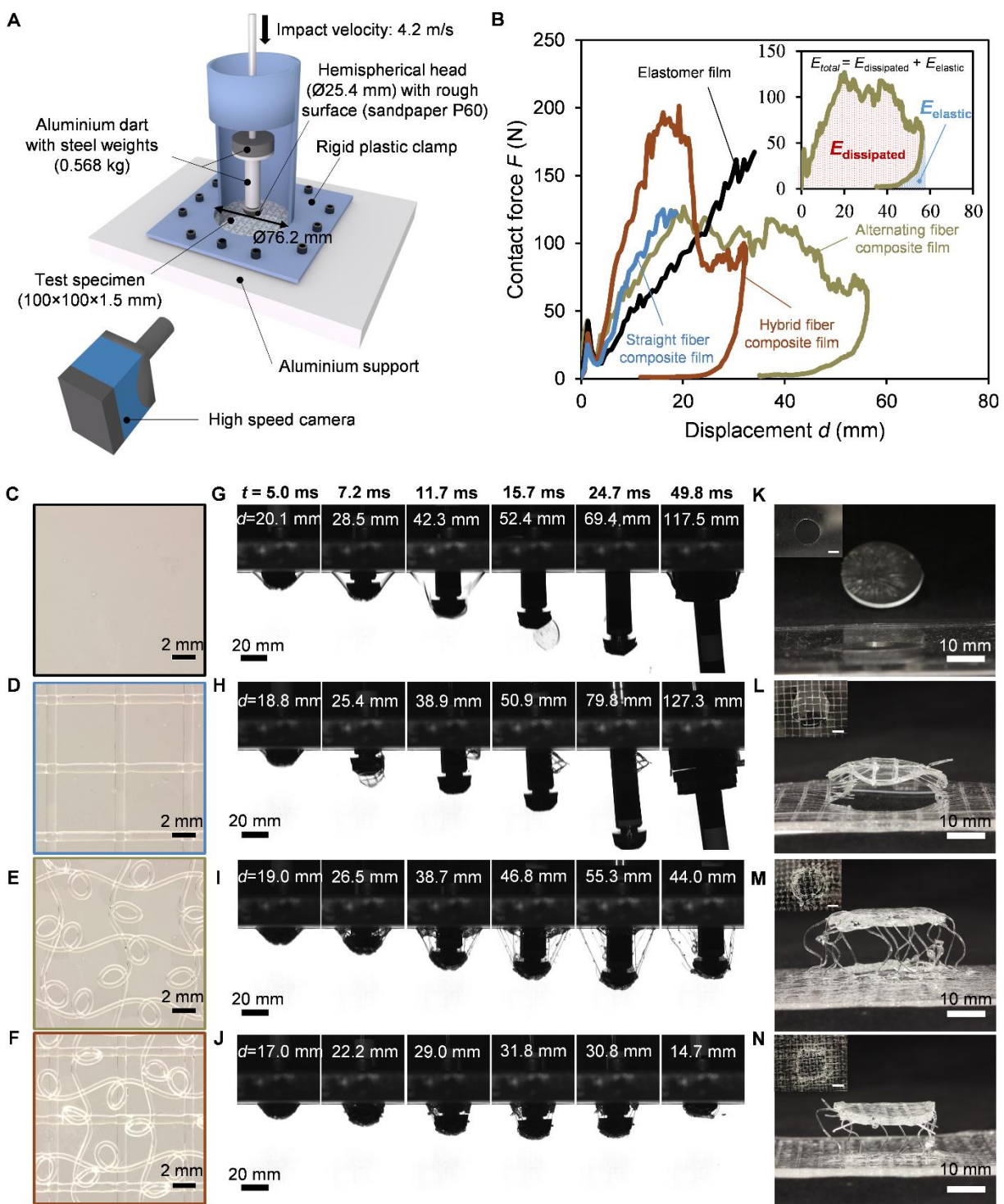


Figure 5.4 Impact tests of different transparent films based on the low RI elastomer.

(A) Schematic of the in-house designed impact test setup. The hemispherical dart head is covered with a medium grit size (P60) sandpaper, in order to simulate a realistic projectile with a rough surface.

(B) Contact force-displacement curves of the elastomer film (in black), straight fiber composite film (in blue), alternating fiber composite film (in green), and hybrid fiber composite film (in red). The inset illustrates the dissipated energy $E_{\text{dissipated}}$ (4.7 J) between the loading and unloading curves, and the elastic energy E_{elastic} (0.2 J) under the unloading curve of the alternating fiber composite film. All test films have a thickness of 1.5 mm.

(C–F) Optical images of the (C) Elastomer film, (D) Straight fiber composite film, (E) Alternating fiber composite film, (F) Hybrid fiber composite film.

(G–J) High-speed camera snapshots of the impact tests of the (G) Elastomer film, (H) Straight fiber composite film, (I) Alternating fiber composite film, (J) Hybrid fiber composite film at six different instants after the initial contact ($t = 0$ ms). Since the stiffness varies among the four different specimens, the dart appears at different positions among the four specimens at the same instant. The displacement d , which is defined as the vertical displacement of the dart after the initial contact, is marked on each snapshot for each specimen. Under the same impact energy (5 J), the impactor penetrates the elastomer film and straight fiber composite film. Both the alternating fiber composite film and the hybrid fiber composite film catch the impactor by absorbing a large amount of energy. The releasing of elastic energy springs the dart back up and results in the unloading curves in (B).

(K–N) Optical images of the fractured (K) Elastomer film, (L) Straight fiber composite film, (M) Alternating fiber composite film, (N) Hybrid fiber composite film after the impact tests. Scale bars in the insets are 10 mm.

Under impact, the elastomer film shows an elastic force increase until the crack initiates at the displacement $d = 34.1$ mm (Fig. 5.4B, black curve). The crack propagates very quickly around the dart head (Fig. 5.4G), due to the low fracture resistance of this elastomer which has been demonstrated by previous studies^{18,40}. The fractured elastomer film shows a smooth fracture surface (Fig. 5.10A). The dart then penetrates through the circular hole punched in the film (Fig. 5.4K; Video S2). The elastomer film slows down the falling dart from 4.2 m/s to 2.6 m/s. Most of

the kinetic energy is stored as elastic strain energy in the film. Hence after penetration, the residual film bounces up and down drastically.

The straight fiber composite film shows a higher effective stiffness (9.1 N/mm) under impact on the contact force-displacement curve (Fig. 5.4B, blue curve), compared to the elastomer film (5.0 N/mm). The dart also penetrates the straight fiber composite film (Fig. 5.4H; Video S3), but the circular crack propagation is finally stopped by the fiber (Fig. 5.4L). The crack is deflected by the straight fiber fabric, resulting in a more irregular crack path than that of the elastomer film. Fiber breakage happens mostly at the grid intersections (Fig. 5.10B), where the fibers were weakened due to the squeezing of two layers at a restricted height by the nozzle during the printing process. The plastic deformation and fracture of the straight fibers, as well as fiber pull-outs dissipate a certain amount of energy which would otherwise drive the propagation of the crack.

The alternating fiber composite film shows a similar stiffening behavior (Fig. 5.4B, green curve) as the straight fiber composite film at the beginning of the impact, but a lower effective stiffness (6.0 N/mm), due to the breaking of sacrificial bonds during the stiffening process (regime II in Fig. 5.1C). After the propagation of the circular crack around the impactor footprint, the alternating loops are exposed and unfolded to further dissipate the kinetic energy. The falling dart is finally caught by the alternating fiber composite film (Fig. 5.4I; Video S4). The contact force-displacement curve shows a 95.6% hysteresis ($E_{\text{dissipated}}/E_{\text{total}}$), meaning that 95.6% of the total absorbed energy is dissipated away and only 4.4% is released as elastic energy (Fig. 5.4B inset). The associated fractured specimen (Fig. 5.4M) shows a much larger energy dissipation zone than the elastomer film (Fig. 5.4K). The fracture surface of the alternating fiber composite film is much rougher than that of the elastomer film, due to the crack deflection of the alternating fiber fabric. Many unfolding fibers are observed in the fractured specimen, indicating the breaking of sacrificial bonds during the deformation. The matrix segmentation around the fiber loops is also observed (Fig. 5.10C), but not as regular as that in the tensile test in Fig. 5.1C. Fiber pull-outs are rare, since the alternating fibers break outside the matrix after the loop unfolding. Instead, fiber cut-outs are found around the main circular crack (Fig. 5.10C), where the fiber cuts out from the matrix transversely. The fiber cut-outs are believed to be related with the transverse loading condition and not seen in the tensile test. The complex fracture pattern indicates that the energy is dissipated by

the breaking of sacrificial bonds, fiber-matrix sliding, matrix cracking and segmentation, fiber cut-outs, plastic deformation and fracture of the unfolding fiber.

We also tested a PC film with a weight of ~ 1.1 times the weight of the alternating fiber fabric under the same impact energy (Fig. 5.9E). The falling dart penetrates the PC film within 5 ms after the initial contact, proving that the high energy dissipation of the alternating fiber composite is from the material architecture rather than material components.

A 2nd impact test with the same amount of energy (5 J) on the fractured alternating fiber composite film leads to the total failure of the specimen with the falling dart penetrating through the film (Fig. 5.11A). In another cyclic impact test with an impact energy of 1.4 J, the alternating fiber composite film is able to catch the falling dart during the first 4 cycles, with the peak contact force reducing less than 40% after the 1st cycle (Fig. 5.11B). Apparently, the cyclic use of the composite at a constant impact location is restricted, because once the alternating fibers are exposed and unfolded, they dissipate much less energy through the final fracture. We assume that the composite can retain its high energy absorption for large cycles at random impact locations, which is beyond the capability of our current impact testing machine.

Embedding both the straight fiber fabric and the alternating fiber fabric inside the elastomer further improves the design. The hybrid fiber composite film shows a 93.7% hysteresis with an even higher effective stiffness (13.9 N/mm) and increased maximum contact force. Similarly in nature, the cribellate spider produces a silk thread composed of one straight fiber and one coiled fiber to increase the energy dissipation during prey capture⁵⁷. The hybrid fiber composite film catches the falling dart with a smaller displacement (Fig. 5.4J; Video S5) than the alternating fiber composite film, due to the extra energy dissipation by the straight fibers. The fractured specimen shows a similar energy dissipation zone (Fig. 5.4N) as that of the alternating fiber composite film. The unfolding of alternating fibers can be seen from the fractured specimen, as well as the breakage and pull-out of straight fibers (Fig. 5.10D), which is similar to the fracture behavior of the alternating fiber composite film and straight fiber composite film. However, matrix segmentation and fiber cut-outs, which are found in the alternating fiber composite film, are rarely observed in the hybrid fiber composite film, probably due to the restriction by the straight fiber fabric.

In order to see if there is a difference in the impact absorption performance between the low RI and high RI elastomer based composites, we made an alternating fiber composite film with the high RI elastomer and tested under the same impact condition (Video S6). The high RI elastomer composite film catches the falling dart with a higher effective stiffness (12.8 N/mm, Fig. 5.12A) than the low RI elastomer composite film (6.0 N/mm, Fig. 5.12A), which is consistent with the fact that the high RI elastomer has a higher Young's modulus (5.1 MPa, Table 5.1) than the low RI elastomer (1.32 ~ 2.97 MPa, Table 5.1). The high RI elastomer composite film shows similar fracture behaviors to the low RI elastomer composite film, such as loop unfolding, matrix cracking and fiber cut-outs. However, the high RI elastomer composite film shows a larger fiber cut-out length (Fig. 5.12B, C), probably due to its lower strength (1.3 MPa, Table 5.1) compared to the low RI elastomer (3.51 ~ 7.65 MPa, Table 5.1). Since the fiber cut-outs expand the energy dissipation zone, the elastomer matrix thickness can be further optimized based on the elastomer property to take advantage of the fiber cut-outs and increase the impact energy dissipation.

5.3 Conclusion

In conclusion, our architected transparent composite reproduces the spider silk's SBHL toughening mechanism at the microscopic scale. The breaking of sacrificial bonds and the unfolding of hidden loops, as well as fiber-matrix sliding, fiber cut-outs, matrix cracking and segmentation contribute together to the high hysteresis, impact absorption, damage tolerance and graceful failure of the composite. The size and pattern of the fabric of microstructured fibers can be further tailored by either instability-assisted 3D printing^{19,21,24,25}, or electrospinning^{50,58}, to ensure the graceful catch of impact projectiles with different sizes and kinetic energies. Nanoscale mechanism⁴¹, such as chain-fracturing, reversible crosslinking and transformable domains in polymer network, can be introduced to both the fiber²⁴ and matrix⁵⁹ to further increase the energy dissipation and add self-healing functionalities. The transparent composite can potentially be used in laminated glasses⁵³ to increase the energy dissipation under impact. The combination of high RI fiber and low RI matrix in our study also makes it possible for the optical sensing^{60,61} of local deformation (Note S3; Fig. 5.13), giving the composite another potential functionality of self-monitoring⁶². The concept of our impact-absorbing composite with SBHL toughening mechanism can be further extended for various applications, transparent or not, by replacing the material

components with other engineering materials such as polyether ether ketone (PEEK), Kevlar fiber, etc. Finally, our composite represents a way to design structures to fail gracefully rather than catastrophically. Adapting this design to high performance materials could allow potential applications in bullet-proof or space craft windows.

5.4 Experimental procedures

5.4.1 Fabric printing

A vacuum oven dried the clear PC filament (1.75 mm in diameter) overnight at 65 °C. A Prusa i3 3D printer printed the filament at 330 °C with a high temperature extruder kit (Dyze Pro, Dyze Design). The Simplify3D software sent the custom-written g-code to the printer. Coogan et al.³³ fitted the following Williams-Landel-Ferry model to the in-line rheological test results of PC filament on an FFF 3D printer:

$$\eta(T) = 5.18 \times 10^9 e^{\left[\frac{-22.2 \times (T-385)}{51.6 + (T-385)} \right]}, \quad (5-2)$$

where $T = 603.15$ K in our study. The model predicts the zero-shear viscosity $\eta = 82.65$ Pa·s. We first assumed that the polymer thread out of the nozzle kept the as-calculated viscosity during the deposition process. Then we used the following dimensionless height \hat{H} defined by Ribe et al.³⁵ to make sure that the deposition stays within the viscous steady coiling regime ($\hat{H} < 0.08$) where gravity and inertia are negligible compared to viscous forces:

$$\hat{H} = h \left[\frac{g}{(\eta/\rho)^2} \right]^{\frac{1}{3}}, \quad (5-3)$$

where, the gravitational acceleration $g = 9.8$ m/s², the PC density $\rho = 1200$ kg/m³, so the deposition height h must be smaller than 6.3 mm in order to stay within the viscous steady coiling regime. We finally chose $h = 5$ mm ($\hat{H} = 0.0637$) for the fabrication of the fabric of microstructured fibers. Since the polymer thread is solidifying during the deposition process, the viscosity would increase, which makes the effective \hat{H} even smaller, ensuring deposition in the viscous steady coiling regime. With this deposition height, we measured the steady coiling radius $R_c = 1.8$ mm. We used the following geometric model that Brun et al.⁴⁸ developed for a molten glass sewing machine to approximately predict the pattern:

$$\begin{cases} r' = \cos\phi + \frac{v_m}{v_e} \cos\psi, & (5-4) \end{cases}$$

$$\begin{cases} r\psi' = \sin\phi - \frac{v_m}{v_e} \sin\psi, & (5-5) \end{cases}$$

$$\begin{cases} \phi' + \psi' = \frac{r}{R_c} \sin\left(\pi \sqrt{\frac{|\phi|}{\pi}} \frac{\phi}{|\phi|}\right) \sin\left(\frac{\pi}{\sqrt{2}}\right)^{-1}, & (5-6) \end{cases}$$

where, r , ψ , ϕ are the three geometric parameters that define the trace of the fiber-platform contact point with respect to the nozzle projection on the platform (Fig. 5.14). The relative moving speed $v_m = V_F$ (V_F is the feedrate parameter in the g-code that defines the relative moving speed between the starting point and ending point). Due to the negligible gravitational stretching⁶³, the steady coiling speed in the original model⁴⁷ was replaced by the extruding speed v_e , which is obtained by the following equation:

$$v_e = \frac{C_1 L_E V_F}{L_D} \left(\frac{D_{\text{filament}}}{C_2 d_{\text{nozzle}}} \right)^2, \quad (5-7)$$

where, the extruding length L_E of the filament (with the diameter $D_{\text{filament}} = 1.75$ mm) and the moving distance L_D between the starting point and ending point are parameters in the g-code. The volume flow rate correction factor C_1 represents the extruding efficiency and was calibrated at different volume flow rates (Note S4; Table 5.2; Fig. 5.15). We chose the volume flow rate $Q = L_E V_F \pi D_{\text{filament}}^2 / 4 L_D = 12.03 \text{ mm}^3/\text{s}$ for the fabrication of microstructured fibers, for which we established a correction factor $C_1 = 0.82$. The fiber expansion factor $C_2 = 1.09$ was measured at this volume flow rate for the nozzle diameter $d_{\text{nozzle}} = 0.4$ mm. The geometric model predicts the occurrence of alternating patterns in the speed ratio range $1.57 < v_e/v_m < 2.23$. We finally chose $v_e/v_m = 2.06$ for the fabrication of the alternating pattern, for the balance of high surface coverage and fabric printing easiness. The as-printed alternating fiber has a measured wavelength $\lambda = 11.8$ mm. Thus, the fiber separation l in both layers was set to 5.9 mm. After the deposition of the 1st layer, an offset was carefully calibrated for the 2nd layer fiber to be mostly deposited in-between the 1st layer loops. The straight fiber fabric was printed using the same g-code file in which only the deposition height h was set to 0.4 mm. No instability was involved under this deposition height. The weight of the straight fiber fabric equals to that of the alternating fiber fabric.

5.4.2 Composite fabrication

We used polydimethylsiloxane (Sylgard 184, Dow) and methylphenylsiloxane (OE-6550, Dow) as the low RI and high RI elastomers, respectively. For each elastomer, a vacuum chamber degassed the resin mixture, then we transferred the mixture to a 20 ml syringe. A micropump (78-8111C, Cole-Parmer) infiltrated the resin from the syringe into the bottom of the plastic mold (Fig. 5.16) via a Teflon tube. No bubbles were generated during the infiltration process. We selected the mold material based on the curing temperature of the elastomer: acrylic mold (glass transition temperature: 105 °C) for the low RI elastomer and PC mold (glass transition temperature: 147 °C) for the high RI elastomer. All the molds have the same cavity size of 100 × 100 × 1.5 mm (length × width × height). After the infiltration, an oven cured the low RI elastomer at 65 °C for 4 hours, and the high RI elastomer at 140 °C for 2 hours. We can easily peel the material off the plastic mold, without the need of demolding agent.

5.4.3 Optical characterization

A vertical ellipsometer (RC2, J.A. Woollam) measured the RI spectrum of the PC fiber and both elastomers (Fig. 5.5). To prepare the PC sample, we cut the filament into small pellets. Then a thermal compressing machine molded the pellets into a thin plate. We used the elastomer film made by the above-mentioned infiltration and curing process directly on the ellipsometer.

An ultraviolet-visible spectrometer (Lambda 1050, PerkinElmer) with a 150 mm integrating sphere acquired the optical transmittance⁵⁶ of the samples within the visible light spectrum (400 to 760 nm)⁶⁴. All test films have a thickness of 1.5 mm. The spectrometer measured the samples in transmittance with a reference beam collected in air. Each sample was tested in both total transmittance and diffuse transmittance. For the latter, we used a light trap at the reflectance port on the integrating sphere to exclude the normally transmitted light beam.

A high-speed camera (MotionBLITZ Cube4, Mikrotron) captured the printing of the fabric of alternating fibers at a frame rate of 2790 Hz in Fig. 5.2B and 5.2C. We used a Canon EOS Rebel T4i camera for the photography of the samples in this paper. The sunset pictures in Fig. 5.3 were taken with a standard zoom lens (Canon EF-S 18-135mm f/3.5-5.6) at 1 sec. exposure time and

f/5.6. The QR code pictures in Fig. 5.3 were taken with a macro lens (Canon EF 100mm f/2.8) at 1 sec. exposure time and f/5.6.

5.4.4 Mechanical characterization

An electromechanical machine (MTS Insight) tested the tensile properties of the single microstructured fiber reinforced composite and the fibers from each layer of the bidirectional fabric of alternating fibers with a crosshead speed of 500 mm/min. The former had a width of 5 mm, a thickness of 1.5 mm, and a gauge length of 32 mm. The latter had a gauge length of 51 mm and each fiber consisted of eight alternating loops.

We built a falling dart impact tester based on ASTM D1709⁶⁵. We scaled down the dart head diameter and the inner diameter of the annular clamp to 25.4 mm and 76.2 mm, respectively. A pneumatic clamp (G94, TestResources) dropped the dart into a guiding tube. We selected a drop height of 0.9 m and total drop weight of 0.568 kg to achieve the impact energy of 5 J. We integrated an electroresistive force sensor (A201-445N, Tekscan) into the falling dart (Fig. 5.17) to measure the contact force. We calibrated the force sensor under static loading. The sensor showed a linear response between the conductance and the applied force (Fig. 5.18). During the impact test, a digital multimeter (PCI-4070, National Instruments) and a LabVIEW program measured the conductance of the sensor at a sampling frequency of 6475 Hz. A high-speed camera (MotionBLITZ Cube4, Mikrotron) captured the dart motion during the impact at a frame rate of 2230 Hz. We wrote a MATLAB program to read the dart displacement from the high-speed camera snapshots (Fig. 5.19). We manually chose the initial contact frame from these snapshots and correlated the displacement with the contact force. This correlation was evaluated by the discrepancy δ between the impulse J and the momentum change Δp :

$$\delta = \left| \frac{J - \Delta p}{\Delta p} \right| \times 100\%, \quad (5-8)$$

where, the impulse $J = \int_0^t (F + mg) dt$ was calculated with the contact force-time curve from the LabVIEW measurements, the momentum change $\Delta p = mv_t - mv_0$ was calculated with the velocity measurements from the high-speed camera snapshots. The as-calculated discrepancy was within 20% for all test specimens.

Acknowledgements

We are thankful for the instruments access kindly provided by Prof. Nick Virgilio, Prof. Marie-Claude Heuzey, Prof. Eduardo-Antonio-Julian Ruiz, Prof. Thomas Gervais, and the technical advice from research associate Dr. Kambiz Chizari, technicians Christian-Charles Martel and Anic Desforges. We would like to specially thank Prof. Stéphane Étienne and Prof. Cédric Béguin for kindly lending us their high-speed camera, Dr. Bill Baloukas for the suggestions and discussions with optical tests and illustrations, technicians Yanik Landry-Ducharme and Bénédict Besner for the help with the hardware and software of the impact tester, respectively. We acknowledge the support of the Fonds de Recherche du Québec: Nature et Technologies (FRQNT), [funding reference number 63014], the Natural Sciences and Engineering Research Council of Canada (NSERC), [funding reference number 175791953], and the Canadian Foundation for Innovation.

References

1. Denny, M. (1976). The Physical Properties of Spider's Silk and Their Role in the Design of Orb-Webs. *Journal of Experimental Biology* 65, 483–506.
2. Gosline, J.M., Guerette, P.A., Ortlepp, C.S., and Savage, K.N. (1999). The mechanical design of spider silks: from fibroin sequence to mechanical function. *Journal of Experimental Biology* 202, 3295–3303.
3. Kelly, S.P., Sensenig, A., Lorentz, K.A., and Blackledge, T.A. (2011). Damping capacity is evolutionarily conserved in the radial silk of orb-weaving spiders. *Zoology* 114, 233–238.
4. Ker, R. (2007). Mechanics of tendon, from an engineering perspective. *International Journal of Fatigue* 29, 1001–1009.
5. Bennett, M.B., Ker, R.F., Imery, N.J., and Alexander, R.McN. (1986). Mechanical properties of various mammalian tendons. *Journal of Zoology* 209, 537–548.
6. Gosline, J.M., DeMont, M.E., and Denny, M.W. (1986). The structure and properties of spider silk. *Endeavour* 10, 37–43.

7. Eles, P.T., and Michal, C.A. (2004). Strain Dependent Local Phase Transitions Observed during Controlled Supercontraction Reveal Mechanisms in Spider Silk. *Macromolecules* *37*, 1342–1345.
8. Sensenig, A.T., Lorentz, K.A., Kelly, S.P., and Blackledge, T.A. (2012). Spider orb webs rely on radial threads to absorb prey kinetic energy. *J. R. Soc. Interface* *9*, 1880–1891.
9. van Beek, J.D., Hess, S., Vollrath, F., and Meier, B.H. (2002). The molecular structure of spider dragline silk: Folding and orientation of the protein backbone. *Proceedings of the National Academy of Sciences* *99*, 10266–10271.
10. Nova, A., Keten, S., Pugno, N.M., Redaelli, A., and Buehler, M.J. (2010). Molecular and Nanostructural Mechanisms of Deformation, Strength and Toughness of Spider Silk Fibrils. *Nano Lett.* *10*, 2626–2634.
11. Fantner, G.E., Oroudjev, E., Schitter, G., Golde, L.S., Thurner, P., Finch, M.M., Turner, P., Gutschmann, T., Morse, D.E., Hansma, H., et al. (2006). Sacrificial Bonds and Hidden Length: Unraveling Molecular Mesostuctures in Tough Materials. *Biophysical Journal* *90*, 1411–1418.
12. Sun, J.-Y., Zhao, X., Illeperuma, W.R.K., Chaudhuri, O., Oh, K.H., Mooney, D.J., Vlassak, J.J., and Suo, Z. (2012). Highly stretchable and tough hydrogels. *Nature* *489*, 133–136.
13. Sun, T.L., Kurokawa, T., Kuroda, S., Ihsan, A.B., Akasaki, T., Sato, K., Haque, Md.A., Nakajima, T., and Gong, J.P. (2013). Physical hydrogels composed of polyampholytes demonstrate high toughness and viscoelasticity. *Nature Mater* *12*, 932–937.
14. Luo, F., Sun, T.L., Nakajima, T., Kurokawa, T., Zhao, Y., Sato, K., Ihsan, A.B., Li, X., Guo, H., and Gong, J.P. (2015). Oppositely Charged Polyelectrolytes Form Tough, Self-Healing, and Rebuildable Hydrogels. *Adv. Mater.* *27*, 2722–2727.
15. Ducrot, E., Chen, Y., Bulters, M., Sijbesma, R.P., and Creton, C. (2014). Toughening Elastomers with Sacrificial Bonds and Watching Them Break. *Science* *344*, 186–189.
16. Wu, J., Cai, L.-H., and Weitz, D.A. (2017). Tough Self-Healing Elastomers by Molecular Enforced Integration of Covalent and Reversible Networks. *Adv. Mater.* *29*, 1702616.

17. Filippidi, E., Cristiani, T.R., Eisenbach, C.D., Waite, J.H., Israelachvili, J.N., Ahn, B.K., and Valentine, M.T. (2017). Toughening elastomers using mussel-inspired iron-catechol complexes. *Science* 358, 502–505.
18. Wang, Z., Xiang, C., Yao, X., Le Floch, P., Mendez, J., and Suo, Z. (2019). Stretchable materials of high toughness and low hysteresis. *Proc Natl Acad Sci USA* 116, 5967–5972.
19. Guo, S.-Z., Gosselin, F., Guerin, N., Lanouette, A.-M., Heuzey, M.-C., and Therriault, D. (2013). Solvent-Cast Three-Dimensional Printing of Multifunctional Microsystems. *Small* 9, 4118–4122.
20. Pugno, N.M. (2014). The “Egg of Columbus” for Making the World’s Toughest Fibres. *PLoS ONE* 9, e93079.
21. Passieux, R., Guthrie, L., Rad, S.H., Lévesque, M., Therriault, D., and Gosselin, F.P. (2015). Instability-Assisted Direct Writing of Microstructured Fibers Featuring Sacrificial Bonds. *Adv. Mater.* 27, 3676–3680.
22. Zhu, F., Cheng, L., Wang, Z.J., Hong, W., Wu, Z.L., Yin, J., Qian, J., and Zheng, Q. (2017). 3D-Printed Ultratough Hydrogel Structures with Titin-like Domains. *ACS Appl. Mater. Interfaces* 9, 11363–11367.
23. Zou, S., Therriault, D., and Gosselin, F.P. (2018). Failure mechanisms of coiling fibers with sacrificial bonds made by instability-assisted fused deposition modeling. *Soft Matter* 14, 9777–9785.
24. Wu, Q., Zou, S., Gosselin, F.P., Therriault, D., and Heuzey, M.-C. (2018). 3D printing of a self-healing nanocomposite for stretchable sensors. *J. Mater. Chem. C* 6, 12180–12186.
25. Wei, H., Cauchy, X., Navas, I.O., Abderrafai, Y., Chizari, K., Sundararaj, U., Liu, Y., Leng, J., and Therriault, D. (2019). Direct 3D Printing of Hybrid Nanofiber-Based Nanocomposites for Highly Conductive and Shape Memory Applications. *ACS Appl. Mater. Interfaces* 11, 24523–24532.
26. Cooper, C.B., Joshipura, I.D., Parekh, D.P., Norkett, J., Mailen, R., Miller, V.M., Genzer, J., and Dickey, M.D. (2019). Toughening stretchable fibers via serial fracturing of a metallic core. *Sci. Adv.* 5, eaat4600.

27. King, D.R., Okumura, T., Takahashi, R., Kurokawa, T., and Gong, J.P. (2019). Macroscale Double Networks: Design Criteria for Optimizing Strength and Toughness. *ACS Appl. Mater. Interfaces* *11*, 35343–35353.
28. Koebley, S.R., Vollrath, F., and Schniepp, H.C. (2017). Toughness-enhancing metastructure in the recluse spider's looped ribbon silk. *Mater. Horiz.* *4*, 377–382.
29. Magrini, T., Bouville, F., Lauria, A., Le Ferrand, H., Niebel, T.P., and Studart, A.R. (2019). Transparent and tough bulk composites inspired by nacre. *Nat Commun* *10*, 2794.
30. Petty, G.W. (2006). *A first course in atmospheric radiation* (Sundog Pub).
31. Kendall, M.J., and Siviour, C.R. (2014). Experimentally simulating high-rate behaviour: rate and temperature effects in polycarbonate and PMMA. *Phil. Trans. R. Soc. A* *372*, 20130202.
32. Gauthier, M.M. (1995). Optical Testing of Polymers. In *Engineered Materials Handbook Desk Edition*, M.M. Gauthier, ed. (ASM International), pp. 439–443.
33. Coogan, T.J., and Kazmer, D.O. (2019). In-line rheological monitoring of fused deposition modeling. *Journal of Rheology* *63*, 141–155.
34. Maleki, M., Habibi, M., Golestanian, R., Ribe, N.M., and Bonn, D. (2004). Liquid Rope Coiling on a Solid Surface. *Phys. Rev. Lett.* *93*, 214502.
35. Ribe, N.M., Habibi, M., and Bonn, D. (2012). Liquid Rope Coiling. *Annu. Rev. Fluid Mech.* *44*, 249–266.
36. Lin, S., Cao, C., Wang, Q., Gonzalez, M., Dolbow, J.E., and Zhao, X. (2014). Design of stiff, tough and stretchy hydrogel composites via nanoscale hybrid crosslinking and macroscale fiber reinforcement. *Soft Matter* *10*, 7519–7527.
37. King, D.R., Sun, T.L., Huang, Y., Kurokawa, T., Nonoyama, T., Crosby, A.J., and Gong, J.P. (2015). Extremely tough composites from fabric reinforced polyampholyte hydrogels. *Mater. Horiz.* *2*, 584–591.
38. Huang, Y., King, D.R., Cui, W., Sun, T.L., Guo, H., Kurokawa, T., Brown, H.R., Hui, C.-Y., and Gong, J.P. (2019). Superior fracture resistance of fiber reinforced polyampholyte

- hydrogels achieved by extraordinarily large energy-dissipative process zones. *J. Mater. Chem. A* *7*, 13431–13440.
39. Feng, X., Ma, Z., MacArthur, J.V., Giuffre, C.J., Bastawros, A.F., and Hong, W. (2016). A highly stretchable double-network composite. *Soft Matter* *12*, 8999–9006.
40. Chang, R., Chen, Z., Yu, C., and Song, J. (2019). An Experimental Study on Stretchy and Tough PDMS/Fabric Composites. *Journal of Applied Mechanics* *86*, 011012.
41. Zhao, X. (2014). Multi-scale multi-mechanism design of tough hydrogels: building dissipation into stretchy networks. *Soft Matter* *10*, 672–687.
42. Morris, S.W., Dawes, J.H.P., Ribe, N.M., and Lister, J.R. (2008). Meandering instability of a viscous thread. *Physical Review E* *77*, 066218.
43. Brun, P.-T., Ribe, N.M., and Audoly, B. (2012). A numerical investigation of the fluid mechanical sewing machine. *Physics of Fluids* *24*, 043102.
44. Chiu-Webster, S., and Lister, J.R. (2006). The fall of a viscous thread onto a moving surface: a ‘fluid-mechanical sewing machine.’ *Journal of Fluid Mechanics* *569*, 89.
45. Klein, J., Stern, M., Franchin, G., Kayser, M., Inamura, C., Dave, S., Weaver, J.C., Houk, P., Colombo, P., Yang, M., et al. (2015). Additive Manufacturing of Optically Transparent Glass. *3D Printing and Additive Manufacturing* *2*, 92–105.
46. Jawed, M.K., Da, F., Joo, J., Grinspun, E., and Reis, P.M. (2014). Coiling of elastic rods on rigid substrates. *Proceedings of the National Academy of Sciences* *111*, 14663–14668.
47. Brun, P.-T., Audoly, B., Ribe, N.M., Eaves, T.S., and Lister, J.R. (2015). Liquid Ropes: A Geometrical Model for Thin Viscous Jet Instabilities. *Phys. Rev. Lett.* *114*, 174501.
48. Brun, P.-T., Inamura, C., Lizardo, D., Franchin, G., Stern, M., Houk, P., and Oxman, N. (2017). The molten glass sewing machine. *Phil. Trans. R. Soc. A* *375*, 20160156.
49. Jawed, M.K., Brun, P.-T., and Reis, P.M. (2015). A Geometric Model for the Coiling of an Elastic Rod Deployed Onto a Moving Substrate. *Journal of Applied Mechanics* *82*, 121007.

50. Li, J., Kong, T., Yu, J., Lee, K.H., Tang, Y.H., Kwok, K.-W., Kim, J.T., and Shum, H.C. (2019). Electrocoiling-guided printing of multiscale architectures at single-wavelength resolution. *Lab Chip* 19, 1953–1960.
51. Lipton, J.I., and Lipson, H. (2016). 3D Printing Variable Stiffness Foams Using Viscous Thread Instability. *Sci Rep* 6, 29996.
52. Wang, D., Jing, L., Liu, H., Huang, D., and Sun, J. (2019). Microscale scaffolds with diverse morphology via electrohydrodynamic jetting for *in vitro* cell culture application. *Biomed. Phys. Eng. Express* 5, 025011.
53. Yin, Z., Hannard, F., and Barthelat, F. (2019). Impact-resistant nacre-like transparent materials. *Science* 364, 1260–1263.
54. Chen, R., Liu, J., Yang, C., Weitz, D.A., He, H., Li, D., Chen, D., Liu, K., and Bai, H. (2019). Transparent Impact-Resistant Composite Films with Bioinspired Hierarchical Structure. *ACS Appl. Mater. Interfaces* 11, 23616–23622.
55. Hébert, M., Hersch, R.D., and Emmel, P. (2014). Fundamentals of Optics and Radiometry for Color Reproduction. In *Handbook of Digital Imaging*, M. Kriss, ed. (John Wiley & Sons, Ltd), pp. 1–57.
56. ASTM. ASTM D1003 - 13. Standard Test Method for Haze and Luminous Transmittance of Transparent Plastics. <https://www.astm.org/Standards/D1003>.
57. Piorkowski, D., Blackledge, T.A., Liao, C.-P., Joel, A.-C., Weissbach, M., Wu, C.-L., and Tso, I.-M. (2020). Uncoiling springs promote mechanical functionality of spider cribellate silk. *J Exp Biol* 223, jeb215269.
58. Choe, Y.E., and Kim, G.H. (2020). A PCL/cellulose coil-shaped scaffold *via* a modified electrohydrodynamic jetting process. *Virtual and Physical Prototyping* 1–14.
59. Wang, D., Xu, J., Chen, J., Hu, P., Wang, Y., Jiang, W., and Fu, J. (2020). Transparent, Mechanically Strong, Extremely Tough, Self-Recoverable, Healable Supramolecular Elastomers Facilely Fabricated via Dynamic Hard Domains Design for Multifunctional Applications. *Adv. Funct. Mater.* 30, 1907109.

60. Zhao, H., O'Brien, K., Li, S., and Shepherd, R.F. (2016). Optoelectronically innervated soft prosthetic hand via stretchable optical waveguides. *Sci. Robot. 1*, eaai7529.
61. Leber, A., Cholst, B., Sandt, J., Vogel, N., and Kolle, M. (2018). Stretchable Thermoplastic Elastomer Optical Fibers for Sensing of Extreme Deformations. *Adv. Funct. Mater.* 1802629.
62. Rifaie-Graham, O., Apebende, E.A., Bast, L.K., and Bruns, N. (2018). Self-Reporting Fiber-Reinforced Composites That Mimic the Ability of Biological Materials to Sense and Report Damage. *Adv. Mater.* 30, 1705483.
63. Yuk, H., and Zhao, X. (2018). A New 3D Printing Strategy by Harnessing Deformation, Instability, and Fracture of Viscoelastic Inks. *Adv. Mater.* 30, 1704028.
64. ASTM. ASTM E2297 - 15. Standard Guide for Use of UV-A and Visible Light Sources and Meters used in the Liquid Penetrant and Magnetic Particle Methods. <https://www.astm.org/Standards/E2297>.
65. ASTM. ASTM D1709 - 16ae1. Standard Test Methods for Impact Resistance of Plastic Film by the Free-Falling Dart Method. <https://www.astm.org/Standards/D1709>.
66. Johnston, I.D., McCluskey, D.K., Tan, C.K.L., and Tracey, M.C. (2014). Mechanical characterization of bulk Sylgard 184 for microfluidics and microengineering. *J. Micromech. Microeng.* 24, 035017.
67. Christopher Love, J., Wolfe, D., and Whitesides, G. (2004). Nanostructures Replicated by Polymer Molding. In *Dekker Encyclopedia of Nanoscience and Nanotechnology*, Second Edition - Six Volume Set (Print Version), J. Schwarz, and C. Contescu, eds. (CRC Press), pp. 2657–2666.
68. Dow Corning (2010). Dow Corning® 184 Silicone Elastomer. <https://www.dow.com/content/dam/dcc/documents/en-us/productdatasheet/11/11-31/11-3184-sylgard-184-elastomer.pdf>.
69. Dow Corning (2013). Dow Corning® OE-6550 Optical Encapsulant. https://samaro.fr/pdf/FT/DOW_CORNING_ELECTRONICS_FT_OE-6550.pdf.

5.5 Supporting information

5.5.1 Refractive index of the materials

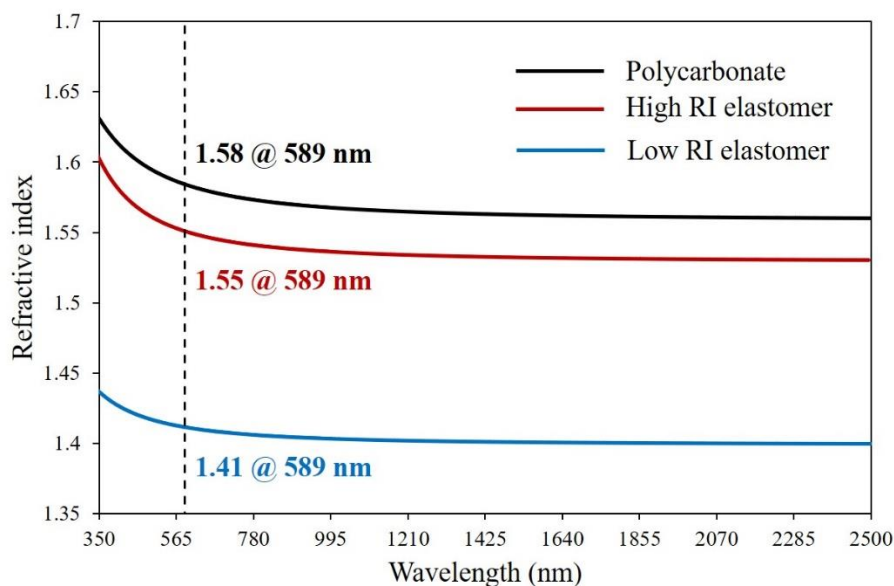


Figure 5.5 Ellipsometry analysis of the polycarbonate, high RI elastomer and low RI elastomer. The refractive index was obtained by the Cauchy model from 350 to 2500 nm.

5.5.2 Properties of the two elastomers

Table 5.1 Comparison of the physical and mechanical properties of the low RI⁶⁶⁻⁶⁸ and high RI⁶⁹ elastomer.

	Low RI elastomer (Sylgard 184)	High RI elastomer (OE-6550)
Refractive index	1.41 @589 nm	1.55 @589 nm
Viscosity (Mixed, cP)	3500	3800
Coefficient of linear thermal expansion (ppm/°C)	260 – 310 ⁶⁷	210

Young's Modulus (MPa)	1.32 – 2.97 ⁶⁶	5.1
Tensile strength (MPa)	3.51 – 7.65 ⁶⁶	1.3
Elongation at break (%)	50 – 93 ⁶⁶	75
Hardness	Shore A, 44 – 54	Shore A, 55

5.5.3 Two-layer fiber fabric based on Brun et al.'s model

Note S1. Two-layer fiber fabric based on Brun et al.'s model.

Based on Brun et al.'s model described in the Experimental Procedures of the paper, we first generated the geometry of a single fiber and then manually aligned them to a 2D array in Fig. 5.6. This way we are able to see how much the 2nd layer loops fall on top of the 1st layer loops. At a smaller speed ratio, the alternating pattern has a larger wavelength, making it easier for the 2nd layer loops to avoid falling on top of the 1st layer loops (Fig. 5.6a). But the surface coverage of the fiber is low due to the large wavelength. At a higher speed ratio which leads to coiling pattern, the 2nd layer loops always fall on top of the 1st layer loops (Fig. 5.6d). This will cause highly distorted fibers in the 2nd layer due to the 3D structure of the 1st layer loops in a real experiment. Therefore, we selected the alternating pattern with a wavelength as small as possible, in order to achieve a high surface coverage, as well as the fully functional sacrificial bonds and hidden lengths system in both layers.

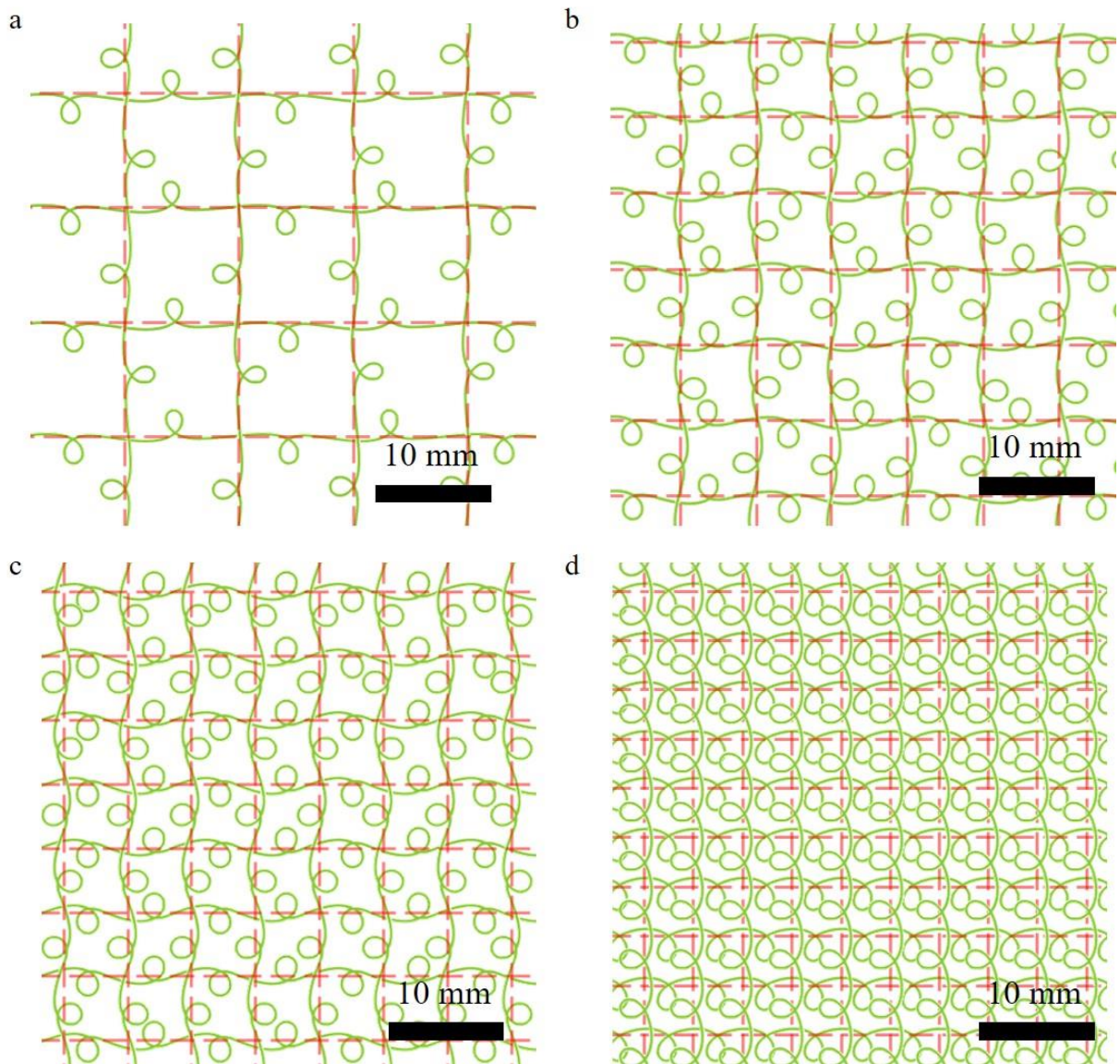


Figure 5.6 An ideal thought experiment of two-layer fiber fabric based on Brun et al.'s model. The single fiber pattern is generated at a speed ratio $v_c/v_m =$: **a**, 1.6; **b**, 1.9; **c**, 2.1; **d**, 2.4. Then the fiber was manually aligned to a 2D array (red dashed lines) with a unit size equalling to the distance between adjacent loops along the fiber. The steady coiling radius $R_c = 1.8$ mm was used for all calculations. The three ordinary differential equations in the model were solved via the ode23 function in MATLAB, with initial conditions $[r, \psi, \phi] = [1, 0, 3\pi/4]$.

5.5.4 Matrix-fiber debonding

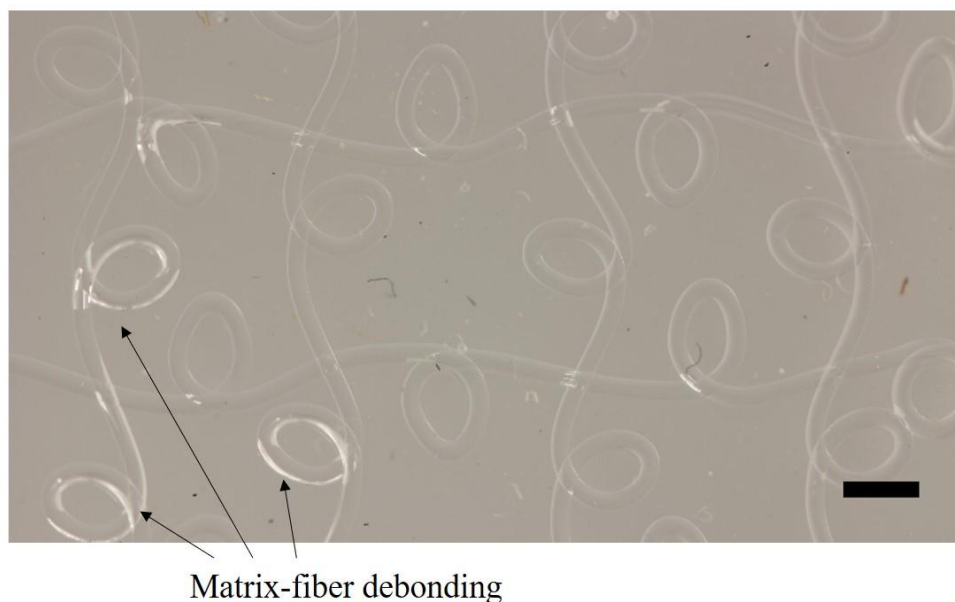


Figure 5.7 Matrix-fiber debonding due to thermal expansion in the alternating fiber composite film with the high RI elastomer. The composite was cured at 140 °C for 2 hours. The photo was taken after the cooling down of the composite. The scale bar is 2 mm.

5.5.5 Static puncture test

Note S2. Static puncture test of different transparent films based on the low RI elastomer.

In order to evaluate the total energy to puncture of different specimens, we conducted the static puncture test on an electromechanical machine (MTS Insight). The puncture head diameter (25.4 mm) and the inner diameter of the annular clamp (76.2 mm) are the same as those on the impact tester. The puncture head was covered with a P60 grade sandpaper and moved at a speed of 10 mm/min. Based on the low RI elastomer (Sylgard 184), pure elastomer film, straight fiber composite film, alternating fiber composite film and hybrid fiber composite film were fabricated as mentioned in the Experimental Procedures section and all have a thickness of 1.5 mm. The specimen was clamped by two acrylic plates (thickness: 12.7 mm) and tightened by 12 screws around it to avoid slipping inside the clamps.

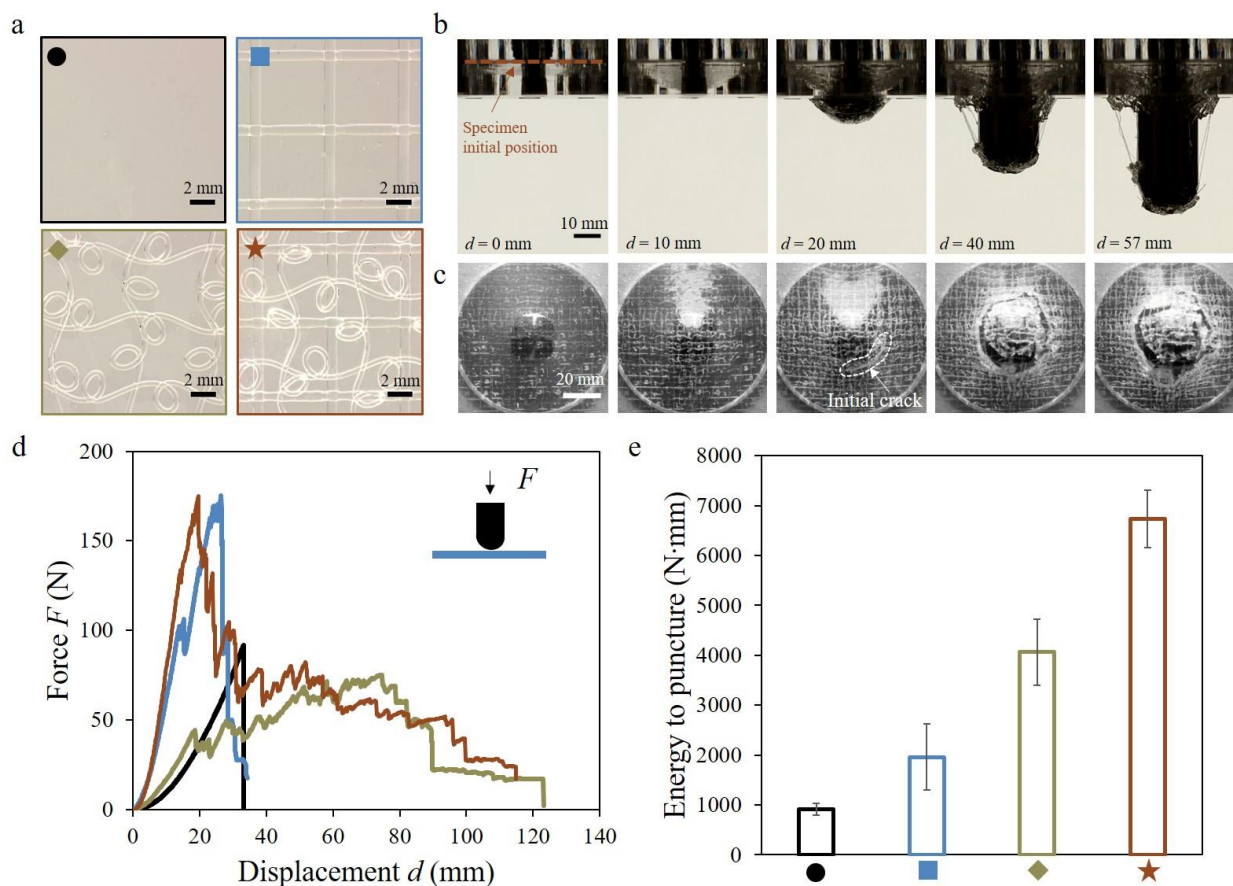


Figure 5.8 Static puncture test of different transparent films based on the low RI elastomer. **a**, Optical images of the pure elastomer film (black circle), straight fiber composite film (blue square), alternating fiber composite film (green diamond) and hybrid fiber composite film (red star). **b**, Front view and **c**, Bottom view of the static puncture test of a hybrid fiber composite specimen. **d**, Representative force-displacement curves for the pure elastomer film (black curve), straight fiber composite film (blue curve), alternating fiber composite film (green curve) and hybrid fiber composite film (red curve). **e**, Energy to puncture calculated by the integration of the force-displacement curve. Three repeats were conducted for each specimen, and the standard deviation was plotted as the error bar. All tests were conducted with a puncture head covered with a P60 grade sandpaper.

5.5.6 Contact force-time curves from the impact tests

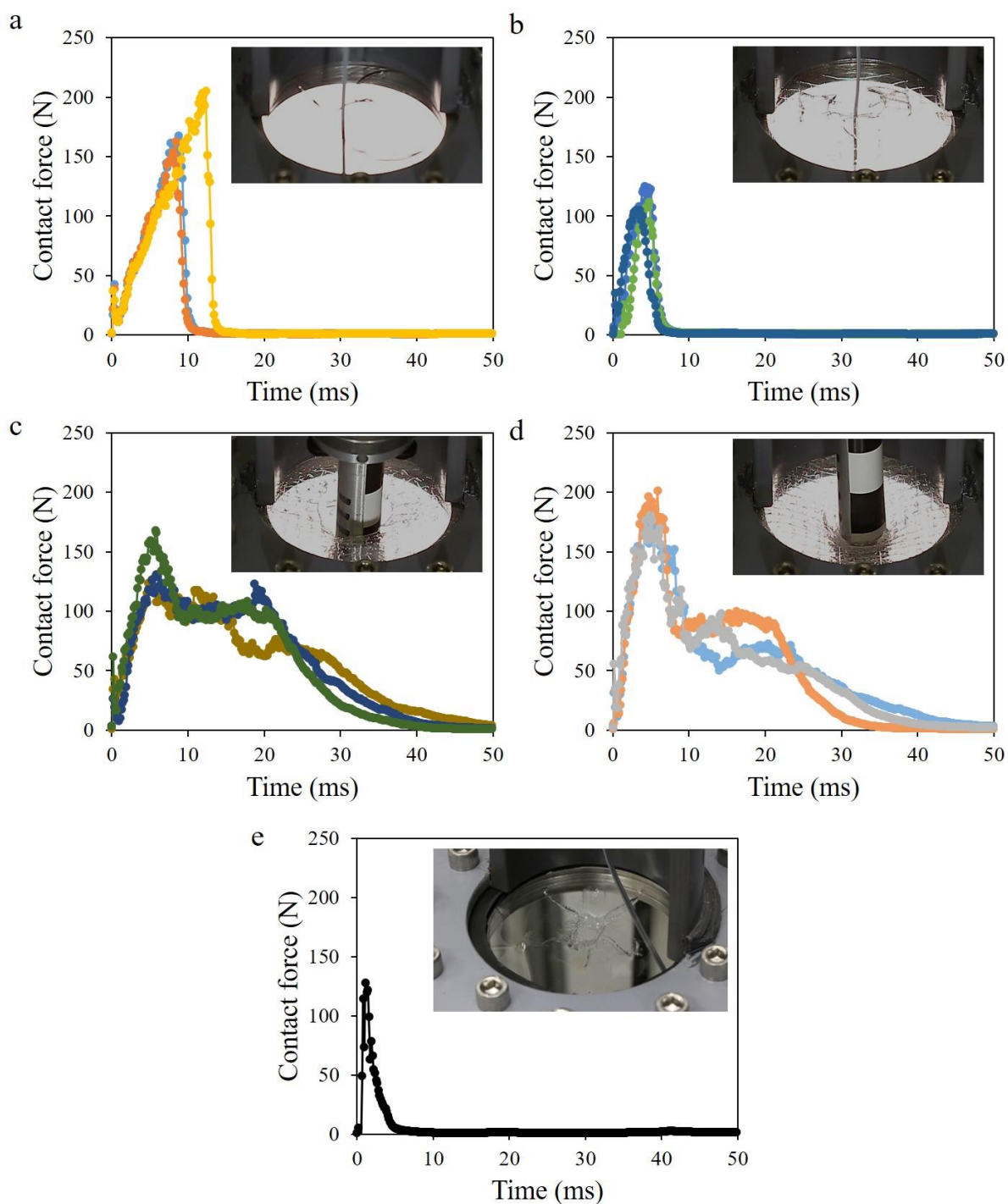


Figure 5.9 Contact force-time curves of different transparent films from the falling dart impact test. **a**, Elastomer film; **b**, Straight fiber composite film; **c**, Alternating fiber composite film; **d**, Hybrid

fiber composite film; **e**, Polycarbonate (PC) film. The images of the films after the test are shown in the insets. The test was repeated three times in **a-d**. The dart penetrated all test films in **a** and **b**, but was successfully caught by all test films in **c** and **d**, due to the high energy dissipation of the architected composites. All test films have a length of 100 mm and width of 100 mm. The test films in **a-d** are all based on the low RI elastomer and have a thickness of 1.5 mm. The PC film (McMaster-Carr, 85585K102) in **e** has a thickness of 0.127 mm. The weight of the test PC film is 1.524 g, which is even more than the weight of the fabric of alternating fibers (1.333 g) in **c**. The fact that the dart penetrated both the elastomer film and PC film, but was caught by the alternating fiber composite film, proves the dominating contribution from the composite architecture to the high energy dissipation over the material components.

5.5.7 Optical images of fractured specimens

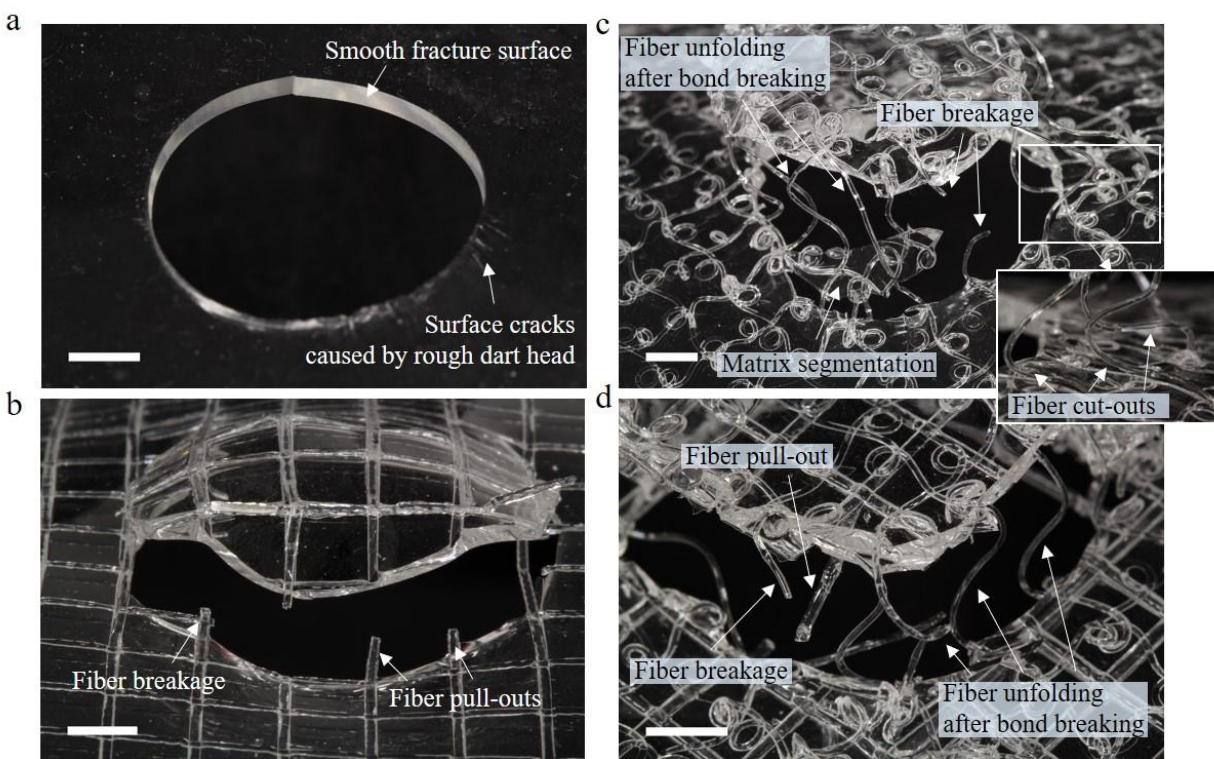


Figure 5.10 Optical images of fractured transparent films after impact test. **a**, Elastomer film; **b**, Straight fiber composite film; **c**, Alternating fiber composite film; **d**, Hybrid fiber composite film. The inset in **c** shows a close view of the fiber cut-outs. All scale bars are 5 mm.

5.5.8 Cyclic tests of alternating fiber composite specimens

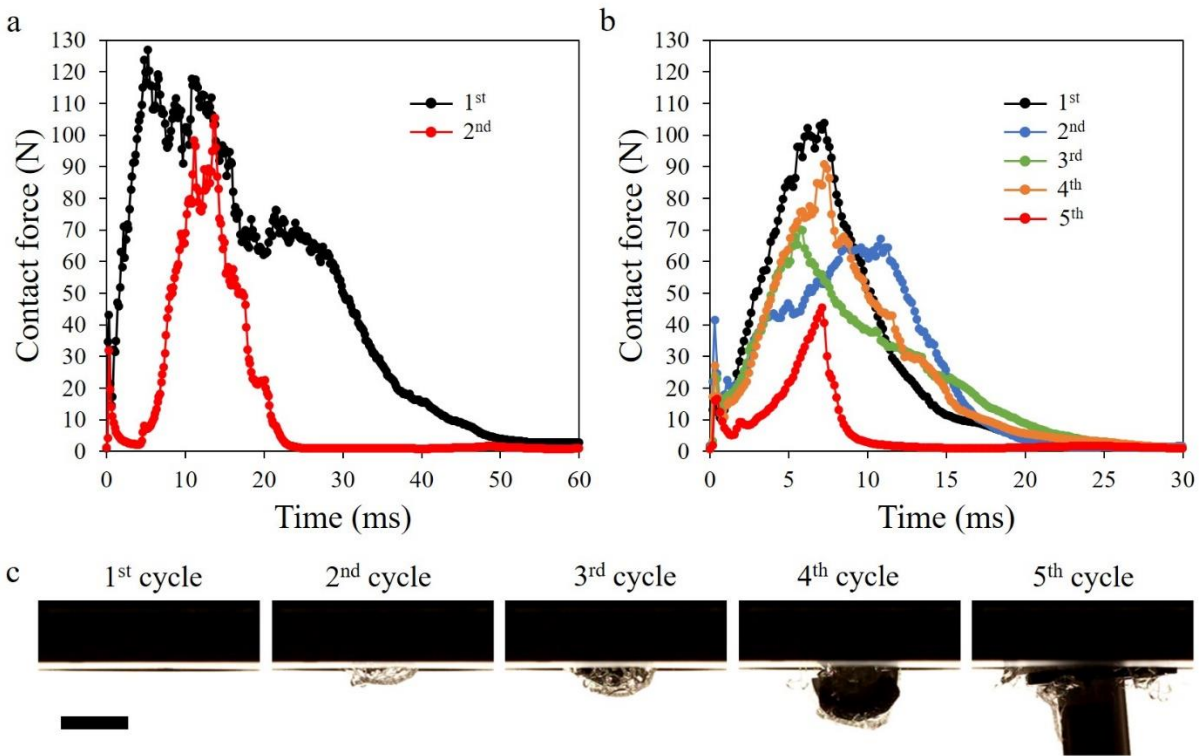


Figure 5.11 Cyclic impact test of the alternating fiber composite film based on the low RI elastomer. Two specimens were tested at different impact energy levels: **a**, 5 J and **b**, 1.4 J, respectively. **c**, Snapshots of the specimen at the end of each cycle of the impact test at 1.4J. For the impact test at 5J, the snapshots of the 1st cycle can be seen in Figure 4I. The same drop height (0.9 m) was used in both tests, leading to an impact velocity of 4.2 m/s. To achieve the corresponding impact energy level, the drop weight was 0.568 kg in **a**, and 0.158 kg in **b**. The drop weight fell on the same location on the specimen during the cyclic test. The drop weight fully penetrated the specimen in the 2nd cycle in **a**, and the 5th cycle in **b**. The scale bar is 20 mm.

5.5.9 Impact behavior of low RI and high RI elastomer composites

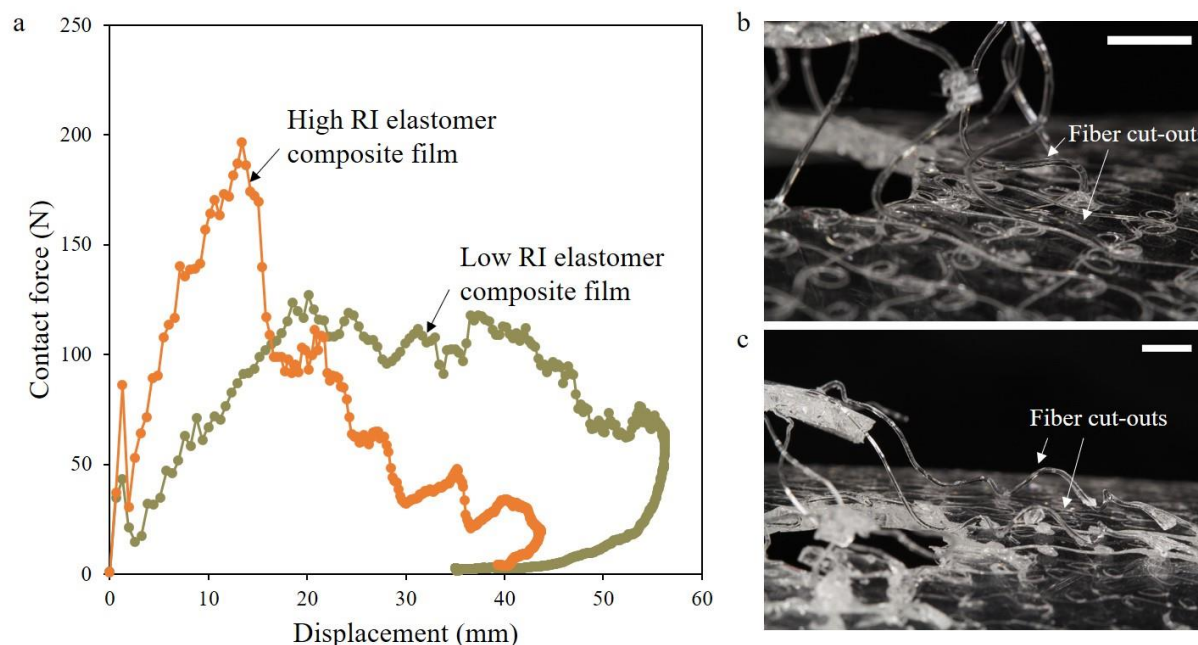


Figure 5.12 Comparison of the impact absorption performance between the alternating fiber composite films made from the low RI elastomer and high RI elastomer. **a.** Contact-displacement curves; **b.** Optical image of the fractured low RI elastomer composite film; **c.** Optical image of the fractured high RI elastomer composite film. Both specimens were tested with an impact energy of 5 J and impact velocity of 4.2 m/s. All scale bars are 5 mm.

5.5.10 Optical sensing

Note S3. Optical strain sensor based on the transparent composite from the low RI elastomer.

In the as-fabricated composite in our study, the polycarbonate core has a higher RI than the elastomer matrix, making the composite an optical waveguide with strain sensing functionality. In order to demonstrate this functionality, we used the low RI elastomer (Sylgard 184) as the matrix, and the microstructured polycarbonate fiber (printed by 1 mm nozzle) as the core. We made two different optical waveguides with the meandering fiber-elastomer composite and alternating fiber-elastomer composite.

In the sensing system (Fig. 5.13A), a red LED was connected to one end of the waveguide. We use aluminium foils seal the connection and prevent the light from transmitting into the matrix. A photoresistor was connected to the other end of the waveguide to measure the light transmission through the meandering fiber. The resistance of the photoresistor decreases when the light intensity increases. As demonstrated by the meandering fiber waveguide in Fig. 5.13A, when the LED is off, the photoresistor has a very large resistance (1.041 M Ω). When the LED is on and the sensor is at rest, the resistance of the photoresistor decreases to 224.5 k Ω . When the sensor is stretched by hand, the resistance further decreases to 185.0 k Ω , indicating a light transmission increase under stretching. We believe that this light transmission increase is due to the straightening of the meandering fiber, which results in less reflectance by the matrix-fiber interfaces and thus more transmittance. We further tested the sensor's repeatability through cyclic tensile test (Fig. 5.13B). The sample was clamped with a constant force of 100N at both ends by a pair of pneumatic grips (TestResources G94). The initial gauge length was 80 mm. A cyclic displacement of 5 mm was applied at 0.017 Hz with a constant speed of 10 mm/min for a total of 105 cycles. We measured the resistance change of the photoresistor with an inverting operational amplifier (Fig. 5.13C) and acquired the output voltage at 100 Hz by an Arduino Uno with an Adafruit SD card data logger (Library: AnalogBinLogger). As shown in Fig. 5.13D, the meandering fiber waveguide shows a very good repeatability under cyclic loading.

Under stretching, the alternating fiber waveguide shows a more complex behavior (Fig. 5.13E). As explained in Figure 1C in the paper, there are four regimes during the tensile test of the alternating fiber composite. The light transmission shows a short increase during regime I, probably due to the straightening of the curved fiber segment between each sacrificial bond. In regime II, the sacrificial bonds break inside the matrix, the light path thus becomes longer and causes more reflectance and thus transmission loss. Also, the fiber detaches from the matrix, so the relative RI n^* increases from $n_{\text{fiber}}/n_{\text{matrix}} = 1.12$ to $n_{\text{fiber}}/n_{\text{air}} = 1.58$, causing more reflectance according to Fresnel's formula. In regime III, the matrix cracks and the alternating loop is unfolded, the plastic deformation of the fiber possibly further contributes to the light transmission loss. Because the alternating fiber waveguide shows a light transmission change spanning in a much larger range, we measured the resistance of the photoresistor with an electrometer (6517B, Keithley) at 50V. This test was conducted in a dark environment in order to prevent the environmental light from blocking the low

transmission in the waveguide under large deformation. The transmission was calculated by $\log_{10}(I/I_0)$, where I is the measured current from the electrometer.

Under stretching, the meandering fiber waveguide and alternating fiber waveguide show a linear light transmission increase and light transmission loss, respectively. This strain sensing functionality can be integrated into the transparent impact-absorbing composite for impact protection and damage detection applications.

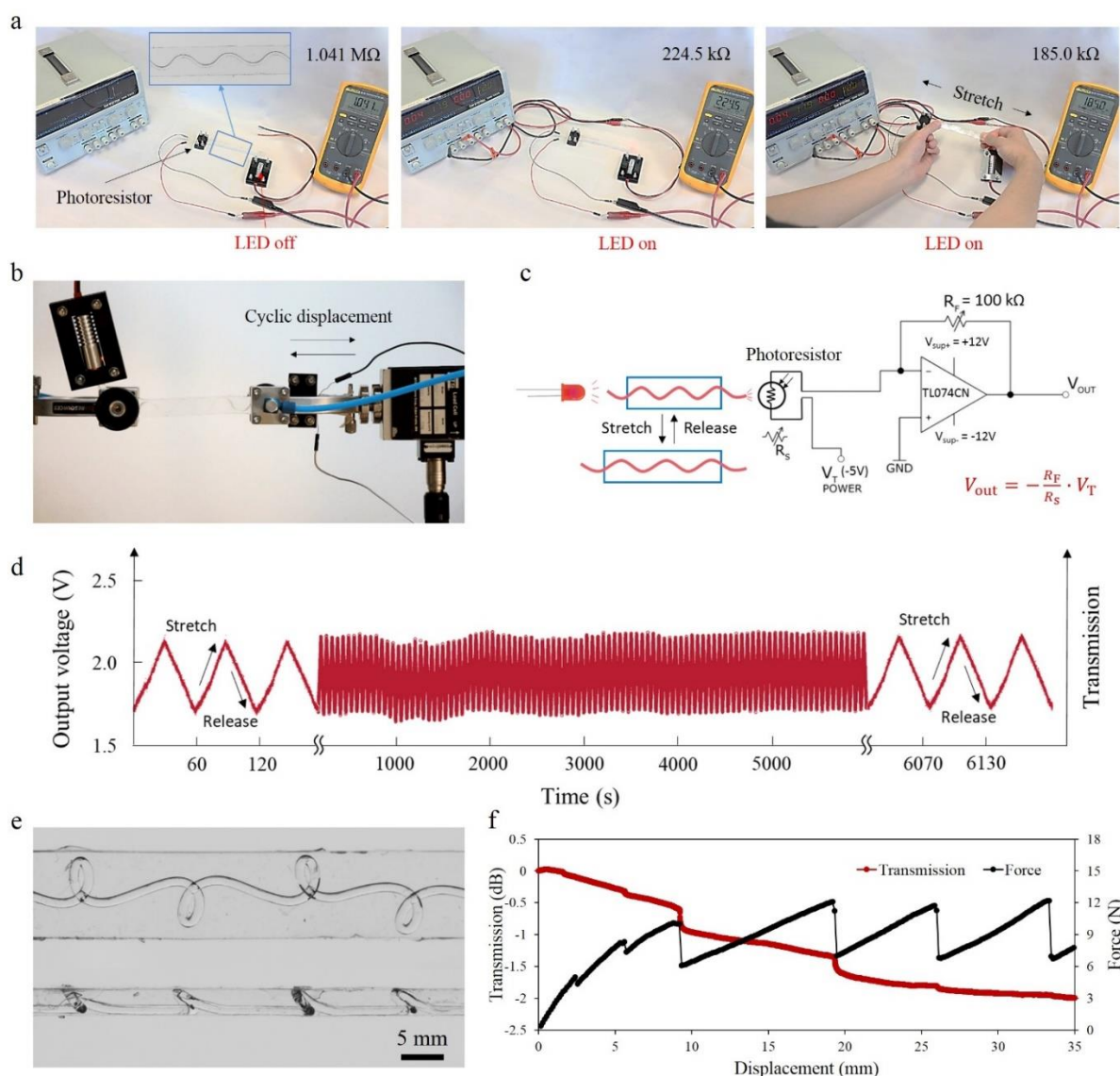


Figure 5.13 Optical waveguides made from the transparent composites based on the low RI elastomer. **a**, Demonstration of the strain sensing with the meandering fiber composite waveguide.

b, Cyclic tensile test of the meandering fiber composite waveguide. **c**, Design of the electric circuit to measure the resistance of the photoresistor during the tensile cyclic test. **d**, Measured output voltage under the cyclic tensile test. Under stretching, more light was transmitted through the waveguide to the photoresistor, resulting in the decrease of the resistance and the increase of the circuit output voltage. **e**, Optical images (top view and side view) of the alternating fiber composite waveguide. **f**, The light transmission loss of the alternating fiber composite waveguide under uniaxial tensile test (gauge length: 45 mm; crosshead speed: 5 mm/min). The force-displacement curve is similar as Figure 1C and has been explained in the paper.

5.5.11 Geometric model by Brun et al.

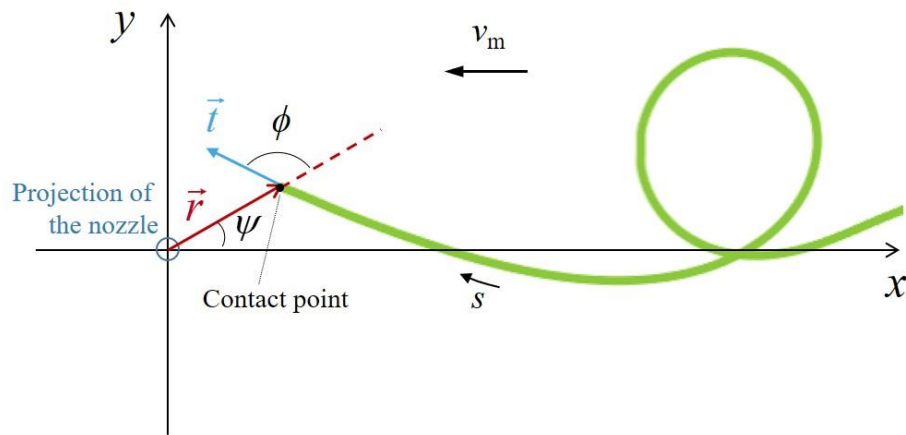


Figure 5.14 Schematic of the deposition trace with respect to the projection of the nozzle. The speed v_m is the horizontal moving speed of the extruder relative to the printing bed. The vector \vec{r} represents the position of the fiber-platform contact point regarding to the nozzle's projection point. The angle ψ is measured between the vector \vec{r} and the x axis (direction of the relative moving speed v_m). The angle ϕ is measured between the vector \vec{r} and the tangent vector \vec{t} of the polymer thread at the contact point. These three geometric parameters are functions of the Lagrangian coordinate s which is a time-like variable and represents the arc length along the deposition trace. The coordinates of the deposited trace can be reconstructed by the solution of the geometric model: $x(s) = r(s) \cdot \cos [\psi(s)] + v_m(s_{\text{last}} - s)/v_e$, $y(s) = r(s) \cdot \sin [\psi(s)]$ (s_{last} is the last point from the solution). This schematic was modified from Brun et al.'s work⁴⁸.

5.5.12 Volume flow rate calibration on the Prusa printer

Note S4. Volume flow rate calibration on the Prusa 3D printer.

The theoretical volume flow rate can be calculated by the following equation:

$$Q = \frac{L_E V_F \pi D_{\text{filament}}^2}{L_D 4}, \quad (5-9)$$

where, L_D is the moving distance of the printing head between the starting point and the ending point, L_E is the extruding length of the 1.75 mm filament from the starting point and the ending point, V_F is the feedrate that defines the relative moving speed of the extruder to the printing platform, the diameter of the feeding filament $D_{\text{filament}} = 1.75$ mm.

The actual volume flow rate can be lower than the theoretical one due to the pressure loss. In order to measure the actual volume flow rate, we kept the L_D and V_F constant in the g-code and varied the L_E . For each set, eight polycarbonate fibers were produced with a deposition height of 5 mm and a 0.4 mm tungsten carbide nozzle at 330°C on the Prusa printer. We weighed the eight fibers together on an analytical balance (GH-202, A&D), and calculate the average value as the actual extruding mass M^* . Then we calculate the actual volume flow rate Q^* by the following equation:

$$Q^* = \frac{V_F M^*}{L_D \rho}, \quad (5-10)$$

where, the density of polycarbonate ρ is 1.20 g/cm³. Therefore, we obtain the volume flow rate correction factor $C_1 = Q^*/Q$ for each set (Table 5.2 and Fig. 5.15).

Table 5.2 Calculation of the volume flow rate correction factor C_1 for eight different printing parameter settings. Eight fibers were produced for each setting. Due to the small weight of each fiber, the eight fibers were measured together on a balance, then the weight was divided by eight to get the average value as the measured extruding mass in this table.

L_D (mm)	L_E (mm)	V_F (mm/min)	Theoretical volume flow rate (mm ³ /s)	Measured extruding mass (g)	Measured volume flow rate (mm ³ /s)	C_1
---------------	---------------	-------------------	--	-----------------------------------	---	-------

120	4	1929.3	2.5781	0.0119	2.6517	1.03
120	8	1929.3	5.1561	0.0206	4.6027	0.89
120	10	1929.3	6.4452	0.0253	5.6439	0.88
120	12	1929.3	7.7342	0.0293	6.5454	0.85
120	16	1929.3	10.3122	0.0383	8.5412	0.83
120	18.66	1929.3	12.0267	0.0441	9.8531	0.82
120	20	1929.3	12.8903	0.0483	10.7797	0.84
120	24	1929.3	15.4684	0.0568	12.6778	0.82

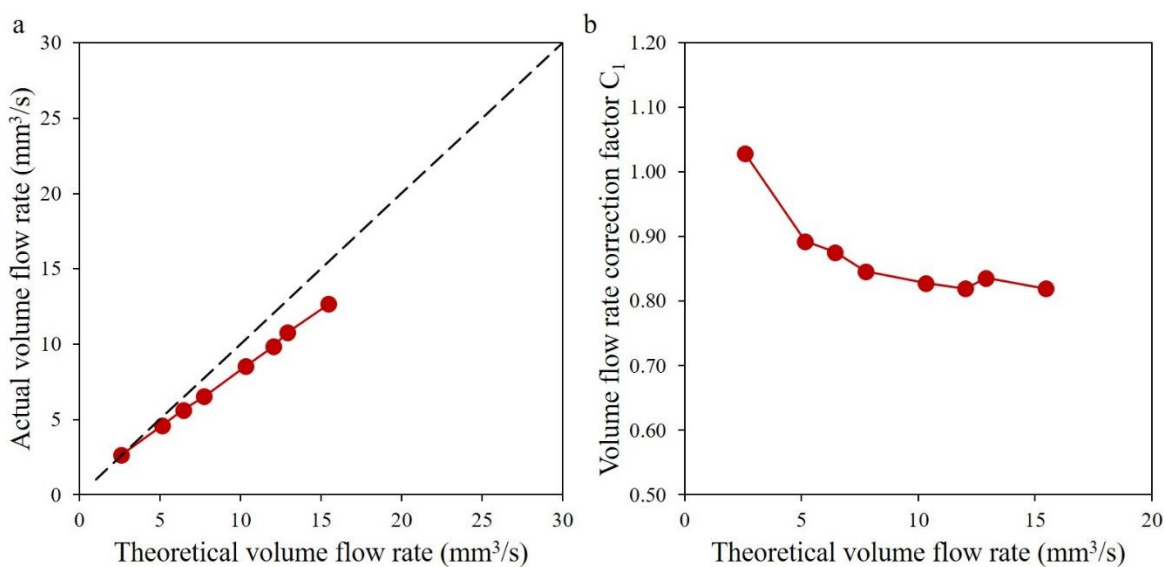


Figure 5.15 Calibration of the volume flow rate of polycarbonate filament on the Prusa 3D printer. The dashed line in **a** represents that the actual volume flow rate equals to the theoretical one.

5.5.13 Resin infiltration

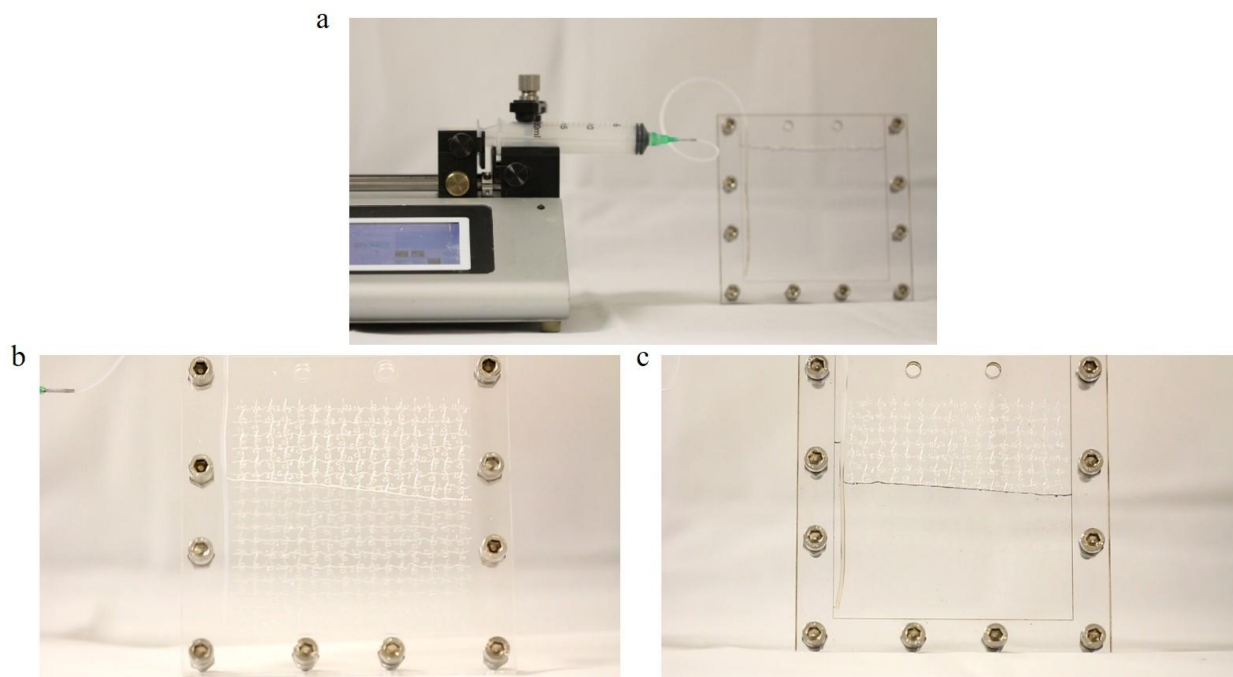


Figure 5.16 Resin infiltration setup. **a**, A micropump infiltrates the resin from the syringe into the bottom of the plastic mold via a Teflon tube. **b**, Close-up view of the infiltration process with the low RI elastomer ($RI = 1.41 @ 589\text{nm}$). **c**, Close-up view of the infiltration process with the high RI elastomer ($RI = 1.55 @ 589\text{nm}$). The alternating fiber fabric almost disappears inside the high RI elastomer resin, due to the small RI difference between the fiber ($RI = 1.58 @ 589\text{nm}$) and the high RI elastomer.

5.5.14 Design of the falling dart

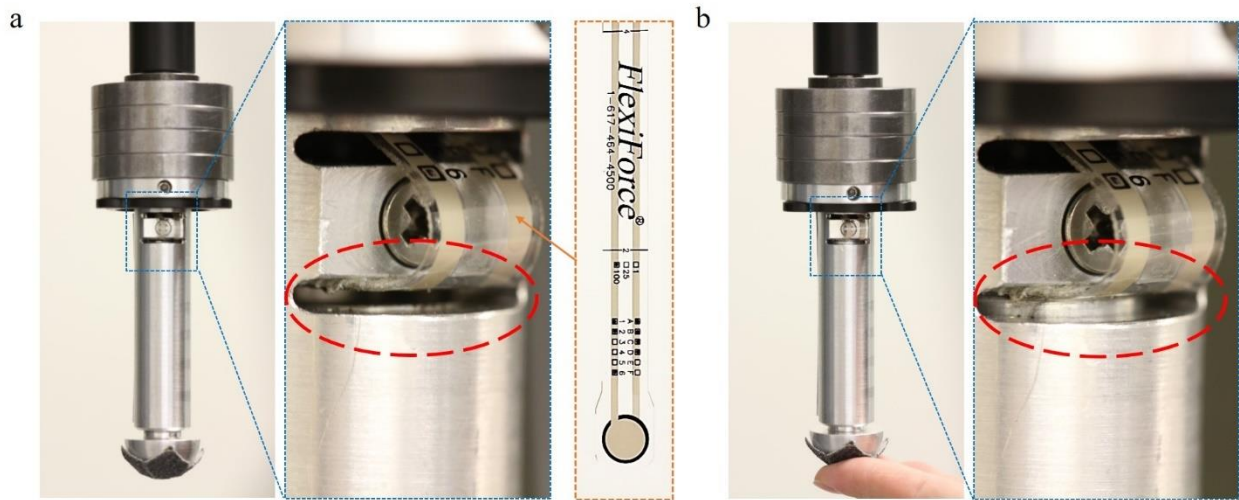


Figure 5.17 Design of the falling dart integrated with a force sensor. **a**, When the dart is overhanging, there is a gap between the force sensor and the aluminium rod inside the dart, ensuring no force is measured. **b**, When the dart is pressed, the aluminium rod will hit on the force sensor. The cross-sectional area of the aluminium rod is the same as the sensing area of the force sensor.

5.5.15 Calibration of the force sensor

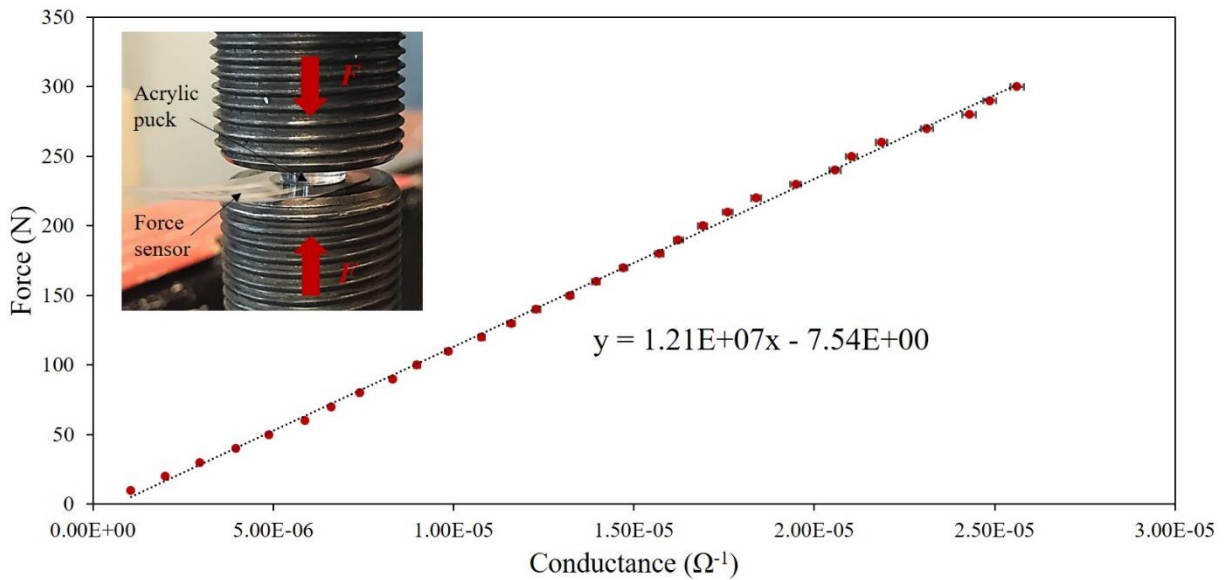


Figure 5.18 Calibration of the force sensor under static loading. We calibrated the sensor on an electromechanical machine (MTS Insight). The inset shows the setup. We used an acrylic puck with the cross-sectional area matching the sensing area of the force sensor. A compressive displacement was manually applied on the top clamp, until a certain force is reached. Then the conductance was measured under this force value with a digital multimeter (PCI-4070, National Instruments) and a LabVIEW program. The linear fitting was shown in the plot.

5.5.16 Impact tester calibration

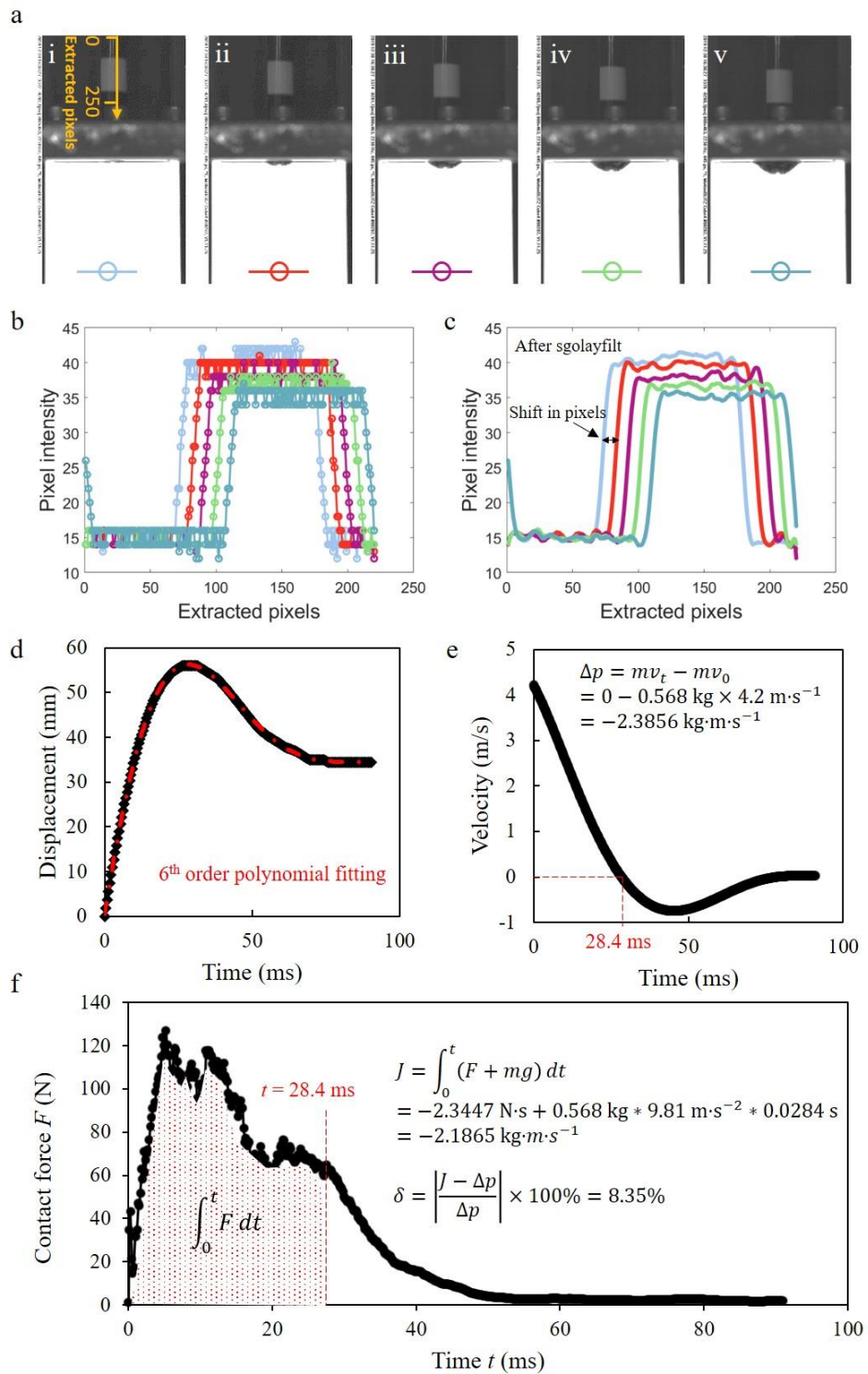


Figure 5.19 Displacement measurement and calibration in the falling dart impact test. **a**, Five consecutive high-speed camera snapshots from the impact test of the alternating fiber composite specimen. A black and white calibration paper was attached on the falling dart. **b**, The intensities of the pixels along the yellow arrow in **a** extracted by a MATLAB code. **c**, Sgolayfilt fitting of the curves in **b** with a polynomial order of 9 and frame size of 41. The MATLAB code automatically measures the shift of each curve in the unit of pixels. **d**, Displacement of the dart which is converted from the shift in pixels in **c** by the MATLAB code. The time 0 ms corresponds to the initial contact and is selected manually from the high-speed camera snapshots. **e**, Velocity of the dart which is calculated based on the 6th order polynomial fitting function in **d**. The time 28.4 ms corresponds to zero velocity. The calculation of momentum change between the initial contact and the zero-velocity time is shown in the plot. **f**, Contact force-time curve measured from the force sensor. The impulse between the initial contact and the zero-velocity time is calculated, based on the direction of gravity. The as-conducted calibration for the impact test of the alternating fiber composite specimen has a discrepancy $\delta = 8.35\%$.

CHAPTER 6 ARTICLE 3: TOUGHENING ELASTOMERS VIA MICROSTRUCTURED THERMOPLASTIC FIBERS WITH SACRIFICIAL BONDS AND HIDDEN LENGTHS

Shibo Zou¹, Daniel Therriault¹, Frédéric P. Gosselin¹

¹Laboratory for Multiscale Mechanics (LM²), Department of Mechanical Engineering, École Polytechnique de Montréal, Montréal, Canada

Submitted to Extreme Mechanics Letters on October 9th, 2020

Abstract

Soft materials capable of large inelastic deformation play an essential role in high-performance nacre-inspired architected materials with a combination of stiffness, strength and toughness. The rigid “building blocks” made from glass or ceramic in these architected materials lack inelastic deformation capabilities and thus rely on the soft interface material that bonds together these building blocks to achieve large deformation and high toughness. Here, we demonstrate the concept of achieving large inelastic deformation and high energy dissipation in soft materials by embedding microstructured thermoplastic fibers with sacrificial bonds and hidden lengths in a widely used elastomer. The microstructured fibers are fabricated by harnessing the fluid-mechanical instability of a molten polycarbonate (PC) thread on a commercial 3D printer. Polydimethylsiloxane (PDMS) resin is infiltrated around the fibers, creating a soft composite after curing. The failure mechanism and damage tolerance of the composite are analyzed through fracture tests. The high energy dissipation is found to be related to the multiple fracture events of both the sacrificial bonds and elastomer matrix. Combining the microstructured fibers and straight fibers in the elastomer composite results in a ~ 17 times increase in stiffness and a ~ 7 times increase in total energy to failure compared to the neat elastomer. Our findings in applying the sacrificial bonds and hidden lengths toughening mechanism in soft materials at the microscopic scale will facilitate the development of novel bioinspired laminated composite materials with high mechanical performance.

6.1 Introduction

Nature often assembles materials with intricate architectures, achieving functional properties that are superior than the intrinsic properties of their constituents¹⁻⁴. For example, nacre from mollusk shells, a composite of 95 vol% minerals and 5 vol% organic materials, is 3000 times more fracture resistant than the mineral component⁵. The “brick-and-mortar” architecture with microscale tablets of calcium carbonate bonded by nanoscale interlayer of chitin and protein in nacre leads to an attractive combination of stiffness, strength and toughness, which has inspired the development of advanced composite materials⁶⁻¹⁰. Soft organic materials, despite their small amounts in nacre, play a critical role in spreading nonlinear deformations over large volumes and achieving high toughness at the macroscopic scale¹¹. Saw-tooth patterns were observed on the force-extension curves of the soft organic materials in nacre¹², attributing to the breaking of sacrificial bonds and unfolding of hidden lengths at the molecular scale¹³. The sacrificial bonds and hidden lengths toughening mechanism is also found in bone¹⁴, spider silk¹⁵ and mussel byssus threads¹⁶. Recent studies⁶⁻¹⁰ on bioinspired composites often focus on duplicating the architecture in nacre at the microscopic scale to achieve crack deflection and bridging or interfacial sliding toughening mechanisms, while few^{17,18} focuses on the development of soft interface materials that mimic the large inelastic deformation and high energy dissipation of natural organic materials. The challenge lies in reproducing the sacrificial bonds and hidden lengths toughening mechanism in engineering materials.

Synthetic elastomers have a similar large deformation behavior to the soft organic materials in nacre. Previous studies⁶⁻¹⁰ using elastomers as the soft interface in nacre-inspired architected composites successfully improved the crack growth resistance, damage tolerance and impact resistance. Cavities and ligaments are formed at the elastomer interface under large deformation⁶, which is consistent with the behavior of nacre. However, the deformation of elastomers is mostly elastic and thus recoverable, while the soft organic interface in natural materials shows large inelastic deformations and high energy dissipation. Strategies like introducing sacrificial bonds and folded domains into elastomers at the molecular scale^{19,20} are effective to achieve large inelastic deformations and improve the energy dissipation in synthetic elastomers. Researchers also explored the possibility of reinforcing elastomers with rigid mesh at the microscopic or

macroscopic scale to achieve the large inelastic deformation and high energy dissipation^{21–23}. A saw-tooth tensile behavior was accomplished through the multiple fracture of the rigid mesh inside the elastomer matrix. Feng *et al.*²¹ incorporated a polyamide fabric mesh in between acrylic tapes with viscoelastic properties. The interlayer sliding induces shear stresses between the mesh and tape, which fracture the mesh into multiple islands until a critical length scale is reached. Their resulting composite shows a ~ 5 times increase in stiffness and a ~ 2 times increase in total energy to failure compared to the acrylic tape. King *et al.*²³ embedded a 3D-printed plastic mesh inside an elastomer matrix. The multiple fracture of the plastic mesh triggered by a topological interlocking mechanism leads to a ~ 60 times increase in stiffness and ~ 0.5 time increase in total energy to failure compared to the neat elastomer. Both examples adopted the double network strategy^{24,25} which uses rigid mesh as the first network to ensure high stiffness and energy dissipation, and soft matrix as the second network to maintain the structural integrity. Since the soft matrix is still intact after the rigid mesh fractures, the deformation of the composite is recoverable. The energy dissipation can be further increased by introducing molecular-level sacrificial bonds into the matrix²². Recently, we demonstrated large inelastic deformation and high energy dissipation in elastomer composites under low-velocity impact²⁶ by combining the widely used elastomer PDMS and the microstructured thermoplastic fibers with sacrificial bonds and hidden lengths^{27,28}.

The microstructured fibers with sacrificial bonds and hidden lengths are made by instability-assisted fused filament fabrication (IFFF) as shown in Fig. 6.1a. A molten polymer thread falls from a certain height onto a platform with a relative movement in the horizontal direction. Depending on the ratio of the extruding speed v_e to the printing head moving speed v_m , a series of nonlinear patterns can be produced due to the fluid-mechanical instability²⁹. In the alternating pattern that we chose for this study, the self-intersections of the molten polymer thread form weakly fused bonds after cooling, which act as sacrificial bonds under mechanical loading. Fig. 6.1b shows a representative force-effective strain curve of an alternating PC fiber (dia. = 0.44 mm) with six loops under tensile loading. Each force peak corresponds to the breaking of a sacrificial bond. After the bond breaking, the hidden length, i.e., the fiber loop, is released and unfolded. The unfolding of hidden lengths leads to large-scale plastic deformation along the fiber³⁰. Embedding the microstructured fibers in PDMS produces a transparent elastomer composite with graceful failure and superior damage tolerance²⁶. Although large inelastic deformation and high energy dissipation

were demonstrated in the elastomer composite under impact loading²⁶, the composite's fracture mechanism and damage tolerance under static loading remain to be investigated. In this work, we perform uniaxial tensile tests of the alternating fiber composite specimens in the pure shear geometry³¹ with and without a precrack to understand the interactions between crack propagation, bond breaking and fiber unfolding. Two levels of multiple fracture events are observed during tensile tests: the multiple breaking of sacrificial bonds along the fiber and the multiple cracking of the PDMS matrix. The breaking of sacrificial bonds, unfolding of fiber loops and the formation of voids in PDMS dissipate the mechanical energy which would otherwise drive the propagation of a precrack (Fig. 6.1c). The voids and exposed fibers are analogous to the micro cavities and ligaments at the soft organic interface of nacre. We also compare the total energy to failure and damage tolerance between the plain elastomer and its composites with different fiber reinforcements under uniaxial tensile loading. In the end, static puncture tests are carried out to evaluate the energy absorption and damage tolerance of the composite under transverse loading.

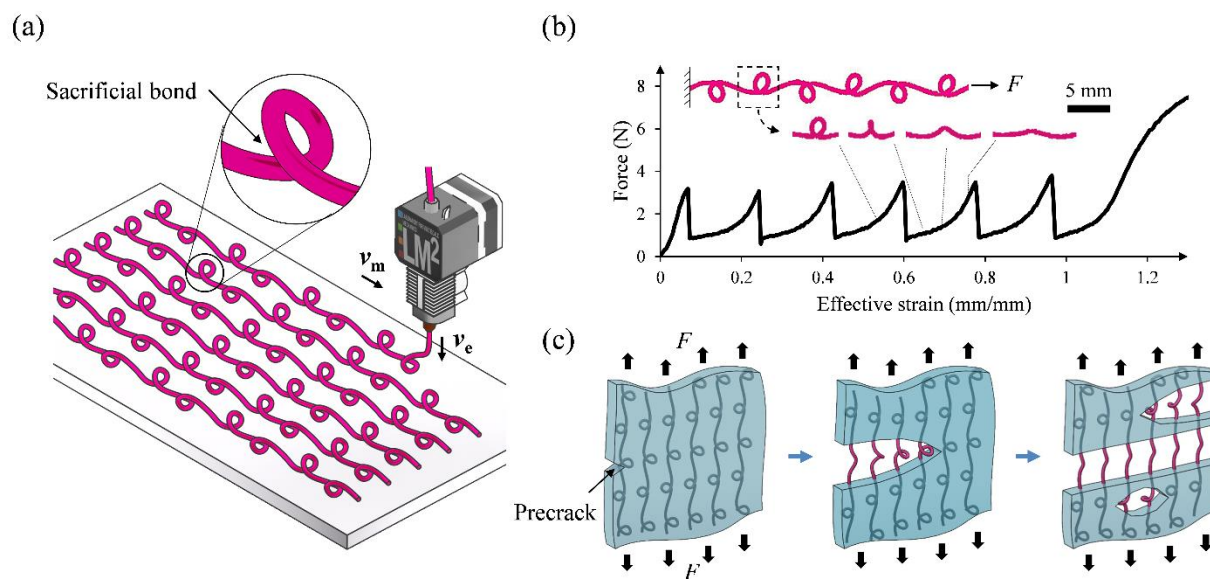


Figure 6.1 Overview of toughening elastomers via microstructured thermoplastic fibers with sacrificial bonds and hidden lengths. (a) Schematic illustration of the IFFF process. The extruding speed v_e is 2.06 times faster than the extruder moving speed v_m , producing the alternating pattern. (b) Force-effective strain curve of the as-fabricated microstructured fibers with six alternating loops. The breaking of sacrificial bonds and the unfolding of hidden lengths from one of the six loops are illustrated as an example. The fiber contours with fake color are traced from camera

snapshots during the tensile test of the microstructured fiber. (c) Schematic illustration of multiple breaking of sacrificial bonds and multiple cracking of the matrix in an elastomer composite with a precrack under tension.

6.2 Experiments

6.2.1 Microstructured fiber printing

We adopted the instability-assisted fused filament fabrication technique²⁸ to make microstructured fibers with sacrificial bonds and alternating loops. A PC filament (Top3d Filament, Dongguan, China) with a diameter $D_{\text{filament}} = 1.75$ mm was dried overnight in a vacuum oven at 65 °C before printing on a Prusa i3 printer with a nozzle diameter $d_{\text{nozzle}} = 0.4$ mm at 330 °C. We used the Simplify3D software to send the custom-written g-code to the printer. In the g-code, we chose a deposition height of 5 mm for the whole printing process to keep the deposition within the viscous steady coiling regime³². In order to produce the alternating pattern, the speed ratio v_e/v_m should be in the range of 1.57 to 2.23 according to the geometric model developed by Brun *et al.*³³. The horizontal moving speed v_m is directly determined by the printing head moving feedrate V_F from the g-code. Based on the continuity equation for incompressible fluids, the extruding speed v_e is determined by the following equation:

$$C_1 \frac{\pi}{4} D_{\text{filament}}^2 \cdot \frac{L_E}{(L_D/V_F)} = \frac{\pi}{4} (C_2 d_{\text{nozzle}})^2 \cdot v_e, \quad (6-1)$$

$$\text{i.e., } v_e = \frac{C_1 L_E V_F}{L_D} \left(\frac{D_{\text{filament}}}{C_2 d_{\text{nozzle}}} \right)^2, \quad (6-2)$$

where, the extruding length L_E of the 1.75 mm filament, the moving distance L_D of the printing head, and the printing head moving feedrate V_F are independent parameters in the g-code. We first fixed V_F at 1929.3 mm/min. Then we measured the volume flow rate correction factor C_1 (0.82) and the fiber expansion factor C_2 (1.09) experimentally²⁶. The speed ratio v_e/v_m is proportional to the ratio of two independent g-code parameters L_E/L_D :

$$r = v_e/v_m = \frac{C_1 L_E}{L_D} \left(\frac{D_{\text{filament}}}{C_2 d_{\text{nozzle}}} \right)^2. \quad (6-3)$$

We chose a speed ratio $v_c/v_m = 2.06$ to produce the alternating pattern in this work. Therefore, for a target printing distance L_D , the extruding length L_E can be calculated by equation (6-3). The horizontal printing direction was kept the same for all fibers. The fiber separation was defined in the g-code. After the printing of all fibers, a rectangular frame was printed on top of the fibers for the easy handling of the fibers without altering the distance between each fiber. The straight fibers were printed using the same g-code for alternating fibers in which the deposition height was changed to 0.4 mm. Therefore, the straight fiber has the same weight as the alternating fiber.

6.2.2 PDMS-Microstructured Fiber Composite Fabrication

Polydimethylsiloxane (Sylgard 184, Dow) was used to make all test specimens. The prepolymer base and the curing agent were thoroughly mixed at a ratio of 10:1, and then degassed in a vacuum oven at room temperature for one hour. Two acrylic plates were laser-cut and assembled into a rectangular mold with a chamber size of $100 \times 80 \times 1.5$ mm (length \times width \times depth). Before placing the as-printed fibers into the mold, two sides of the rectangular frame which are parallel to the fibers were cut, and the other two sides were cast in PDMS together with the fibers. Hence, the fibers stay aligned during the molding process. Any bubbles generated during casting would disappear after a short period in ambient environment. Then we put the mold into an oven and cured the mixture at 65°C for 4 h. The as-fabricated specimen had a thickness of 1.5 mm. We used the same process to make the plain PDMS specimen and PDMS-unidirectional fiber composite specimens. We first prepared the PDMS-alternating fiber composite specimen with 23 evenly distributed fibers and a fiber separation of 4.35 mm for the failure mechanism and crack growth resistance analysis of the composite. In order to compare the tensile behavior of different composite specimens, we then prepared the PDMS-alternating fiber and PDMS-straight fiber composite specimens with 12 evenly distributed fibers and a fiber separation of 8.7 mm, and the PDMS-hybrid fiber composite specimen with 12 alternating fibers, 11 straight fibers and a fiber separation of 4.35 mm. For the PDMS-hybrid fiber composite specimen, the alternating fibers were manually aligned to be in the middle of the straight fibers in the mold before pouring the PDMS resin. The PDMS-bidirectional fiber composite specimens for the static puncture test all have a size of $100 \times 100 \times 1.5$ mm (length \times width \times thickness) and were fabricated using the procedure described by Zou *et al.*²⁶.

6.2.3 Mechanical testing

We conducted all the mechanical tests on an MTS Insight electromechanical machine with a 100N or 1000N load cell depending on the test load range. Tensile test of the alternating fiber with six loops was carried out with a gauge length of 32 mm and crosshead speed of 500 mm/min. The pure shear specimens have a length of 100 mm and a thickness of 1.5 mm. The grips opening is 20 mm. The crosshead speed is 10 mm/min for all pure shear specimens. We glued the pure shear specimens to laser-cut polycarbonate grips with 3M silicone sealant 8661. Mounted screws were also used to tighten the grips in order to make sure that there is no slippage of the specimen. We used scissors to create the precrack with a length of 30 mm on the test specimen. Any fibers along the precrack were also cut. The crack extension of the notched plain PDMS specimen was measured by a custom-written MATLAB code which can detect the crack tip movement based on digital image analysis. The crack extension of the notched PDMS-alternating fiber composite specimen was manually measured in Image J. For a purely elastic material, the energy release rate G can be calculated by the following equation³¹:

$$G = W(\lambda)H, \quad (6-4)$$

where H is the height of the undeformed specimen, $\lambda = 1 + \varepsilon = 1 + d/H$ is the stretch ratio, d is the crosshead displacement, ε is the effective strain, $W(\lambda)$ is the strain energy density of the material ahead of the crack tip measured by integrating the area under the stress-strain curve of an unnotched sample with identical dimensions^{34,35}. The energy release rate of hyperelastic materials like PDMS can be directly calculated by equation (6-4)³⁶. A critical energy release rate G_c was calculated at the onset of crack growth with a critical stretch ratio λ_c . The G_c was taken as the fracture toughness according to previous studies^{25,37,38}. Since the PDMS-alternating fiber composite is highly dissipative, we used equation (6-4) to calculate the effective energy release rate and effective fracture toughness of the composite in order to compare with the neat elastomer. The static puncture test was carried out with a hemispherical indenter head (diameter: 25.4 mm). The specimen was clamped by two acrylic plates (thickness: 12.7 mm) with a circular opening (diameter: 76.2 mm). Mounted screws were used to tighten the plates and avoid the slippage of the specimen inside the clamps. The indenter speed was 10 mm/min for all static puncture test specimens.

6.3 Results and discussion

We first tested a PDMS-alternating fiber composite specimen without a precrack (Fig. 6.2). Three regimes were observed from the test: I. homogeneous stretching of the fiber and PDMS; II. breaking of sacrificial bonds inside PDMS, void formation in PDMS, unfolding of the released loop and segmentation of PDMS; III. Onset of fiber breakage and final failure of the specimen. Due to the similar refractive indexes of the PC fiber and PDMS²⁶, the fiber is almost invisible inside PDMS when the specimen is at rest (see Fig. 6.2a i). Once the specimen is stretched, the nonuniform deformations induce small gaps between the fiber and matrix, making the fiber contour more apparent. Fig. 6.2b shows that the force linearly increases with respect to the effective strain in regime I. In regime II, the force-effective strain curve first reaches a plateau (see Fig. 6.2b ii, $\epsilon = 0.24$ mm/mm) due to the breaking of sacrificial bonds inside the matrix. Since the adhesion between the PC fiber and PDMS is weak, the loop unfolds inside the matrix as the stretching continues, resulting in fiber-matrix sliding. The unfolding of the loop enlarges the void inside the matrix (see Fig. 6.2a ii). The void acts like an embedded crack and propagates transversely through the thickness of the specimen. Once the embedded crack becomes a through crack, the fiber is fully exposed, and the loop is free to unfold (see Fig. 6.2a iii). Then the crack propagates longitudinally in PDMS and exposes more loops. The multiple breaking of sacrificial bonds inside the matrix initiates more voids that evolve into running cracks. The interlocking between the fiber loop and the matrix triggers the multiple fracture of PDMS (see Fig. 6.2a iv). Similar fracture behavior was observed by Chang *et al.*³⁹ in PDMS-polyamide fabric composite. The detaching of fiber and PDMS makes the voids into running cracks under large deformation. In Chang *et al.*'s work, after matrix cracking, the polyamide fabric goes through a bending to stretching transition as the stretching continues³⁹. In our case, the loop first unfolds after matrix cracking with a coupled deformation of bending, torsion and axial tension⁴⁰. As the stretching continues, the straightened fiber yields under tension. The strain hardening of the fibers results in the force increase in regime II. In regime III, the fibers break one by one (see Fig. 6.2a v), leading to the gradual failure of the specimen.

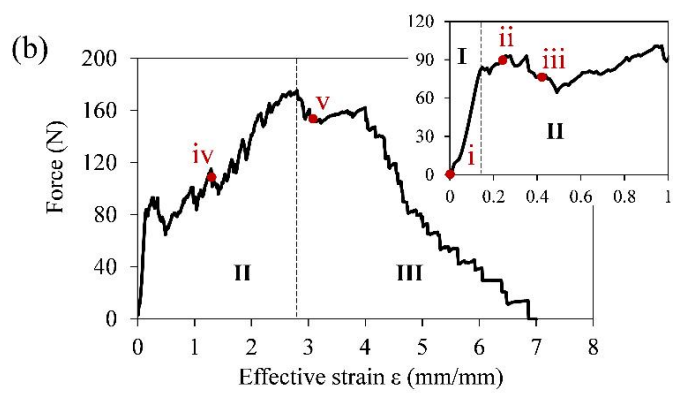
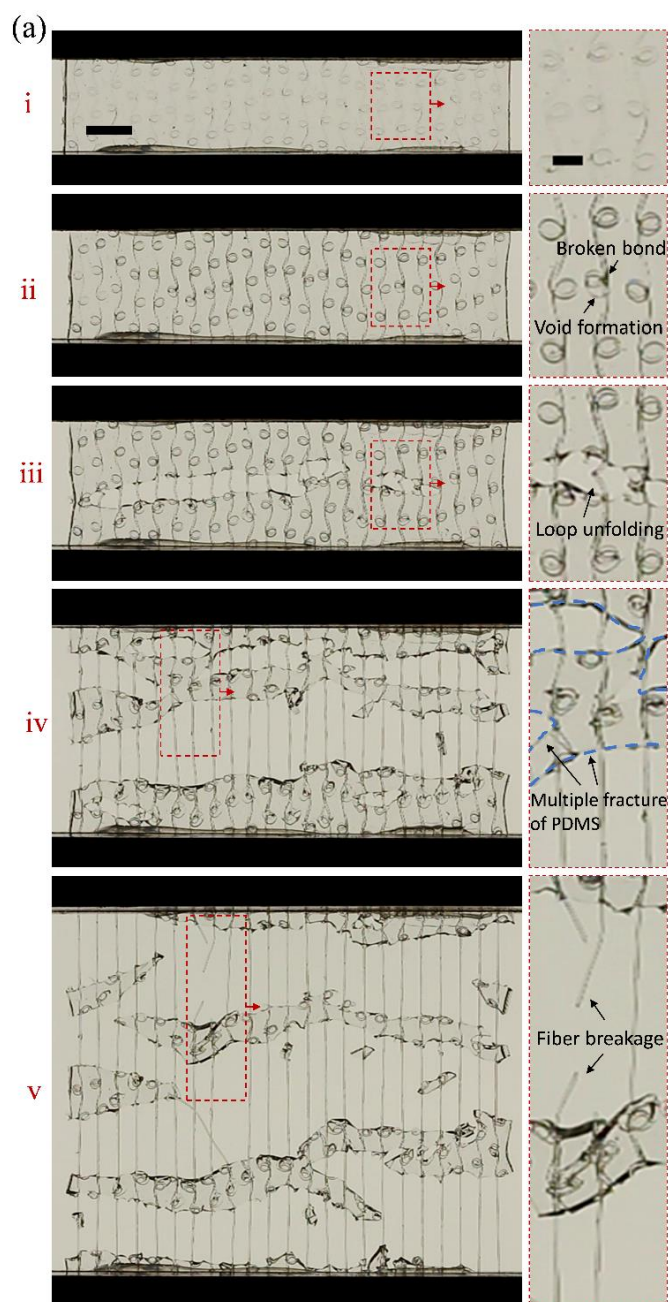


Figure 6.2 Fracture of the unnotched PDMS-alternating fiber composite specimen under uniaxial tension. (a) Camera snapshots of the fracture of the specimen at different effective strains: i. $\varepsilon = 0$; ii. $\varepsilon = 0.24$; iii. $\varepsilon = 0.41$; iv. $\varepsilon = 1.32$; v. $\varepsilon = 3.04$. Scale bar is 10 mm in the camera snapshot and 3 mm in the inset. (b) Force-effective strain curve of the PDMS-alternating fiber composite.

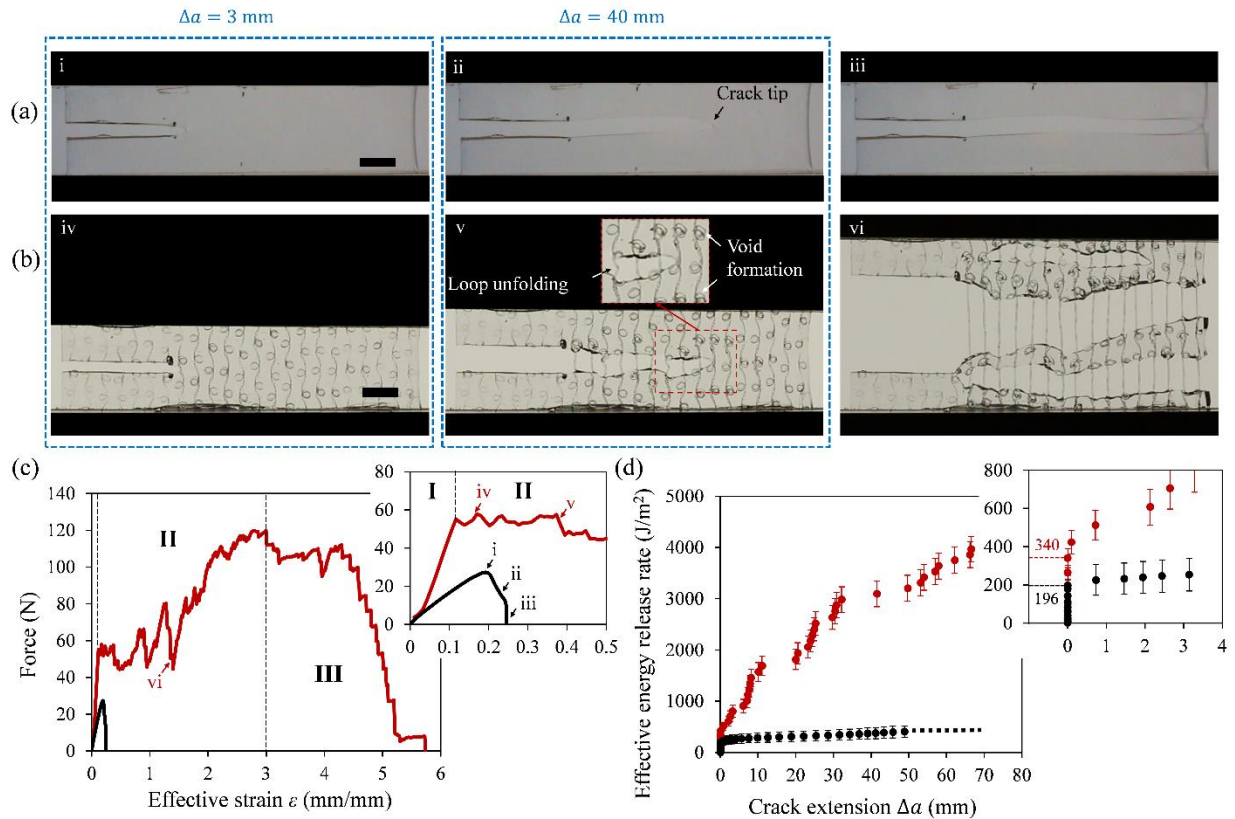


Figure 6.3 Comparison of the fracture behavior of the notched plain PDMS specimen and the notched PDMS-alternating fiber composite specimen under tensile loading. (a) Camera snapshots of the notched plain PDMS specimen at different effective strains: i. $\varepsilon = 0.19$; ii. $\varepsilon = 0.23$; iii. $\varepsilon = 0.25$. (b) Camera snapshots of the notched PDMS-alternating fiber composite specimen at different effective strains: iv. $\varepsilon = 0.17$; v. $\varepsilon = 0.38$; vi. $\varepsilon = 1.38$. All scale bars are 10 mm. (c) Force-effective strain curves of the notched plain PDMS (in black) and PDMS-alternating fiber composite (in red) specimens. (d) Crack growth resistance curves of the notched plain PDMS (in black) and PDMS-alternating fiber composite (in red) specimens. The error bar represents the standard deviation of the effective energy release rate with the strain energy density measured from three unnotched specimens with identical dimensions as the notched specimen. In the notched plain PDMS

specimen, when the crack extension exceeds 50 mm, the crack propagation accelerates rapidly, making it difficult to measure the crack extension from the camera snapshots. Since the effective energy release rate stays almost at the same level, we extrapolated the dashed line after the crack extension exceeds 50 mm. The inset shows the critical effective energy release rate of the plain PDMS ($196 \pm 74 \text{ J/m}^2$) and PDMS-alternating fiber composite ($340 \pm 49 \text{ J/m}^2$) at the onset of crack growth.

The low fracture resistance of PDMS has been previously reported^{38,39}. Fig. 6.3a shows the fracture of a notched PDMS specimen in the pure shear geometry. The crack starts to propagate at $\varepsilon = 0.18$ and runs through the whole specimen very quickly. The mechanical behavior of a notched PDMS-alternating fiber composite specimen also includes three regimes (Fig. 6.3b and c). The fiber and PDMS are co-stretched in regime I. The breaking of sacrificial bonds and the fiber-matrix detaching produce voids in regime II. With the voids developing into running cracks, the fiber is exposed and straightened, and the specimen is segmented into several isolated PDMS islands. Finally, the specimen fails after the breaking of fibers in regime III. The precrack of the PDMS-alternating fiber composite specimen starts to propagate at $\varepsilon = 0.12$ in regime II. During the crack propagation (Fig. 6.3b v), the exposed loops unfold behind the crack tip, acting as “extrinsic toughening”, while the sacrificial bonds break and voids form ahead of the crack tip, acting as “intrinsic toughening”⁴¹. In the notched PDMS specimen, the energy dissipation happens only at the crack tip, via breaking of molecule chains. While in the notched PDMS-alternating fiber composite specimen, more energy dissipation mechanisms are introduced by the breaking of sacrificial bonds, unfolding of hidden loops, growing of voids and fiber-matrix sliding, both behind and ahead of the crack tip. The crack growth resistance curves of the two specimens in Fig. 6.3d show that these extra energy dissipation mechanisms contribute to the rising crack growth resistance during the crack propagation in the composite specimen. The effective fracture toughness is not otherwise improved significantly in the composite ($340 \pm 49 \text{ J/m}^2$, Fig. 6.3d inset) specimen compared to the neat elastomer ($196 \pm 74 \text{ J/m}^2$, Fig. 6.3d inset). Compared to the tough elastomers with sacrificial bonds at the molecular scale¹⁹, our composite shows a much larger energy dissipation zone. Due to the large size of this energy dissipation zone, it should be noted that the “fracture toughness” and “energy release rate” would depend on the size of the composite specimen. Therefore, we used the term effective fracture toughness and effective energy release

rate here to show the contribution of the energy dissipation mechanisms compared to the neat elastomer. After the precrack cuts through the composite specimen longitudinally at $\varepsilon = 0.48$, the fiber continues to carry the load via plastic deformation. Further stretching develops more voids into running cracks, dissipating more energy till the final failure of the specimen.

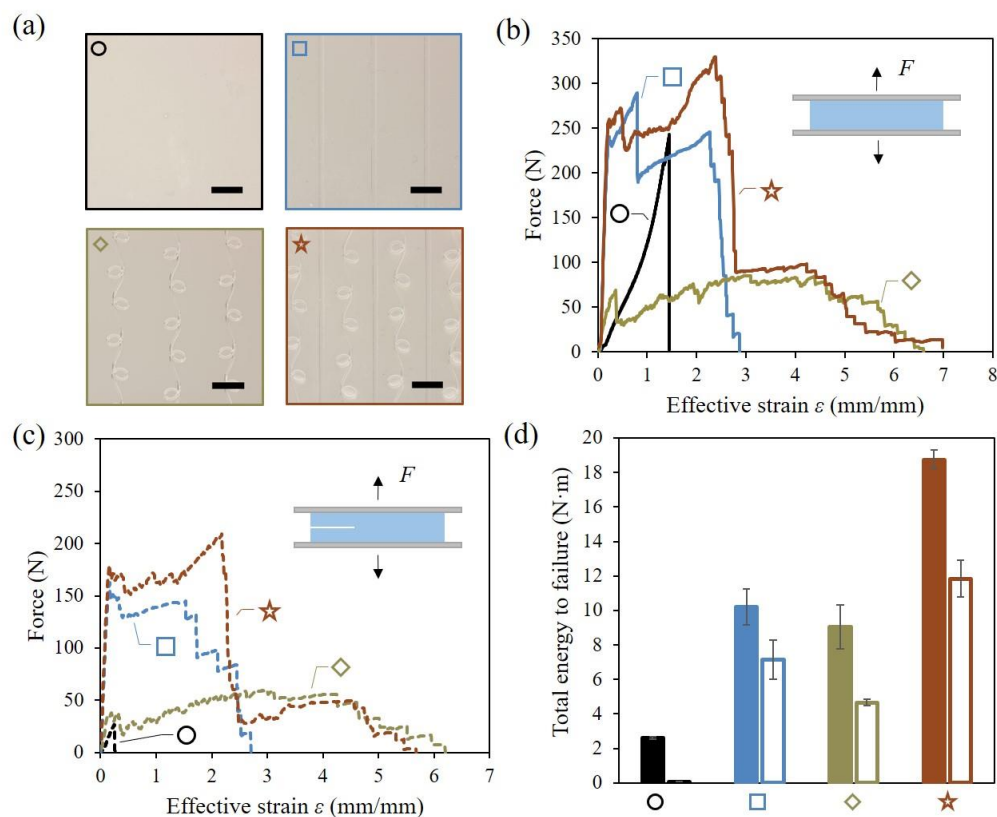


Figure 6.4 Tensile test of the plain PDMS specimen and PDMS-unidirectional fiber composite specimens with and without a precrack. (a) Optical images of test specimens: plain PDMS (○), PDMS-straight fiber composite (□), PDMS-alternating fiber composite (◇), PDMS hybrid fiber composite (★). (b) Force-effective strain curves of unnotched specimens. (c) Force-effective strain curves of notched specimens. (d) Comparison of total energy to failure of test specimens. Solid blocks represent unnotched specimens, while hollow blocks represent notched specimens. All scale bars are 5 mm.

To compare the difference in mechanical performance between the microstructured fiber and the straight fiber in the composite, we prepared four specimens in the pure shear geometry as shown in Fig. 6.4a: plain PDMS, PDMS-straight fiber composite, PDMS-alternating fiber composite, and

PDMS-hybrid fiber composite which contains both straight fiber and alternating fiber. The unnotched plain PDMS specimen exhibits a stiffness around 118 N/mm/mm and fractures at $\varepsilon = 1.45$. The unnotched alternating fiber composite specimen shows the aforementioned three regimes with a stiffness around 272 N/mm/mm and final failure at $\varepsilon = 6.61$. The unnotched straight fiber composite specimen shows a linear regime until $\varepsilon = 0.20$ on the force-effective strain curve and a high stiffness around 1718 N/mm/mm. At $\varepsilon = 0.80$, a crack initiates at the straight fiber-matrix interface and ruptures through the whole matrix, leading to the force drop on the force-effective strain curve. Then the straight fibers continue to carry the load. The strain hardening of the straight fibers leads to an increase on the force-effective strain curve. At $\varepsilon = 2.27$, the fibers start to break one by one, resulting in the final failure of the specimen at $\varepsilon = 2.86$. Compared to the as-printed straight fiber, the average fiber width of the broken straight fibers reduced by 28.3%, indicating the fibers' plastic deformation. The force-effective strain curve of the hybrid specimen is almost the sum of that of the alternating fiber and the straight fiber composite specimens, with a strain-at-failure ($\varepsilon = 6.98$) similar to the alternating fiber composite and a stiffness (2052 N/mm/mm) similar to the straight fiber composite. The notched plain PDMS specimen shows a large decrease in strength and strain at failure, while the notched composite specimens keep similar stiffness and strain at failure to their unnotched counterparts, with only a decrease in strength due to the cut of fibers along the precrack. The total energy to failure of the notched plain PDMS specimen is only 2.2% of that of the unnotched specimen, while the notched composite specimens keeps 50% – 70% of the total energy to failure of their unnotched counterparts. The high damage tolerance of the composites is mainly attributed to the plastic deformation of the alternating and/or straight fibers after matrix cracking.

We further evaluated the composite's energy absorption performance under transverse loading. Fig. 6.5a shows the four types of specimens: plain PDMS, PDMS-straight fiber composite, PDMS-alternating fiber composite, and PDMS-hybrid fiber composite. We first carried out the static puncture test with a smooth indenter head. The plain PDMS specimen endures a high transverse force up to 448 N. The specimen fails when a crack initiates at the edge of the indenter head and propagates rapidly and circularly around the indenter head. The failure of the plain PDMS specimen produces a popping sound with the remaining pieces bouncing up and down rapidly, indicating that a large amount of the energy absorption releases and transforms into sound and

kinetic energy after unloading. The material failure is more graceful in the alternating and hybrid fiber composite specimen (Fig 5b), with mechanical energies dissipated away instead of stored inside the material.

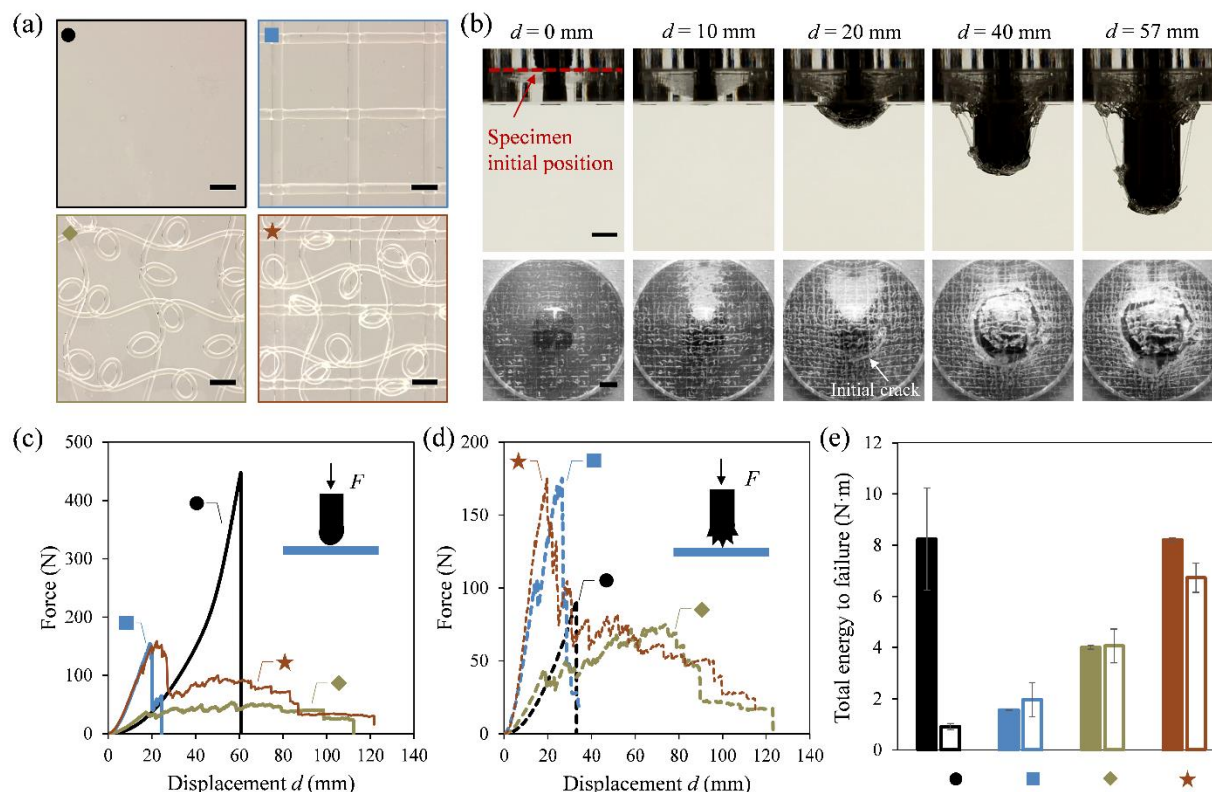


Figure 6.5 Static puncture test of the plain PDMS specimen and PDMS-bidirectional fiber composite specimens. (a) Optical images of test specimens: plain PDMS (●), PDMS-straight fiber composite (■), PDMS-alternating fiber composite (◆), PDMS-hybrid fiber composite (★). Scale bars are 2 mm. (b) Camera snapshots of the static puncture test of PDMS-hybrid fiber composite with a rough indenter head in front and bottom views. Scale bars are 10 mm. Force-displacement curves of test specimens with (c) a smooth indenter head, and (d) a rough indenter head attached with a P60 grade sandpaper. (e) Total energy to failure of test specimens. Solid blocks represent tests with the smooth indenter head, while hollow blocks represent tests with the rough indenter head.

The alternating fiber composite specimen fails with a circular crack propagation similar to that of the plain PDMS specimen, but in a much slower pace. After the circular crack propagates fully

around the indenter head, the alternating fibers continue to unfold and the interlocking between the alternating fiber and matrix leads to the multiple cracking of PDMS. In some cases, the alternating fiber cuts out from the matrix transversely, which are not observed in the tensile tests. The fiber cut-outs mostly happen at the bottom layer of the bidirectional fabric, where the alternating fibers are easier to cut through the matrix than the top layer fibers. Due to the limitation in clamping force with screws and the short clamping length (~ 12 mm) of the fiber in this study, after the cut-outs, the fibers often slide out of the matrix instead of breaking. Since the sliding of the fibers always happens before the final breaking of those fibers without cutting out from the matrix, we believe the sliding only affects the load-bearing capability, not the extensibility. In our tests, the breaking of those fibers without cutting out from the matrix results in the final failure of the alternating fiber composite.

After matrix cracking, the straight fiber composite specimen does not show large yielding of the fibers similarly to the results shown in Fig. 6.4. Conversely, the matrix cracks after the breaking of the straight fibers at the grid intersection point. The printing of the straight fiber fabric weakens the fibers at the intersections, hindering the strain hardening potential of the fibers. Fig. 6.5c shows that the loading capacities of the three composite specimens are 13% - 33% of that of the plain PDMS specimen, under current fiber volume fraction. The hybrid fiber composite specimen achieves almost the same total energy to failure as the plain PDMS specimen (Fig. 6.5e). Considering that only three alternating fibers and three straight fibers in each direction contribute to the penetration resistance under the current indenter size, the loading capacity and energy absorption can be further improved with a higher fiber volume fraction.

To evaluate the specimen's damage tolerance under transverse loading, we attached a P60 grade sandpaper to the hemispherical indenter which introduces surface cracks to the specimen during loading. Compared to the test results with a smooth indenter head, the loading capacity and energy absorption of the plain PDMS specimen with a rough indenter head reduce by 80% and 89%, respectively (Fig. 6.5d-e). In contrast, the loading capacities and energy absorptions of the composite specimens with a rough indenter head are almost the same as these with a smooth indenter head. Since the adhesion between the two layers of the fabric is weak, the alternating fiber fabric itself has very low load-bearing capability under puncture due to the slipping of the fiber around the indenter head. The high damage tolerance of the composites under transverse loading

comes from the combination of the fiber fabric and the elastomer matrix, and various resulting energy dissipation mechanisms, including the plastic deformation of the fibers and the multiple fracture of the matrix, as well as the fiber-matrix sliding and fiber cut-outs.

6.4 Conclusion

We demonstrated large inelastic deformation and high energy dissipation under tensile and transverse loads in a commercially available elastomer reinforced by microstructured fibers with sacrificial bonds and hidden lengths. The deformation and failure of the composite material are dominated by the multiple breaking of sacrificial bonds at the microscale and the multiple fracture of the elastomer matrix at the macroscale. During these multiple fracture events, the composite material dissipates energy by the breaking of sacrificial bonds, yielding and fracture of the unfolding fiber, voids formation and crack growth in the matrix, as well as fiber-matrix sliding. We show that the mechanical properties of the composite material can be tuned by controlling the pattern, volume fraction and arrangement of the reinforcing fibers. The mechanical performance of the composite may also depend on the fiber-matrix adhesion and matrix properties, which will deserve further investigations. Instability-assisted 3D printing^{27,28,42,43}, electrospinning⁴⁴⁻⁴⁶ and melt electrowriting^{47,48} provide the opportunity for the miniaturization of the microstructured fiber to accommodate different indenter sizes in real-world applications. The transparency of the composite materials can be improved by matching the refractive indexes of the fiber and the elastomer matrix for applications that require high optical transparency²⁶. The concept that we demonstrated here could be applied to any soft materials including elastomers and hydrogels in order to achieve large inelastic deformation and high energy dissipation. Combining our composite with other successful implementations of nature's toughening mechanisms in the literature⁸⁻¹⁰ is a promising way to make advanced laminate composites with high energy dissipations at multiple length scales.

Acknowledgments

We acknowledge the support of the Fonds de Recherche du Québec: Nature et Technologies (FRQNT), [funding reference number 63014], the Natural Sciences and Engineering Research Council of Canada (NSERC), [funding reference number 175791953], and the Canadian Foundation for Innovation. We are thankful for the technical advice from research associate Dr.

Kambiz Chizari, technicians Bénédict Besner and Nour Aimene. We would like to specially thank technician Yanik Landry-Ducharme for the help with the hardware of the static puncture test setup.

References

1. G. Mayer, Rigid Biological Systems as Models for Synthetic Composites, *Science*. 310 (2005) 1144–1147. <https://doi.org/10.1126/science.1116994>.
2. A.R. Studart, Towards High-Performance Bioinspired Composites, *Adv. Mater.* 24 (2012) 5024–5044. <https://doi.org/10.1002/adma.201201471>.
3. U.G.K. Wegst, H. Bai, E. Saiz, A.P. Tomsia, R.O. Ritchie, Bioinspired structural materials, *Nature Mater.* 14 (2015) 23–36. <https://doi.org/10.1038/nmat4089>.
4. S.E. Naleway, M.M. Porter, J. McKittrick, M.A. Meyers, Structural Design Elements in Biological Materials: Application to Bioinspiration, *Adv. Mater.* 27 (2015) 5455–5476. <https://doi.org/10.1002/adma.201502403>.
5. A.P. Jackson, J.F.V. Vincent, R.M. Turner, The mechanical design of nacre, *Proc. R. Soc. Lond. B*. 234 (1988) 415–440. <https://doi.org/10.1098/rspb.1988.0056>.
6. M. Mirkhalaf, A.K. Dastjerdi, F. Barthelat, Overcoming the brittleness of glass through bio-inspiration and micro-architecture, *Nat Commun.* 5 (2014) 3166. <https://doi.org/10.1038/ncomms4166>.
7. Z. Yin, A. Dastjerdi, F. Barthelat, Tough and deformable glasses with bioinspired cross-ply architectures, *Acta Biomaterialia*. 75 (2018) 439–450. <https://doi.org/10.1016/j.actbio.2018.05.012>.
8. Z. Yin, F. Hannard, F. Barthelat, Impact-resistant nacre-like transparent materials, *Science*. 364 (2019) 1260–1263. <https://doi.org/10.1126/science.aaw8988>.
9. H. Yazdani Sarvestani, M. Mirkhalaf, A.H. Akbarzadeh, D. Backman, M. Genest, B. Ashrafi, Multilayered architected ceramic panels with weak interfaces: energy absorption and multi-hit capabilities, *Materials & Design*. 167 (2019) 107627. <https://doi.org/10.1016/j.matdes.2019.107627>.

10. H. Yazdani Sarvestani, C. Beausoleil, M. Genest, B. Ashrafi, Architected ceramics with tunable toughness and stiffness, *Extreme Mechanics Letters*. 39 (2020) 100844. <https://doi.org/10.1016/j.eml.2020.100844>.
11. F. Barthelat, Z. Yin, M.J. Buehler, Structure and mechanics of interfaces in biological materials, *Nat Rev Mater*. 1 (2016) 16007. <https://doi.org/10.1038/natrevmats.2016.7>.
12. B.L. Smith, J.B. Thompson, N.A. Frederick, J. Kindt, A. Belcher, G.D. Stucky, P.K. Hansma, Molecular mechanistic origin of the toughness of natural adhesives, fibres and composites, *Nature*. 399 (1999) 761–763.
13. G.E. Fantner, E. Oroudjev, G. Schitter, L.S. Golde, P. Thurner, M.M. Finch, P. Turner, T. Gutschmann, D.E. Morse, H. Hansma, P.K. Hansma, Sacrificial Bonds and Hidden Length: Unraveling Molecular Mesostructures in Tough Materials, *Biophysical Journal*. 90 (2006) 1411–1418. <https://doi.org/10.1529/biophysj.105.069344>.
14. G.E. Fantner, T. Hassenkam, J.H. Kindt, J.C. Weaver, H. Birkedal, L. Pechenik, J.A. Cutroni, G.A.G. Cidade, G.D. Stucky, D.E. Morse, P.K. Hansma, Sacrificial bonds and hidden length dissipate energy as mineralized fibrils separate during bone fracture, *Nature Mater*. 4 (2005) 612–616. <https://doi.org/10.1038/nmat1428>.
15. A. Nova, S. Keten, N.M. Pugno, A. Redaelli, M.J. Buehler, Molecular and Nanostructural Mechanisms of Deformation, Strength and Toughness of Spider Silk Fibrils, *Nano Lett*. 10 (2010) 2626–2634. <https://doi.org/10.1021/nl101341w>.
16. M.J. Harrington, H.S. Gupta, P. Fratzl, J.H. Waite, Collagen insulated from tensile damage by domains that unfold reversibly: In situ X-ray investigation of mechanical yield and damage repair in the mussel byssus, *Journal of Structural Biology*. 167 (2009) 47–54. <https://doi.org/10.1016/j.jsb.2009.03.001>.
17. S. Cavelier, C.J. Barrett, F. Barthelat, The Mechanical Performance of a Biomimetic Nanointerface Made of Multilayered Polyelectrolytes, *Eur. J. Inorg. Chem*. 2012 (2012) 5380–5389. <https://doi.org/10.1002/ejic.201200626>.
18. Z. Tang, N.A. Kotov, S. Magonov, B. Ozturk, Nanostructured artificial nacre, *Nature Mater*. 2 (2003) 413–418. <https://doi.org/10.1038/nmat906>.

19. E. Ducrot, Y. Chen, M. Bulters, R.P. Sijbesma, C. Creton, Toughening Elastomers with Sacrificial Bonds and Watching Them Break, *Science*. 344 (2014) 186–189. <https://doi.org/10.1126/science.1248494>.
20. J. Wu, L.-H. Cai, D.A. Weitz, Tough Self-Healing Elastomers by Molecular Enforced Integration of Covalent and Reversible Networks, *Adv. Mater.* 29 (2017) 1702616. <https://doi.org/10.1002/adma.201702616>.
21. X. Feng, Z. Ma, J.V. MacArthur, C.J. Giuffre, A.F. Bastawros, W. Hong, A highly stretchable double-network composite, *Soft Matter*. 12 (2016) 8999–9006. <https://doi.org/10.1039/C6SM01781A>.
22. R. Takahashi, T.L. Sun, Y. Saruwatari, T. Kurokawa, D.R. King, J.P. Gong, Creating Stiff, Tough, and Functional Hydrogel Composites with Low-Melting-Point Alloys, *Advanced Materials*. 30 (2018) 1706885. <https://doi.org/10.1002/adma.201706885>.
23. D.R. King, T. Okumura, R. Takahashi, T. Kurokawa, J.P. Gong, Macroscale Double Networks: Design Criteria for Optimizing Strength and Toughness, *ACS Appl. Mater. Interfaces*. 11 (2019) 35343–35353. <https://doi.org/10.1021/acsami.9b12935>.
24. J.P. Gong, Y. Katsuyama, T. Kurokawa, Y. Osada, Double-Network Hydrogels with Extremely High Mechanical Strength, *Adv. Mater.* 15 (2003) 1155–1158. <https://doi.org/10.1002/adma.200304907>.
25. J.-Y. Sun, X. Zhao, W.R.K. Illeperuma, O. Chaudhuri, K.H. Oh, D.J. Mooney, J.J. Vlassak, Z. Suo, Highly stretchable and tough hydrogels, *Nature*. 489 (2012) 133–136. <https://doi.org/10.1038/nature11409>.
26. S. Zou, D. Therriault, F. Gosselin, Spider Web-Inspired Transparent Impact-Absorbing Composite, *Social Science Research Network*, Rochester, NY, 2020. <https://doi.org/10.1016/j.xcrp.2020.100240>.
27. S.-Z. Guo, F. Gosselin, N. Guerin, A.-M. Lanouette, M.-C. Heuzey, D. Therriault, Solvent-Cast Three-Dimensional Printing of Multifunctional Microsystems, *Small*. 9 (2013) 4118–4122. <https://doi.org/10.1002/sml.201300975>.

28. R. Passieux, L. Guthrie, S.H. Rad, M. Lévesque, D. Therriault, F.P. Gosselin, Instability-Assisted Direct Writing of Microstructured Fibers Featuring Sacrificial Bonds, *Adv. Mater.* 27 (2015) 3676–3680. <https://doi.org/10.1002/adma.201500603>.
29. S. Chiu-Webster, J.R. Lister, The fall of a viscous thread onto a moving surface: a ‘fluid-mechanical sewing machine,’ *Journal of Fluid Mechanics.* 569 (2006) 89. <https://doi.org/10.1017/S0022112006002503>.
30. S. Zou, D. Therriault, F.P. Gosselin, Failure mechanisms of coiling fibers with sacrificial bonds made by instability-assisted fused deposition modeling, *Soft Matter.* 14 (2018) 9777–9785. <https://doi.org/10.1039/C8SM01589A>.
31. R.S. Rivlin, A.G. Thomas, Rupture of rubber. I. Characteristic energy for tearing, *J. Polym. Sci.* 10 (1953) 291–318. <https://doi.org/10.1002/pol.1953.120100303>.
32. N.M. Ribe, M. Habibi, D. Bonn, Liquid Rope Coiling, *Annu. Rev. Fluid Mech.* 44 (2012) 249–266. <https://doi.org/10.1146/annurev-fluid-120710-101244>.
33. P.-T. Brun, C. Inamura, D. Lizardo, G. Franchin, M. Stern, P. Houk, N. Oxman, The molten glass sewing machine, *Phil. Trans. R. Soc. A.* 375 (2017) 20160156. <https://doi.org/10.1098/rsta.2016.0156>.
34. C. Creton, M. Ciccotti, Fracture and adhesion of soft materials: a review, *Rep. Prog. Phys.* 79 (2016) 046601. <https://doi.org/10.1088/0034-4885/79/4/046601>.
35. R. Long, C.-Y. Hui, Fracture toughness of hydrogels: measurement and interpretation, *Soft Matter.* 12 (2016) 8069–8086. <https://doi.org/10.1039/C6SM01694D>.
36. Y. Qi, Z. Zou, J. Xiao, R. Long, Mapping the nonlinear crack tip deformation field in soft elastomer with a particle tracking method, *Journal of the Mechanics and Physics of Solids.* 125 (2019) 326–346. <https://doi.org/10.1016/j.jmps.2018.12.018>.
37. S. Lin, C. Cao, Q. Wang, M. Gonzalez, J.E. Dolbow, X. Zhao, Design of stiff, tough and stretchy hydrogel composites via nanoscale hybrid crosslinking and macroscale fiber reinforcement, *Soft Matter.* 10 (2014) 7519–7527. <https://doi.org/10.1039/C4SM01039F>.

38. Z. Wang, C. Xiang, X. Yao, P. Le Floch, J. Mendez, Z. Suo, Stretchable materials of high toughness and low hysteresis, *Proc Natl Acad Sci USA*. 116 (2019) 5967–5972. <https://doi.org/10.1073/pnas.1821420116>.
39. R. Chang, Z. Chen, C. Yu, J. Song, An Experimental Study on Stretchy and Tough PDMS/Fabric Composites, *Journal of Applied Mechanics*. 86 (2019) 011012. <https://doi.org/10.1115/1.4041679>.
40. S. Zou, D. Therriault, F.P. Gosselin, Finite Element Simulation of Microstructured Fibers with Sacrificial Bonds, in: *Proceedings of the 2017 International Conference in Aerospace for Young Scientists*, Beihang University, Beijing, China, 2017: pp. 34–41.
41. R.O. Ritchie, The conflicts between strength and toughness, *Nature Mater*. 10 (2011) 817–822. <https://doi.org/10.1038/nmat3115>.
42. Q. Wu, S. Zou, F.P. Gosselin, D. Therriault, M.-C. Heuzey, 3D printing of a self-healing nanocomposite for stretchable sensors, *J. Mater. Chem. C*. 6 (2018) 12180–12186. <https://doi.org/10.1039/C8TC02883D>.
43. H. Wei, X. Cauchy, I.O. Navas, Y. Abderrafai, K. Chizari, U. Sundararaj, Y. Liu, J. Leng, D. Therriault, Direct 3D Printing of Hybrid Nanofiber-Based Nanocomposites for Highly Conductive and Shape Memory Applications, *ACS Appl. Mater. Interfaces*. 11 (2019) 24523–24532. <https://doi.org/10.1021/acsami.9b04245>.
44. J. Li, T. Kong, J. Yu, K.H. Lee, Y.H. Tang, K.-W. Kwok, J.T. Kim, H.C. Shum, Electrocoiling-guided printing of multiscale architectures at single-wavelength resolution, *Lab Chip*. 19 (2019) 1953–1960. <https://doi.org/10.1039/C9LC00145J>.
45. J. Tian, J. Li, A. Sauret, T. Kong, X. Wu, Y. Lu, H.C. Shum, Facile Control of Liquid-Rope Coiling With Tunable Electric Field Configuration, *Phys. Rev. Applied*. 12 (2019) 014034. <https://doi.org/10.1103/PhysRevApplied.12.014034>.
46. Y.E. Choe, G.H. Kim, A PCL/cellulose coil-shaped scaffold *via* a modified electrohydrodynamic jetting process, *Virtual and Physical Prototyping*. (2020) 1–14. <https://doi.org/10.1080/17452759.2020.1808269>.

47. I. Liashenko, A. Hrynevich, P.D. Dalton, Designing Outside the Box: Unlocking the Geometric Freedom of Melt Electrowriting using Microscale Layer Shifting, *Advanced Materials*. 32 (2020) 2001874. <https://doi.org/10.1002/adma.202001874>.
48. J.C. Kade, P.D. Dalton, Polymers for Melt Electrowriting, *Advanced Healthcare Materials*. n/a (n.d.) 2001232. <https://doi.org/10.1002/adhm.202001232>.

CHAPTER 7 GENERAL DISCUSSION

Around 1500 B.C.E., Egyptians developed composite clay bricks using straws as the reinforcement to improve the mechanical properties of bricks. The 20th Century witnessed the rapid growth of fiber-reinforced polymer composites which basically share the same principle as Egyptians' straw-bricks, *i.e.* strong fibers are embedded in a less strong matrix to achieve combined mechanical properties which are bounded by the rule of mixtures [86]. With the advent of modern characterization technologies since the late 20th Century, various intricate hierarchical architectures have been more and more recognized in many biological materials that achieve superior properties than their material constituents. The advent of various advanced manufacturing technologies such as additive manufacturing offers great opportunities to duplicate the hierarchical architectures of biological materials in engineering materials, leading to much more complex structures and superior functional properties than current fiber-reinforced polymer composites. Bioinspired architected engineering materials will be one of the focuses in advanced materials research in the coming decades.

Advanced transparent composite materials with impressive functional properties [87]–[91] have emerged during the last five years, with intricate nanoscale or microscale architectures inspired by biological materials such as nacre from mollusk shells. Nacre is a composite of 95 vol% minerals and 5 vol% organic materials and is 3000 times more fracture resistant than its mineral component [3]. The high toughness of nacre comes from its “brick-and-mortar” architecture, in which microscale tablets of calcium carbonate are bonded by nanoscale interlayer of chitin and protein. Multiscale toughening mechanisms, including the crack deflection and tablet sliding at the microscale and the breaking of sacrificial bonds at the molecular scale, contribute to the large deformation and high energy dissipation of nacre under a mechanical load. The nacre's brick wall-like microstructure has been successfully reproduced in engineering materials by “bottom-up” (freeze [92]/vacuum casting [89]) or “top-down” (laser engraving [88]) approaches. Due to the convenience of infiltration/lamination, synthetic polymers like methacrylate [92] or ethylene-vinyl acetate [88] are often used as “mortar” in conducted studies to assist the implementation of crack deflection and tablet sliding toughening mechanisms. However, the sacrificial bonds mechanism that exists in nacre's organic interface is still missing in available studies. Our transparent energy-absorbing composite with microstructured sacrificial bonds and hidden lengths described in

Chapter 5 and 6 has the potential to be integrated as “mortar” with the engineering brick-wall structure to further improve the damage tolerance and energy absorption capabilities of advanced transparent composite materials.

Our transparent energy-absorbing composite described in Chapter 5 and 6 is a first proof-of-concept of introducing microstructured sacrificial bonds and hidden lengths in engineering bulk materials. Even though we demonstrated with polycarbonate fiber and soft elastomeric matrix, the concept of energy-absorbing composite with microstructured sacrificial bonds and hidden lengths can be applied to other engineering materials, transparent or not, such as Kevlar fiber, polyamide fiber, epoxy resin, and PEEK, in order to meet the thermal, mechanical and humidity requirements in various engineering applications.

Buckling is traditionally considered as a sign of material failure which leads to the catastrophic collapse of engineering structures. Hence, buckling is often avoided in engineering practice. During the last decade, there are new trends of harnessing the buckling instability of slender structures to create new functionalities. Besides the instability-assisted deposition processes reviewed in Section 2.3, the buckling instability has also been exploited in thin shells for solar cells [93] and smart morphing [94], and ribbon networks for stretchable electronics [95] and 3D materials assembly [96]. The instability-assisted fabrication is opening exciting new opportunities for advanced materials research which would not be possible with traditional methods. Whereas this dissertation focuses on the instability harnessing on a fused filament fabrication 3D printer, other processes such as solvent-cast direct write [15], electrospinning [84], melt electro-writing [85] are also worth exploring to produce microscale or even nanoscale fibers with sacrificial bonds and hidden lengths based on any materials that can be melted or dissolved in a solvent. Other 3D printing technologies like stereolithography can also be potentially used to create materials with sacrificial bonds and hidden lengths through a classic bottom-up approach and possibly lead to different innovative structures other than coiling or alternating loops. However, the extrusion-based instability-assisted deposition process proposed in this thesis provides a low-cost, time-efficient and scalable production of fiber fabrics with sacrificial bonds and hidden lengths, compared to other bottom-up technologies.

In order to avoid the premature failures in as-fabricated fibers with sacrificial bonds and hidden lengths, the experimental and simulation results described in Chapter 4 provide an essential guide

for the material selection. Even though the premature failures of the fiber backbone in various failure modes are all attributed to high local tensile stresses, a strain at break criterion is recommended for material selections, since the full release of the hidden loop, *i.e.* the ultimate straightening of the fiber, poses a geometry requirement, not a load requirement on the material. The strain at break of the fiber material had better exceed ~ 0.2 to avoid premature failures according to Fig. 4.4d. However, the high strength of the material is still preferable in order to achieve higher energy absorption (the area under the loading curve). Further optimization studies of material and structural parameters would be necessary to achieve the maximal energy absorption in microstructured fibers with sacrificial bonds and hidden lengths.

The breaking of sacrificial bonds and unfolding of hidden lengths in IFFF-printed fibers under mechanical loads not only contribute to high energy dissipation and toughness enhancement, but also unlock more functionalities such as strain sensing. When the microstructured fiber is made from conductive materials, the breaking of sacrificial bond and unfolding of hidden length result in a stepwise increase in the overall electrical resistance of the fiber, making large strain sensing possible with brittle conductive materials. When the microstructured fiber is made from transparent light-attenuating materials, the breaking of sacrificial bond increases the light propagation path, then the unfolding of the hidden length further decreases the light transmission. As shown in Chapter 5, embedding the transparent light-attenuating microstructured fibers in a transparent matrix with a lower refractive index than the fiber leads to high optical transmittance and strain sensing capability of the composite material. Since the photoresistor used in the optical sensing system in Chapter 5 absorbs visible light with a wide wavelength range, the ambient light predominantly affects the photoresistor readings at large deformations of the fiber, making the current optical strain-sensing system unable to function under daylight. In future developments, the photoresistor and light source can be replaced with infrared photodiode and infrared emitting diode, respectively, with a matching peak wavelength to reduce the influence of ambient light. The hierarchical architecture of sacrificial bonds and hidden lengths can also be combined with other functional materials such as self-healing or shape memory materials to unlock new functionalities in future advanced materials.

This dissertation deals with one-dimensional and two-dimensional systems with microstructured fibers. Printing microstructured fibers into 3D architectures has been demonstrated by Lipton et al.

[80] and Brun et al. [63] and results in complex foams with variable stiffness (Fig. 2.24b) and glass architectures with stacking coiling loops (Fig. 2.24c). However, none of the two studies focused on the comprehensive characterization of the sacrificial bonds and hidden lengths in the 3D architecture. In fact, the printing method in these studies involves the deposition of coiling loops directly onto previous coiling loops, leading to interlayer bonding between coiling loops. The interlayer bonding would join the competition between the fiber backbone and sacrificial bond, making the fracture behavior less controllable than the fracture of one-dimensional or two-dimensional systems. Advanced topological design and printing control would be needed to take advantage of the full energy-absorbing potential of sacrificial bonds and hidden lengths in 3D architectures with sacrificial bonds and hidden lengths. As an alternative, the energy-absorbing composite described in Chapter 5 and 6 can be stacked with plastic or glass plates to produce 3D bulk materials for safety-critical engineering applications that demand high energy dissipation at large deformations.

CHAPTER 8 CONCLUSION AND RECOMMENDATIONS

8.1 Conclusion

In this dissertation, the sacrificial bonds and hidden lengths toughening mechanism was introduced to microstructured thermoplastic fibers and later to a transparent elastomeric composite through IFFF. The failure mechanisms of the microstructured fibers and the toughening mechanisms of the elastomeric composite were studied. The following conclusions are drawn from this work:

- The premature failures of the fiber backbone in microstructured PLA fibers with sacrificial bonds and coiling loops are caused by high local tensile stresses along the fiber during the bending-torsion-tension coupled deformation of the unfolding loop. Simulation results show that the successful straightening of the coiling loop involves a large-scale plastic deformation along the fiber, indicating that material yielding is indispensable to fully release the hidden lengths in microstructured fibers with sacrificial bonds. A strain at break of ~ 0.2 is recommended for the microstructured fiber material in order to fully straighten the fiber loops.
- High energy dissipation and high damage tolerance are achieved in transparent elastomeric composites reinforced by microstructured PC fibers with sacrificial bonds and hidden lengths. A bidirectional fiber fabric with functional sacrificial bonds and hidden lengths in both layers was fabricated in alternating patterns by instability-assisted fused filament fabrication. The fiber-matrix refractive index matching effectively reduces the haze of the composite. Under impact, the large-scale plastic deformation of the unfolding loops significantly increases energy dissipation and leads to hysteresis of 95.6% (dissipated energy/total absorbed energy $\times 100\%$).
- In the elastomeric composite reinforced by microstructured PC fibers with sacrificial bonds and hidden lengths, the deformation and failure of the composite are dominated by the multiple breaking of sacrificial bonds at the microscale and the multiple fracture of the elastomeric matrix at the macroscale. During these multiple fracture events, the composite material dissipates energy by the breaking of sacrificial bonds, yielding and fracture of the unfolding fiber, voids formation and crack growth in the matrix, as well as fiber-matrix sliding. Combining the microstructured fibers and straight fibers in the elastomeric

composite results in a ~ 17 times increase in stiffness and a ~ 7 times increase in total energy to failure compared to the neat elastomer.

8.2 Recommendations

Future research is recommended in the following aspects:

- The effects of bond strength on the mechanical performance of the microstructured fibers could be investigated experimentally and numerically.
- The effects of material properties on the mechanical performance of the microstructured fibers could be investigated experimentally and numerically.
- Optimization studies of material and structural parameters of the microstructured fiber should be conducted based on the finite element simulation tool.
- Shape-memory polymer or alloy could be used to make the microstructured fibers with sacrificial bonds and hidden lengths. The shape recovering behavior of the fiber would be interesting to investigate.
- Nanoscale fibers could be fabricated by electrospinning or melt electro-writing. The mechanical behavior of a single fiber and fiber fabric should be investigated.
- The effects of periodic forcing of the nozzle along the direction perpendicular to the deposition pathway could be investigated experimentally and numerically based on Brun *et al.*'s model [72]. It is possible to open up new opportunities to build complex structures as what has been achieved by Liashenko *et al.* [85].
- Current commercial laminated glass includes polymeric interlayers, which help hold together the glass fragments during fracture, but contribute little to the impact resistance. The transparent energy-absorbing composite described in Chapter 5 has huge potential to replace the polymeric interlayers in laminated glass and significantly increase the energy dissipation under impact. One challenge in developing the new laminated glass is to create a strong bonding between the transparent energy-absorbing composite and glass plates, while still maintain the full functionality of microstructured fibers with sacrificial bonds and hidden lengths inside the laminated structure.

- The soft energy-absorbing composite described in Chapter 5 and 6 could be potentially used as the “mortar” in nacre-inspired transparent composites [88] with the “brick-and-mortar” architecture to further increase the energy dissipation of the composite material.
- The fiber-matrix refractive index matching could be fulfilled using ethylene-vinyl acetate fibers (RI = ~ 1.48) and the mixture of the elastomers (Sylgard 184, RI = 1.41; OE-6550, RI = 1.55) used in Chapter 5.
- More fiber orientations in the composite material should be investigated other than the $0^\circ/90^\circ$ configuration used in this work, in order to study the influence of the orientation angle on the mechanical properties.
- The energy absorbing performance of the composite material in this work should be compared with other energy absorbing materials such as foam or cellular materials in terms of energy absorption and/or dissipation per unit mass.
- Energy-absorbing composites based on short microstructured fibers with sacrificial bonds and hidden lengths could be investigated.
- Due to the large size of the energy dissipation zone in the elastomeric composite with microstructured fibers, fracture test specimens with different sizes could be tested to see the full energy-dissipation potential of the composite.
- The effects of matrix thickness on the mechanical behavior of the elastomeric composite described in Chapter 6 should be studied experimentally and analytically. The analytical model could be potentially built based on the rule of mixtures [51].
- Digital image correlation could be used to measure the crack tip deformation field and evaluate the local energy release rate, instead of the effective energy release rate calculated in Chapter 6, through the J-integral [97].

BIBLIOGRAPHY

- [1] R. O. Ritchie, 'The conflicts between strength and toughness', *Nature Mater*, vol. 10, no. 11, pp. 817–822, Nov. 2011, doi: 10.1038/nmat3115.
- [2] A. Nova, S. Keten, N. M. Pugno, A. Redaelli, and M. J. Buehler, 'Molecular and Nanostructural Mechanisms of Deformation, Strength and Toughness of Spider Silk Fibrils', *Nano Lett.*, vol. 10, no. 7, pp. 2626–2634, Jul. 2010, doi: 10.1021/nl101341w.
- [3] B. L. Smith *et al.*, 'Molecular mechanistic origin of the toughness of natural adhesives, fibres and composites', *Nature*, vol. 399, pp. 761–763, 1999.
- [4] G. E. Fantner *et al.*, 'Sacrificial bonds and hidden length dissipate energy as mineralized fibrils separate during bone fracture', *Nature Mater*, vol. 4, no. 8, pp. 612–616, Aug. 2005, doi: 10.1038/nmat1428.
- [5] M. Rief, M. Gautel, F. Oesterhelt, J. M. Fernandez, and H. E. Gaub, 'Reversible Unfolding of Individual Titin Immunoglobulin Domains by AFM', *Science, New Series*, vol. 276, no. 5315, pp. 1109–1112, 1997.
- [6] J. P. Gong, Y. Katsuyama, T. Kurokawa, and Y. Osada, 'Double-Network Hydrogels with Extremely High Mechanical Strength', *Adv. Mater.*, vol. 15, no. 14, pp. 1155–1158, Jul. 2003, doi: 10.1002/adma.200304907.
- [7] Md. A. Haque, T. Kurokawa, and J. P. Gong, 'Super tough double network hydrogels and their application as biomaterials', *Polymer*, vol. 53, no. 9, pp. 1805–1822, Apr. 2012, doi: 10.1016/j.polymer.2012.03.013.
- [8] J.-Y. Sun *et al.*, 'Highly stretchable and tough hydrogels', *Nature*, vol. 489, no. 7414, pp. 133–136, Sep. 2012, doi: 10.1038/nature11409.
- [9] Z. Chen and H. Lu, 'Constructing sacrificial bonds and hidden lengths for ductile graphene/polyurethane elastomers with improved strength and toughness', *J. Mater. Chem.*, vol. 22, no. 25, p. 12479, 2012, doi: 10.1039/c2jm30517h.
- [10] E. Ducrot, Y. Chen, M. Bulters, R. P. Sijbesma, and C. Creton, 'Toughening Elastomers with Sacrificial Bonds and Watching Them Break', *Science*, vol. 344, no. 6180, pp. 186–189, Apr. 2014, doi: 10.1126/science.1248494.

- [11] J. Wu, L.-H. Cai, and D. A. Weitz, ‘Tough Self-Healing Elastomers by Molecular Enforced Integration of Covalent and Reversible Networks’, *Adv. Mater.*, vol. 29, no. 38, p. 1702616, Oct. 2017, doi: 10.1002/adma.201702616.
- [12] E. Filippidi *et al.*, ‘Toughening elastomers using mussel-inspired iron-catechol complexes’, *Science*, vol. 358, no. 6362, pp. 502–505, Oct. 2017, doi: 10.1126/science.aao0350.
- [13] M. J. Palmeri, K. W. Putz, and L. C. Brinson, ‘Sacrificial Bonds in Stacked-Cup Carbon Nanofibers: Biomimetic Toughening Mechanisms for Composite Systems’, *ACS Nano*, vol. 4, no. 7, pp. 4256–4264, Jul. 2010, doi: 10.1021/nn100661a.
- [14] N. M. Pugno, ‘The “Egg of Columbus” for Making the World’s Toughest Fibres’, *PLoS ONE*, vol. 9, no. 4, p. e93079, Apr. 2014, doi: 10.1371/journal.pone.0093079.
- [15] S.-Z. Guo, F. Gosselin, N. Guerin, A.-M. Lanouette, M.-C. Heuzey, and D. Therriault, ‘Solvent-Cast Three-Dimensional Printing of Multifunctional Microsystems’, *Small*, vol. 9, no. 24, pp. 4118–4122, Dec. 2013, doi: 10.1002/sml.201300975.
- [16] R. Passieux, L. Guthrie, S. H. Rad, M. Lévesque, D. Therriault, and F. P. Gosselin, ‘Instability-Assisted Direct Writing of Microstructured Fibers Featuring Sacrificial Bonds’, *Adv. Mater.*, vol. 27, no. 24, pp. 3676–3680, Jun. 2015, doi: 10.1002/adma.201500603.
- [17] F. Zhu *et al.*, ‘3D-Printed Ultratough Hydrogel Structures with Titin-like Domains’, *ACS Appl. Mater. Interfaces*, vol. 9, no. 13, pp. 11363–11367, Apr. 2017, doi: 10.1021/acsami.7b02007.
- [18] L. L. Lebel, B. Aissa, M. A. E. Khakani, and D. Therriault, ‘Ultraviolet-Assisted Direct-Write Fabrication of Carbon Nanotube/Polymer Nanocomposite Microcoils’, *Advanced Materials*, vol. 22, no. 5, pp. 592–596, 2010, doi: 10.1002/adma.200902192.
- [19] B. N. Turner, R. Strong, and S. A. Gold, ‘A review of melt extrusion additive manufacturing processes: I. Process design and modeling’, *Rapid Prototyping Journal*, vol. 20, no. 3, pp. 192–204, Apr. 2014, doi: 10.1108/RPJ-01-2013-0012.
- [20] R. D. Farahani, M. Dubé, and D. Therriault, ‘Three-Dimensional Printing of Multifunctional Nanocomposites: Manufacturing Techniques and Applications’, *Advanced Materials*, vol. 28, no. 28, pp. 5794–5821, 2016, doi: 10.1002/adma.201506215.

- [21] A. Tarakanova and M. J. Buehler, 'The role of capture spiral silk properties in the diversification of orb webs', *J. R. Soc. Interface.*, vol. 9, no. 77, pp. 3240–3248, Dec. 2012, doi: 10.1098/rsif.2012.0473.
- [22] J. M. Gosline, P. A. Guerette, C. S. Orllepp, and K. N. Savage, 'The mechanical design of spider silks: from fibroin sequence to mechanical function', *Journal of Experimental Biology*, vol. 202, no. 23, pp. 3295–3303, Dec. 1999.
- [23] B. O. Swanson, T. A. Blackledge, J. Beltrán, and C. Y. Hayashi, 'Variation in the material properties of spider dragline silk across species', *Appl. Phys. A*, vol. 82, no. 2, pp. 213–218, Feb. 2006, doi: 10.1007/s00339-005-3427-6.
- [24] D. R. Lide, *CRC Handbook of Chemistry and Physics, 85th Edition*. Taylor & Francis, 2004.
- [25] 'Kevlar® Aramid Fiber Technical Guide', p. 24.
- [26] B. D. Opell and J. E. Bond, 'Capture thread extensibility of orb-weaving spiders: testing punctuated and associative explanations of character evolution', *Biological Journal of the Linnean Society*, vol. 70, no. 1, pp. 107–120, May 2000, doi: 10.1111/j.1095-8312.2000.tb00203.x.
- [27] J. White, Ed., *Rubber technologist's handbook. Vol. 2: ed. by J. White*. Shrewsbury: Smithers Rapra Techn, 2009.
- [28] A. T. Sensenig, K. A. Lorentz, S. P. Kelly, and T. A. Blackledge, 'Spider orb webs rely on radial threads to absorb prey kinetic energy', *J. R. Soc. Interface*, vol. 9, no. 73, pp. 1880–1891, Aug. 2012, doi: 10.1098/rsif.2011.0851.
- [29] S. W. Cranford, A. Tarakanova, N. M. Pugno, and M. J. Buehler, 'Nonlinear material behaviour of spider silk yields robust webs', *Nature*, vol. 482, no. 7383, pp. 72–76, Feb. 2012, doi: 10.1038/nature10739.
- [30] J. D. van Beek, S. Hess, F. Vollrath, and B. H. Meier, 'The molecular structure of spider dragline silk: Folding and orientation of the protein backbone', *Proceedings of the National Academy of Sciences*, vol. 99, no. 16, pp. 10266–10271, Aug. 2002, doi: 10.1073/pnas.152162299.
- [31] N. Du, X. Y. Liu, J. Narayanan, L. Li, M. L. M. Lim, and D. Li, 'Design of Superior Spider Silk: From Nanostructure to Mechanical Properties', *Biophysical Journal*, p. 8.

- [32] N. Du, Z. Yang, X. Y. Liu, Y. Li, and H. Y. Xu, ‘Structural Origin of the Strain-Hardening of Spider Silk’, *Adv. Funct. Mater.*, vol. 21, no. 4, pp. 772–778, Feb. 2011, doi: 10.1002/adfm.201001397.
- [33] S. Keten, Z. Xu, B. Ihle, and M. J. Buehler, ‘Nanoconfinement controls stiffness, strength and mechanical toughness of β -sheet crystals in silk’, *Nature Materials*, vol. 9, no. 4, pp. 359–367, Apr. 2010, doi: 10.1038/nmat2704.
- [34] E. Oroudjev, J. Soares, S. Arcidiacono, J. B. Thompson, S. A. Fossey, and H. G. Hansma, ‘Segmented nanofibers of spider dragline silk: Atomic force microscopy and single-molecule force spectroscopy’, *Proceedings of the National Academy of Sciences*, vol. 99, no. Supplement 2, pp. 6460–6465, Apr. 2002, doi: 10.1073/pnas.082526499.
- [35] S. P. Kelly, A. Sensenig, K. A. Lorentz, and T. A. Blackledge, ‘Damping capacity is evolutionarily conserved in the radial silk of orb-weaving spiders’, *Zoology*, vol. 114, no. 4, pp. 233–238, Sep. 2011, doi: 10.1016/j.zool.2011.02.001.
- [36] T. E. Fisher, A. F. Oberhauser, M. Carrion-Vazquez, P. E. Marszalek, and J. M. Fernandez, ‘The study of protein mechanics with the atomic force microscope’, *Trends Biochem Sci*, vol. 24, no. 10, pp. 379–384, Oct. 1999, doi: 10.1016/s0968-0004(99)01453-x.
- [37] Y. Cao and H. Li, ‘Polyprotein of GB1 is an ideal artificial elastomeric protein’, *Nature Mater*, vol. 6, no. 2, pp. 109–114, Feb. 2007, doi: 10.1038/nmat1825.
- [38] G. E. Fantner *et al.*, ‘Sacrificial Bonds and Hidden Length: Unraveling Molecular Mesostuctures in Tough Materials’, *Biophysical Journal*, vol. 90, no. 4, pp. 1411–1418, Feb. 2006, doi: 10.1529/biophysj.105.069344.
- [39] C. Bustamante, J. F. Marko, E. D. Siggia, and S. Smith, ‘Entropic elasticity of lambda-phage DNA’, *Science*, vol. 265, no. 5178, pp. 1599–1600, Sep. 1994, doi: 10.1126/science.8079175.
- [40] A. E. Elbanna and J. M. Carlson, ‘Dynamics of Polymer Molecules with Sacrificial Bond and Hidden Length Systems: Towards a Physically-Based Mesoscopic Constitutive Law’, *PLOS ONE*, vol. 8, no. 4, p. e56118, Apr. 2013, doi: 10.1371/journal.pone.0056118.
- [41] J. Vera-Agullo, H. Varela-Rizo, J. A. Conesa, C. Almansa, C. Merino, and I. Martin-Gullon, ‘Evidence for growth mechanism and helix-spiral cone structure of stacked-cup carbon

nanofibers’, *Carbon*, vol. 45, no. 14, pp. 2751–2758, Nov. 2007, doi: 10.1016/j.carbon.2007.09.040.

[42] P. Wang, W. Liu, X. Zhang, X. Lu, and J. Yang, ‘Enhanced fracture toughness of carbon fabric/epoxy laminates with pristine and functionalized stacked-cup carbon nanofibers’, *Engineering Fracture Mechanics*, vol. 148, pp. 73–81, Nov. 2015, doi: 10.1016/j.engfracmech.2015.09.010.

[43] F. Gojny, M. Wichmann, B. Fiedler, and K. Schulte, ‘Influence of different carbon nanotubes on the mechanical properties of epoxy matrix composites – A comparative study’, *Composites Science and Technology*, vol. 65, no. 15–16, pp. 2300–2313, Dec. 2005, doi: 10.1016/j.compscitech.2005.04.021.

[44] M. J. Palmeri, K. W. Putz, T. Ramanathan, and L. C. Brinson, ‘Multi-scale reinforcement of CFRPs using carbon nanofibers’, *Composites Science and Technology*, vol. 71, no. 2, pp. 79–86, Jan. 2011, doi: 10.1016/j.compscitech.2010.10.006.

[45] S. R. Koebley, F. Vollrath, and H. C. Schniepp, ‘Toughness-enhancing metastructure in the recluse spider’s looped ribbon silk’, *Mater. Horiz.*, vol. 4, no. 3, pp. 377–382, 2017, doi: 10.1039/C6MH00473C.

[46] Q. Wu, S. Zou, F. P. Gosselin, D. Therriault, and M.-C. Heuzey, ‘3D printing of a self-healing nanocomposite for stretchable sensors’, *J. Mater. Chem. C*, vol. 6, no. 45, pp. 12180–12186, 2018, doi: 10.1039/C8TC02883D.

[47] H. Wei *et al.*, ‘Direct 3D Printing of Hybrid Nanofiber-Based Nanocomposites for Highly Conductive and Shape Memory Applications’, *ACS Appl. Mater. Interfaces*, vol. 11, no. 27, pp. 24523–24532, Jul. 2019, doi: 10.1021/acsami.9b04245.

[48] A. Berardo, M. F. Pantano, and N. M. Pugno, ‘Slip knots and unfastening topologies enhance toughness without reducing strength of silk fibroin fibres’, *Interface Focus*, vol. 6, no. 1, p. 20150060, Feb. 2016, doi: 10.1098/rsfs.2015.0060.

[49] M. F. Pantano, A. Berardo, and N. M. Pugno, ‘Tightening slip knots in raw and degummed silk to increase toughness without losing strength’, *Scientific Reports*, vol. 6, no. 1, Art. no. 1, Feb. 2016, doi: 10.1038/srep18222.

- [50] F. Bosia, E. Lepore, N. T. Alvarez, P. Miller, V. Shanov, and N. M. Pugno, ‘Knotted synthetic polymer or carbon nanotube microfibrils with enhanced toughness, up to 1400 J/g’, *Carbon*, vol. 102, pp. 116–125, Jun. 2016, doi: 10.1016/j.carbon.2016.02.025.
- [51] X. Feng, Z. Ma, J. V. MacArthur, C. J. Giuffre, A. F. Bastawros, and W. Hong, ‘A highly stretchable double-network composite’, *Soft Matter*, vol. 12, no. 44, pp. 8999–9006, 2016, doi: 10.1039/C6SM01781A.
- [52] C. B. Cooper *et al.*, ‘Toughening stretchable fibers via serial fracturing of a metallic core’, *Sci. Adv.*, vol. 5, no. 2, p. eaat4600, Feb. 2019, doi: 10.1126/sciadv.aat4600.
- [53] R. Takahashi, T. L. Sun, Y. Saruwatari, T. Kurokawa, D. R. King, and J. P. Gong, ‘Creating Stiff, Tough, and Functional Hydrogel Composites with Low-Melting-Point Alloys’, *Advanced Materials*, vol. 30, no. 16, p. 1706885, 2018, doi: 10.1002/adma.201706885.
- [54] D. R. King, T. Okumura, R. Takahashi, T. Kurokawa, and J. P. Gong, ‘Macroscale Double Networks: Design Criteria for Optimizing Strength and Toughness’, *ACS Appl. Mater. Interfaces*, vol. 11, no. 38, pp. 35343–35353, Sep. 2019, doi: 10.1021/acsami.9b12935.
- [55] Z. Wang, C. Xiang, X. Yao, P. Le Floch, J. Mendez, and Z. Suo, ‘Stretchable materials of high toughness and low hysteresis’, *Proc Natl Acad Sci USA*, vol. 116, no. 13, pp. 5967–5972, Mar. 2019, doi: 10.1073/pnas.1821420116.
- [56] C. Li, H. Yang, Z. Suo, and J. Tang, ‘Fatigue-Resistant elastomers’, *Journal of the Mechanics and Physics of Solids*, vol. 134, p. 103751, Jan. 2020, doi: 10.1016/j.jmps.2019.103751.
- [57] G. Barnes and R. Woodcock, ‘Liquid rope-coil effect’, *American Journal of Physics*, vol. 26, no. 4, pp. 205–209, 1958.
- [58] M. Maleki, M. Habibi, R. Golestanian, N. M. Ribe, and D. Bonn, ‘Liquid Rope Coiling on a Solid Surface’, *Phys. Rev. Lett.*, vol. 93, no. 21, p. 214502, Nov. 2004, doi: 10.1103/PhysRevLett.93.214502.
- [59] L. Mahadevan, W. S. Ryu, and A. D. Samuel, ‘Fluid’rope trick’investigated’, *Nature*, vol. 392, no. 6672, pp. 140–140, 1998.
- [60] N. M. Ribe, ‘Periodic folding of viscous sheets’, *Physical Review E*, vol. 68, no. 3, Sep. 2003, doi: 10.1103/PhysRevE.68.036305.

- [61] M. K. Jawed, F. Da, J. Joo, E. Grinspun, and P. M. Reis, ‘Coiling of elastic rods on rigid substrates’, *Proceedings of the National Academy of Sciences*, vol. 111, no. 41, pp. 14663–14668, Oct. 2014, doi: 10.1073/pnas.1409118111.
- [62] J. Klein *et al.*, ‘Additive Manufacturing of Optically Transparent Glass’, *3D Printing and Additive Manufacturing*, vol. 2, no. 3, pp. 92–105, Sep. 2015, doi: 10.1089/3dp.2015.0021.
- [63] P.-T. Brun *et al.*, ‘The molten glass sewing machine’, *Phil. Trans. R. Soc. A*, vol. 375, no. 2093, p. 20160156, May 2017, doi: 10.1098/rsta.2016.0156.
- [64] N. M. Ribe, ‘Coiling of viscous jets’, *Proceedings of the Royal Society A: Mathematical, Physical and Engineering Sciences*, vol. 460, no. 2051, pp. 3223–3239, Nov. 2004, doi: 10.1098/rspa.2004.1353.
- [65] N. M. Ribe, M. Habibi, and D. Bonn, ‘Liquid Rope Coiling’, *Annu. Rev. Fluid Mech.*, vol. 44, no. 1, pp. 249–266, Jan. 2012, doi: 10.1146/annurev-fluid-120710-101244.
- [66] N. M. Ribe, H. E. Huppert, M. A. Hallworth, M. Habibi, and D. Bonn, ‘Multiple coexisting states of liquid rope coiling’, *Journal of Fluid Mechanics*, vol. 555, p. 275, May 2006, doi: 10.1017/S0022112006009153.
- [67] S. Chiu-Webster and J. R. Lister, ‘The fall of a viscous thread onto a moving surface: a “fluid-mechanical sewing machine”’, *Journal of Fluid Mechanics*, vol. 569, p. 89, Dec. 2006, doi: 10.1017/S0022112006002503.
- [68] N. M. Ribe, J. R. Lister, and S. Chiu-Webster, ‘Stability of a dragged viscous thread: Onset of “stitching” in a fluid-mechanical “sewing machine”’, *Physics of Fluids*, vol. 18, no. 12, p. 124105, 2006, doi: 10.1063/1.2409617.
- [69] R. L. Welch, B. Szeto, and S. W. Morris, ‘Frequency structure of the nonlinear instability of a dragged viscous thread’, *Phys. Rev. E*, vol. 85, no. 6, p. 066209, Jun. 2012, doi: 10.1103/PhysRevE.85.066209.
- [70] P.-T. Brun, N. M. Ribe, and B. Audoly, ‘A numerical investigation of the fluid mechanical sewing machine’, *Physics of Fluids*, vol. 24, no. 4, p. 043102, 2012, doi: 10.1063/1.3703316.

- [71] M. Bergou, B. Audoly, E. Vouga, M. Wardetzky, and E. Grinspun, ‘Discrete viscous threads’, *ACM Transactions on Graphics*, vol. 29, no. 4, p. 1, Jul. 2010, doi: 10.1145/1778765.1778853.
- [72] P.-T. Brun, B. Audoly, N. M. Ribe, T. S. Eaves, and J. R. Lister, ‘Liquid Ropes: A Geometrical Model for Thin Viscous Jet Instabilities’, *Phys. Rev. Lett.*, vol. 114, no. 17, p. 174501, Apr. 2015, doi: 10.1103/PhysRevLett.114.174501.
- [73] S. W. Morris, J. H. P. Dawes, N. M. Ribe, and J. R. Lister, ‘Meandering instability of a viscous thread’, *Physical Review E*, vol. 77, no. 6, Jun. 2008, doi: 10.1103/PhysRevE.77.066218.
- [74] M. Habibi, J. Najafi, and N. M. Ribe, ‘Pattern formation in a thread falling onto a moving belt: An “elastic sewing machine”’, *Physical Review E*, vol. 84, no. 1, Jul. 2011, doi: 10.1103/PhysRevE.84.016219.
- [75] M. K. Jawed, P.-T. Brun, and P. M. Reis, ‘A Geometric Model for the Coiling of an Elastic Rod Deployed Onto a Moving Substrate’, *Journal of Applied Mechanics*, vol. 82, no. 12, p. 121007, 2015.
- [76] J. I. Lipton, M. Cutler, F. Nigl, D. Cohen, and H. Lipson, ‘Additive manufacturing for the food industry’, *Trends in Food Science & Technology*, vol. 43, no. 1, pp. 114–123, May 2015, doi: 10.1016/j.tifs.2015.02.004.
- [77] Y. E. Choe and G. H. Kim, ‘A PCL/cellulose coil-shaped scaffold *via* a modified electrohydrodynamic jetting process’, *Virtual and Physical Prototyping*, pp. 1–14, Aug. 2020, doi: 10.1080/17452759.2020.1808269.
- [78] B. Jia, L. Yu, F. Fu, L. Li, J. Zhou, and L. Zhang, ‘Preparation of helical fibers from cellulose-cuprammonium solution based on liquid rope coiling’, *RSC Adv.*, vol. 4, no. 18, pp. 9112–9117, 2014, doi: 10.1039/C3RA47031H.
- [79] H. Yuk and X. Zhao, ‘A New 3D Printing Strategy by Harnessing Deformation, Instability, and Fracture of Viscoelastic Inks’, *Adv. Mater.*, vol. 30, no. 6, p. 1704028, Feb. 2018, doi: 10.1002/adma.201704028.
- [80] J. I. Lipton and H. Lipson, ‘3D Printing Variable Stiffness Foams Using Viscous Thread Instability’, *Sci Rep*, vol. 6, no. 1, p. 29996, Sep. 2016, doi: 10.1038/srep29996.

- [81] T. Luelf, C. Bremer, and M. Wessling, ‘Rope coiling spinning of curled and meandering hollow-fiber membranes’, *Journal of Membrane Science*, vol. 506, pp. 86–94, May 2016, doi: 10.1016/j.memsci.2016.01.037.
- [82] J. Tian *et al.*, ‘Facile Control of Liquid-Rope Coiling With Tunable Electric Field Configuration’, *Phys. Rev. Applied*, vol. 12, no. 1, p. 014034, Jul. 2019, doi: 10.1103/PhysRevApplied.12.014034.
- [83] H. Yuan, Q. Zhou, B. Li, M. Bao, X. Lou, and Y. Zhang, ‘Direct printing of patterned three-dimensional ultrafine fibrous scaffolds by stable jet electrospinning for cellular ingrowth’, *Biofabrication*, vol. 7, no. 4, p. 045004, Nov. 2015, doi: 10.1088/1758-5090/7/4/045004.
- [84] J. Li *et al.*, ‘Electrocoiling-guided printing of multiscale architectures at single-wavelength resolution’, *Lab Chip*, vol. 19, no. 11, pp. 1953–1960, 2019, doi: 10.1039/C9LC00145J.
- [85] I. Liashenko, A. Hrynevich, and P. D. Dalton, ‘Designing Outside the Box: Unlocking the Geometric Freedom of Melt Electrowriting using Microscale Layer Shifting’, *Advanced Materials*, vol. 32, no. 28, p. 2001874, 2020, doi: 10.1002/adma.202001874.
- [86] T. H. Courtney, *Mechanical behavior of materials*. Long Grove, Illinois: Waveland, 2000.
- [87] Z. Yin, A. Dastjerdi, and F. Barthelat, ‘Tough and deformable glasses with bioinspired cross-ply architectures’, *Acta Biomaterialia*, vol. 75, pp. 439–450, Jul. 2018, doi: 10.1016/j.actbio.2018.05.012.
- [88] Z. Yin, F. Hannard, and F. Barthelat, ‘Impact-resistant nacre-like transparent materials’, *Science*, vol. 364, no. 6447, pp. 1260–1263, Jun. 2019, doi: 10.1126/science.aaw8988.
- [89] T. Magrini, F. Bouville, A. Lauria, H. Le Ferrand, T. P. Niebel, and A. R. Studart, ‘Transparent and tough bulk composites inspired by nacre’, *Nat Commun*, vol. 10, no. 1, p. 2794, Dec. 2019, doi: 10.1038/s41467-019-10829-2.
- [90] T. Magrini, S. Moser, M. Fellner, A. Lauria, F. Bouville, and A. R. Studart, ‘Transparent Nacre-like Composites Toughened through Mineral Bridges’, *Adv. Funct. Mater.*, vol. 30, no. 27, p. 2002149, Jul. 2020, doi: 10.1002/adfm.202002149.

- [91] Q.-F. Guan, Z.-C. Ling, Z.-M. Han, H.-B. Yang, and S.-H. Yu, 'Ultra-Strong, Ultra-Tough, Transparent, and Sustainable Nanocomposite Films for Plastic Substitute', *Matter*, vol. 3, no. 4, pp. 1308–1317, Oct. 2020, doi: 10.1016/j.matt.2020.07.014.
- [92] G. Tan *et al.*, 'Nature-Inspired Nacre-Like Composites Combining Human Tooth-Matching Elasticity and Hardness with Exceptional Damage Tolerance', *Adv. Mater.*, vol. 31, no. 52, p. 1904603, Dec. 2019, doi: 10.1002/adma.201904603.
- [93] J. B. Kim *et al.*, 'Wrinkles and deep folds as photonic structures in photovoltaics', *Nature Photon*, vol. 6, no. 5, pp. 327–332, May 2012, doi: 10.1038/nphoton.2012.70.
- [94] D. Terwagne, M. Brojan, and P. M. Reis, 'Smart Morphable Surfaces for Aerodynamic Drag Control', *Adv. Mater.*, vol. 26, no. 38, pp. 6608–6611, Oct. 2014, doi: 10.1002/adma.201401403.
- [95] Y. Sun, W. M. Choi, H. Jiang, Y. Y. Huang, and J. A. Rogers, 'Controlled buckling of semiconductor nanoribbons for stretchable electronics', *Nature Nanotech*, vol. 1, no. 3, pp. 201–207, Dec. 2006, doi: 10.1038/nnano.2006.131.
- [96] S. Xu *et al.*, 'Assembly of micro/nanomaterials into complex, three-dimensional architectures by compressive buckling', *Science*, vol. 347, no. 6218, pp. 154–159, 2015.
- [97] Y. Qi, Z. Zou, J. Xiao, and R. Long, 'Mapping the nonlinear crack tip deformation field in soft elastomer with a particle tracking method', *Journal of the Mechanics and Physics of Solids*, vol. 125, pp. 326–346, Apr. 2019, doi: 10.1016/j.jmps.2018.12.018.